

Theoretische Physik

# **Analysis of the Active Phase-Field-Crystal Model**

Inaugural-Dissertation  
zur Erlangung des Doktorgrades  
der Naturwissenschaften im Fachbereich Physik  
der Mathematisch-Naturwissenschaftlichen Fakultät  
der Westfälischen Wilhelms-Universität Münster

vorgelegt von  
**Lukas Ophaus**  
aus Coesfeld

2019



---

Dekan: Prof. Dr. Gerhard Wilde

Erster Gutachter: Prof. Dr. Uwe Thiele

Zweiter Gutachter: Prof. Dr. Stefan J. Linz

Tag der mündlichen Prüfung: \_\_\_\_\_

Tag der Promotion: \_\_\_\_\_

# Kurzzusammenfassung

Mithilfe des Phasenfeld-Kristall-Modells (PFC-Modell, auch konservierte Swift-Hohenberg-Gleichung genannt) lassen sich Übergänge zwischen flüssigen und kristallinen Zuständen verhältnismäßig einfach auf mikroskopischer Ebene beschreiben. Menzel und Löwen [Phys. Rev. Lett. **110**, 055702 (2013)] haben das PFC-Modell mit Elementen der Toner-Tu-Theorie für selbstangetriebene Teilchen kombiniert und ein Modell für Kristallisation in aktiver Materie entwickelt. Dabei können aktive Kristalle als Schwärme mit sehr hoher räumlicher Ordnung interpretiert werden. Im Rahmen des resultierenden aktiven PFC-Modells untersuchen wir lokalisierte und periodische Zustände, das heißt kristalline Cluster beziehungsweise räumlich ausgedehnte, periodische Kristalle. Als Folge der Aktivität können kristalline Zustände eine Drift-Instabilität durchlaufen und unter Beibehaltung ihrer räumlichen Struktur in bewegte Zustände übergehen.

Basierend auf linearen Stabilitätsanalysen, Zeitsimulationen und numerischer Kontinuierung stellen wir eine detaillierte Analyse der Bifurkationsstruktur von ruhenden und bewegten Zuständen im aktiven PFC-Modell vor. Auf diese Weise können wir zum Beispiel untersuchen, wie Aktivität das geneigte homokline *Snaking* von stationären lokalisierten Zuständen, das für das passive PFC-Modell beschrieben ist, verändert. Ein besonderer Schwerpunkt liegt dabei auf dem Einsetzen von Bewegung. Hier können wir zeigen, dass es entweder durch eine Drift-Pitchfork- oder eine transkritische Drift-Bifurkation erfolgt. Ein entsprechendes allgemeines analytisches Kriterium wird hergeleitet.

Die Analyse des Modells wird in einer und zwei räumlichen Dimensionen durchgeführt. Morphologische Phasendiagramme, die die Resultate der verschiedenen Analysemethoden verbinden, präsentieren Existenzbereiche verschiedener Lösungsarten. In 2d untersuchen wir außerdem, wie Aktivität die Kristallstruktur mit Übergängen von Hexagonen zu Rauten- und Streifenmustern beeinflusst.

Nach der Betrachtung von individuellen Lösungen des aktiven PFC-Modells untersuchen wir, wie zwei oder mehr bewegte lokalisierte Zustände wechselwirken. Hierfür werden numerische Kollisionsexperimente durchgeführt. Es zeigt sich, dass eine kritische minimale Weglänge notwendig ist, um die Anzahl der kollidierenden lokalisierten Zustände zu erhalten.

Schließlich werden zwei weitere Modelle für aktive Musterbildung vorgestellt, die den Selbstantrieb wie im aktiven PFC-Modell durch ein Polarisationsfeld implementieren. Durch die Analyse von ruhenden und bewegten Lösungen kann eine eingeschränkte Universalität des hergeleiteten Kriteriums für das Einsetzen der Bewegung gezeigt werden. Es ist unter anderem bei linearen Evolutionsgleichungen für die Polarisation gültig.

Die umfangreiche Analyse des vergleichsweise einfachen PFC-Modells für aktive Kristalle und Schwarmbildung erlaubt uns, ein allgemeines Verständnis der beobachteten Multistabilitäten, Hystereseeffekte und Schwellenwerte für qualitative Veränderungen zu gewinnen. Diese Analyse kann als Referenz für zukünftige Studien detaillierterer und realistischerer Modelle für aktive Kristalle dienen.



# Abstract

The phase-field-crystal (PFC) model (or conserved Swift-Hohenberg equation) provides a simple microscopic mean field description of the transition between fluid and crystalline states. Combining it with elements of the Toner-Tu theory for self-propelled particles, Menzel and Löwen [Phys. Rev. Lett. **110**, 055702 (2013)] obtained a model for crystallization in active systems. Those active crystals can be regarded as swarms of high spatial order. Within the resulting active PFC model, we study the occurrence of localized and periodic states, i.e., crystalline clusters and spatially extended crystals, respectively. Due to the activity, crystalline states can undergo a drift instability and start to travel while keeping their spatial structure.

Based on linear stability analyses, time simulations and numerical continuation of the fully nonlinear states, we present a detailed analysis of the bifurcation structure of resting and traveling states in the active PFC model. This allows us, for instance, to explore how the slanted homoclinic *snaking* of steady localized states found for the passive PFC model is amended by activity. A particular focus lies on the onset of motion, where we show that it occurs either through a drift-pitchfork bifurcation or a drift-transcritical bifurcation. A corresponding general analytical criterion is derived.

The analysis is carried out for the model in one and two spatial dimensions. Morphological phase diagrams with regions of the existence of various solution types are presented merging results from all applied analysis tools. In 2d, we study how activity influences the crystal structure with transitions from hexagons to rhombic and stripe patterns.

Having studied individual solutions of the active PFC model, we explore how two and more traveling crystallites interact by performing numerical collision experiments. A critical minimal free path is necessary to preserve the number of colliding localized states.

Finally, two more models for active patterns are presented implementing activity as done in the active PFC model. Analyzing resting and traveling solutions, a certain universality of the derived criterion for the onset of motion can be demonstrated.

The in-depth analysis of the simple PFC model for active crystals and swarm formation provides a clear general understanding of observed multistabilities, hysteresis effects and thresholds for qualitative changes of behavior. This study can serve as a reference for future analyses of more detailed models for active crystals.



# Contents

<b>Kurzzusammenfassung</b>	<b>iii</b>
<b>Abstract</b>	<b>v</b>
<b>1 Introduction</b>	<b>1</b>
1.1 Active matter and crystallization . . . . .	1
1.2 Outline . . . . .	6
<b>2 The Active Phase-Field-Crystal Model</b>	<b>7</b>
2.1 Phase-field-crystal modeling . . . . .	7
2.1.1 Density functional theory . . . . .	7
2.1.2 Dynamical density functional theory . . . . .	9
2.1.3 Derivation of PFC models . . . . .	10
2.2 Derivation of the active PFC model . . . . .	12
2.3 Governing equations . . . . .	14
2.4 Numerical approach . . . . .	15
2.4.1 Time simulations . . . . .	15
2.4.2 Continuation in parameter space . . . . .	18
2.4.3 Numerical linear stability analysis . . . . .	19
<b>3 The Liquid State and its Linear Stability</b>	<b>21</b>
3.1 Morphological phase diagram . . . . .	21
3.2 Drift velocity of crystals from LSA . . . . .	23
<b>4 Active Crystals and Crystallites in One Spatial Dimension</b>	<b>27</b>
4.1 The aPFC model in 1d . . . . .	27
4.1.1 Steady and stationary states . . . . .	27
4.1.2 Numerical continuation in 1d . . . . .	28
4.2 Periodic states . . . . .	29
4.3 Localized states . . . . .	32
4.3.1 Bifurcation structure . . . . .	37
4.3.2 Fold continuation . . . . .	39
4.3.3 Linear stability . . . . .	41
4.4 Drift instability: onset of motion . . . . .	44
4.4.1 Velocity expansion . . . . .	44
4.4.2 Translational symmetry and Goldstone modes . . . . .	47
4.4.3 The adjoint linearized operator . . . . .	48
4.4.4 Determining the adjoint eigenfunctions . . . . .	48
4.4.5 Solvability condition . . . . .	50

4.5	Morphological phase diagram . . . . .	50
4.5.1	Resting and traveling crystals and LS . . . . .	50
4.5.2	Oscillatory states . . . . .	53
4.6	Diffusion arrests motion . . . . .	55
4.7	Temperature and the onset of motion . . . . .	56
4.8	Spontaneous polarization . . . . .	57
<b>5</b>	<b>Active Crystals and Crystallites in Two Spatial Dimensions</b>	<b>59</b>
5.1	The aPFC model in 2d . . . . .	59
5.1.1	Steady and stationary states . . . . .	59
5.1.2	Numerical continuation in 2d . . . . .	60
5.2	Localized states . . . . .	61
5.2.1	Passive PFC model: slanted snaking . . . . .	62
5.2.2	Active PFC model: onset of motion . . . . .	66
5.2.3	Morphological phase diagram . . . . .	73
5.2.4	Snaking of active crystallites . . . . .	76
5.3	Periodic States . . . . .	80
5.3.1	Crystal structure and activity $v_0$ . . . . .	80
5.3.2	Pattern selection and bifurcation structure . . . . .	80
5.3.3	Morphological phase diagram . . . . .	88
<b>6</b>	<b>Interaction of Active Crystallites</b>	<b>91</b>
6.1	Collision experiments . . . . .	91
6.1.1	Two colliding crystallites . . . . .	91
6.1.2	Elastic collisions . . . . .	95
6.1.3	Free path and recovery . . . . .	96
6.2	Gas of colliding crystallites . . . . .	97
6.3	Scattering behavior in 2d . . . . .	97
<b>7</b>	<b>Towards Other Models for Active Patterns</b>	<b>101</b>
7.1	Active Swift-Hohenberg equation . . . . .	101
7.1.1	The model . . . . .	101
7.1.2	Resting and traveling patterns . . . . .	103
7.1.3	Onset of motion . . . . .	103
7.2	Active Cahn-Hilliard model . . . . .	105
7.2.1	The model . . . . .	105
7.2.2	Resting and traveling patterns . . . . .	107
7.2.3	Onset of motion . . . . .	107
7.3	Universality of the criterion for the onset of motion . . . . .	108
<b>8</b>	<b>Summary and Outlook</b>	<b>111</b>
	<b>List of Publications</b>	<b>115</b>
	<b>Bibliography</b>	<b>117</b>



# 1 Introduction

## 1.1 Active matter and crystallization

The formation of patterns has always been a fascinating phenomenon. Regular spatial, temporal and spatio-temporal patterns universally occur in nature with examples ranging from physical, chemical and biological systems to geological and even social systems [BB99, Lam98, Pis06]. When classifying macroscopic physical systems, one can distinguish, on the one hand, passive systems that are normally closed and develop towards thermodynamic equilibrium. The resulting structures can show spatial patterns, like, e.g., crystalline structures. Usually they are related to self-assembly as typical structure lengths directly result from the properties of individual constituents. On the other hand, there are active or out-of-equilibrium systems that are open and develop under permanent energy flow. There, structures are self-organized and dissipative, i.e., typical structure lengths result from transport coefficients [CH93]. One example are systems composed of active particles. Active particles like bacteria, animals or artificial micro-swimmers [WN07, RNS<sup>+</sup>99, SSG<sup>+</sup>06, Sum10] are able to transform different forms of energy into self-propelled directed motion [MJR<sup>+</sup>13, BDLL<sup>+</sup>16]. They use various energy sources to drive an internal motor mechanism and represent out of equilibrium systems driven by a continuous energy flow. Artificial micro-swimmers, for instance, turn chemical energy [HJR<sup>+</sup>07] or radiation like light [PSS<sup>+</sup>13, JYS10] or ultrasound [WCHM12] into an actively driven, self-propelled motion. Also, vibrated granular media in confined geometries are employed as good model systems for certain aspects of active matter [UMS96, AT03, WHD<sup>+</sup>13, NMR06].

In non-equilibrium systems with a large number of active particles, intriguing collective phenomena arise. In particular, short- and long-range interactions between individual particles result in alignment mechanisms that can cause directional ordering (so-called *polar ordering*) and synchronized motion of the self-propelled particles [UG11, GYU11]. The resulting collective modes of motion are often referred to as *swarming* [MJR<sup>+</sup>13]. Figure 1.1 impressively illustrates the polar ordering of a school of sardines. Without a leader, the swarm is aligned and moves as an entity in a collective motion. An example of a terrestrial swarm is given in the right panel of Fig. 1.1. A large number of sheep flock together. In their center, the sheep form a hole to avoid close distances to possible threats, e.g., a shepherd. Animals often form swarms for a better protection from predators. Further proposed functions include social interaction [AC85], enhanced foraging [PJK83, PL14] and increased efficiency of motion as often observed for birds [Fis95].

One of the most famous approaches to collective motion is the Vicsek model [VCBJ<sup>+</sup>95], where each individual particle adopts to the average direction of motion of particles in some neighborhood and in the presence of noise. In general, depending on the specific interactions between particles, their density and strength of driving (called in the following *activity*) one observes different regimes of clustering, ordering and motion that one may, in analogy to equilibrium behavior, call gas, liquid, liquid-crystalline and crystalline states [BDLL<sup>+</sup>16, MVC18]. Much recent attention focused on an actively driven condensation

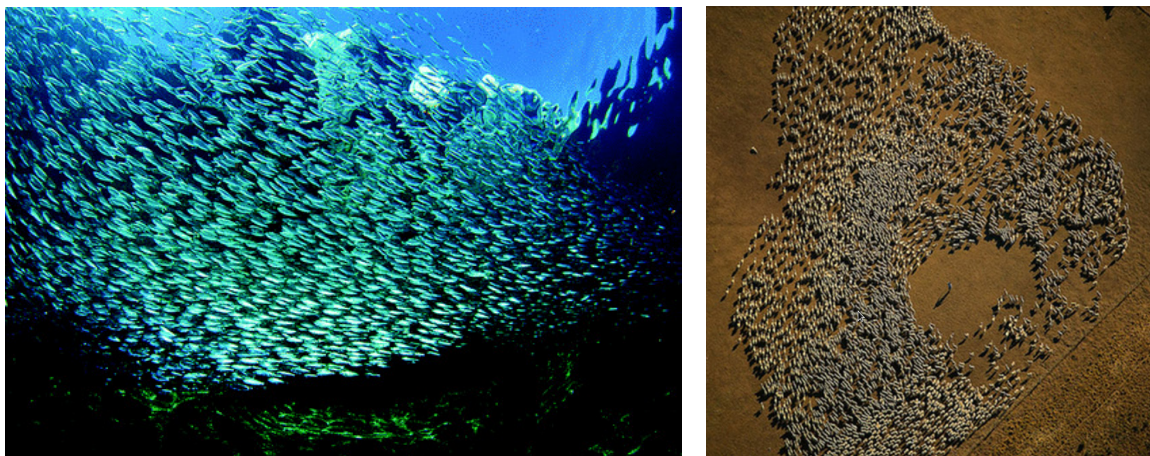


Figure 1.1: (left) School of sardines showing polar ordering. Reprinted with permission from [MJR<sup>+</sup>13], ©APS (2013). (right) Flock of sheep avoiding a shepherd. Reprinted with permission from [CK14], ©The Royal Society (2014).

phenomenon, the motility-induced phase separation between a gaseous and a liquid state that is purely due to self-propulsion [GTL<sup>+</sup>15, SSW<sup>+</sup>15, CT15].

However, for certain particle interactions and/or at quite high densities, active particles can also form crystalline ordered states, in particular, resting [TK02, TK05] or traveling [PSS<sup>+</sup>13, TCBP<sup>+</sup>12, PWL15, GTD<sup>+</sup>18] patches with nearly crystalline order [TTR05]. Figure 1.2 shows examples of crystalline structures formed by different bacteria. In the left panel, rotating cells of *Thiovulum majus*, a very fast and smoothly swimming, large and nearly spherical bacterium with flagella [GSB<sup>+</sup>06], are attracted to each other due to flow fields created by their rotation and bacterial crystals form. The connected cells can pull nutrient-rich water towards the swarm by collective motion of flagella [PL14].

The center panel depicts an inverse honeycomb structure with marine bacteria colonizing the bright areas. The right panel illustrates nematic order of elongated *Myxobacteria* cells (yellow), that can often be found in soil. *Myxobacteria* usually travel in swarms and glide possessing no flagella [MMYZ10].

These “active crystals” [ML13, MOL14] (called “flying crystals” in [TTR05] and “living crystals” in [PSS<sup>+</sup>13, MSAU<sup>+</sup>13, BDLL<sup>+</sup>16]) have properties that differ from passive crystalline clusters [SBML14, BBK<sup>+</sup>13]. The activity due to self-propulsion can change the critical temperature and density at which crystallization sets in or can even be necessary for crystalline clusters to emerge. Besides, activity can induce organized translational and rotational motion [TCBP<sup>+</sup>12, RBH13, GTL<sup>+</sup>15, GTD<sup>+</sup>18]. Patches of rotating cells of *Thiovulum majus* as depicted in Fig. 1.2(left) can also rotate as a whole.

Many particle-based models are studied that show resting, traveling and rotating, active, crystalline and amorphous clusters [EE03, REESG08, MSAU<sup>+</sup>13, NKEG14] as well as cluster-crystals [Men13, DLHG17]. For instance, a systematic study of the interplay of a short-range attraction and self-propulsion in Brownian dynamics simulations shows that clusters form at low activity (due to attraction) as well as at high activity (motility-induced) with a homogeneous active fluid phase in between [RBH13].

Besides discrete models like Vicsek’s, there exist many continuum models for active matter [TTR05, MJR<sup>+</sup>13, Men15, RKBH18]. An important example is the Toner-Tu model of

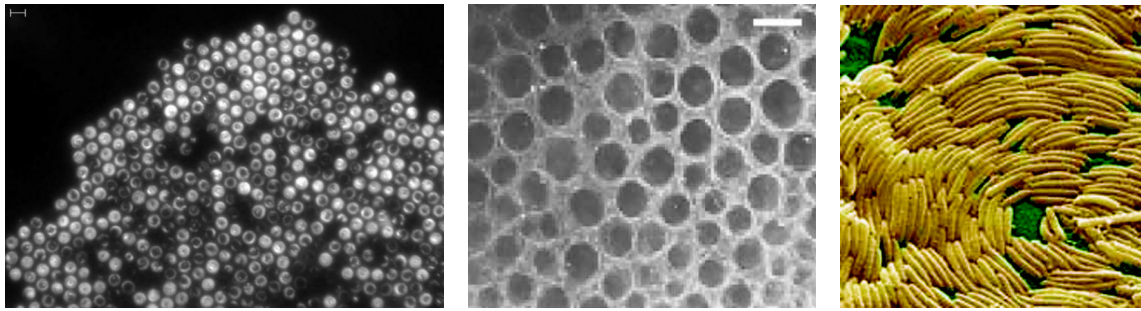


Figure 1.2: (left) Rotating cells of *Thiovulum majus* form a bacterial crystal. Individual cells glow bright in dark-field illumination. Scale bar:  $10\ \mu\text{m}$ . Reprinted with permission from [PWL15], ©Oxford University Press (2015). (center) Sulfidic marine sediment with veil formed by marine vibroid bacteria. Bacteria colonize the bright areas forming an inverse hexagonal pattern. Scale bar:  $0.5\ \text{mm}$ . Reprinted with permission from [TK05], ©APS (2005). (right) *Myxobacterial* swarm in nematic order. Reprinted with permission from [MJR<sup>+</sup>13], ©APS (2013).

swarming [TT95, TT98]. It represents a generalization of the compressible Navier-Stokes equations of hydrodynamics to systems without Galilei invariance, i.e., with preferred velocities. Recently, a simple active phase-field-crystal model (aPFC) has been proposed that describes transitions between the liquid state, on the one hand, and resting and traveling crystalline states, on the other hand [ML13]. It combines elements of the Toner-Tu theory and the (passive) phase-field-crystal model (PFC). The PFC model, or conserved Swift-Hohenberg equation (cSH), is an intensively studied microscopic mean field model for the dynamics of crystallization processes on diffusive time scales [ELW<sup>+</sup>12].

The PFC model was introduced by Elder and coworkers [EKHG02] and is applied for passive colloidal particles but also used for atomic systems [TGT<sup>+</sup>09, ERK<sup>+</sup>12]. Mathematically, it corresponds to the conserved Swift-Hohenberg equation [TAR<sup>+</sup>13] in the form of a continuity equation. In contrast to the PFC model, the regular Swift-Hohenberg (SH) equation represents non-conserved dynamics [EGU<sup>+</sup>19]. It is the standard equation for pattern formation close to the onset of a monotonous short-wave instability in systems without a conservation law, e.g., a Turing instability in reaction-diffusion systems or the onset of convection in a Bénard system [CH93]. The cSH equation was first derived as the equation governing the evolution of binary fluid convection between thermally insulating boundaries [Kno89]. In the PFC context, recent derivations from classical Dynamical Density Functional Theory (DDFT) of colloidal crystallization can be found in Refs. [ELW<sup>+</sup>12, ARTK12, ARRS19]. In the course of the derivation, the one-particle density of DDFT is shifted and scaled to obtain the order parameter field of PFC. For brevity, in the following we refer to it as “density”. Figure 1.3 depicts a typical density field in the crystalline phase as obtained by PFC models. It is taken from the original paper by Elder *et al.* [EKHG02] introducing PFC modeling.

Both, SH and PFC models, represent gradient dynamics on the same class of energy functionals [EGU<sup>+</sup>19]. However, in the active PFC model the coupling between density and polarization (quantified by the activity parameter coupling the two fields) breaks the gradient dynamics structure. Therefore, sustained motion is possible. Note that non-variational amendments of the standard non-conserved SH equation are also studied and can also show

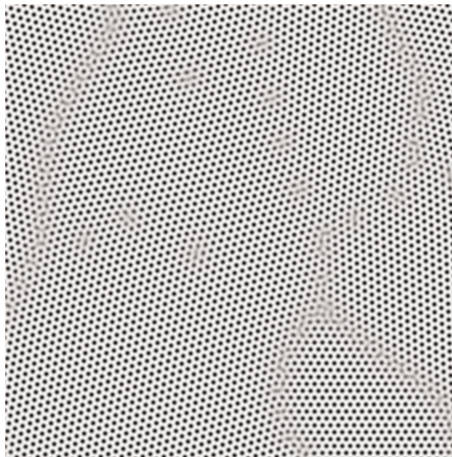


Figure 1.3: PFC models describe crystals in terms of a one-particle density. Here, a snapshot of the density field is given in gray scale. Several grain boundaries and defects in the hexagonal structure can be spotted. Reprinted with permission from [EKHG02], ©APS (2002).

traveling states, though with different onset behavior [KT07, HK11, BD12].

Up to now, the active phase-field-crystal model has mainly been employed to study the linear stability of the liquid state with respect to the development of resting and traveling crystalline patterns and in the study of domain-filling resting and traveling crystals by direct time simulations in different geometries [ML13, MOL14, CGT16, PVWL18].

The main purpose of the present work is to investigate resting and traveling, periodic and localized states and the related transitions as described by the active phase-field-crystal model. Our aim is to present a detailed analysis of the underlying bifurcation structure that can serve as a reference for future similar analyses of other models describing active crystals. This shall allow one to develop a clearer understanding of observed multistabilities of states, hysteresis effects and critical threshold states for the occurrence of qualitative changes.

Here, a particular focus is on the transitions from resting to traveling states that will turn out to occur at drift-pitchfork bifurcations and drift-transcritical bifurcations. Drift-pitchfork bifurcations are widely studied in the literature and occur in many systems [FDT91, GGGC91]. This includes the onset of motion of self-aggregating membrane channels [LNH06], drifting liquid column arrays [BFL01], chemically-driven running droplets [JBT05] and traveling localized states in reaction-diffusion systems [SOGBP97, Pis01, GBM<sup>+</sup>04]. The onset of motion for localized structures is studied, for instance, in Refs. [KM94, OGBSP98, BZB01, AASC96] while Refs. [MOL14, Osi96, PVWL18] focus on domain-filling patterns.

In the PFC and aPFC models, spatially localized states correspond to finite crystalline patches (i.e., patches of periodic states) that coexist with a liquid background (i.e., a homogeneous state). A great variety of resting localized states has been analyzed in detail for the PFC model in Ref. [TAR<sup>+</sup>13] where detailed bifurcation diagrams are given in the case of one spatial dimension (1d) while the two (2d) and three (3d) dimensional cases are investigated via direct numerical simulations. An example of a bifurcation diagram in 2d is given in [EGU<sup>+</sup>19]. We expect such resting localized states (i.e., resting crystalline patches) to exist also for the aPFC model at least at small values of the activity parameter similar

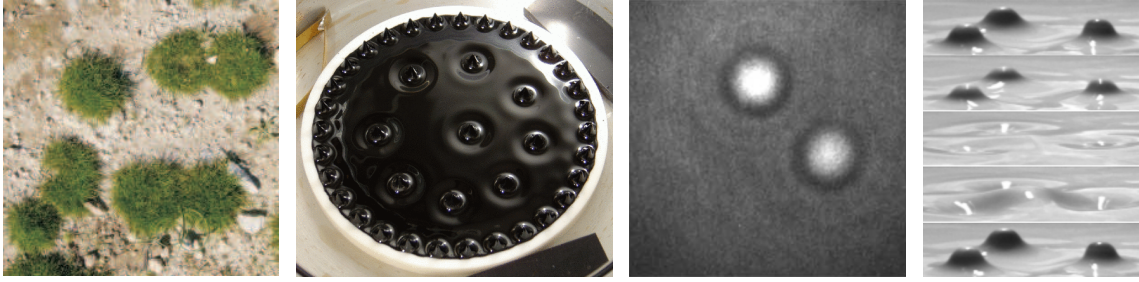


Figure 1.4: From left to right: vegetation patterns (Northern Negev, Israel). Reprinted with permission from [MGvH<sup>+</sup>04], ©Elsevier (2004). Solitons on magnetic fluids. Reprinted with permission from [RB05], ©APS (2005). Optical solitons in alkali metal vapor. Reprinted with permission from [SFAL00], ©APS (2000). Time series of oscillons in colloidal suspension. Reprinted with permission from [LHA<sup>+</sup>99], ©APS (1999).

to the clusters observed at small activity in [RBH13]. Increasing activity brings the system further out of equilibrium and we expect that the localized states begin to travel. However, we also expect that activity might destroy the crystalline patches as it increases the typical temperature for crystallization.

In general, localized states are experimentally observed and modeled in various areas of biology, chemistry and physics [Mur93, Mei82, CRT00, Kap95, BK06]. Examples (cf. Fig. 1.4) range from localized patches of vegetation patterns [MGvH<sup>+</sup>04], local arrangements of free-surface spikes of magnetic fluids closely below the onset of the Rosenzweig instability [RB05] and localized spot patterns in nonlinear optical systems [SFAL00] to oscillating localized states (oscillons) in vibrated layers of colloidal suspensions [LHA<sup>+</sup>99].

In the context of solidification described by PFC models, localized states are observed in and near the thermodynamic coexistence region of liquid and crystal state. Crystalline patches of various size and symmetry can coexist with a liquid environment depending on control parameters as mean density and undercooling [RATK12, TAR<sup>+</sup>13, EGU<sup>+</sup>19]. For instance, increasing the mean density, the crystals are enlarged as further density peaks (or “bumps”, or “spots”) are added at their borders. Ultimately, the whole finite domain is filled and the branches of localized states terminate on the branch of space filling periodic states. Within their existence region, the localized states form “snaking” branches in the bifurcation diagram [BK07, BKL<sup>+</sup>09]. An important difference between conserved systems like the PFC model and non-conserved systems like the SH model is that the snaking curves of localized states are slanted [TAR<sup>+</sup>13, BCR08, Daw08, LJBK11, PAC<sup>+</sup>17] and straight [Kno16, BK07, ALB<sup>+</sup>10, LSAC08], respectively. Note that besides mass conservation also boundary conditions can influence the type of snaking [KAC09].

We use the active phase-field-crystal model to explore how slanted snaking of localized states as a characteristic feature of pattern-forming systems with a conserved quantity is amended by activity. This includes the question when and how resting localized states start to travel and whether and how they are destroyed by activity. Furthermore, it is explored if also traveling localized states can exhibit the generic slanted snaking.

Besides the bifurcation structure, we investigate the interaction of active crystallites. A helpful and common interpretation of spatially extended patterns is to regard it as a

superposition of spatially localized units, interpreted as “particles”. Since particles interact when encountering each other, we explore the interplay in ensembles of active localized states. By collisions of traveling states, we determine a general scattering behavior and a critical free path necessary for fully elastic collisions.

Having obtained an extensive description of active crystals and crystallites in the active PFC model, we raise the question how other pattern forming models react to activity implemented by a coupled polarization field. We sketch two more models for active patterns by introducing an active Swift-Hohenberg-type model and an active Cahn-Hilliard (CH) equation [CH58, Cah65]. The two models are chosen to study a non-conserved model (SH) and an additional prominent model with a conserved dynamics (CH). Besides the paradigmatic Swift-Hohenberg equation, the Cahn-Hilliard equation is a basic model for phase separation and decomposition dynamics [CH58, Cah65]. Results are compared to the active PFC-framework.

The main purpose of this thesis is to provide an in-depth analysis of a simple model for active crystals and swarm formation in order to develop a clearer general understanding of observed multistabilities, hysteresis effects and thresholds for qualitative changes of solutions. This study can serve as a reference for future analyses of more detailed models for active crystals.

## 1.2 Outline

The thesis is organized as follows: Chapter 2 introduces phase-field-crystal modeling and its theoretical background. Furthermore, the derivation of the active PFC model and numerical approaches are presented. Chapter 3 analyzes the linear stability of the uniform state (liquid state) and offers a first morphological phase diagram. Then, chapters 4 and 5 employ numerical continuation techniques to determine bifurcation diagrams for resting and traveling periodic states (crystal) and localized states (crystallites coexisting with liquid). The mean density and the activity parameter act as main control parameters. In particular, we study the onset of motion where resting states undergo a drift instability and start to travel while keeping their spatial structure. An analytical criterion for the drift bifurcation is derived and numerically verified. Note that chapter 4 deals with crystalline states in one spatial dimension (1d), while chapter 5 investigates the active PFC model in 2d.

The bifurcation diagrams provide suitable parameters for collision trials. Chapter 6 studies the interaction of localized states focusing on numerical scattering experiments. In chapter 7, two more models for active patterns are stated and analyzed. We introduce an active Swift-Hohenberg equation and an active Cahn-Hilliard equation and study resting and traveling solutions. Finally, we conclude the thesis in chapter 8 by offering a summary and an outlook.

## 2 The Active Phase-Field-Crystal Model

In this chapter, we first schematically outline the basic concept of the passive phase-field-crystal (PFC) model and present its derivation from dynamical density functional theory (DDFT) as done in the review [ELW<sup>+</sup>12]. The review offers an extensive overview of concepts and applications of the PFC method. Besides, [ARRS19] provides additional insights into the derivation of PFC models and consequences of employed approximations.

Secondly, also on the basis of DDFT, the active PFC model is derived following the approach in [MOL14].

### 2.1 Phase-field-crystal modeling

Since its introduction by Elder and coworkers in 2002 [EKHG02], PFC models have proven to be an efficient method for modeling crystalline self-organization and solidification with particle resolution. The method contains the essential physics for transitions between liquid and crystalline states and can be regarded as a simple microscopic mean field description for various crystallization and freezing phenomena.

Mathematically, the PFC model corresponds to the conserved Swift-Hohenberg equation (cSH) [TAR<sup>+</sup>13]. The fairly simple free-energy functional from which it is obtained is of Swift-Hohenberg type [CH93] with essentially only one control parameter (setting an effective temperature). Despite the small number of parameters, PFC models exhibit a rather complex phase diagram and can even reach a quantitative level for specific applications. However, designing materials with specific properties from PFC computations has not been accomplished yet [ELW<sup>+</sup>12].

Even though PFC modeling has been linked to DDFT, initially it was proposed as a phase-field theory (PF) with incorporated microscopic material properties. Figure 2.1 illustrates to which level of granularity DDFT, PFC and PF modeling correspond.

The next sections schematically present how PFC models can be derived from classical DDFT and its static correspondent DFT.

#### 2.1.1 Density functional theory

DFT describes crystallization on particle level by treating it as a classical interacting many-body system. Starting from effective particle interactions, free-energy functionals and particle-particle correlations are calculated. These energy functionals provide a starting point for PFC approaches that can be regarded as more coarse-grained models in comparison with DFT.

As Fig. 2.1 illustrates, classical DFT is a microscopic theory. It describes liquids in equilibrium, with the only input being particle correlations and thermodynamic conditions. The central idea is to express the free energy of the many-particle systems as a functional of a one-particle density. In the scope of DFT, all quantities are static.

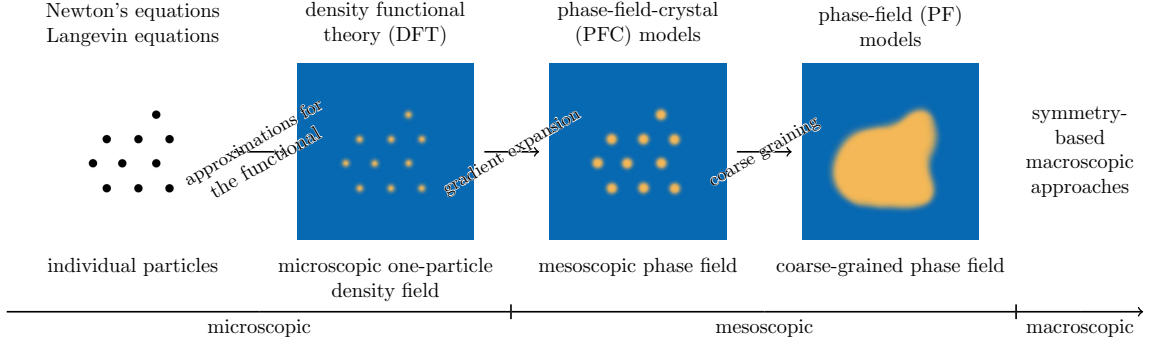


Figure 2.1: Schematic levels of granularity and corresponding models. The starting point of the hierarchy of theories are classical particles subject to Brownian motion governed by Langevin equations. cf. [ELW<sup>+</sup>12]

In detail, DFT describes a system of  $N$  classical particles at position  $\mathbf{r}_i$  ( $i = 1, \dots, N$ ) by the microscopic one-particle density  $\rho(\mathbf{r})$ . Thermodynamic conditions of the problem are set by the temperature  $T$  and the chemical potential  $\mu$ .  $\rho$  is given by

$$\rho(\mathbf{r}) = \left\langle \sum_{i=1}^N \delta(\mathbf{r} - \mathbf{r}_i) \right\rangle \quad (2.1)$$

with  $\langle \cdot \rangle$  denoting a normalized canonical ensemble average.

The theory is based on the pioneering work in the context of quantum physics of Hohenberg and Kohn [HK64] (for which Kohn won the Nobel Prize in chemistry in 1998) stating that there exists a unique grand canonical free-energy functional  $\Omega(T, \mu, \rho(\mathbf{r}))$  of the one-particle density that is minimized at equilibrium, i.e.,

$$\frac{\delta\Omega[T, \mu, \rho(\mathbf{r})]}{\delta\rho(\mathbf{r})} = 0. \quad (2.2)$$

The functional is unknown, however, and needs to be approximated. It is usually expressed in terms of the Helmholtz free-energy functional  $\mathcal{F}[T, \rho(\mathbf{r})]$  which is connected to  $\Omega$  by a Legendre transformation:

$$\Omega[T, \mu, \rho] = \mathcal{F}[T, \rho] - \mu \int_V d\mathbf{r} \rho(\mathbf{r}) = \mathcal{F}[T, \rho] - \mu N. \quad (2.3)$$

The functional derivative (2.2) follows as

$$\frac{\delta\Omega}{\delta\rho} = \frac{\delta\mathcal{F}}{\delta\rho} - \mu \quad (2.4)$$

and  $\delta\mathcal{F}/\delta\rho = \mu$  at equilibrium.  $\mathcal{F}$  is usually decomposed into three contributions

$$\mathcal{F}[T, \rho] = \mathcal{F}_{\text{id}}[T, \rho] + \mathcal{F}_{\text{exc}}[T, \rho] + \mathcal{F}_{\text{ext}}[T, \rho], \quad (2.5)$$

where  $\mathcal{F}_{\text{id}}$  corresponds to the ideal gas free energy. It is exactly known and reads

$$\mathcal{F}_{\text{id}}[T, \rho] = k_{\text{B}}T \int_V d\mathbf{r} \rho(\mathbf{r}) (\ln(\Lambda^3 \rho(\mathbf{r})) - 1), \quad (2.6)$$



with  $k_B$  being Boltzmann's constant and  $\Lambda = h/\sqrt{2\pi mk_B T}$  (mass  $m$ , Planck's constant  $h$ ) being the thermal de Broglie wavelength. The last term  $\mathcal{F}_{\text{ext}}$  in Eq. (2.5) incorporates contributions from an external potential and is not discussed here as it usually neglected in derivations of PFC theory.

$\mathcal{F}_{\text{exc}}$  corresponds to the free energy exceeding contributions from the ideal gas. It contains all correlations from interactions between particles. As expected, it is not known in general and has to be approximated. In a first step, an expression for  $\mathcal{F}_{\text{exc}}$  is obtained by a functional Taylor expansion around a uniform reference density  $\rho_{\text{ref}}$ . The expansion is carried out in  $\Delta\rho = \rho(\mathbf{r}) - \rho_{\text{ref}}$  and yields

$$\mathcal{F}_{\text{exc}}[T, \rho] = \mathcal{F}_{\text{exc}}^{(0)}[\rho_{\text{ref}}] + \sum_{n=1}^{\infty} \int d\mathbf{r}_1 \dots \int d\mathbf{r}_n \frac{1}{n!} \frac{\delta^n \mathcal{F}_{\text{exc}}[T, \rho(\mathbf{r})]}{\delta\rho(\mathbf{r}_1) \dots \delta\rho(\mathbf{r}_n)} \Bigg|_{\rho_{\text{ref}}} \prod_{i=1}^n \Delta\rho(\mathbf{r}_i) \quad (2.7)$$

being formally still exact. We can identify  $n$ -th order direct correlation functions as

$$c^{(n)}(\mathbf{r}_1, \dots, \mathbf{r}_n) \propto \frac{\delta^n \mathcal{F}_{\text{exc}}[T, \rho(\mathbf{r})]}{\delta\rho(\mathbf{r}_1) \dots \delta\rho(\mathbf{r}_n)} \quad (2.8)$$

in the expansion (2.7). There, the zeroth order term is constant and, hence, can be dropped since only (functional) derivatives are taken into account. The same holds for the first-order term ( $n = 1$ ) that turns out to be constant due to the isotropy of the bulk fluid and corresponding translational and rotational symmetries.

Truncating the expansion (2.7) at second order and assuming that the pair correlation  $c^{(2)}(\mathbf{r}) \equiv c(\mathbf{r})$  only depends on the relative distance between two particles results in

$$\mathcal{F}_{\text{exc}}[T, \rho] = -\frac{k_B T}{2} \int d\mathbf{r}_1 \int d\mathbf{r}_2 c(\mathbf{r}_1 - \mathbf{r}_2) \Delta\rho(\mathbf{r}_1) \Delta\rho(\mathbf{r}_2). \quad (2.9)$$

Equation (2.9) is known as Ramakrishnan-Yussouf theory [RY79]. To evaluate the approximation, the pair correlation  $c$  needs to be specified; various expressions for it can be found in the literature [vRBMF95].

Having established the basic concept of DFT, next, the dynamics of a time-dependent one-particle density  $\rho(\mathbf{r}, t)$  is studied.

### 2.1.2 Dynamical density functional theory

In DDFT, the one-particle density depends on time:  $\rho(\mathbf{r}, t)$ . The theory describes the time evolution of  $\rho$  for a non-equilibrium system of  $N$  interacting classical particles. The central equation of DDFT is given as the conserved dissipative dynamics

$$\partial_t \rho(\mathbf{r}, t) = \nabla \cdot \left[ (k_B T)^{-1} M(\rho) \nabla \frac{\delta \mathcal{F}}{\delta \rho} \right]. \quad (2.10)$$

Equation (2.10) is a generalized deterministic diffusion equation (also referred to as a generalized Fick's law of diffusion) and corresponds to a continuity equation. The latter guarantees the mass-conserving character of the dynamics. The spatial integral over  $\rho$  (equal to  $N$ ) is conserved.  $M(\rho)$  is the mobility and usually taken as  $M(\rho) = D_t \rho$  with  $D_t$  being the translational diffusion coefficient.

Applying suitable boundary conditions, it can easily be shown that the Helmholtz free energy decreases monotonically with time, i.e.,  $d\mathcal{F}/dt \leq 0$ , and at equilibrium ( $\partial_t \rho = 0$  and  $d\mathcal{F}/dt = 0$ ) it follows

$$\frac{\delta \mathcal{F}}{\delta \rho} = \mu \quad (2.11)$$

as already seen in the static case of DFT (Eq. (2.4)). Of course, equilibria still correspond to extreme values of the grand canonical free-energy functional  $\Omega$ .

Note that the key equation of DDFT, Eq. (2.10), can be derived from Langevin equations modeling the stochastic motion of isotropic colloidal particles in an incompressible liquid in the Stokes limit. This derivation can be found, e.g., in [ELW<sup>+</sup>12] and is not discussed here. Next, we use equations from DFT and DDFT to sketch the derivation of PFC models.

### 2.1.3 Derivation of PFC models

Despite the presented approximations, DFT and DDFT achieve a high level of exactness in describing crystallization phenomena microscopically. As Fig. 2.1 shows, PFC modeling incorporates further coarse-graining.

The PFC approach is derived in two steps by various approximations whose consequences are studied in detail in [ARRS19]. Here, only a general scheme of deriving PFC models is sketched by first deducing a free-energy functional from DFT. Second, the equation of motion is derived on the basis of DDFT.

#### Free energy

Deriving a free-energy functional for PFC models follows three basic steps:

1. Introduce a new order parameter field describing the deviation from the reference density.
2. Taylor-expand the free energy in terms of this order parameter field (assuming small density deviations).
3. Gradient-expand the correlation functions in the excess free-energy functional.

The new dimensionless order parameter  $\psi(\mathbf{r})$  is defined as the relative deviation from the reference density  $\rho_{\text{ref}}$  (that was introduced at Eq. (2.7)).

$$\rho(\mathbf{r}) = \rho_{\text{ref}}(1 + \psi(\mathbf{r})) \quad (2.12)$$

where  $\psi(\mathbf{r})$  is assumed to be small. Next,  $\psi(\mathbf{r})$  is introduced into the Helmholtz free energy  $\mathcal{F}$  as given in Eq. (2.5) and a Taylor expansion in  $\psi(\mathbf{r})$  is performed.

For the ideal gas part of the free-energy, one finds

$$\mathcal{F}_{\text{id}}[T, \psi(\mathbf{r})] = \mathcal{F}_{\text{id}}^{(0)}(T) + \rho_{\text{ref}} k_{\text{B}} T \int d\mathbf{r} \left( \psi + \frac{\psi^2}{2} - \frac{\psi^3}{6} + \frac{\psi^4}{12} \right), \quad (2.13)$$

where the expansion keeps terms up to the fourth order of  $\psi$ . They are necessary for a stable crystalline phases, i.e., to have well defined minima at finite values of  $\psi$ . Note that the constant term  $\mathcal{F}_{\text{id}}^{(0)}$  is again irrelevant as only derivatives of  $\mathcal{F}$  are evaluated.

The excess free-energy part is approximated by a gradient expansion. Recall that it only includes pair correlations  $c^{(2)}(\mathbf{r}_1, \mathbf{r}_2)$  following Ramakrishnan-Yussouf theory (cf. Sec. 2.1.1). For two spherical particles at distance  $r$  it is

$$c^{(2)}(\mathbf{r}_1, \mathbf{r}_2) = c^{(2)}(\mathbf{r}_1 - \mathbf{r}_2) = c^{(2)}(r). \quad (2.14)$$

With this correlation,  $\mathcal{F}_{\text{exc}}$  from Eq. (2.9) becomes a convolution. Its non-locality is tackled by a gradient expansion of  $c^{(2)}$

$$c^{(2)}(\mathbf{r}) = c_0^{(2)} - c_2^{(2)}\nabla^2 + c_4^{(2)}\nabla^4 + \mathcal{O}(\nabla^6) \quad (2.15)$$

with gradient expansion coefficients  $c_{2i}^{(2)}$ . Odd terms have to vanish due to the symmetry of pair-correlations:  $c^{(2)}(\mathbf{r}) = c^{(2)}(-\mathbf{r}) = c^{(2)}(r)$ . The gradient expansion can also be regarded as a Taylor expansion in Fourier space around  $\mathbf{k} = \mathbf{0}$ . From this point of view, the origin of the minus sign of  $c_2^{(2)}$  is obvious. Again, terms up to fourth order are needed for stable crystalline phases.

The gradient expansion yields

$$\mathcal{F}_{\text{exc}}[\psi(\mathbf{r})] = \mathcal{F}_{\text{exc}}^{(0)}(\rho_{\text{ref}}) - \frac{\rho_{\text{ref}}}{2}k_{\text{B}}T \int d\mathbf{r}(a_1\psi^2 + a_2\psi\nabla^2\psi + a_3\psi\nabla^4\psi) \quad (2.16)$$

with suitable coefficients  $a_i$  containing the direct pair correlation  $c^{(2)}$ . The constant term is again dropped.

Collecting the contributions  $\mathcal{F}_{\text{id}}$  and  $\mathcal{F}_{\text{exc}}$  results in the free-energy functional

$$\mathcal{F}[\psi(\mathbf{r})] = \rho_{\text{ref}}k_{\text{B}}T \int d\mathbf{r} \left( b_1\psi^2 + b_2\psi\nabla^2\psi + b_3\psi\nabla^4\psi - \frac{\psi^3}{6} + \frac{\psi^4}{12} \right) \quad (2.17)$$

with rescaled coefficients  $b_i$  (cf. [ELW<sup>+</sup>12]). Further scaling (ibid.) finally yields the original dimensionless Swift-Hohenberg-type free-energy functional as introduced in [EKHG02]

$$\tilde{\mathcal{F}}_{\text{PFC}}[\tilde{\psi}(\mathbf{r})] = \int d\tilde{\mathbf{r}} \left\{ \frac{\tilde{\psi}}{2} [\epsilon + (k_0^2 + \nabla^2)^2] \tilde{\psi} + \frac{\tilde{\psi}^4}{4} \right\}. \quad (2.18)$$

Summarizing and physically speaking,  $\tilde{\psi}$  is an effective particle density and  $\epsilon$  an effective temperature. The wave vector  $\mathbf{k}_0$  measures the characteristic length scales of the crystalline phase. It will be set equal to one throughout this thesis.

## Dynamics

Having specified the free energy, dynamical equations of motion can be determined. Recalling the key equation from DDF<sup>T</sup> (2.10) and approximating the mobility  $M(\rho)$  to be constant by  $M = D_{\text{t}}\rho_{\text{ref}}$ , after suitable rescaling, the equation of motion reads

$$\begin{aligned} \partial_t \tilde{\psi}(\mathbf{r}, t) &= \nabla^2 \frac{\delta \tilde{\mathcal{F}}_{\text{PFC}}}{\delta \tilde{\psi}}, \\ &= \nabla^2 \left\{ \left[ \epsilon + (1 + \nabla^2)^2 \right] \tilde{\psi} + \tilde{\psi}^3 \right\}. \end{aligned} \quad (2.19)$$

Equation (2.19) is the dynamical equation that will also form the core of the density equation of the active PFC. We refer to this model as the passive PFC model.

Since Eq. (2.19) is a continuity equation, the total density is conserved

$$\frac{1}{V} \int d\mathbf{r} \tilde{\psi}(\mathbf{r}, t) = \bar{\psi} \quad (2.20)$$

with mean density  $\bar{\psi}$ . In the course of this thesis, we refer to this as a conserved system or synonymously as a system with conserved dynamics.

## 2.2 Derivation of the active PFC model

Having linked PFC modeling to DFT and having systematically derived the passive PFC model Eq. (2.19), we next present a derivation of the active PFC model. Based on DDFT (Sec. 2.1.2), the derivation follows Menzel and colleagues in [MOL14].

The active PFC (aPFC) model describes self-propelled particles. The particles can exchange momentum with the environment. This holds for swimming particles in the Stokes limit as required for deriving DDFT from Langevin equations on particle level and obviously for active agents on a planar solid ground.

Due to an active drive of magnitude  $v$ , individual particles move. The direction of motion is given by the unit vector  $\mathbf{u}$ . Hence, the one-particle density now also depends on a direction:  $\rho(\mathbf{r}, \mathbf{u}, t)$ . Restricting space to two dimensions, we can express  $\mathbf{u}$  in terms of a single angle  $\theta$ . As done to formulate the key equation of DDFT (2.10), a general equation of motion for the density can be obtained from Langevin equations. As in [WL08], the result reads

$$\partial_t \rho(\mathbf{r}, \mathbf{u}, t) = \nabla \cdot \tilde{\mathbf{D}}_t \cdot \left( (k_B T)^{-1} \rho \nabla \frac{\delta \tilde{\mathcal{F}}}{\delta \rho} \right) + \tilde{D}_r \partial_\theta \left( (k_B T)^{-1} \rho \partial_\theta \frac{\delta \tilde{\mathcal{F}}}{\delta \rho} \right) - \nabla \cdot \tilde{\mathbf{D}}_t \cdot (\rho v \mathbf{u} / \tilde{D}_\parallel). \quad (2.21)$$

On account of possible anisotropy, the translational diffusion coefficient is extended to a diffusion tensor by  $\tilde{\mathbf{D}}_t = \tilde{D}_\parallel \mathbf{u} \mathbf{u} + \tilde{D}_\perp (\mathbf{1} - \mathbf{u} \mathbf{u})$ .  $\tilde{D}_r$  in the second term of Eq. (2.21) sets the rotational diffusion. The last term originates from the self-propulsion of particles. It is proportional to the strength of propulsion  $v$ .

In the next steps, Eq. (2.21) is simplified before the free energy is specified and dynamical equations for the order parameter are obtained.

First, the average density is determined in order to obtain a reduced particle density:

$$\bar{\rho} = \frac{1}{VS} \int d\mathbf{u} \int d\mathbf{r} \rho(\mathbf{r}, \mathbf{u}, t), \quad (2.22)$$

where  $S$  is the surface area of the unit sphere and  $V$  the volume of the considered system. In this system,  $\bar{\rho}$  is conserved over time. Next, the orientational dependency is eliminated by

$$\bar{\rho} \tilde{\phi}(\mathbf{r}, t) = \frac{1}{S} \int d\mathbf{u} \rho(\mathbf{r}, \mathbf{u}, t) - \bar{\rho}. \quad (2.23)$$

$\mathbf{u}$  is integrated out and, after subtracting the mean density, we are left with the modulation  $\bar{\rho} \tilde{\phi}(\mathbf{r}, t)$  around  $\bar{\rho}$ .

Now a polarization field  $\tilde{\mathbf{P}}(\mathbf{r}, t)$  is introduced by evaluating the first orientational moment of  $\rho(\mathbf{r}, \mathbf{u}, t)$ . For technical reasons it is also scaled by  $\bar{\rho}$ .

$$\bar{\rho}\tilde{\mathbf{P}}(\mathbf{r}, t) = \frac{n}{S} \int d\mathbf{u} \rho(\mathbf{r}, \mathbf{u}, t) \mathbf{u} \quad (2.24)$$

with spatial dimension  $n \in \{1, 2\}$ . The right-hand side of Eq. (2.24) makes clear that  $\tilde{\mathbf{P}}$  is a measure for the local orientational order of the directions  $\mathbf{u}$  of the active driving of the individual particles. Strong polarization arises where particles are aligned.

The one-particle density is now expanded in terms of its  $\mathbf{u}$ -dependency. The expansion (methodically similar to a multipole expansion) yields

$$\rho(\mathbf{r}, \mathbf{u}, t) = \bar{\rho} + \bar{\rho}\tilde{\phi}(\mathbf{r}, t) + \bar{\rho}\mathbf{u} \cdot \tilde{\mathbf{P}}(\mathbf{r}, t) + \mathcal{O}(\mathbf{u}^2). \quad (2.25)$$

The first term is the constant spatial and oriental mean density and the second term incorporates spatial dependency by the modulation around  $\bar{\rho}$ . The last term considers directional dependency and corresponds to a projection onto the polarization that can be regarded as the mean orientation at  $\mathbf{r}$ . Higher order terms of  $\mathbf{u}$  are neglected. This expansion is plugged into Eq. (2.21). Calculating Fourier modes in terms of the angle  $\theta$  of the obtained equation yields dynamical equations for the reduced density and polarization. In detail,  $\mathbf{u}$  is expressed as  $\exp(i\theta)$  and the equation is integrated over  $\theta$  (after a multiplication with  $\exp(-i\theta)$  to obtain the second equation). These equations significantly further simplify under the assumption of an isotropic translational diffusion, i.e.,

$$\tilde{D}_{\parallel} \approx \tilde{D}_{\perp} \approx \tilde{D}, \quad (2.26)$$

and the assumption of constant mobility,  $M(\rho) = \tilde{D}\bar{\rho}$ . Then the dynamical equations read

$$\partial_t(\bar{\rho}\tilde{\phi}) = \frac{\tilde{D}\bar{\rho}}{2\pi k_B T} \nabla^2 \frac{\delta\tilde{\mathcal{F}}}{\delta(\bar{\rho}\tilde{\phi})} - \frac{v}{2} \nabla \cdot (\bar{\rho}\tilde{\mathbf{P}}), \quad (2.27)$$

$$\partial_t(\bar{\rho}\tilde{\mathbf{P}}) = \frac{\tilde{D}\bar{\rho}}{\pi k_B T} \nabla^2 \frac{\delta\tilde{\mathcal{F}}}{\delta(\bar{\rho}\tilde{\mathbf{P}})} - \frac{\tilde{D}_r\bar{\rho}}{\pi k_B T} \frac{\delta\tilde{\mathcal{F}}}{\delta(\bar{\rho}\tilde{\mathbf{P}})} - v\nabla(\bar{\rho}\tilde{\phi}). \quad (2.28)$$

Lastly, the free-energy functional needs to be specified. For the crystallization part, a slightly amended PFC energy function is used:

$$\tilde{\mathcal{F}}_{\text{PFC}}[\phi] = \int d\mathbf{r} \left\{ \frac{\phi}{2} [a\Delta T + \lambda(q_0^2 + \nabla^2)^2] \phi + \frac{u}{4}\phi^4 \right\}, \quad (2.29)$$

where it is  $\phi = \bar{\phi} + \bar{\rho}\tilde{\phi}$  and parameters  $a$ ,  $\lambda$ ,  $\Delta T$  and  $u$  are specifying the influence of various energetic contributions.  $\tilde{\mathcal{F}}_{\text{PFC}}$  encodes the crystallization process with uniform liquid-like states on the one hand and crystalline states on the other.

The polarization is governed by

$$\tilde{\mathcal{F}}_{\tilde{\mathbf{P}}}[\tilde{\mathbf{P}}] = \int d\mathbf{r} \left\{ \frac{\tilde{C}_1}{2} (\bar{\rho}\tilde{\mathbf{P}})^2 + \frac{\tilde{C}_2}{4} [(\bar{\rho}\tilde{\mathbf{P}})^2]^2 \right\} \quad (2.30)$$

incorporating ideas of Toner and Tu [TT95, TT98].

A more detailed discussion of the employed free-energy functionals can be found in the next section. There, we also present the final dynamical equation following extensive rescaling along the lines of [MOL14].  $\tilde{\phi}(\mathbf{r}, t)$  is rescaled to a new density modulation  $\psi(\mathbf{r}, t)$  and  $\tilde{\mathbf{P}}(\mathbf{r}, t)$  is rescaled to  $\mathbf{P}(\mathbf{r}, t)$ .

## 2.3 Governing equations

The local state variables of the aPFC model as introduced in Ref. [ML13] are the scalar order parameter field  $\psi(\mathbf{r}, t)$ ,  $\mathbf{r} \in \tilde{\Omega} \subset \mathbb{R}^n$  (called in the following “density”) where  $\tilde{\Omega}$  denotes the considered domain with volume  $V$ , and the vectorial order parameter field  $\mathbf{P}(\mathbf{r}, t)$  (called in the following “polarization”) that describes the local ordering and direction of the active drive. The field  $\psi(\mathbf{r}, t)$  is conserved, i.e.,  $\int_{\tilde{\Omega}} d\mathbf{r} \psi = 0$  is constant in time, and specifies the modulation about the mean density  $\bar{\psi}$  that itself encodes the deviation from the critical point [ELW<sup>+</sup>12]. The field  $\mathbf{P}(\mathbf{r}, t)$  is non-conserved. The uncoupled dynamics of  $\psi(\mathbf{r}, t)$  and  $\mathbf{P}(\mathbf{r}, t)$  correspond to a purely conserved and a mixed non-conserved and conserved gradient dynamics on an underlying free energy functional  $\mathcal{F}[\psi, \mathbf{P}]$ , respectively. The functional contains no terms mixing the two fields and the coupling is purely non-variational, i.e., no part of it can be written as a gradient dynamics. The coupling keeps the conserved character of the  $\psi$ -dynamics, i.e., the evolution of  $\psi$  follows a continuity equation  $\partial_t \psi = -\nabla \cdot \mathbf{j}$  where  $\mathbf{j}$  is a flux. The non-dimensional evolution equations rescaled from Eqs. (2.27) and (2.28) are [ML13]

$$\partial_t \psi = \nabla^2 \frac{\delta \mathcal{F}}{\delta \psi} - v_0 \nabla \cdot \mathbf{P}, \quad (2.31)$$

$$\partial_t \mathbf{P} = \nabla^2 \frac{\delta \mathcal{F}}{\delta \mathbf{P}} - D_r \frac{\delta \mathcal{F}}{\delta \mathbf{P}} - v_0 \nabla \psi \quad (2.32)$$

where  $v_0$  is the coupling strength, also called activity parameter or strength of self-propulsion. Physically speaking,  $\mathbf{P}$  is subject to translational and rotational diffusion with  $D_r$  being the rotational diffusion coefficient. The functional  $\mathcal{F}[\psi, \mathbf{P}]$  is the sum of the standard phase-field-crystal functional  $\mathcal{F}_{\text{PFC}}[\psi]$  Eq. (2.18) [EKHG02, EG04, ELW<sup>+</sup>12] and an orientational part  $\mathcal{F}_{\mathbf{P}}[\mathbf{P}]$

$$\mathcal{F} = \mathcal{F}_{\text{PFC}} + \mathcal{F}_{\mathbf{P}} \quad (2.33)$$

with

$$\mathcal{F}_{\text{PFC}}[\psi] = \int d\mathbf{r} \left\{ \frac{1}{2} \psi \left[ \epsilon + (1 + \nabla^2)^2 \right] \psi + \frac{1}{4} (\psi + \bar{\psi})^4 \right\} \quad (2.34)$$

and

$$\mathcal{F}_{\mathbf{P}}[\mathbf{P}] = \int d\mathbf{r} \left( \frac{C_1}{2} \mathbf{P}^2 + \frac{C_2}{4} \mathbf{P}^4 \right). \quad (2.35)$$

The functional (2.33) encodes the phase transition between liquid and crystal state [ELW<sup>+</sup>12]. It contains a negative interfacial energy density ( $\sim |\nabla \psi|^2$ ) that favors the creation of interfaces, a bulk energy density and a stabilizing stiffness term ( $\sim (\Delta \psi)^2$ ) – this can be seen by partial integration. The parameter  $\epsilon$  encodes temperature. Namely, negative values correspond to an undercooling of the liquid phase and result in solid (periodic) states for suitable mean densities  $\bar{\psi}$ , whereas positive values result in a liquid (homogeneous) phase. The functional (2.35) with  $C_1 < 0$  and  $C_2 > 0$  allows for spontaneous polarization (pitchfork bifurcation at  $C_1 = 0$ ). However, in most of our work we avoid spontaneous polarization using positive  $C_1 > 0$  and  $C_2 = 0$  as also done in most of the analyses of Refs. [ML13, MOL14, CGT16]. With  $C_1 > 0$  diffusion reduces the polarization.

Determining the variations of Eqs. (2.33) and (2.35) and introducing them in the governing

equations (2.32) we obtain the dynamical equations

$$\partial_t \psi = \nabla^2 \left\{ \left[ \epsilon + (1 + \nabla^2)^2 \right] \psi + (\bar{\psi} + \psi)^3 \right\} - v_0 \nabla \cdot \mathbf{P}, \quad (2.36)$$

$$\partial_t \mathbf{P} = C_1 \nabla^2 \mathbf{P} - D_r C_1 \mathbf{P} - v_0 \nabla \psi. \quad (2.37)$$

Throughout this thesis, we study resting and traveling solutions of these equations in the spatially one-dimensional and two-dimensional case with a special emphasis on the onset of motion.

## 2.4 Numerical approach

The aPFC model (Eqs. (2.36) and (2.37)) is an example of a system of nonlinear partial differential equations (PDEs) whose exact solutions can usually not be found by analytical calculations. Apart from the trivial state (discussed in chapter 3), solutions of such systems have to be obtained by numerical methods. In this section, we outline two numerical techniques used in this thesis to study solutions of the aPFC model: time simulations and parameter continuation. Besides, the last section deals with numerical stability analysis we employ to study the linear stability of found solutions.

Time simulations are a fundamental tool to study the temporal behavior of a system starting from given initial conditions. Within PFC modeling, for instance, the crystallization of an unstable under-cooled liquid starting from a small perturbation (like a crystal nucleus) can be observed in time simulations. Continuation, on the other hand, is able to follow converged steady or stationary states in parameter space. In this way, one can construct complete bifurcation diagrams including branches of unstable solutions. Unstable solutions are usually not accessible by time simulations. Both methods are sketched in the following.

### 2.4.1 Time simulations

The aPFC model consists of two coupled (nonlinear) PDEs: Eqs. (2.36) and (2.37). The temporal evolution of the two spatially extended order parameter fields is governed by spatial derivatives. In order to solve PDEs numerically and to evaluate the spatio-temporal behavior of the fields, first, they have to be discretized in space. A finite spatial grid (often also called mesh) and suitable boundary conditions (BC) are needed. Second, spatial derivatives have to be approximated. Finite difference methods (FDM) or finite element methods (FEM) are two widely used numerical approaches for this approximation. We briefly introduce FDM that we use for the numerical stability analysis (cf. Sec. 2.4.3), while FEM are not discussed here. For details on these methods see, e.g., [PS05].

An alternative to FEM and FDM are spectral methods, where spatial derivatives are evaluated in Fourier space. We briefly introduce a pseudo-spectral scheme that is employed in all time simulations presented in this thesis.

Having established a spatial discretization, BC and an approximation for spatial derivatives, the last step is to advance the solutions in time from initial values using a time-stepping scheme. Various implicit and explicit schemes exist, details can be found, e.g., in [But16]. We use a semi-implicit Euler method that is also sketched in the following.

### Spatial discretization and approximation of derivatives by finite differences

The first step of numerically solving PDEs like Eqs. (2.36) and (2.37) is to discretize the system. The discretization transforms PDEs into a (usually large) set of ordinary differential equations (ODEs). Here, we schematically present this discretization and the method of finite differences. Note that this section mainly follows [Bes06].

All models we investigate have the structure

$$\partial_t u_j(x_1, \dots, x_d, t) = F_j(u_1, \dots, u_N, x_1, \dots, x_d), \quad j = 1, \dots, K, \quad (2.38)$$

where functions  $F_j$  are usually nonlinear and can contain arbitrary partial derivatives w.r.t  $x_i$ . The index  $d$  corresponds to the number of spatial dimensions. Here, it is  $d \leq 2$ .

In this section, for the sake of simplicity, we reduce the system of PDEs (Eq. (2.38)) to one equation and also keep space one dimensional:

$$\partial_t u(x, t) = F(u, \partial_x u, \partial_{xx} u, \dots, x). \quad (2.39)$$

Equation (2.39) is to be solved on an interval of length  $L$ , i.e.,  $0 \leq x \leq L$ . Then, the PDE is reduced to a finite system of ODEs by introducing discrete grid points  $x_i$ , where

$$x_i = (i - 1)\Delta x, \quad \text{with} \quad \Delta x = L/(N - 1) \quad (2.40)$$

and evaluating  $u$  on the grid:

$$u(x, t) \rightarrow u(x_i, t) \equiv u_i(t), \quad i = 1, \dots, N. \quad (2.41)$$

The spacing of grid points can be equidistant or also adaptive.

Next, spatial derivatives are approximated by difference quotients as

$$\partial_x u \Big|_{x_i} = \frac{u(x_i + \Delta x) - u(x_i)}{\Delta x} + \mathcal{O}(\Delta x^2) = \frac{u_{i+1} - u_i}{\Delta x} + \mathcal{O}(\Delta x^2), \quad (2.42)$$

also called *forward finite difference*, or alternatively symmetrically centered

$$\partial_x u \Big|_{x_i} = \frac{u_{i+1} - u_{i-1}}{2\Delta x} + \mathcal{O}(\Delta x^2). \quad (2.43)$$

For higher order derivatives, respective stencils can be found in the literature [Bes06]. Stencils specify the weights of neighboring  $u_j$  used to calculate a higher order derivative. After discretizing the PDE and approximating spatial derivatives by finite differences, one obtains an explicit point-wise algebraic expression for the temporal evolution at each grid point with couplings to certain neighboring points.

### Spectral methods

An alternative to approximating spatial derivatives by finite differences are spectral methods. The idea is to transform the PDE into Fourier space and benefit from the fact that spatial derivatives transform into products with the wave vector. A drawback are nonlinearities that have to be solved as computationally expensive convolutions. Using the highly efficient algorithm *fast Fourier transform* (FFT) [CT65], it turns out to be computationally cheaper to calculate nonlinearities in real space and undertake transformations back and fourth. This method is called pseudo-spectral.



Consider the PDE (2.39) and separate linear and nonlinear operators of the right-hand side:

$$\partial_t u(x, t) = F(u, \partial_x u, \partial_{xx} u, \dots, x, t) = \mathcal{L}(u(x, t)) + \mathcal{N}(u(x, t)). \quad (2.44)$$

The linear part may contain linear functions or linear differential operators.  $\mathcal{N}$  denotes a nonlinear operator that, e.g., includes powers of  $u$  or nonlinear differential operators like  $(\partial_x u)^2$ . Fourier transforming Eq. (2.44) yields

$$\partial_t \tilde{u}(k, t) = \tilde{\mathcal{L}}(\tilde{u}(k, t)) + FT[\mathcal{N}(u(x, t))], \quad (2.45)$$

where  $FT[\cdot]$  and tildes indicate transformed fields and operators and  $k$  is the corresponding wave vector.

During numerical simulations, the whole problem is treated in Fourier space. However, due to smaller computational costs,  $FT[\mathcal{N}]$  is transformed back to real space where  $\mathcal{N}(u)$  is evaluated efficiently. Afterwards the result is transformed to Fourier space at cost scaling with  $N \log N$  for  $N$  grid points. Convolutions in Fourier space would involve, e.g., at least  $N^2$  operations for convoluting  $FT(u^2) = \tilde{u} * \tilde{u}$  and even more operations for higher order nonlinearities.

Results from time simulations shown in this thesis are obtained by a pseudo-spectral method and a semi-implicit Euler method for time-stepping which is briefly explained in the next paragraph.

### Time stepping

The last necessary step for time simulations is the iteration of time. Time is discretized by steps  $\Delta t$

$$t_n = n\Delta t, \quad n \in \mathbb{Z}, \quad (2.46)$$

that can be of constant size or adapted to the dynamics.

Commonly, time-stepping methods are classified as *explicit* or *implicit* methods. Explicit methods calculate  $u(t_{i+1})$  directly from  $u(t_i)$ . In contrast, implicit methods find the next  $u$  by solving an equation involving both  $u(t_{i+1})$  and  $u(t_i)$ . Obviously, implicit methods require additional computing and are, in general, more complicated to implement. Yet, they usually exhibit better numerical stability [Bes06].

The semi-implicit Euler scheme that we employ for time simulations of the aPFC model in this thesis is a combination of both methods. Using the notation of Eq. (2.44) and approximating  $\partial_t u$  again by a difference quotient, it reads

$$\frac{u(t_{i+1}) - u(t_i)}{\Delta t} = \mathcal{L}(u(t_{i+1})) + \mathcal{N}(u(t_i)). \quad (2.47)$$

For the linear (and invertible) part, we use an implicit method, while the rest of the right-hand side is evaluated explicitly. This may seem rather arbitrary at first glance, but the corresponding error is of order  $\mathcal{O}(\Delta t)$  and the method is well justifiable as it increases the numerical stability [Bes06].

Most of our simulations start from a homogeneous state with small random perturbations, integrating Eqs. (2.36) and (2.37) in Fourier space forward in time.

### 2.4.2 Continuation in parameter space

Time simulations are helpful to study the temporal behavior of systems. They provide an insight into the transient of a system and are particularly utile when the system shows time-dependent dynamics as, e.g., oscillations. However, systems often converge towards steady states without any temporal evolution. If the transient dynamics is not of interest, instead of integrating forward in time, *numerical path continuation* [DWC<sup>+</sup>14, KOGV07, Kuz10, EGU<sup>+</sup>19] can be applied to solve the stationary problem and compute steady states for large ranges of control parameters.

Note that this schematic description of numerical continuation mainly follows explanations in [Tri18] and [Wil16]. Setting time derivatives to zero, the model at hand can be expressed by

$$\frac{d\mathbf{u}}{dt} = \mathbf{F}(\mathbf{u}, \lambda) = 0. \quad (2.48)$$

In this (usually nonlinear) set of equations,  $\mathbf{u}$  is the solution array and  $\lambda$  is the control parameter to be varied. The solution array contains all order parameters, such as, e.g., for the aPFC model, the density field  $\psi$  and the polarization  $\mathbf{P}$  on the employed spatial grid points.

Continuation methods are based on the fact that any solution  $\mathbf{u}^0$  for a corresponding parameter  $\lambda_0$  is part of a so-called solution *branch*. This branch is a unique continuum of solutions. According to the *implicit function theorem* small changes in  $\lambda$  only result in a slightly changed solution. Constraints are an invertible Jacobian  $\mathbf{J} = \partial_{u_j} F_i(\mathbf{u}, \lambda)$  and that  $\mathbf{F}$  and  $\mathbf{J}$  are smooth near  $(\mathbf{u}^0, \lambda_0)$ . If these mild conditions on the partial derivatives are fulfilled, then there exists a *family* of solutions  $\mathbf{u}(\lambda)$  in some neighborhood of  $(\mathbf{u}^0, \lambda_0)$ . A precise formulation of the theorem can be found, e.g., in [KP12]. The strategy of continuation methods is to follow the solution  $\mathbf{u}$  along the solution branch for varying control parameter  $\lambda$ .

The procedure works as follows: Starting from a known solution  $\mathbf{u}^0$  at  $\lambda_0$  a guess  $\tilde{\mathbf{u}}^1$  for the solution  $\mathbf{u}^1$  at  $\lambda_1 = \lambda_0 + \Delta\lambda$  is predicted. The prediction step can, e.g., be a tangential extrapolation as indicated in Fig. 2.2. The starting point  $(\mathbf{u}^0, \lambda_0)$  is often an analytical solution or obtained by sufficiently converged time simulations. The second step is to correct the guess  $\tilde{\mathbf{u}}^1$  until it solves Eq. (2.48) to an arbitrary exactness. The corrected solution  $\mathbf{u}^1$  is obtained by Newton's method [Deu04]. According to the implicit function theorem, Newton's method converges if  $\Delta\lambda$  is small enough. The size of  $\Delta\lambda$  can be dynamically adapted during the continuation to ensure efficient computations.

Figure 2.2 illustrates a drawback of natural parameter continuation. The procedure fails at folds of the solution branch. Changes of direction of  $\lambda$  cannot be realized by the method. However, with *pseudo-arclength continuation* [Kel79] solution branches can be followed around folds. Arclength continuation, also referred to as Keller method, introduces an additional independent parameter to the problem. The parameter  $s$  represents an approximated arclength along the branch. The system is rewritten and parametrized by  $s$ :  $\mathbf{u}(\lambda(s))$ . Then, the new Jacobian does not diverge at folds and the correction step is performed at fixed  $s$ . Hence, the procedure enables changes of the direction of  $\lambda$ .

In order to guarantee unique solutions, occurring symmetries of the system under study have to be broken. The aPFC system (Eqs. (2.36), (2.37)), for instance, is translationally invariant. There exists a continuum of solutions with identical profiles just shifted in space.

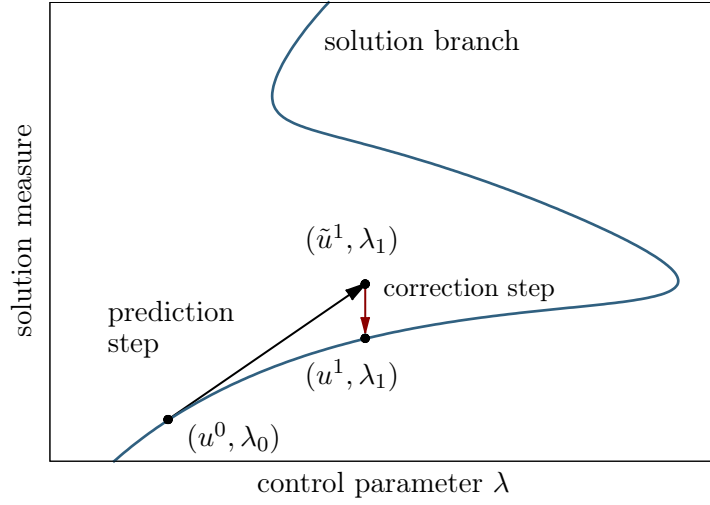


Figure 2.2: Natural parameter continuation following a family of solutions  $u^i$  on a solution branch. Starting from a known solution  $u^0$  at a given parameter  $\lambda_0$ , the solution is tangentially extrapolated in a prediction step. The resulting prediction  $\tilde{u}^1$  is corrected by iterative Newton steps at constant  $\lambda_1$ . As the tangential construction suggests, the procedure of natural parameter continuation fails at saddle-node bifurcations where the branch folds.

An integral condition can break this symmetry and guarantee the uniqueness of  $\mathbf{u}$ .

$$0 = \int_{\tilde{\Omega}} dx \frac{\partial \mathbf{u}^{i-1}}{\partial x} (\mathbf{u}^i - \mathbf{u}^{i-1}) \quad (2.49)$$

keeps the projection of the step to the  $i$ -th solution onto the translation mode of the previous solution at zero.

In conclusion, numerical continuation provides an efficient technique for obtaining whole families of solutions. In contrast to time simulations, also branches of unstable solutions are accessible. That is often beneficial or even necessary for a full understanding of the model.

In chapter 4, the software package AUTO07P [DKK91, DOC<sup>+</sup>12] is employed to obtain steady states of the aPFC model in one spatial dimension. For the continuation of solutions in 2d (chapter 5), the MATLAB package PDE2PATH [UWR14] is used. Note that PDE2PATH uses FEM to approximate spatial derivatives, while AUTO07P uses a spatial collocation method.

### 2.4.3 Numerical linear stability analysis

Since, in general, numerical continuation does not specify the stability of solutions, a numerical linear stability analysis (LSA) can help to determine corresponding stabilities. Linearizing Eq. (2.44) about a solution  $\mathbf{u}^0$  yields the eigenvalue problem

$$\partial_t \delta \mathbf{u} \Big|_{\mathbf{u}^0} = \mathcal{L}(\mathbf{u}^0) \delta \mathbf{u} = \sigma \delta \mathbf{u} \quad (2.50)$$

with eigenvalue  $\sigma$  for the growth of a small perturbation  $\delta\mathbf{u}$ . Approximating spatial derivatives in  $\mathcal{L}$  by finite differences as previously explained transforms Eq. (2.50) into a linear algebraic eigenvalue problem that can be solved by standard routines.

We use this method to determine the linear stability of steady states in 1d obtained by AUTO07P. PDE2PATH is intrinsically capable of determining linear stabilities of PDE solutions.

## 3 The Liquid State and its Linear Stability

In this chapter, we construct a morphological phase diagram of the active PFC model. By considerations about the linear stability of the trivial solution, we can distinguish between the uniform liquid state and resting and traveling crystals in the plane spanned by activity  $v_0$  and mean density  $\bar{\psi}$ .

Note that this chapter has been published in

[OGT18] L. Ophaus, S. V. Gurevich and U. Thiele. Resting and traveling localized states in an active phase-field-crystal model. *Phys. Rev. E*, 98:022608, August 2018.

### 3.1 Morphological phase diagram

The trivial solution of the aPFC model (Eqs. (2.36) and (2.37)) is the homogeneous, uniform state that represents the *liquid* phase where on diffusive time scales the probability of finding a particle is uniform in space. In analogy, we also call the uniform state  $(\psi_0, \mathbf{P}_0) = (0, \mathbf{0})$  of the present aPFC model “liquid phase”. Although it exists at all parameter values, for  $\epsilon < 0$  it is only stable at high  $|\bar{\psi}|$  and at lower  $|\bar{\psi}|$  becomes unstable w.r.t. coupled density and polarization fluctuations. However, in the context of colloidal particles the region  $\bar{\psi} > 0$  is unphysical [TAR<sup>+</sup>13] and we focus on  $\bar{\psi} < 0$  where the liquid state is stable at low values of  $\bar{\psi}$  (high  $|\bar{\psi}|$ ) while the crystalline state is stable at high  $\bar{\psi}$  (low  $|\bar{\psi}|$ ). To determine the linear stability of the homogeneous state, Eqs. (2.36) and (2.37) are linearized in small perturbations  $(\delta\psi, \delta\mathbf{P})$  about  $(0, \mathbf{0})$  yielding

$$\partial_t \delta\bar{\psi} = \nabla^2 \left( \epsilon + 3\bar{\psi}^2 + (1 + \nabla^2)^2 \right) \delta\psi - v_0 \nabla \cdot \delta\mathbf{P}, \quad (3.1)$$

$$\partial_t \delta\mathbf{P} = \nabla^2 (C_1 \delta\mathbf{P}) - D_r C_1 \delta\mathbf{P} - v_0 \nabla \delta\psi. \quad (3.2)$$

We restrict our analysis to one spatial dimension, expand the spatial dependency of the perturbation into decoupled harmonic modes and, in consequence, use the exponential ansatz  $\delta\psi(x, t), \delta P(x, t) \propto \exp(ikx + \lambda t)$  in Eqs. (3.1) and (3.2) to obtain the eigenvalues

$$\lambda_{\pm} = \frac{1}{2} (L_1(k) + L_2(k)) \pm \frac{1}{2} \sqrt{(L_1(k) - L_2(k))^2 - 4v_0^2 k^2} \quad (3.3)$$

where

$$L_1(k) = -k^2 \left( \epsilon + 3\bar{\psi}^2 + (1 - k^2)^2 \right) \quad (3.4)$$

$$L_2(k) = -k^2 C_1 - D_r C_1. \quad (3.5)$$

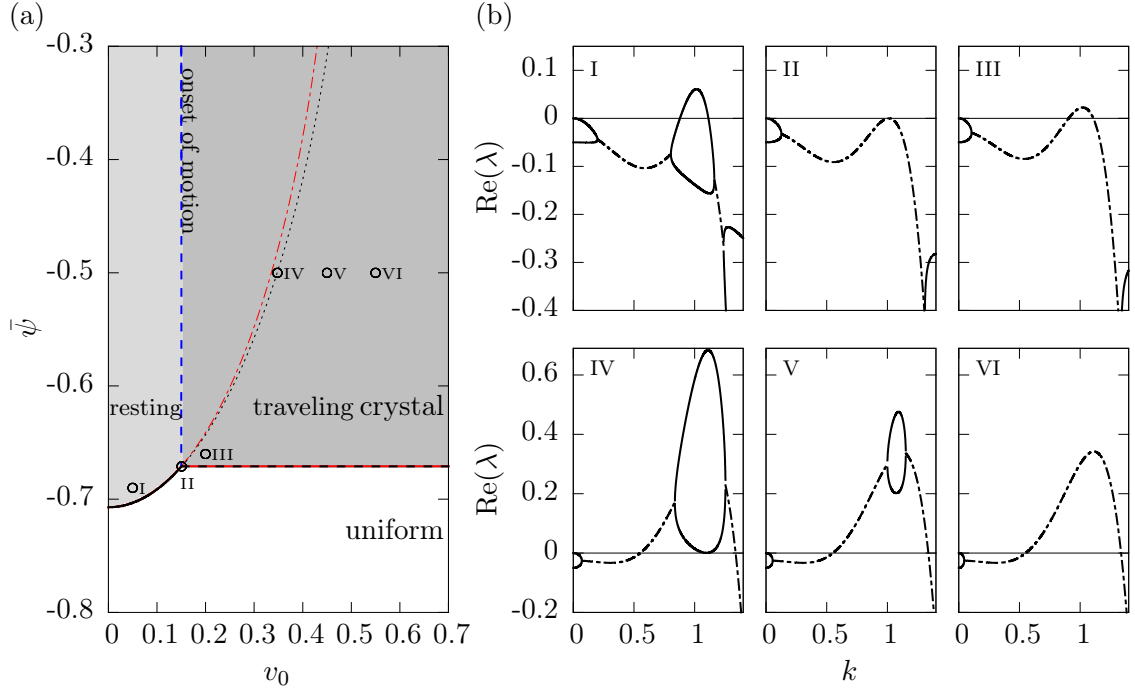


Figure 3.1: (a) Morphological phase diagram of the active PFC model in the 1d case in the plane spanned by activity  $v_0$  and mean concentration  $\bar{\psi}$  as obtained by linear and nonlinear analysis. The remaining parameters are  $\epsilon = -1.5$ ,  $C_1 = 0.1$ ,  $C_2 = 0.0$  and  $D_r = 0.5$ . Labels I to VI in (a) indicate parameters for which the real part of the dispersion relation  $\lambda(k)$  is shown in (b) with solid (dashed) lines corresponding to real (complex) eigenvalues. In (a) gray shading indicates the linearly unstable region where  $\text{Re}(\lambda(k)) > 0$  for a band of wavenumbers  $k$ . There, periodic (crystalline) patterns are formed. The analytically obtained curved solid and horizontal dashed black lines indicate the onset of the monotonic and oscillatory finite wavelength instability, respectively. For the coinciding red lines the critical wavenumber is approximated as  $k_c \approx 1$ . The gray-shaded region of the linearly unstable homogeneous (liquid) phase is separated by the vertical dashed blue line into regions where stable resting (light gray) and stable traveling (dark gray) crystals are found in the fully nonlinear regime. The thin dotted black and dot-dashed red lines indicate changes in the primary bifurcation behavior and indicate where the (then unstable) resting crystals cease to exist (see Sec. 4.2). (cf. [OGT18])

We investigate the stability of  $(\psi_0, P_0) = (0, 0)$  in the  $(\bar{\psi}, v_0)$ -plane and determine the boundary, where the largest real part of an eigenvalue  $\lambda$  crosses zero at a finite critical wavenumber  $k_c$ , i.e., a maximum of the dispersion relation  $\text{Re}(\lambda(k))$  touches zero. This can either occur with a zero or with a finite imaginary part corresponding to unstable modes that result in the development of a resting or traveling crystalline state (i.e., spatially-periodic solution), respectively. Setting  $\text{Re}(\lambda) = 0$  and substituting  $k^2 = z$  gives a cubic equation for  $z$ . Considering Cardano's method and the desired number of roots, we are able to find analytical expressions for the stability boundaries in both cases.

The results are presented in Fig. 3.1(a). The white area at low  $\bar{\psi}$  corresponds to a linearly stable liquid phase, whereas the gray shading marks regions where the liquid phase is unstable w.r.t. spatially periodic perturbations. The dashed horizontal line (red and black) at  $\bar{\psi} \approx -0.67$  separates the linearly stable liquid phase and a traveling crystal. It is independent of activity  $v_0$ , as can be seen in Eq. (3.3). There,  $v_0$  only appears in the (then negative) discriminant and therefore only influences  $\text{Im}(\lambda)$ , i.e., the drift velocity  $c$  of the perturbation modes. The upwards curved black line that separates white and light gray regions at low activity ( $v_0 < 0.15$ ) indicates the stability border of the liquid phase related to a purely real eigenvalue, i.e., a monotonic instability. Alternatively to Cardano's method, the critical wavenumber can be approximated by  $k_c \approx 1$  as used in Ref. [CGT16]. This approximation gives the red lines in Fig. 3.1(a). The resulting stability border cannot be distinguished by eye from the exact results indicating a well justified approximation.

Corresponding dispersion relations are displayed in Fig. 3.1(b) showing  $\text{Re}(\lambda)$  of the leading two eigenvalues with solid (dashed) lines for real (complex) eigenvalues. The roman numbering corresponds to labels in the stability diagram 3.1(a). Case I shows a dominant (i.e., at the maximum) instability mode that is real (i.e., monotonic), and likely results in a resting crystal. However, with increasing activity  $v_0$  the "bubble" of real eigenvalues around the maximum shrinks. At the codimension-2 point (case II) this bubble shrinks to zero and the marginally stable eigenvalue at the maximum becomes complex. Considering the maximum of the dispersion relation, a pitchfork bifurcation becomes a Hopf bifurcation with infinite period exactly at point II, where the lines meet. Case III then shows a dominant mode that is complex (i.e. oscillatory, finite period), and likely results in crystallization into a traveling crystal. Cases IV to VI give further qualitatively different dispersion relations. In particular, points V and VI illustrate the important change in the character of the dominant mode at  $k \approx 1$  from monotonic to oscillatory. Case IV is located on the thin dotted black line in Fig. 3.1(a) that marks where the minimum of  $\text{Re}(\lambda)$  touches zero. The dot-dashed red line is the corresponding approximation obtained by assuming the minimum of  $\text{Re}(\lambda)$  to be at  $k_{\min} = 1$ . Crossing this line does not influence the linear stability but changes the number of expected primary bifurcations. Accordingly, in Fig. 4.1 (that represents a horizontal cut through Fig. 3.1(a) at  $\bar{\psi} = -0.5$ ), at  $v_0 \approx 0.34$  the branch of the (then unstable) resting crystals ends in a subcritical bifurcation.

## 3.2 Drift velocity of crystals from LSA

As discussed above the two phase boundaries in Fig. 3.1(a) between the liquid phase and, respectively, stable resting and stable traveling crystals collide in point II. From there, the boundary between fully nonlinear resting and traveling crystals continues nearly vertically upwards (blue dashed line). This separating line cannot be determined by the present linear

considerations and is obtained by numerical continuation of fully nonlinear states. The resulting dashed blue line marks the onset of crystal motion and confirms Ref. [CGT16], where a similar straight line in a different parameter plane was deduced from direct time simulations. Note that to the right of the vertical line, there is a region where resting crystals still exist as unstable steady states.

Comparing the velocity  $c_{\text{lin}}$  of the dominant linear mode and the fully nonlinearly determined drift velocity  $c$  allows us to rate how well the linear analysis performs. Fig. 3.2(a) shows that close to but above the liquid-solid boundary at  $\bar{\psi} = -0.67$  (Fig. 3.1), the linear (dashed black line) and the fully nonlinear results (dot-dashed orange line) coincide in the onset of motion and the drift velocity in the entire  $v_0$ -range. However, in the nonlinear regime at  $\bar{\psi} = -0.5$ , Fig. 3.2(b) shows that there is a considerable offset in the onset of motion. Yet, at high activities  $v_0$  the linear and nonlinear velocities still converge. The nonlinear drift velocity  $c$  corresponds to the branch of traveling crystals shown in Fig. 4.1.



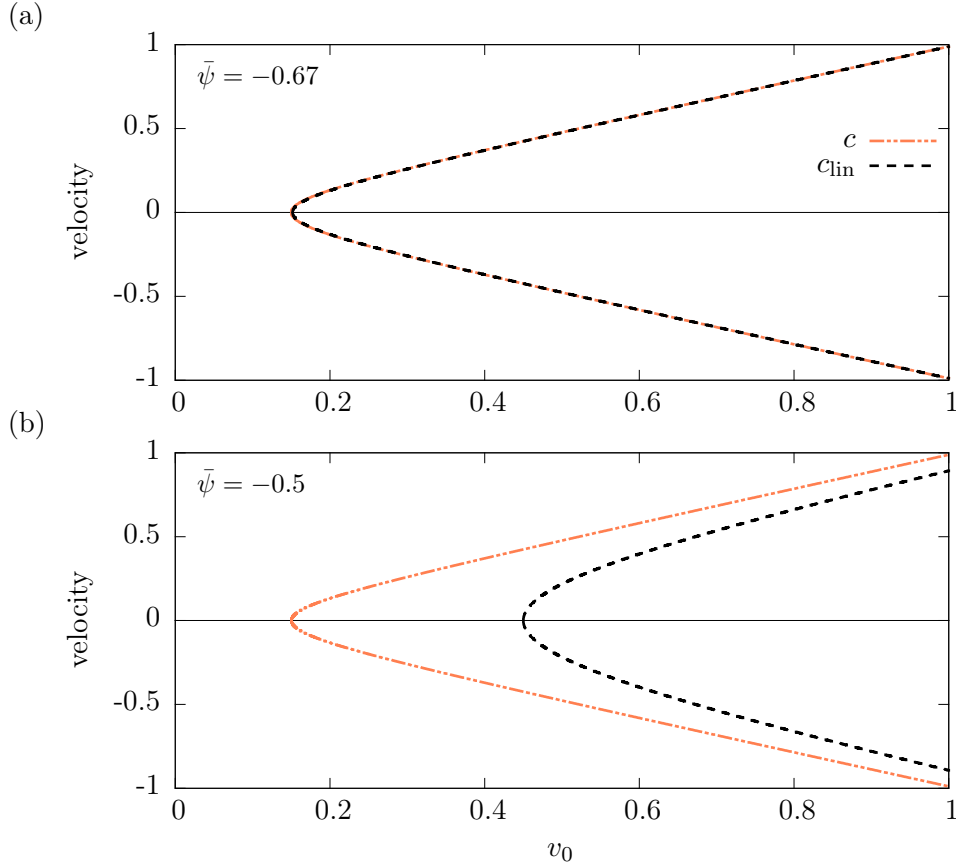


Figure 3.2: Velocity  $c_{\text{lin}}$  of the dominant linear mode (black dashed line) and drift velocity  $c$  (orange dot-dashed) of fully nonlinear moving crystals in dependence of activity  $v_0$  for (a)  $\bar{\psi} = -0.67$  and (b)  $\bar{\psi} = -0.5$ . Remaining parameters are as in Fig. 3.1. The speed  $c_{\text{lin}}$  corresponds to  $\text{Im}(\lambda)/k$ , i.e.,  $c_{\text{lin}} = \text{Im}(\lambda)$  for  $k = 1$ , where the eigenvalue  $\lambda$  is obtained from the linear stability analysis of the homogeneous state. The velocity  $c$  of the fully nonlinear traveling crystals is determined by numerical continuation. (a) In the linear regime close to the onset of crystallization  $c_{\text{lin}}$  and  $c$  coincide. (b) Deep in the unstable regime,  $c_{\text{lin}}$  does not provide a suitable approximation for the onset of motion of the crystal. However,  $c_{\text{lin}}$  and  $c$  approach each other at high  $v_0$ . (cf. [OGT18])



## 4 Active Crystals and Crystallites in One Spatial Dimension

In this chapter, we study spatially modulated solutions of the active PFC model in one spatial dimension. Spatially extended, periodic solutions represent *crystals*. Spatially localized states (LS) that coexist with the uniform liquid are often termed *crystallites*.

Having determined the limits of the linear stability of the liquid phase in chapter 3, we use numerical continuation techniques to determine bifurcation diagrams for resting and traveling crystals and crystallites. We employ the activity  $v_0$  and the mean density  $\bar{\psi}$  as the main control parameters and briefly discuss the influence of the remaining parameters of the model. In addition, oscillatory states and their origin in Hopf bifurcations are discussed.

Note that results presented in this chapter have in large parts been published<sup>1</sup> in

[OGT18] L. Ophaus, S. V. Gurevich and U. Thiele. Resting and traveling localized states in an active phase-field-crystal model. *Phys. Rev. E*, 98:022608, August 2018.

### 4.1 The aPFC model in 1d

Restricting space to one dimension (1d), the active PFC model (Eqs. (2.36) and (2.37)) with a linear equation for the polarization (i.e.,  $C_2 = 0$ ) reads:

$$\partial_t \psi = \partial_{xx} \left\{ \left[ \epsilon + (1 + \partial_{xx})^2 \right] \psi + (\bar{\psi} + \psi)^3 \right\} - v_0 \partial_x P, \quad (4.1)$$

$$\partial_t P = C_1 \partial_{xx} P - D_r C_1 P - v_0 \partial_x \psi. \quad (4.2)$$

In 1d,  $P$  becomes a scalar quantity. It indicates the strength and sense of polarization.

#### 4.1.1 Steady and stationary states

To investigate steady and stationary states (where the latter are steady states in a comoving frame that moves with velocity  $c$ ) we consider Eqs. (4.1) and (4.2) with  $\partial_t \psi = -c \partial_x \psi$  and  $\partial_t P = -c \partial_x P$ . Hence, positive velocities  $c$  correspond to a propagation to the right. Then Eq. (2.36) can be integrated once and we obtain the coupled fifth- and second-order ordinary differential equations

$$0 = \partial_x \left\{ \left[ \epsilon + (1 + \partial_{xx})^2 \right] \psi + (\bar{\psi} + \psi)^3 \right\} - v_0 P + c \psi - J, \quad (4.3)$$

$$0 = C_1 \partial_{xx} P - D_r C_1 P - v_0 \partial_x \psi + c \partial_x P, \quad (4.4)$$

<sup>1</sup>Secs. 4.1-4.4 closely follow [OGT18] and contain figures and text from there. ©APS (2018).

where the integration constant  $J$  represents a flux. We emphasize that for resting states the velocity  $c$  is equal to zero. For traveling states it represents a nonlinear eigenvalue that has to be determined along with the solution profile.

Beside the trivial steady state ( $\psi = 0, P = 0$ ) there exist spatially-modulated states ( $\psi = \psi(x), P = P(x)$ ) that solve Eqs. (4.3) and (4.4). We will determine their bifurcation diagrams employing continuation techniques. In the treated special case of  $C_2 = 0$  (cf. Eq. (4.2)), for periodic states one may integrate the linear Eq. (4.4) over one period  $\ell$  and finds  $\int_\ell dx P(x) = 0$ . As  $\int_\ell dx \psi(x) = 0$  by definition, Eq. (4.3) implies  $J = 0$ . Note that as  $\psi(x)$  is the deviation from the mean  $\bar{\psi}$ , for  $J = 0$  the flux of material is given by  $c\bar{\psi}$ . Note that the system is invariant under the transformation  $(\psi, P, x, c) \rightarrow (\psi, -P, -x, -c)$ . In the case of  $\bar{\psi} = 0$ , also the symmetry  $(\psi, P, x, c) \rightarrow (-\psi, -P, x, c)$  holds.

Throughout the bifurcation analysis of active crystals and active LS in 1d, we will keep the following parameters fixed:

$$\epsilon = -1.5, \quad C_1 = 0.1, \quad C_2 = 0.0, \quad D_r = 0.5. \quad (4.5)$$

Their influence is briefly discussed in Secs. 4.7, 4.6 and 4.8 at the end of this chapter.

### 4.1.2 Numerical continuation in 1d

In the spatially one-dimensional case, we employ numerical path-continuation techniques [KOGV07, Kuz10, DWC<sup>+</sup>14, EGU<sup>+</sup>19] bundled in the package AUTO07P [DKK91, DOC<sup>+</sup>12] to determine steady ( $c = 0$ ) and stationary ( $c \neq 0$ ) periodic and localized solutions of Eqs. (4.3) and (4.4) on a domain of size  $L$ . The techniques allow one to follow branches of solutions in parameter space, detect bifurcations, switch branches and in turn follow the bifurcating branches. The pseudo-arclength continuation implemented in AUTO07P is also able to follow branches when they fold back at saddle-node bifurcations. It allows us to determine the entire bifurcation diagram. In the literature the method is extensively applied to the SH equation [BK06, MBK10, BD12] and PFC-type models [Thi10, RATK12, TAR<sup>+</sup>13, SAKR18]. To our knowledge, continuation has not yet been applied to the aPFC model. For details on numerical continuation see Sec. 2.4.2.

To use AUTO07P, our system of Eqs. (4.3) and (4.4) is transformed into a seven-dimensional dynamical system (with  $x$  being the independent variable with seven periodic boundary conditions). A phase condition that breaks translational invariance and a constraint that controls the volume are included as integral conditions (cf. Refs. [TKG14, EGU<sup>+</sup>19] for examples of using such conditions for several related equations). This implies that in each continuation run beside the main control parameter one has two further parameters that have to be adapted. Here, we use either the mean density  $\bar{\psi}$  or the activity  $v_0$  as main control parameter while velocity  $c$  and flux  $J$  are adapted.

The resulting bifurcation diagrams are given in terms of the  $L^2$ -norm of the solution array that we use as main solution measure. It is defined by

$$\|\underline{\psi}, \underline{P}\|_2 = \sqrt{\frac{1}{L} \int_0^L \sum_{i=1}^7 a_i^2 dx} \quad (4.6)$$

where the  $a_i$  stand for the elements of the solution array

$$(\underline{\psi}, \underline{P}) = (\psi, \partial_x \psi, \partial_{xx} \psi, \partial_{xxx} \psi, \partial_x^4 \psi, P, \partial_x P). \quad (4.7)$$

## 4.2 Periodic states

In the standard PFC model (Eq. (4.1) with  $v_0 = 0$ ), at sufficient distance from the critical point ( $\epsilon$  sufficiently negative or  $\bar{\psi} < 0$  sufficiently large) the transition from the liquid state (uniform solution) to a crystalline state (periodic solution) corresponds to a first order liquid-solid phase transition with a parameter region – limited by the binodal lines – where the two states coexist [TAR<sup>+</sup>13]. As  $\psi$  is a conserved quantity this does not automatically imply that one has a subcritical bifurcation from the homogeneous to the periodic solution branch. For a detailed discussion of this intricate point see the conclusion of Ref. [TAR<sup>+</sup>13].

As the aPFC model is non-variational, here, the transition between the states does not correspond anymore to a thermodynamic phase transition, i.e., arguments based on a free energy do not hold anymore. Furthermore, now also the activity  $v_0$  may be used to induce the transition. In particular, for the parameters of Fig. 3.1 at  $\bar{\psi}$  approximately between  $-0.71$  and  $-0.67$  increasing  $v_0$  beyond the solid line melts the resting crystal. More striking is the behavior at higher densities (in Fig. 3.1(a) for  $\bar{\psi}$  above  $-0.67$ ). As illustrated in the bifurcation diagram Fig. 4.1, there, increasing  $v_0$  does not destroy the resting crystal but results in the onset of motion at a critical activity  $v_c \approx 0.15$  (corresponding to the vertical dashed line in Fig. 3.1(a)), i.e., in a transition from a stable resting to a stable traveling crystal.

Specifically, for the resting crystals, Fig. 4.1(a) shows that with increasing activity the norm of  $\psi$  monotonically decreases while, in contrast, the amplitude of the polarization field (see inset) first increases from zero (at  $v_0 = 0$ ) until at some  $v_0 = v_c$  its norm equals the one of  $\psi$ . There, the branch of traveling crystals bifurcates and the resting crystals become unstable and ultimately cease to exist (after further undergoing a Hopf bifurcation) at about  $v_0 = 0.34$  where the branch ends in a subcritical pitchfork bifurcation on the branch of homogeneous states. As mentioned in section 3.1, this bifurcation corresponds to point IV in Fig. 3.1. There, a double real eigenvalue of the linear stability problem of the liquid state crosses zero indicating a bifurcation of the uniform state. For a discussion of oscillatory states associated with the Hopf bifurcation see section 4.5.2 .

At  $v_c$ , a drift-pitchfork bifurcation [Fri05] occurs, i.e., a real eigenvalue crosses zero (see stability analysis in section 4.3.3) and two branches of moving periodic states (i.e., traveling crystals) emerge from the branch of resting crystals. An analytical condition for drift bifurcations is derived in section 4.4.

The two bifurcating branches with the same norm are related by the symmetry  $(\psi, P, x, c) \rightarrow (\psi, -P, -x, -c)$  and the velocity close to the bifurcation is  $c \propto (v_0 - v_c)^{1/2}$ . The individual solutions on the emerging branches do not anymore have the symmetry  $(\psi, P, x) \rightarrow (\psi, -P, -x)$  of the resting crystal states (i.e., zero crossings of  $P$  do not anymore coincide with the position of the peak maxima of  $\psi$ ). Instead, for the traveling crystals, the individually practically unchanged  $\psi(x)$  and  $P(x)$  profiles are shifted w.r.t. each other. The profiles keep their spatial periodicity and always move with a constant drift velocity. The velocity  $|c|$  increases monotonically for  $v_0 > v_c$ , the spatial phase shift between profiles of  $\psi$  and  $P$  decreases monotonically. Indeed, for  $v_0 \gg 1$  one finds  $c \approx \pm v_0$  and  $\psi(x) \approx \pm P(x)$ . Typical density and polarization profiles are given in Fig. 4.1(b).

Studying the spatial phase shift  $\Delta$  between the two fields in detail, Fig. 4.2 reveals a power law between  $\Delta$  and  $v_0$ . The phase shift  $\Delta$  is evaluated by tracking the positions of a peak of  $\psi$  and of the nearest peak of  $P$ . To fulfill the symmetry  $(\psi, P, x) \rightarrow (\psi, -P, -x)$ , the two profiles of a resting crystal need  $\Delta = \ell/4$  (cf. Fig. 4.1(b)(I)). For traveling crystals, with

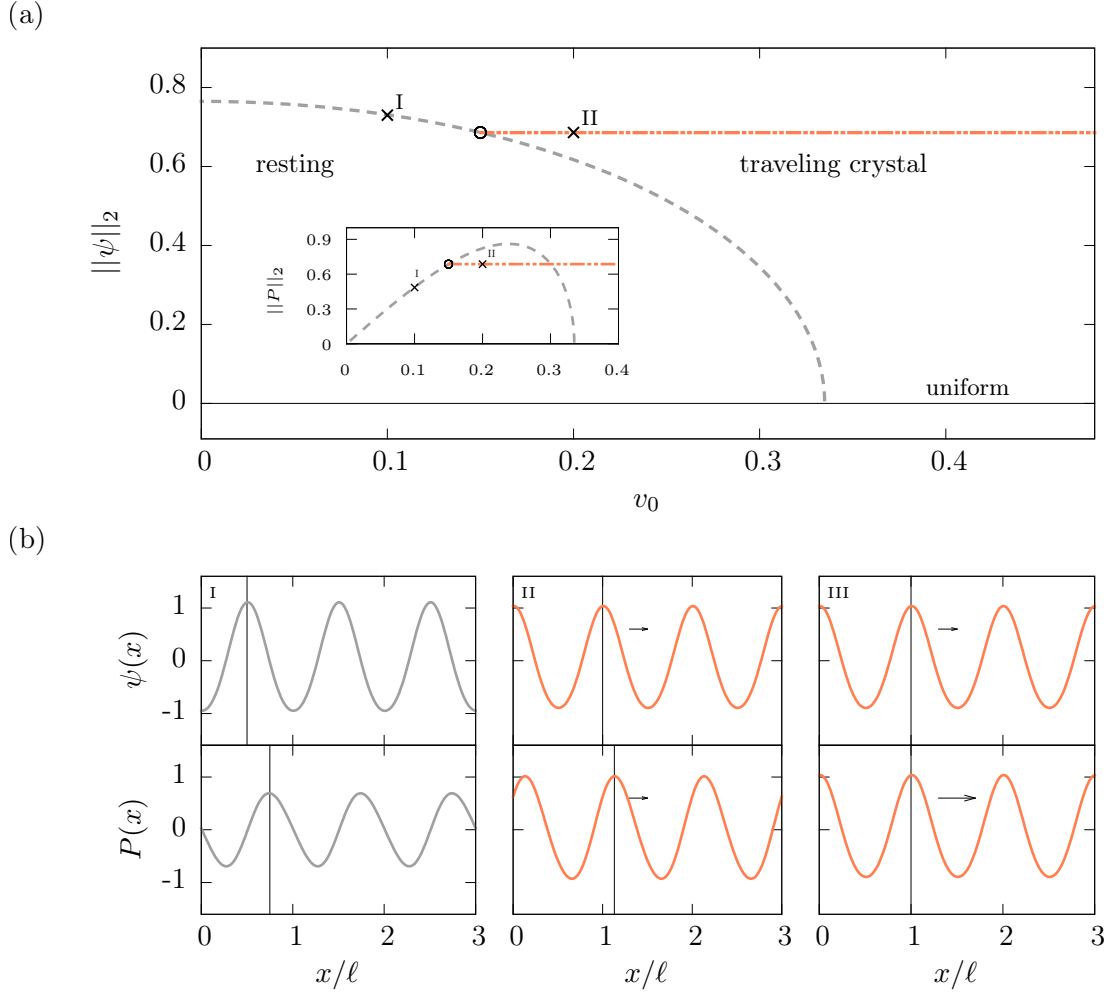


Figure 4.1: Resting and traveling crystals as a function of activity  $v_0$  in the one-dimensional aPFC model. (a) The solution profiles of the periodic crystalline states are characterized by the  $L^2$ -norms of  $\psi$ ,  $\|\psi\|_2 = \sqrt{\frac{1}{L} \int_0^L \psi^2 dx}$ , and  $P$  (inset). Branches of resting structures are shown in dashed gray, while traveling crystals are in dot-dashed orange. At a critical value of  $v_c \approx 0.15$  (indicated by circles), the resting crystal is destabilized and starts to move. The spatial periodicity remains unchanged. (b) depicts parts (3 times period  $\ell$ ) of the profiles of the structures at points indicated by roman numerals in (a). Crystals I and II are close to the onset of motion. Profile III shows an active crystal at a high activity of  $v_0 = 10.0$  beyond the range of (a). The drift velocity  $c$  of the moving crystals increases monotonically with  $v_0$  as shown in Fig. 3.2(b). Note that the spatial phase shift  $\Delta$  between  $\psi$  and  $P$  changes for traveling crystals (on the orange branch) when varying  $v_0$ , highlighted by vertical lines.  $\bar{\psi} = -0.5, L = 100$ , remaining parameters are as in Fig. 3.1. (cf. [OGT18])

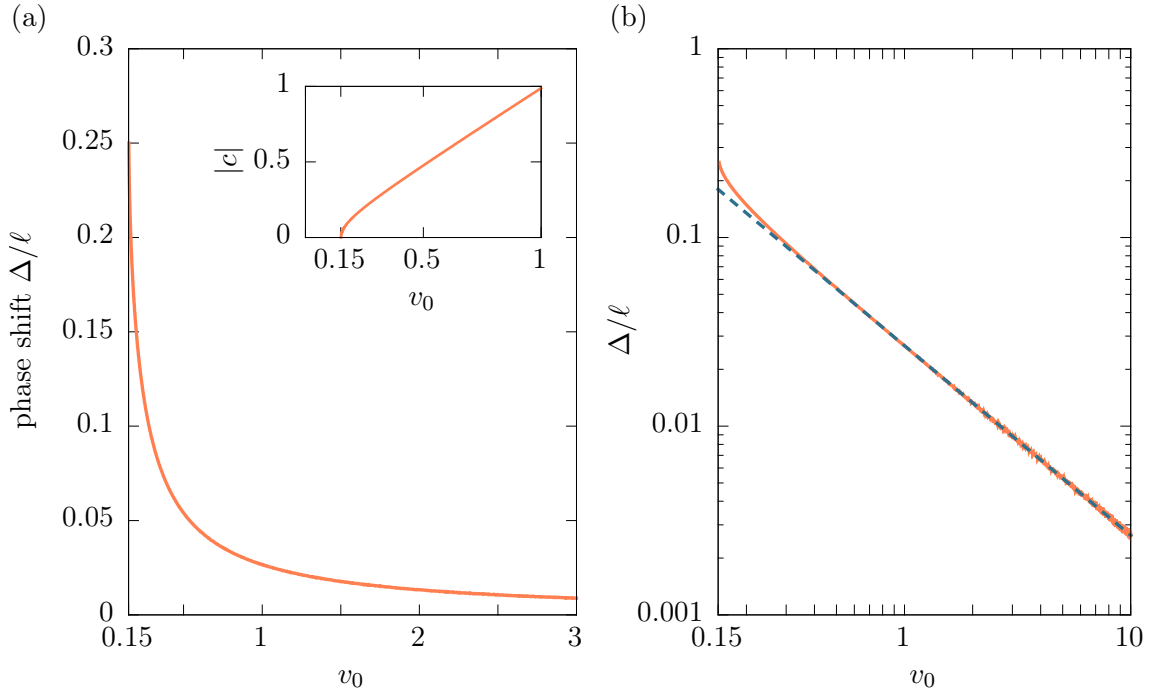


Figure 4.2: (a) Spatial phase shift  $\Delta$  between  $\psi$  and  $P$  of a traveling crystal as a function of activity  $v_0$ . The shift is indicated by vertical lines in Fig. 4.1(b).  $\Delta$  decreases monotonically with  $v_0$  resulting in a monotonically growing drift velocity  $|c|$  (inset) above the onset of motion at  $v_c \approx 0.15$ . For resting crystals with zero net polarization, peaks of  $\psi$  coincide with zeros in  $P$ . Resting crystals exhibit a spatial phase shift of a quarter of one spatial period  $\ell$ . The crystal closely matches this value at  $v_c$ . (b) Logarithmic scales reveal a power law. Fitting  $\Delta/\ell$  by  $f(x) = bx^a$  (dashed blue) with  $v_0$  as  $x$  for  $v_0 \geq 0.5$  gives  $a \approx -1.005$ , i.e.,  $\Delta \propto v_0^{-1}$ . Parameters as in Fig. 4.1

increasing  $v_0$ ,  $\Delta$  is rapidly falling from this value. In Fig. 4.2(b) logarithmic scales of the axes exhibit that  $\Delta$  and  $v_0$  are related by a power law. Fitting the corresponding straight line for  $v_0 > 0.5$  by minimizing the weighted sum of squared distances  $(\Delta - f(v_0))^2$  results in  $f(v_0) \propto v_0^{-1}$ . The exact exponent reads  $1.00544 \pm 7.8e - 05$  with asymptotic standard error [You15].

The numerical results are consistent with analytical estimates for the shift. From continuation, we know that for sufficiently large  $v_0$

$$\psi(x) \approx P(x + \Delta) \quad (4.8)$$

$$= P(x) + \Delta \partial_x P(x) + \mathcal{O}(\Delta^2) \quad (4.9)$$

and

$$P(x) \approx \psi(x - \Delta) \quad (4.10)$$

$$= \psi(x) - \Delta \partial_x \psi(x) + \mathcal{O}(\Delta^2). \quad (4.11)$$

Plugging this into the steady state equations for  $\psi$  and  $P$  (Eqs. (4.3) not integrated and (4.4)) one obtains

$$0 = \partial_{xx} \left\{ \left[ \epsilon + (1 + \partial_{xx})^2 \right] \psi(x) + (\bar{\psi} + \psi(x))^3 \right\} \\ - v_0 \partial_x \psi(x) + v_0 \Delta \partial_{xx} \psi(x) + c \partial_x \psi(x), \quad (4.12)$$

$$0 = C_1 \partial_{xx} P(x) - D_r C_1 P(x) - v_0 \partial_x P(x) - v_0 \Delta \partial_{xx} P(x) + c \partial_x P(x). \quad (4.13)$$

In the sum of (4.12) and (4.13), we can identify the stationary states and corresponding zeros and end up with

$$0 = v_0 \Delta \partial_{xx} \psi(x) - v_0 \Delta \partial_{xx} P(x) \quad (4.14)$$

holding at any  $v_0 > v_c$ .

Substituting  $P(x)$  by  $\psi(x - \Delta)$  again, yields after linearization in  $\Delta$

$$0 = v_0 \Delta^2 \partial_{xxx} \psi(x). \quad (4.15)$$

This has to hold for large  $v_0$  implying that

$$v_0 \Delta^2 \longrightarrow 0 \quad (4.16)$$

for  $v_0 \rightarrow \infty$ , i.e.,

$$\Delta \propto v_0^{-n} \quad (4.17)$$

with  $n > 1/2$ . The numerically obtained exponent  $n \approx 1$  satisfies this inequality.

### 4.3 Localized states

As for the passive PFC model, where the described phase transition between liquid and crystal state is of first order for sufficiently negative  $\epsilon$ , one finds that in the transition region patches of liquid state and crystal state may coexist. In the PFC model this corresponds to the existence of a broad variety of spatially localized states (or crystallites) that in 1d were numerically analyzed in Ref. [RATK12, TAR<sup>+</sup>13] (for selected 2d results see [EGU<sup>+</sup>19, TFHE<sup>+</sup>19]). Next, we systematically explore how the bifurcation structure of these crystallites is amended by activity. We investigate if and to what extent the phenomenon of slanted homoclinic snaking [BKL<sup>+</sup>09] is changed by finite values of activity. Do traveling localized states arise due to self-propulsion? Can motion also be induced by changes in the mean concentration?

Following former works, we classify the localized states according to their spatial symmetry [BK06, TAR<sup>+</sup>13] and their drift velocity [ML13]. There are two kinds of resting localized states (RLS) that have a parity (left-right) symmetry in the  $\psi$ -component and an inversion-symmetric polarization:  $(\psi(x), P(x)) = (\psi(-x), -P(-x))$ . The symmetric localized patches can either have a  $\psi$ -peak or  $\psi$ -trough at the center, resulting in an odd or even number of peaks, respectively. We call them “odd states” (RLS<sub>odd</sub>) and “even states” (RLS<sub>even</sub>). Beside spatially symmetric states, resting asymmetric localized states exist that have no parity symmetry. We refer to them as RLS<sub>asym</sub>. In the PFC model, the RLS states form an intricate slanted snakes-and-ladders structure [TAR<sup>+</sup>13]. Traveling localized states have a nonzero drift velocity and are called TLS. For TLS, the above symmetries in  $\psi$  and  $P$  are not preserved.



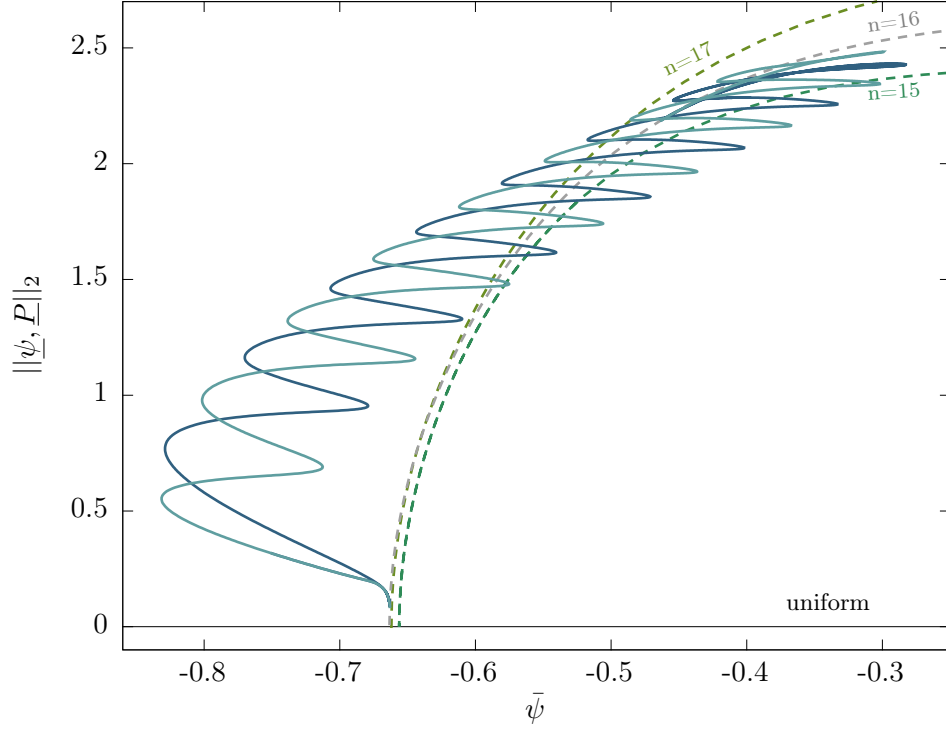


Figure 4.3: Slanted homoclinic snaking of resting symmetric steady states (drift velocity  $c = 0$ ). Shown is the  $L^2$ -norm of the steady states in dependence of the mean concentration  $\bar{\psi}$ . The active drive is fixed at  $v_0 = 0.16475 > v_c$ . The steady localized states bifurcate subcritically from the periodic solution with  $n = 16$  peaks (dashed gray line). The light (dark) blue line represents resting localized structures with a peak (trough) in the middle,  $\text{RLS}_{\text{odd}}$  ( $\text{RLS}_{\text{even}}$ ). Both lines ultimately terminate on the  $n = 16$  periodic state. Beside the spatially extended crystal with  $n = 16$  peaks, there are solutions with  $n = 15$  and  $n = 17$  peaks (dashed green lines). Remaining parameters as in Fig. 4.1. (cf. [OGT18])

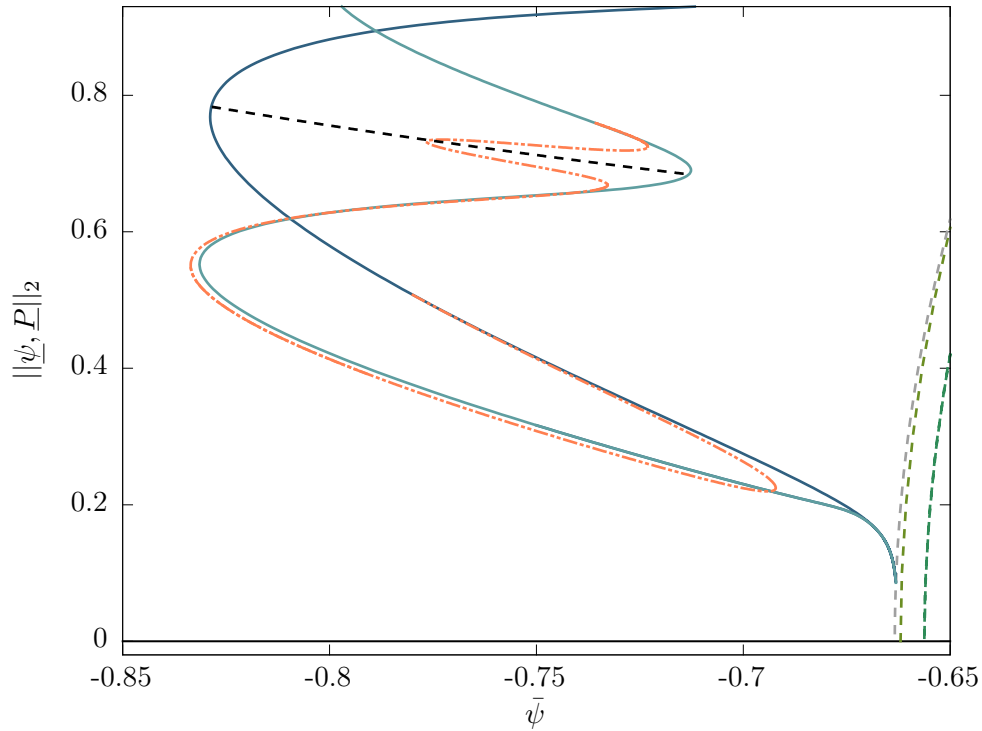


Figure 4.4: Resting and traveling localized states as a function of the mean concentration  $\bar{\psi}$ . The localized states are created in a subcritical bifurcation and branch off from the  $n = 16$  periodic solution branch (dashed gray, more periodic branches in dashed green). Light and dark blue lines:  $\text{RLS}_{\text{odd}}$  and  $\text{RLS}_{\text{even}}$ . The ladder branch (dashed black line) corresponding to asymmetric states connects the two symmetric RLS. Beside snaking branches and the ladder rungs, we find traveling localized states (TLS, dot-dashed orange) that arise due to activity. A zoom of the drift-transcritical bifurcation on the branch of asymmetric RLS can be found in Fig. 4.11. Remaining parameters as in Fig. 4.3. (cf. [OGT18])

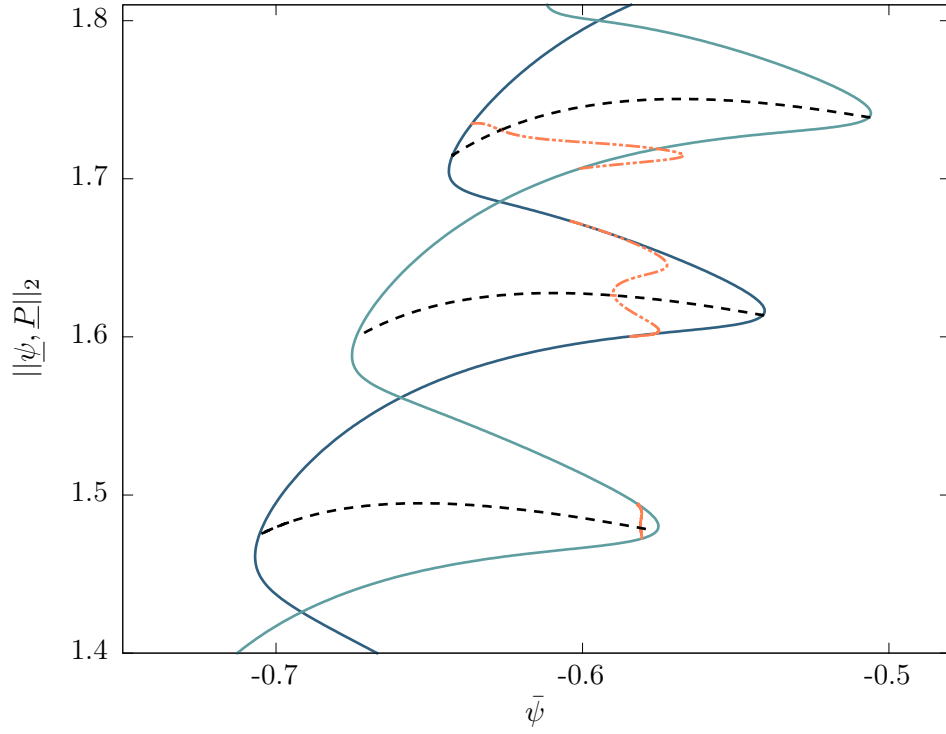


Figure 4.5: Slanted snakes-and-ladders structure for finite active drive. The light (dark) blue line represents odd (even) symmetric localized structures. The dashed black lines correspond to asymmetric localized states. Because of the active drive above  $v_c$  there exist traveling states (TLS, dot-dashed orange line) that emerge in various drift bifurcations. The shown branches of TLS have between 5, 6 and 7 peaks in  $\psi$ . Remaining parameters as in Fig. 4.3. (cf. [OGT18])

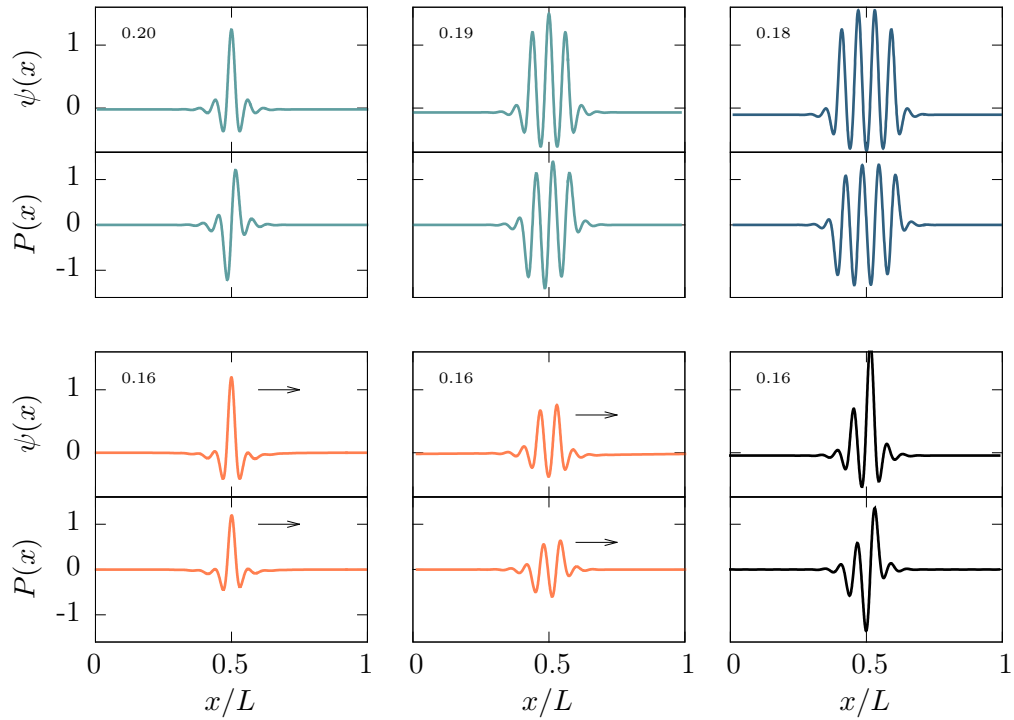


Figure 4.6: Typical density and polarization profiles of localized states for  $\bar{\psi} = -0.75$  and various values of activity  $v_0$  (rounded value given in each panel). Blue colors indicate symmetric RLS. Two states with an odd number of peaks are followed by an even RLS (top, from left to right). An asymmetric resting state is plotted in black. The profiles in orange are traveling localized states. Their profile is slightly asymmetric, too. Note that the integral over  $\psi$  vanishes, as it only describes the modulation around  $\bar{\psi}$ . Remaining parameters as in Fig. 4.1. (cf. [OGT18])

### 4.3.1 Bifurcation structure

Figure 4.3 gives the bifurcation diagram for periodic and localized states of the aPFC model (Eqs. (4.3) and (4.4)) for fixed finite activity  $v_0 \approx 0.16 > v_c$  employing the mean density  $\bar{\psi}$  as control parameter. It illustrates the main characteristics of the resting crystallites (steady localized states) and their snaking path towards a spatially extended crystal that fills the whole considered domain. The appearance of the bifurcation diagram is similar to the one obtained for the conserved Swift-Hohenberg equation (passive PFC) [TAR<sup>+</sup>13], note, in particular, the slanted snaking that also occurs for other systems with conserved quantities [BCR08, Daw08, LJBK11, TAR<sup>+</sup>13]. The liquid state with solution measure  $\|\underline{\psi}, \underline{P}\|_2 = 0$  is destabilized when  $\bar{\psi}$  is increased above a critical mean concentration  $\bar{\psi}_c \approx -0.66$ , coinciding with point II in Fig. 3.1(a). For the employed domain size of  $L = 100$ , three branches of periodic states bifurcate from the uniform state. The dashed gray and dashed green lines correspond to periodic structures with  $n = 15, 16$  and  $17$   $\psi$ -peaks. Slightly beyond the primary bifurcation, the periodic state with  $n = 16$  is destabilized and two branches (light and dark blue) emerge in a subcritical secondary bifurcation. Fig. 4.4 gives a zoom of this region. The two branches correspond to the resting odd and even localized states, respectively. Both branches undergo a series of saddle-node bifurcations where their stabilities change (cf. Fig. 4.5 and subsection 4.3.3). The odd and the even branch of symmetric RLS are connected by many branches of asymmetric RLS that are given in Figs. 4.4 and 4.5 as dashed black lines, but are not included in Fig. 4.3.

Each pair of saddle-node bifurcations adds a couple of peaks to the localized crystalline patch that, in consequence, enlarges until ultimately the whole domain is filled with the crystalline state and the branches of localized states terminate on the  $n = 16$  branch of periodic states. Because of the conserved character of the density  $\psi$  the density of the coexisting uniform state is not constant but changes with the increasing size of the crystalline patch. This results in the slanted snaking structure, i.e., the loci of subsequent saddle-node bifurcations do not form straight vertical lines in Fig. 4.3 but drift towards larger  $\bar{\psi}$ . Increasing the domain size, adds more 'undulations' to the slanted snaking structure and the relative tilt between subsequent saddle-node bifurcations becomes smaller, however, without changing the overall tiltedness.

A qualitatively new feature of the solution structure of the aPFC model are the branches of traveling localized states (TLS) shown as dot-dashed orange lines in Figs. 4.4 and 4.5. The TLS drift with a constant velocity  $c$ . Their  $\psi$  profiles look quite similar to the one of RLS, the left-right symmetry is broken, though. Crossing the onset of motion, the  $P$  profile loses its inversion symmetry and approaches the phase and shape of  $\psi$ . Typical profiles of RLS and TLS are presented in Fig. 4.6. The branches of TLS bifurcate in drift-transcritical bifurcations from the branches of asymmetric RLS and in drift-pitchfork bifurcations from the branches of symmetric RLS. An analytical condition for the detection of the drift bifurcations is derived in Sec. 4.4. This criterion holds for both types of drift bifurcations.

The branches of TLS connect the snaking branches of symmetric RLS like rungs. They may connect two 'sub-branches' of the same symmetry like the two lower orange branches in Fig. 4.5 as well as branches of  $\text{RLS}_{\text{odd}}$  and  $\text{RLS}_{\text{even}}$  like the orange branch with the highest norm in Fig. 4.5. TLS of small extension (one or two peaks, i.e., the ones in Fig. 4.4) exist in a broad range of mean density  $\bar{\psi}$ . Because of their similar profiles, the norm of RLS and TLS is almost equal and the branches seem to nearly coincide in the lower part of Fig. 4.4.

Similar to the case of periodic states, also for RLS an increase of the activity  $v_0$  at fixed  $\bar{\psi}$

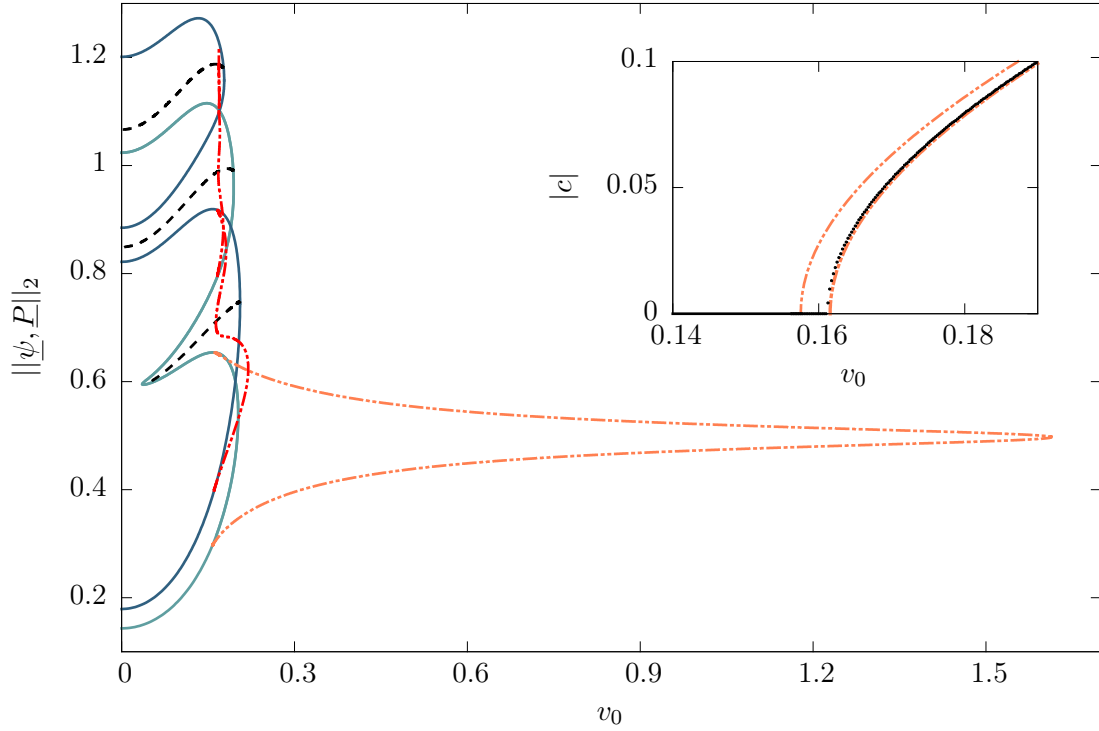


Figure 4.7: Bifurcation diagram of resting and traveling localized states giving the  $L^2$ -norm as a function of the active drive  $v_0$ . The mean concentration is fixed at  $\bar{\psi} = -0.75$ . Resting solutions are indicated by blue (left-right symmetric states) and dashed black (asymmetric states) lines, moving states are dot-dashed red and orange. The traveling single peak exists up to high values of  $v_0 \approx 1.6$ . Inset: Velocity  $|c|$  of the traveling single peak as a function of  $v_0$ . At a critical value of  $v_c \approx 0.16$  the transition from resting to a traveling linearly stable one-peak LS occurs. Black dots (red dashed lines) give the results of direct numerical simulations (numerical continuation). The moving state corresponds to the long finger in the large panel. Its upper half is stable (right part of orange branch in inset). The remaining parameters are  $\epsilon = -1.5$ ,  $C_1 = 0.1$  and  $D_r = 0.5$  as in Fig. 4.1. (cf. [OGT18])

may result in a transition to TLS. Fig. 4.7 gives a typical example of a bifurcation diagram using  $\bar{\psi} = -0.75$ . Thereby, the threshold value for the onset of motion slightly differs for the various RLS (inset of Fig. 4.7). All discussed TLS have density and polarization profiles that are steady in corresponding comoving frames.

Recall that the onset of motion coincides with a symmetry breaking related to a spatial shift between the density and the polar ordering profiles. The density peaks are shifted away from the zeros of  $P$ , resulting in a nonzero value when integrating  $\psi$  times  $P$  over the width of a peak. Above the critical activity  $v_c$ , the left-right symmetry of the density profile is also broken. The same holds for the inversion symmetry of the polarization. As described above and shown in Fig. 4.6 at large  $v_0$  the  $P$  profile approaches the position and shape of  $\psi$ . In fact, the norm of  $\psi$  and  $P$  are equal for traveling structures.

Beside path-continuation we also employ direct time simulations of Eqs. (2.36) and (2.37) to investigate the TLS. In particular, we track the traveling single density peak over time and determine its velocity. This confirms the continuation results as shown in the inset of Fig. 4.7. The two orange dot-dashed lines in the inset correspond to the long nose of traveling one-peak states in the main panel. The upper branch of this nose is stable, losing its stability at the fold at  $v_0 \approx 1.6$ . The lower branch is unstable and corresponds to the left orange branch in the inset. Its onset of motion is at a slightly smaller value of  $v_0$  as compared to the stable one. For the particular value of mean concentration  $\bar{\psi}$  shown in Fig. 4.7, localized states consisting of more than one peak only appear to exist in a fairly narrow range of  $v_0$  around  $v_c$ . The dot-dashed red line in Fig. 4.7 that corresponds to broader TLS with a few peaks wiggles about an almost vertical line before terminating on the blue branch of four connected resting peaks. The region of existence of the TLS is studied via fold continuation in the next section. Note that the velocities of all these different traveling structures are very similar.

### 4.3.2 Fold continuation

A two-parameter continuation allows one to track the loci of various bifurcation points in a two parameter plane [DKK91]. Here, we follow the loci of (i) the saddle-node bifurcations that mark the points where stable and unstable one-peak and two-peak TLS annihilate and (ii) the drift bifurcations where TLS emerge from RLS in the parameter plane spanned by activity  $v_0$  and mean density  $\bar{\psi}$ . This allows us to determine the area of existence of these localized states in the  $(v_0, \bar{\psi})$ -plane.

The result is displayed in Fig. 4.8(a) where drift and saddle-node bifurcations are marked by black solid lines and orange dot-dashed lines, respectively. The plot has to be carefully interpreted as the various bifurcations can be located on different branches in the bifurcation diagrams. To facilitate this we have marked the two values  $\bar{\psi} = -0.71$  and  $\bar{\psi} = -0.78$  by horizontal gray lines and provide the corresponding one parameter bifurcation diagrams as Fig. 4.8 (b) and (c) (also cf. Fig. 4.7). There, the bifurcation points are highlighted by symbols, that also mark the fold continuation lines in (a).

Fig. 4.8 proves that traveling localized states are a generic solution of the active PFC model as they occur in an extended region of the parameter plane. In fact, the values of  $v_0$  at the saddle-node bifurcations that limit their existence diverge at  $\bar{\psi} = -0.74$  and  $\bar{\psi} = -0.69$  for one- and two-peak TLS, respectively. We numerically follow their position up to  $v_0 = 10^3$ . Note that for  $\bar{\psi} = -0.71$  the fold of the one-peak TLS has already moved far outside of the displayed  $v_0$ -interval. At this  $\bar{\psi}$ , the two-peak TLS exists up to  $v_0 \approx 0.38$  while at  $\bar{\psi} = -0.78$

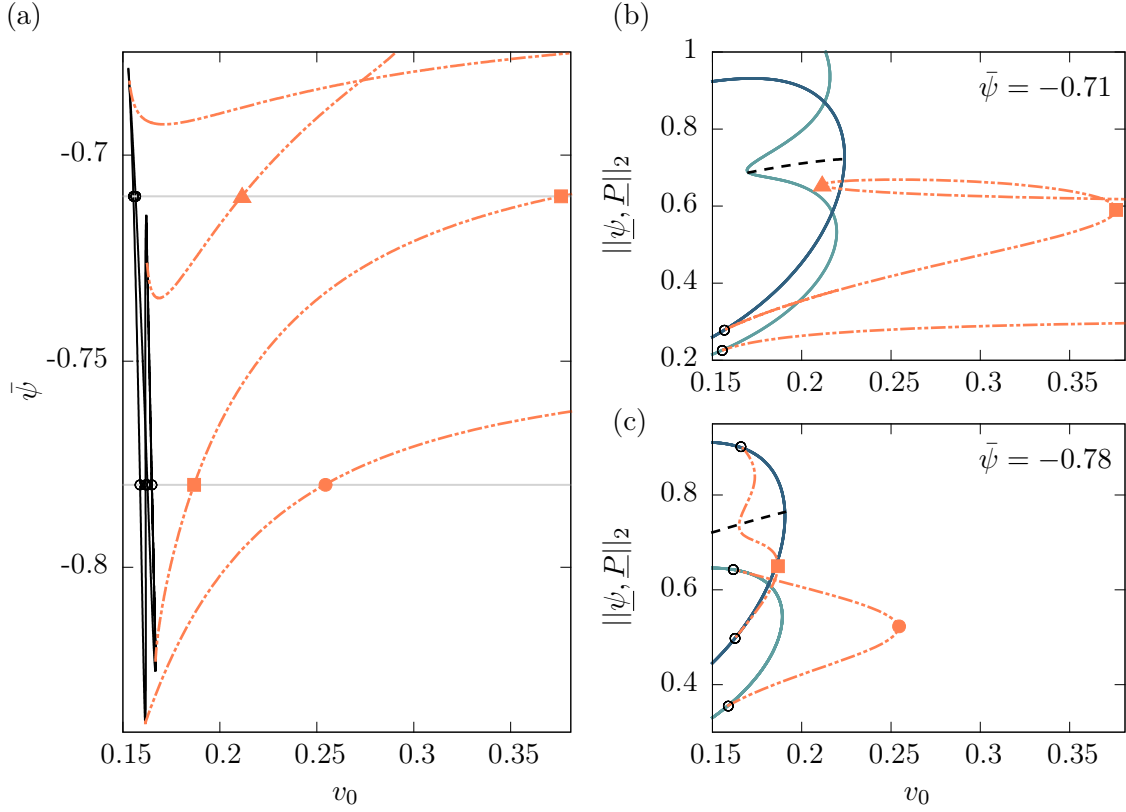


Figure 4.8: (a) Two parameter continuation of the loci of the drift bifurcations (black solid lines) and of the saddle-node bifurcations (orange dot-dashed lines) of the one- and two-peak TLS. (b) and (c) Corresponding one parameter bifurcation diagrams at fixed values of  $\bar{\psi}$  marked by gray horizontal lines in (a). Blue branches correspond to RLS, and dot-dashed orange branches correspond to TLS. The drift bifurcations are marked by circles, and the saddle-node bifurcations are indicated by orange symbols. For increasing mean concentrations, the interval of  $v_0$  in which moving LS exist (onset of motion up to fold) grows and ultimately the activity value at the fold diverges, i.e., TLS exist for arbitrarily high activities. (cf. [OGT18])



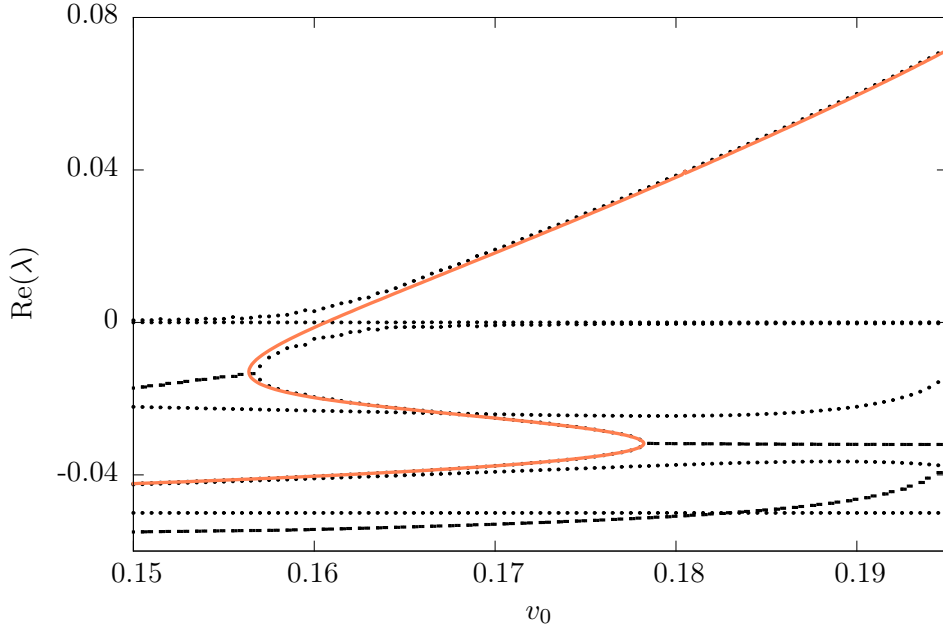


Figure 4.9: Black lines: Real part of eigenvalues obtained from numerical LSA with a finite difference method. The black dashed (dotted) lines indicate a complex (real) eigenvalues. Orange line: Real eigenvalue from continuation. As expected, two neutrally stable modes with  $\text{Re}(\lambda) = 0$  are found (translation mode and volume mode). One mode is destabilized at  $v_c \approx 0.161$ , the detected onset of motion. At  $v_c$ , the mode coincides with the spatial derivative of the localized state and corresponds to a translation. (cf. [OGT18])

its range of existence is smaller. All drift bifurcations are quite close to  $v_0 = 0.15$  with only small variations between different localized states and with  $\bar{\psi}$ . This makes an interpretation of the corresponding diagram region challenging.

Roughly speaking, one-peak [two-peak] TLS exist in the lower part of Fig. 4.8(a) in the area between the nearly vertical blue solid lines and the dot-dashed line marked by the filled circle [square] while in the upper part of Fig. 4.8(a) they exist in the area between the dot-dashed line marked by the filled triangle and the one marked by the filled circle [square]. Remember that in (b) the filled circle has left the displayed interval of  $v_0$ . The uppermost unmarked dot-dashed line in Fig. 4.8(a) is related to three-peak TLS and will here not be further discussed.

### 4.3.3 Linear stability

Up to here we have discussed bifurcation diagrams and existence regions of various states. Although general knowledge about bifurcations allows one to develop quite a good idea about the stability of the various solutions, it is important to explicitly determine the linear stability. The obtained detailed information then permits us to predict which states can persist in experiments or direct numerical simulations (the linearly stable states) and which states may only appear as (possible long-lived) transients. These are given by the unstable states that represent saddles in function space, as they might first attract time-evolutions to

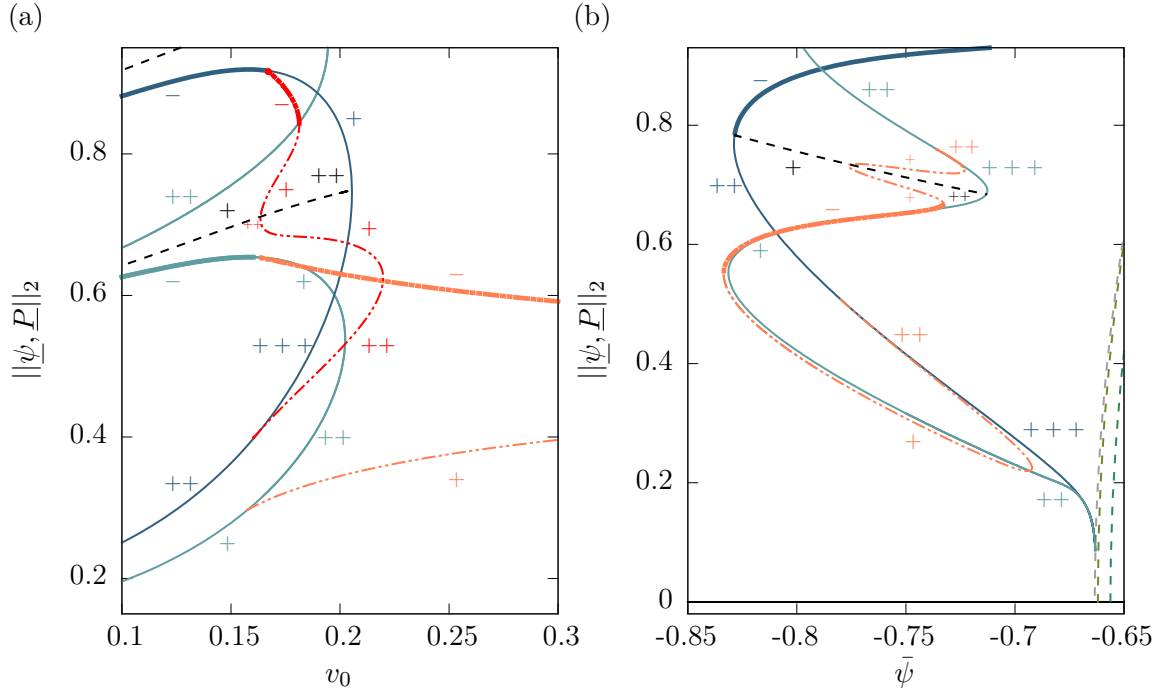


Figure 4.10: Linear stability of localized states. Light and dark blue lines:  $\text{RLS}_{\text{odd}}$  and  $\text{RLS}_{\text{even}}$ . Dashed black: Asymmetric RLS. Dot-dashed orange: TRS. Stable steady states are indicated by  $-$  signs and plotted as heavy lines. For unstable states, the number of  $+$  signs gives the number of unstable eigenmodes with  $\text{Re}(\lambda) > 0$ . (a) Continuation of  $v_0$ ,  $\bar{\psi} = -0.75$ . Symmetric RLS lose their stability in drift bifurcations at  $v_0 \approx 0.16$  and TLS become stable. Asymmetric RLS are always unstable. (b) Continuation of  $\bar{\psi}$ ,  $v_0 = 0.16475$ . LS are created in a subcritical bifurcation, branching off from the periodic branch (dashed gray, more periodic branches in dashed green). Note that vertical cuts at the respective values of  $v_0$  of (b) in (a) and of  $\bar{\psi}$  vice versa correspond to each other. (cf. [OGT18])

then repel them into well defined directions corresponding to the eigenvectors of the most unstable eigenvalues.

For the analysis, Eqs. (2.36) and (2.37) are linearized in small perturbations  $\delta\psi$  and  $\delta P$  about a one-dimensional steady state  $(\psi_0(x), P_0(x))^T$  to obtain

$$\partial_t \delta\psi = \partial_{xx} \left( \epsilon + 3(\bar{\psi} + \psi_0)^2 + (1 + \partial_{xx})^2 \right) \delta\psi - v_0 \partial_x \delta P, \quad (4.18)$$

$$\partial_t \delta P = \partial_{xx} (C_1 \delta P) - D_1 C_1 \delta P - v_0 \partial_x \delta\psi. \quad (4.19)$$

In the case of uniformly moving states  $(\psi_0, P_0)^T = (\psi_0(x + ct), P_0(x + ct))^T$ , a comoving frame term is added to the right-hand side. Assuming exponential growth of the perturbation, i.e.,  $\delta\psi = \psi_1 \exp(\lambda t)$  and  $\delta P = P_1 \exp(\lambda t)$  we have to solve the linear eigenvalue problem:

$$\mathcal{L}(\psi_0, P_0) \begin{pmatrix} \psi_1 \\ P_1 \end{pmatrix} = \lambda \begin{pmatrix} \psi_1 \\ P_1 \end{pmatrix}, \quad (4.20)$$

where the linear operator  $\mathcal{L}(\psi_0, P_0)$  is defined by the right-hand side of Eqs. (4.18) and (4.19) [it is explicitly given below in Eq. (4.30)].

We are not able to pursue an analytical solution of the linear problem because already the steady states  $\psi_0(x)$  and  $P_0(x)$  are obtained by numerical continuation. Instead, we discretize the steady states equidistantly in space, i.e., employ a finite difference method to transform (4.20) into a standard linear algebraic eigenvalue problem that we solve employing standard numerical routines.

The black lines in Fig. 4.9 give an example of a calculated eigenvalue spectrum in dependence of the activity. Shown are the real parts of the leading ten eigenvalues for the branch of one-peak RLS that in Fig. 4.10 is stable at  $v_0 = 0.1$ . The dotted lines indicate purely real eigenvalues whereas the three dashed lines indicate complex eigenvalues. The largest eigenvalue is real and crosses zero at a critical activity of  $v_c \approx 0.161$  where the drift-pitchfork bifurcation occurs, as discussed in detail in Sec. 4.4. The obtained  $v_c$  well agrees with the value we obtain through the numerical continuation of the one-peak TLS that detects the drift-pitchfork bifurcation (as a fold) at the same value. Note that in the discretized eigenvalue problem the zero crossing has to be obtained by extrapolation as the relevant eigenvalue 'interacts' with one of the two zero eigenvalues, in this way 'blurring' the crossing. This is related to the problem of level repulsion or avoided crossing (von Neumann-Wigner theorem [vNW93]). To prevent the blurred zero crossing, we also solve Eq. (4.20) by numerical continuation [Thi15]. The eigenvalue we obtain in this way is given by the orange line in Fig. 4.9. It confirms the finite difference calculations and perfectly matches  $v_c$ .

Two zero eigenvalues exist for all  $v_0$  and represent neutrally stable modes that are related to the symmetries of the model. One of them represents a translation mode that occurs because Eqs. (2.36) and (2.37) are invariant with respect to translation and, therefore, exhibit the neutral eigenmode of translation, often called Goldstone mode of translational symmetry. In addition, an infinitesimal change in the mean concentration  $\bar{\psi}$  does also result in another solution of the equations, i.e., the second mode with zero eigenvalue is a neutral volume mode or Goldstone mode of symmetry with respect to mass change.

Calculating the eigenfunction that is destabilized shows that at  $v_c$  the mode matches the spatial derivative of the investigated localized peak. The derivative corresponds to an infinitesimal shift of the position of the peak and, therefore, to the Goldstone mode of translational symmetry. This fact indicates that the onset of motion is indeed due to a drift bifurcation.

A typical result of a systematic stability analysis is shown in Fig. 4.10, where (a) represents an enlargement of a part of the bifurcation diagram in Fig. 4.7 and (b) is the lowest part of the snakes-and-ladders structure. The branches of linearly stable and unstable states are indicated by “-” and “+” signs, respectively. The number of “+” signs gives the number of unstable eigenmodes. Linearly stable states are represented by heavy lines, indicating that in (a) in the considered parameter range one has stable one- and two-peak RLS and TLS with regions of multistability of (i) one- and two-peak RLS at low activity, (ii) one- and two-peak TLS at slightly larger activity and in between (iii) a very small region where one-peak TLS and two-peak RLS are both linearly stable. In the considered case all the eigenvalues that cross the imaginary axis are real, although stable complex eigenvalues do occur (see dashed lines in Fig. 4.9). Note that Fig. 4.10(a) shows more bifurcations than are followed in Fig. 4.8(a).

Studying Figs. 4.10(b) and 4.5 in detail one finds that - despite the similar shape of the snake and ladder - the stability of the RLS differs from the one found for the PFC model [TAR<sup>+</sup>13]: there the symmetric RLS change their stability as the branches snake along, while the asymmetric RLS are always unstable. Here, however, the stable symmetric RLS are already destabilized before the saddle-node bifurcation is reached as the TLS emerge at the drift-pitchfork bifurcation, i.e., their range of linear stability is diminished. Since  $v_0 = 0.16475 > v_c$  in (b) most of the resting branches are unstable. At a drift-transcritical bifurcation the asymmetric RLS also acquire an additional unstable mode as compared to the case of PFC. For activities lower than  $v_c$  the picture is very similar to the one of the passive PFC model.

Figure 4.11 enlarges a detail of Fig. 4.10(a): the drift-transcritical bifurcation where moving states branch off the asymmetric resting state composed of two density peaks of different height. As already the resting state is asymmetric, the two sub-branches emerging at the drift bifurcation are not related to each other by symmetry, but intrinsically differ. Hence, in this case the creation of the TLS corresponds to a drift-transcritical bifurcation, different from the drift-pitchfork bifurcations in which the symmetric RLS lose their stability. The transcritical bifurcation does not coincide with the fold of the (red) TLS branch and its stability changes twice close to the drift bifurcation. Accordingly, in Fig. 4.10(a) the two sub-branches of TLS seem to have the same stability before and after crossing the resting asymmetric state. There is another the drift-transcritical bifurcation on the asymmetric branch in Fig. 4.10(b).

## 4.4 Drift instability: onset of motion

Next, we discuss the numerically found drift bifurcations more in detail and derive a specific simple analytic condition that allows one to detect drift bifurcations for a class of models that includes the aPFC model. The analytical criterion for the onset of motion is valid for the encountered drift-pitchfork and drift-transcritical bifurcations. It can also be extended to two spatial dimensions.

### 4.4.1 Velocity expansion

We consider the one-dimensional version of the model (2.36) and (2.37) in a comoving frame with coordinate  $x' = x + ct$ , time  $t$  and velocity  $c$ . Note that positive velocities now correspond to a drift to the left, in contrast to the formerly used definition in Eqs. (4.3) and

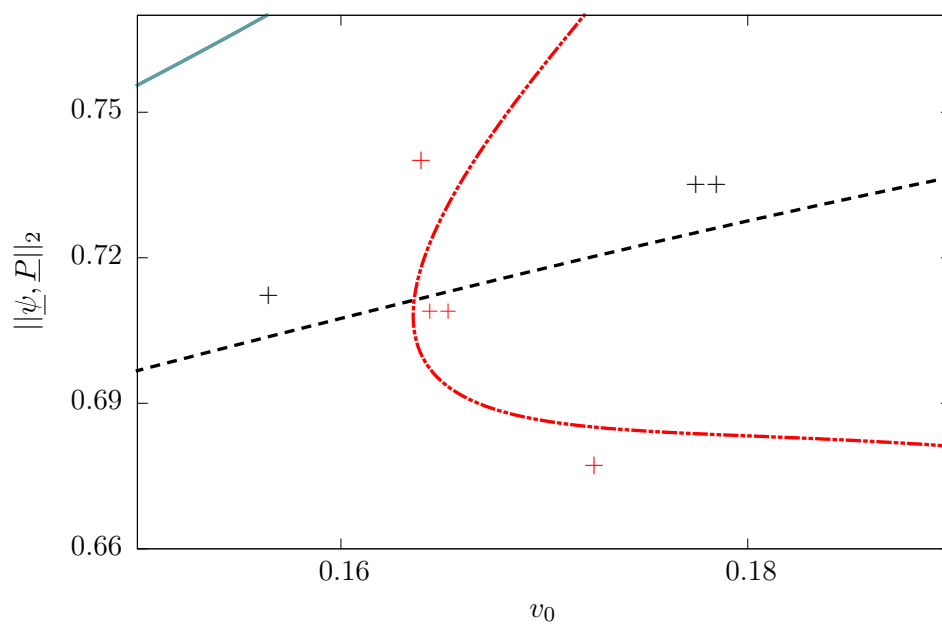


Figure 4.11: Drift-transcritical bifurcation. Enlargement of Fig. 4.10(a). The asymmetric RLS (dashed black, +) acquires an additional unstable mode (++) in a drift-transcritical bifurcation. The moving double bump (dot-dashed red line) changes its stability in the transcritical bifurcation and at the nearby fold. All shown branches are linearly unstable. (cf. [OGT18])

(4.4). For simplicity of the signs in the expansion, the direction of  $c$  is changed here. We use  $(\psi_0(x), P_0(x))^T$  to denote a steady solution, i.e., with  $c = 0$ . Assuming there are only small corrections  $(\tilde{\psi}_i, \tilde{P}_i)^T$  to the steady state when changing parameters close to the drift bifurcation, we introduce a velocity expansion

$$\psi = \psi_0(x) + c \left[ \tilde{\psi}_1(x) + c\tilde{\psi}_2(x) + c^2\tilde{\psi}_3(x) + \dots \right], \quad (4.21)$$

$$P = P_0(x) + c \left[ \tilde{P}_1(x) + c\tilde{P}_2(x) + c^2\tilde{P}_3(x) + \dots \right]. \quad (4.22)$$

Plugging in the expansions (up to order  $c^2$ ) in the dynamic equations (Eqs. (2.36) and (2.37)) leads to

$$\begin{aligned} c \partial_x \left( \psi_0 + c\tilde{\psi}_1 + c^2\tilde{\psi}_2 \right) &= \partial_{xx} \left[ \left( \epsilon + (1 + \partial_{xx})^2 \right) \left( \psi_0 + c\tilde{\psi}_1 + c^2\tilde{\psi}_2 \right) + \left( \bar{\psi} + \psi_0 + c\tilde{\psi}_1 + c^2\tilde{\psi}_2 \right)^3 \right] \\ &\quad - v_0 \partial_x \left( P_0 + c\tilde{P}_1 + c^2\tilde{P}_2 \right), \end{aligned} \quad (4.23)$$

$$\begin{aligned} c \partial_x \left( P_0 + c\tilde{P}_1 + c^2\tilde{P}_2 \right) &= (\partial_{xx} - D_r) \left[ C_1 \left( P_0 + c\tilde{P}_1 + c^2\tilde{P}_2 \right) + C_2 \left( P_0 + c\tilde{P}_1 + c^2\tilde{P}_2 \right)^3 \right] \\ &\quad - v_0 \partial_x \left( \psi_0 + c\tilde{\psi}_1 + c^2\tilde{\psi}_2 \right). \end{aligned} \quad (4.24)$$

By equating coefficients of  $c^n$ , we find for  $c^0$

$$0 = \partial_{xx} \left[ \left( \epsilon + (1 + \partial_{xx})^2 \right) \psi_0 + \left( \bar{\psi} + \psi_0 \right)^3 \right] - v_0 \partial_x P_0, \quad (4.25)$$

$$0 = (\partial_{xx} - D_r) \left( C_1 P_0 + C_2 P_0^3 \right) - v_0 \partial_x \psi_0, \quad (4.26)$$

i.e., we recover the equations for the resting base state. To linear order in  $c$  we obtain

$$\partial_x \psi_0 = \partial_{xx} \left[ \left( \epsilon + (1 + \partial_{xx})^2 \right) \tilde{\psi}_1 + 3 \left( \bar{\psi} + \psi_0 \right)^2 \tilde{\psi}_1 \right] - v_0 \partial_x \tilde{P}_1, \quad (4.27)$$

$$\partial_x P_0 = (\partial_{xx} - D_r) \left( C_1 \tilde{P}_1 + 3 C_2 P_0^2 \tilde{P}_1 \right) - v_0 \partial_x \tilde{\psi}_1, \quad (4.28)$$

a linear system for  $\tilde{\psi}_1$  and  $\tilde{P}_1$ . We write Eqs. (4.27) and (4.28) in matrix form

$$\partial_x \begin{pmatrix} \psi_0 \\ P_0 \end{pmatrix} = \mathcal{L}(\psi_0, P_0) \begin{pmatrix} \tilde{\psi}_1 \\ \tilde{P}_1 \end{pmatrix} \quad (4.29)$$

with the same linear operator  $\mathcal{L}$  already employed in (4.20):

$$\mathcal{L}(\psi_0, P_0) = \begin{pmatrix} \partial_{xx} \left[ \left( \epsilon + (1 + \partial_{xx})^2 \right) + 3 \left( \bar{\psi} + \psi_0(x) \right)^2 \right] & -v_0 \partial_x \\ -v_0 \partial_x & (\partial_{xx} - D_r) \left( C_1 + 3 C_2 P_0(x)^2 \right) \end{pmatrix}. \quad (4.30)$$

In the following, we focus again on the case of a linear equation for  $P$ , i.e.,  $C_2 = 0$ , which is a necessary constraint for the derivation of the criterion for the onset of motion. We notice that the top left component of (4.30)

$$\begin{aligned} L_{11}(x) &= \partial_{xx} \left[ \left( \epsilon + (1 + \partial_{xx})^2 \right) + 3 \left( \bar{\psi} + \psi_0(x) \right)^2 \right] \\ &= \partial_{xx} [-L_{\text{SH}}(\psi_0(x))] \end{aligned} \quad (4.31)$$

is the product of a Laplacian (due to mass conservation) and the linearized operator from a Swift-Hohenberg equation with cubic nonlinearity. This fact will turn out to be very helpful when forming the adjoint operator  $\mathcal{L}^\dagger$ . With  $C_2 = 0$ ,  $L_{22} = (\partial_{xx} - D_r)C_1$  is self-adjoint.

#### 4.4.2 Translational symmetry and Goldstone modes

Adding its first spatial derivative to the base state corresponds to a small shift in the position of the state. Since the aPFC model is translationally invariant,

$$\partial_x \begin{pmatrix} \psi_0 \\ P_0 \end{pmatrix} = \begin{pmatrix} \mathcal{G}_1 \\ \mathcal{G}_2 \end{pmatrix} \equiv \begin{pmatrix} \psi_{\mathcal{G}} \\ P_{\mathcal{G}} \end{pmatrix} \quad (4.32)$$

can be identified as a neutral eigenfunction with eigenvalue zero, often referred to as the Goldstone mode  $\mathcal{G}$  of the translational symmetry. Thus,

$$\mathcal{L} \partial_x \begin{pmatrix} \psi_0 \\ P_0 \end{pmatrix} = \mathcal{L} \mathcal{G} = \mathbf{0}. \quad (4.33)$$

Equation (4.33) can also be derived by explicitly plugging in the shifted steady state  $(\psi_0(x + \Delta), P_0(x + \Delta))^T$ . Expanding the right-hand side (denoted as  $\mathbf{f}$ ) of the evolution equation in  $\Delta x$  yields

$$\partial_t \begin{pmatrix} \psi_0(x + \Delta) \\ P_0(x + \Delta) \end{pmatrix} = \mathbf{f} \begin{pmatrix} \psi_0(x + \Delta) \\ P_0(x + \Delta) \end{pmatrix} \quad (4.34)$$

$$= \mathbf{f} \begin{pmatrix} \psi_0(x) \\ P_0(x) \end{pmatrix} + \mathcal{L} \begin{pmatrix} \psi_0(x) \\ P_0(x) \end{pmatrix} \partial_x \begin{pmatrix} \psi_0(x) \\ P_0(x) \end{pmatrix} \Delta + \mathcal{O}(\Delta^2) \quad (4.35)$$

$$= \mathbf{0}. \quad (4.36)$$

The time derivative is zero as we consider a steady state, the same holds for  $\mathbf{f}$  of the unshifted steady state. Since  $\Delta \neq 0$  by definition

$$\mathcal{G} = \partial_x \begin{pmatrix} \psi_0 \\ P_0 \end{pmatrix} \quad (4.37)$$

with eigenvalue 0 follows. Alternatively, one can differentiate the right-hand side by  $x$  and, as it does not depend explicitly on space, end up with the same result after applying a chain rule.

A typical destabilization occurs when the real part of an eigenvalue crosses zero as parameters of the system are being changed. We now consider the case that the imaginary part also equals zero, so that the corresponding eigenfunctions of  $\mathcal{L}$  can be expressed by a linear combination of the Goldstone modes. The second Goldstone mode mentioned in Sec. 4.3.3 is the volume mode that does not interfere in the drift bifurcation. At the bifurcation point, a real eigenvalue crosses the imaginary axis, i.e., an additional neutral mode exists. In consequence, the system of eigenfunctions of the null space of the linear operator is incomplete and must be supplemented by a generalized neutral eigenfunction [GBM<sup>+</sup>04]. This function is called the propagator mode  $\mathcal{P}$ , defined by

$$\mathcal{L}\mathcal{P} = \mathcal{G}. \quad (4.38)$$

It is exactly the occurrence of  $\mathcal{P}$  that marks the destabilization, i.e., the onset of motion. Using the Fredholm alternative [Eva10], one finds that Eq. (4.38) can be solved iff

$$\langle \mathcal{G}^\dagger | \mathcal{G} \rangle = 0, \quad (4.39)$$

where  $\mathcal{G}^\dagger$  is the neutral eigenfunction of the adjoint operator  $\mathcal{L}^\dagger$  with the same spatial symmetry as  $\mathcal{G}$ . The scalar product  $\langle \cdot | \cdot \rangle$  is defined as a full spatial integration over the considered domain. The values of a set of control parameters for which Eq. (4.39) is fulfilled corresponds to the bifurcation point.

### 4.4.3 The adjoint linearized operator

Let  $\mathcal{G}^\dagger$  be the adjoint neutral eigenfunction, i.e.,

$$\mathcal{L}^\dagger \mathcal{G}^\dagger = \mathbf{0}. \quad (4.40)$$

Equation (4.29) corresponds to

$$\mathcal{G} = \mathcal{L} \begin{pmatrix} \tilde{\psi}_1 \\ \tilde{P}_1 \end{pmatrix} \quad (4.41)$$

showing that  $(\tilde{\psi}_1, \tilde{P}_1)^T$  is a generalized neutral eigenfunction  $\mathcal{P}$ . To find  $\mathcal{G}^\dagger = (\psi_{\mathcal{G}}^\dagger, P_{\mathcal{G}}^\dagger)^T$  we determine the adjoint operator

$$\mathcal{L}^\dagger = \begin{pmatrix} -L_{\text{SH}} \partial_{xx} & v_0 \partial_x \\ v_0 \partial_x & C_1 (\partial_{xx} - D_r) \end{pmatrix} \quad (4.42)$$

using  $(AB)^\dagger = B^\dagger A^\dagger$ , the self-adjointness of  $\partial_{xx}$  and  $L_{\text{SH}}$ , the relation  $\partial_x^\dagger = -\partial_x$ , and  $(v_0, C_1, D_r) \in \mathbb{R}$ .

### 4.4.4 Determining the adjoint eigenfunctions

Componentwise the adjoint problem reads

$$0 = -L_{\text{SH}} \partial_{xx} \psi_{\mathcal{G}}^\dagger + v_0 \partial_x P_{\mathcal{G}}^\dagger \quad (4.43)$$

$$0 = v_0 \partial_x \psi_{\mathcal{G}}^\dagger + C_1 (\partial_{xx} - D_r) P_{\mathcal{G}}^\dagger \quad (4.44)$$

Comparing Eq. (4.43) to the steady state equation for  $\psi$  (4.3) with  $J = 0$  and  $c = 0$  and employing a simple chain rule

$$0 = \partial_x \frac{\delta \mathcal{F}}{\delta \psi}(\psi_0) - v_0 P_0 \quad (4.45)$$

$$= -L_{\text{SH}} \partial_x \psi_0 - v_0 P_0 \quad (4.46)$$

suggests

$$\partial_{xx} \psi_{\mathcal{G}}^\dagger = \partial_x \psi_0, \quad (4.47)$$

$$\partial_x P_{\mathcal{G}}^\dagger = -P_0 \quad (4.48)$$

Integrating yields

$$\psi_{\mathcal{G}}^\dagger(x) = \int_0^x (\psi_0(x') + C) dx' + D, \quad (4.49)$$

$$P_{\mathcal{G}}^\dagger(x) = - \int_0^x P_0(x') dx' + F \quad (4.50)$$

with constants  $C, D, F$ . Eq. (4.44) is consistent with this neutral adjoint eigenfunction. Substituting gives

$$v_0 \psi_0 - C_1 (\partial_{xx} - D_r) \int P_0(x) dx = \text{const.} \quad (4.51)$$

which is true as can be seen by integrating the steady state equation for  $P$ , Eq. (4.4).



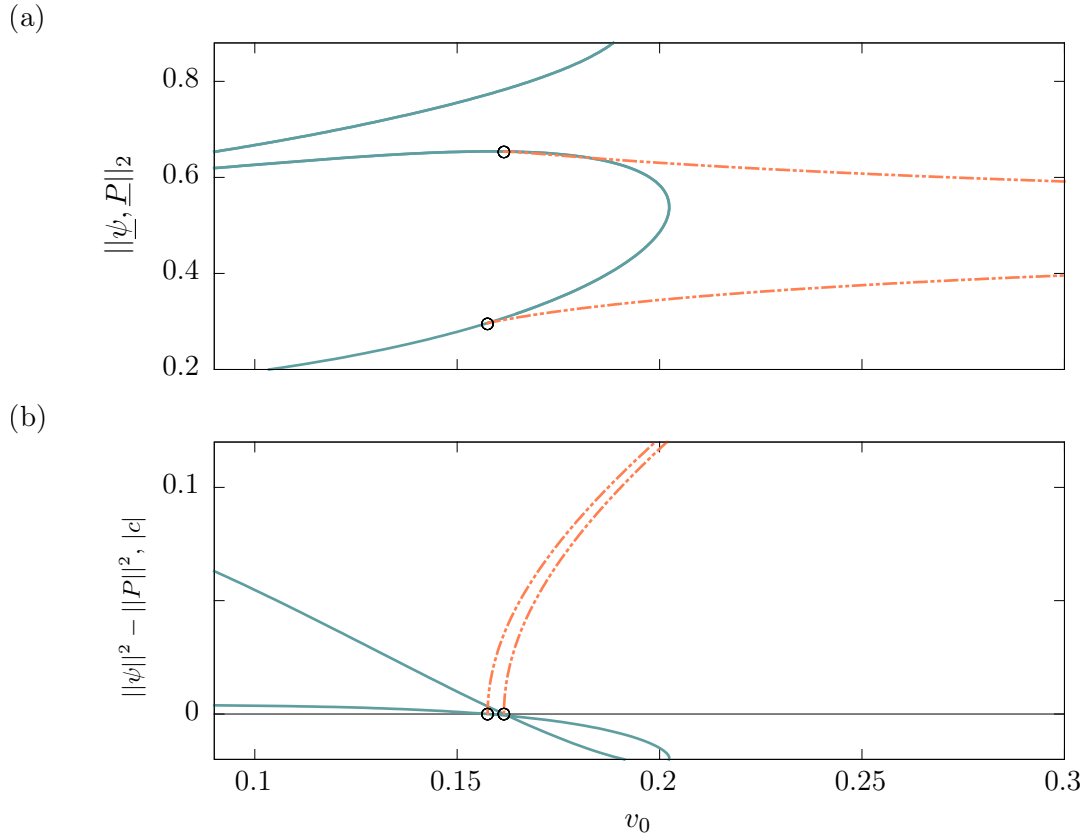


Figure 4.12: Onset of motion. (a)  $L^2$ -norm of steady states in dependence of  $v_0$  for fixed  $\bar{\psi} = -0.75$ . The blue branch corresponds to a RLS with one bump. The RLS are destabilized at two respective  $v_c$  and start to travel with drift velocity  $c$ . The traveling odd LS is indicated by the dashed orange branch. (b) Solvability condition Eq. (4.55)  $\|\psi_0\|_2^2 - \|P_0\|_2^2$  (blue) of the RLS and velocity  $|c|$  (dashed orange line) of TLS vs. activity  $v_0$  showing perfect agreement of the two approaches. (cf. [OGT18])

#### 4.4.5 Solvability condition

Applying all results, the solvability condition (4.39) reads

$$\begin{aligned}
 \langle \mathcal{G}^\dagger | \mathcal{G} \rangle &= \langle \psi_{\mathcal{G}}^\dagger | \psi_{\mathcal{G}} \rangle + \langle P_{\mathcal{G}}^\dagger | P_{\mathcal{G}} \rangle \\
 &= \left\langle \int_0^x (\psi_0(x') + C) dx' + D | \partial_x \psi_0 \right\rangle \\
 &\quad - \left\langle \int_0^x (P_0(x') + E) dx' | \partial_x P_0 \right\rangle
 \end{aligned} \tag{4.52}$$

$$\begin{aligned}
 &= -\langle \partial_x \left( \int_0^x (\psi_0(x') + C) dx' + D \right) | \psi_0 \rangle \\
 &\quad + \langle \partial_x \int_0^x (P_0(x') + E) dx' | P_0 \rangle
 \end{aligned} \tag{4.53}$$

$$= -\langle \psi_0 | \psi_0 \rangle + \langle P_0 | P_0 \rangle = 0. \tag{4.54}$$

$$\Leftrightarrow 0 = \|\psi_0\|_2^2 - \|P_0\|_2^2, \tag{4.55}$$

where we have employed a partial integration and used  $\langle C | \psi_0 \rangle = C \int_0^L \psi_0 dx = 0$ , since  $\psi$  is the modulation around the fixed mean density. The same holds for the integral over  $P_0$  as explained in section 4.1.1. For all TLS, we have found the onset of motion perfectly matches the zero crossing of  $\|\psi_0\|_2^2 - \|P_0\|_2^2$ .

A particular example is given in Fig. 4.12. Panel (a) shows a part of the bifurcation diagram Fig. 4.7. The solid blue branch corresponds to the RLS with a single density peak that loses its stability in a drift-pitchfork bifurcation at  $v_c$ . The emerging traveling bump (upper dot-dashed orange line) is linearly stable (cf. Fig. 4.10(a), the lower orange branch is unstable). In the lower panel, Fig. 4.12(b), we plot the difference of the squared norms as employed in Eq. (4.55). In addition, we also display the velocity of the emerging TLS (dot-dashed orange). The two zero crossings of  $\|\psi_0\|_2^2 - \|P_0\|_2^2$  occur at exactly the same values of  $v_0$  as the onsets of motion. The second root is due to the lower unstable branch of TLS that bifurcates at a slightly lower activity. Notice that the criterion for the onset of motion, Eq. (4.55), also holds for the drift-transcritical bifurcation.

## 4.5 Morphological phase diagram

Collecting all previous results, we can construct a morphological phase diagram of the regions of existence of resting and traveling crystalline and localized states. Having obtained various bounds of existence by linear stability analysis and two-parameter continuation we can restrict the parameter space of interest and compare results from time simulations with analytical results and results obtained by numerical continuation.

### 4.5.1 Resting and traveling crystals and LS

Figure 4.13 gives a condensed overview of the range of existence of resting and traveling crystals and various types of crystallites. A zoom into the  $v_0$ -range close to the onset of motion can be found in Fig. 4.14. The colored area marks where spatially modulated states exist in the plane spanned by activity  $v_0$  and mean density  $\bar{\psi}$ . The color coding corresponds to the number of density peaks that evolve in the periodic domain of  $L = 100 \approx 16 L_c$

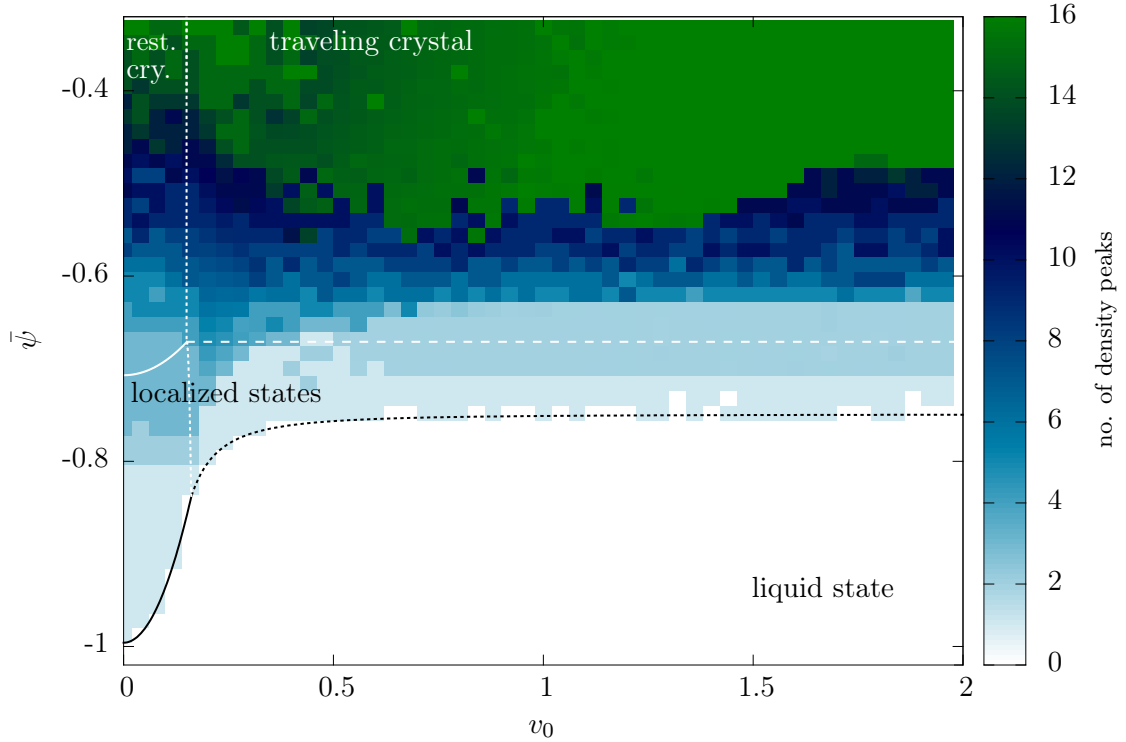


Figure 4.13: Morphological phase diagram for the active PFC model. The liquid state refers to a uniform density phase with zero peaks (white). Different crystalline structures exist in the colored areas. The color code distinguishes their spatial expansion in terms of the number of density peaks. Resting and traveling LS exist in the regions marked in blue with cluster sizes ranging from a single peak (light blue) up to sizes that almost fill the whole domain (dark blue). The domain size is  $L = 100$  allowing for a maximum of 16 stable peaks. Periodic patterns (green) fill the entire domain reaching the number of 16 density bumps. The horizontal white lines (curved solid line and straight dashed line) give limits of the linear stability of the liquid phase (cf. Fig. 3.1). The vertical dotted line marks the onset of motion where resting states undergo a drift-pitchfork bifurcation. The onset of motion for LS is determined by tracking the onset of one-peak TLS by two-parameter continuation. Black lines correspond to the folds of resting (solid) and traveling (dashed) one-peak LS. They denote the limits of existence of one-peak LS as obtained from numerical continuation. As initial conditions for the underlying time simulations for the color coding, one density peak is randomly placed on a background of white noise, the polarization has random initial conditions around  $P = 0$ . Note that the number of density peaks is the median from a time series of counted peaks, as also oscillatory states arise in some small parameter ranges (see Sec. 4.5.2). Increments between simulations:  $\Delta v_0 = 0.04$ ,  $\Delta \bar{\psi} = 0.016$ . Remaining parameters as in Fig. 4.1.

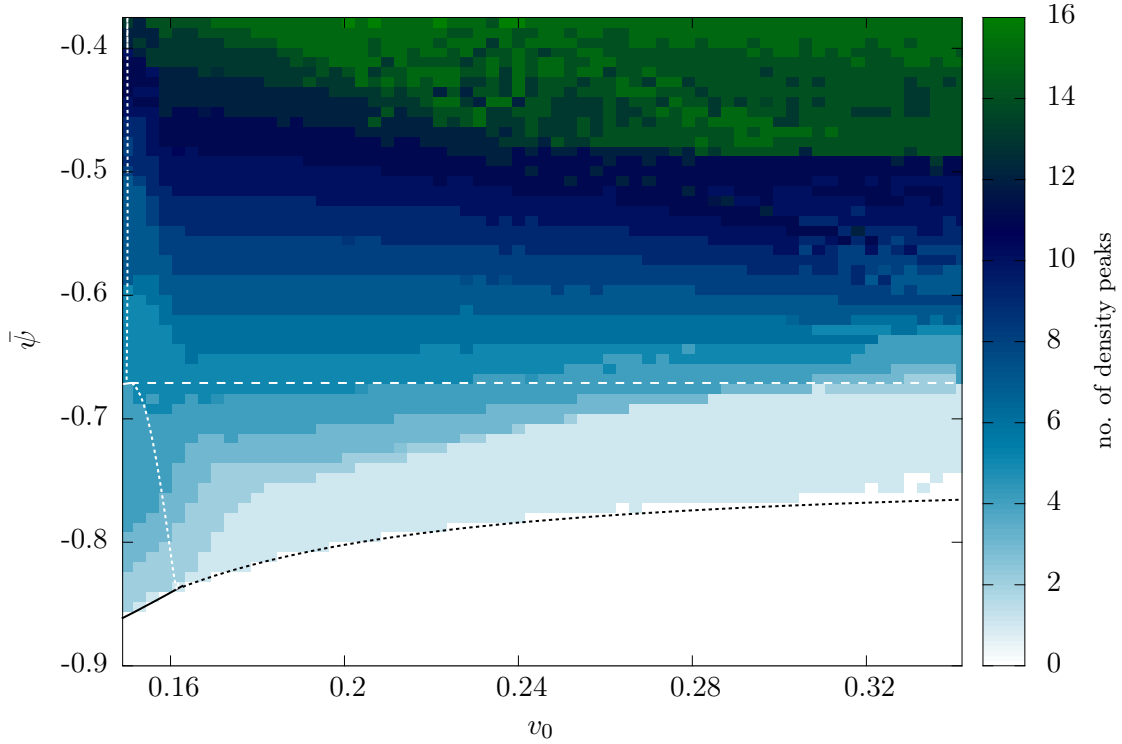


Figure 4.14: Zoom of Fig. 4.13 into  $v_0$ -range close to the onset of motion. Steps in different shades of blue colors illustrate the gradual growth of LS for increasing  $\bar{\psi}$  reflecting the slanted snaking of branches of LS. Increments between simulations:  $\Delta v_0 = 0.003$ ,  $\Delta \bar{\psi} = 0.008$ .

and  $L_c = 2\pi$ . As initial conditions for the underlying time simulations, one density peak is randomly placed on a background of white noise, the polarization has random initial conditions around  $P = 0$ . White regions correspond to the liquid state with  $\psi = 0$  and no peaks. Spatially extended states fill the entire domain with 16 peaks (green). The curved solid white line and the horizontal dashed white line represent the limits of the linear stability of the liquid as determined in chapter 3. The lines are the same as given in Fig. 3.1. In the vicinity of this limit, localized states (blue area) coexist with the liquid state. The LS consist of clusters sized between a single peak (light blue) and large LS that almost fill the whole domain (dark blue).

The area of existence of LS is bounded by the loci of the folds of the resting and the traveling one-peak LS that reach the lowest values of  $\bar{\psi}$ . Their position is tracked by two-parameter continuation and is depicted as black lines. The solid and dotted black lines correspond to the fold of the resting one-peak LS and to the fold of traveling one-peak LS, respectively, cf. Sec. 4.3.2 for details. Similar two-parameter continuation is employed to track the onset of motion where resting states undergo a drift-pitchfork bifurcation. The vertical dotted white line marks the onset of motion for crystals. The lower part of the seemingly vertical line in the area of LS ( $\bar{\psi} < -0.69$ ) represents the position of the drift-pitchfork bifurcation of the one-peak LS.

The color coding and counted density peaks are results from time simulations for different

parameter combinations. Each pixel corresponds to a time simulation with random initial conditions. To stimulate the growth of localized patches, one density peak in the shape of a Gaussian with oscillatory tails ( $\propto \exp(-x^2/5) \cos(x)$ ) is placed at a random position in the considered domain  $L$ . After a sufficiently long transient, the number of density peaks is counted for a period of time and its median is used for the creation of the phase diagram. The median is used because it always yields a whole number of peaks. In a small parameter range oscillating LS arise. This novel type of oscillatory states in the aPFC model is discussed in Sec. 4.5.2.

The phase diagram points out how remarkably well results from time simulations match the existence bounds predicted by parameter continuation. The diagram condenses large parts of the results for active crystals and active LS in the one-dimensional PFC model.

Figure 4.14 enlarges the area of traveling LS close to the onset of motion and depicts the results from time simulations on a finer grid in parameter space. Vertical cuts through the phase diagram correspond to a continuation in the mean density  $\bar{\psi}$  for fixed  $v_0$ . These cuts reveal the gradual growth of LS for increasing  $\bar{\psi}$ . Moreover, Fig. 4.14 illustrates once more how well the black lines from fold continuations limit the area of existence of resting LS and (for larger parts of the shown  $v_0$ -interval) traveling one-peak LS.

### 4.5.2 Oscillatory states

Evaluating all different solution types appearing in the phase diagram in Fig. 4.13 in depth, we describe an additional class of non-resting localized states: oscillatory states. For certain mean densities close to the limit of the linear stability of the uniform phase, we detect Hopf bifurcations of the resting localized states at values of  $v_0$  lower than  $v_c$  where the drift sets in:  $v_{\text{Hopf}} < v_c$ . Here, branches of oscillating states bifurcate.

Figure 4.15 depicts an exemplary bifurcation diagram for oscillatory states. The diagram is constructed combining results from numerical continuation and time simulations. Unfortunately, it turned out to be impossible to follow the emerging branch of oscillating states with the employed continuation tool. That is why data from time simulations are incorporated.

The bifurcation diagram depicts the norm of a localized four-peak LS as a function of activity  $v_0$ . At low activity, the LS is at rest. Figure 4.15(b) shows a resting solution profile (blue). At about  $v_{\text{Hopf}} \approx 0.16$ , the continuation scheme detects a Hopf bifurcation and time simulations at slightly larger  $v_0$  exhibit oscillating LS (dark red). The four-peak structure (Fig. 4.15(b)(II)) is oscillating back and forth without a net drift velocity. Figure 4.16(a) depicts a space-time plot of this oscillatory four-peak LS without net drift at  $v_{\text{Hopf}} < v_0 < v_c$ . At  $v_c \approx 0.167$ , closely above  $v_{\text{Hopf}}$ , a drift bifurcation occurs on the branch of resting LS, cf. inset of Fig. 4.15(a). There, the unstable branch of purely traveling four-peak LS (dotted gray in inset) without any oscillations emerges. Note that the main panel in Fig. 4.15(a) does not include the branch of traveling four-peak LS since they only exist in a very narrow range of  $v_0$  (cf. inset). As in Fig. 4.7, the branch ends on the branch of resting three-peak LS which is also not included. In addition, the extension of the one-peak branch is not shown to keep the focus on oscillatory states.

According to time simulations, the drift instability also occurs on the branch of oscillating states. Hence, the oscillatory LS without a net drift only exist in a very narrow range of activity. Time simulations reveal the onset of a net drift as, close to  $v_c$ , the norm  $\|\psi\|_2$  suddenly increases indicating a jump onto another branch. Corresponding solutions (III) show a rather intricate combination of the destabilized modes of oscillation and translation.

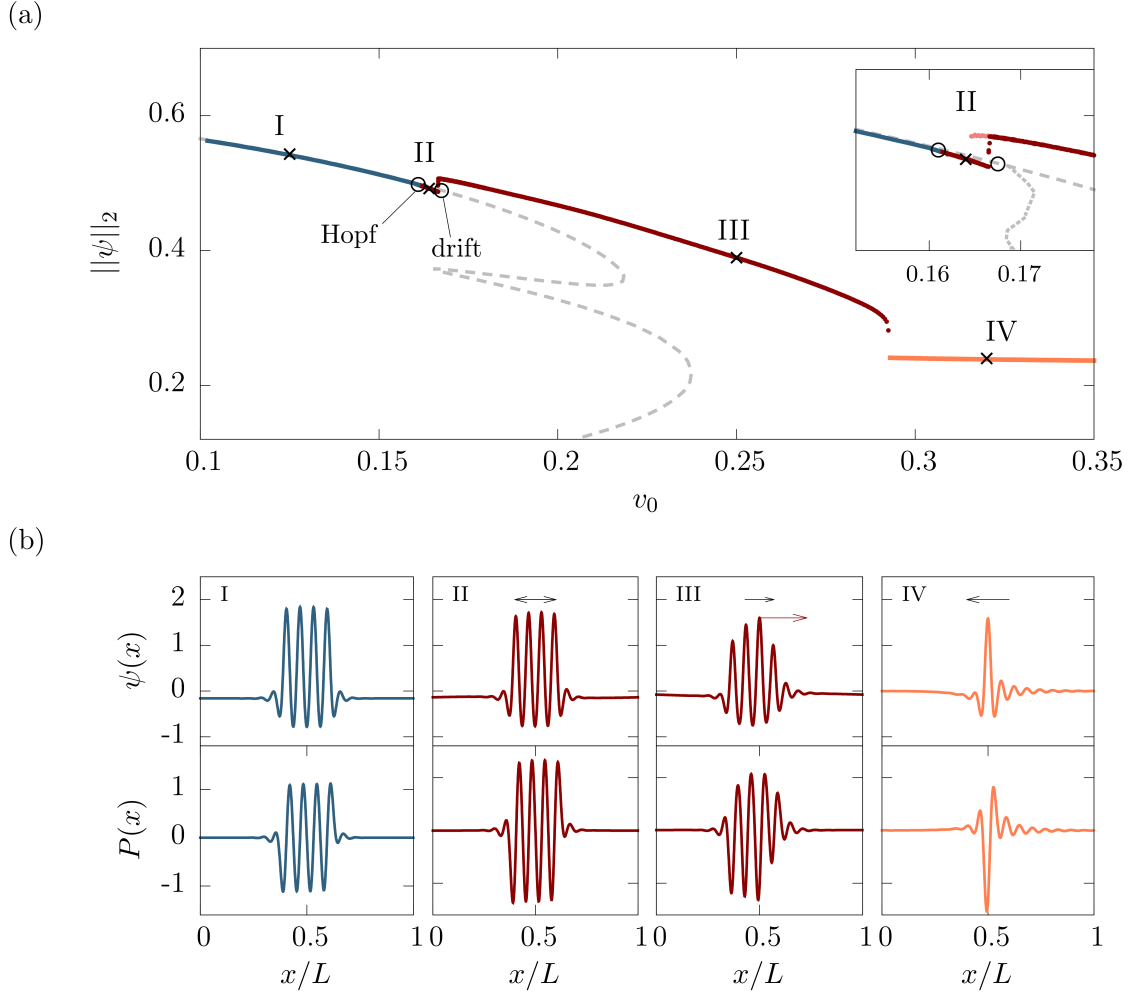


Figure 4.15: (a) Bifurcation diagram of four-peak LS obtained by continuation (gray dashed line) and time simulations (solid lines): The norm  $\|\psi\|_2$  is shown as a function of  $v_0$ . A Hopf bifurcation is detected at  $v_{\text{Hopf}} \approx 0.16$  and oscillatory states (dark red) emerge. The branch of resting states undergoes a drift instability at  $v_c > v_{\text{Hopf}}$ . Hopf and drift bifurcation of the RLS are marked by black circles. The branch of oscillatory states undergoes a fold bifurcation at  $v_0 \approx 0.28$  and traveling one-peak LS (orange) emerge in the time simulation. The inset enlarges the bifurcation structure around the bifurcation points. Following the branch of drifting oscillatory states in negative  $v_0$ -direction (light red branch in inset) reveals a hysteresis and the subcritical nature of the drift bifurcation on the oscillating branch. The branch of purely traveling four-peak LS (gray dotted, unstable, only shown in inset) emerges in the drift bifurcation on the branch of RLS. (b) Solution profiles from loci marked in upper panel. (I) Resting state. (II) oscillates back and forth without a net drift,  $c = 0$ . Note that  $P$  is mirrored for the second half of oscillation period (see next Fig. 4.16 for space-time plots). (III) The envelope of the four-peak LS drifts with a steady velocity  $c = v_{\text{group}} < v_{\text{phase}}$ . Individual peaks travel faster than the envelope and vanish at the tip of the LS. At the rear of group, new peaks come into existence (cf. Fig. 4.16(b)). (IV) Traveling one-peak LS. Directions of motion are indicated by arrows. Domain:  $L = 100$ . Parameters:  $\bar{\psi} = -0.68$ ,  $\epsilon = -1.5$ ,  $C_1 = 0.1$ ,  $C_2 = 0.0$  and  $D_r = 0.5$ .

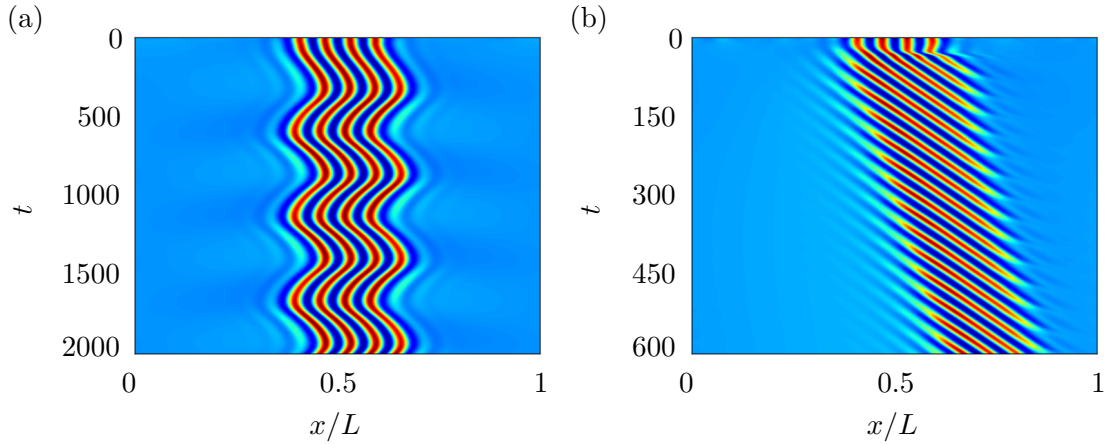


Figure 4.16: Space-time plots of oscillatory states. (a)  $v_{\text{Hopf}} < v_0 = 0.164 < v_c$ , four-peak LS oscillates back and forth, no net drift. (b)  $v_0 = 0.25 > v_c$ , oscillation and drift superpose. Two different velocities  $c = v_{\text{group}} < v_{\text{phase}}$  are visible. (a) and (b) correspond to II and III in Fig. 4.15(b).

They do not simply superpose which would lead to a drifting oscillating state. In fact, the envelope travels with a steady group velocity being equal to the net drift velocity  $c$ . The individual density peaks, however, exhibit a greater velocity  $v_{\text{phase}}$ . The difference in the two speeds leads to an oscillation within the entity of the LS. Figure 4.16(b) presents a space-time plot of the density profile of this kind of oscillatory state. At high activity of  $v_0 > 0.28$  the branch of oscillatory four-peak LS folds back (Fig. 4.15(a)) and a traveling one-peak LS (b, IV) emerges in time simulations.

The inset in Fig. 4.15(a) enlarges the bifurcation structure around the bifurcation points. Following the branch of drifting oscillatory states in negative  $v_0$ -direction (light red branch) reveals a hysteresis and the subcritical nature of the drift bifurcation.

Using data from previous large-scale time simulations for Fig. 4.13, a phase diagram of oscillatory drifting states is constructed by evaluating oscillations in the detected number of density peaks. Figure 4.17 summarizes where oscillatory states with a net drift can be found in the  $(v_0, \bar{\psi})$ -plane.

## 4.6 Diffusion arrests motion

Having discussed the influence of activity  $v_0$  and mean density  $\bar{\psi}$  in detail, next, we briefly investigate the effect of changes in the remaining model parameters. Since our interest mainly focuses on the onset of motion, we employ a two-parameter continuation to track the critical activity for traveling solutions. First, we vary the diffusion coefficient  $C_1$  for the polarization  $P$ .

Figure 4.18 reveals that the onset of motion depends linearly on the diffusion of  $P$ .  $C_1$  scales the critical activity for a drift. This is expected as it also scales the whole evolution equation (4.2) for  $P$ . At low diffusion, motion sets in at low values of activity. In the absence of diffusion, there is no critical activity. Resting crystals do only exist at  $v_0 = 0$  and traveling

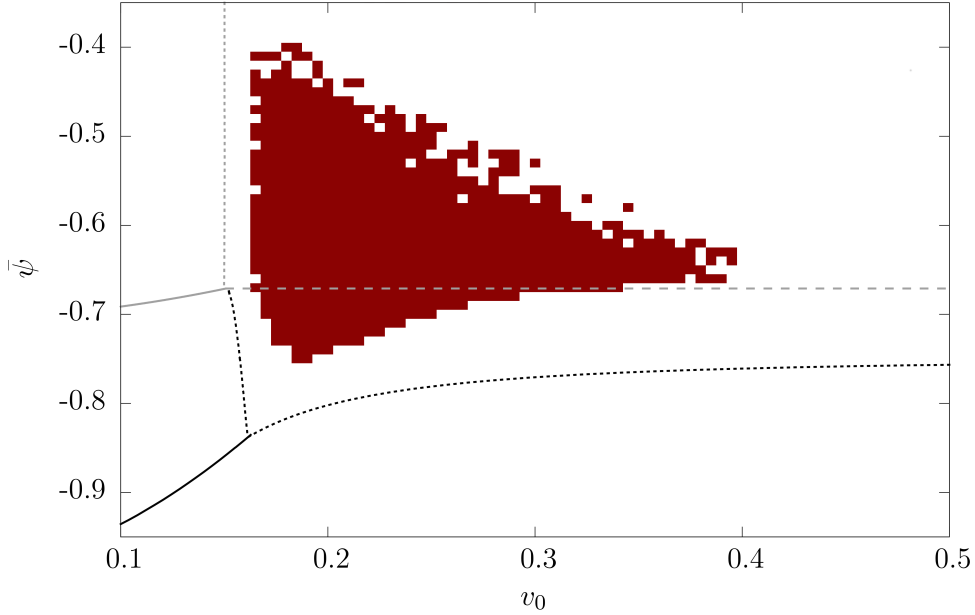


Figure 4.17: Area of existence of oscillatory states as a function of  $v_0$  and  $\bar{\psi}$ . Data from time simulations with same initial conditions and parameters as in Fig. 4.13. Oscillations without a net drift only appear in a very narrow range of  $v_0$  that is not resolved here, cf. Fig. 4.15(a). Gray lines indicate the linear stability of the liquid phase. Black lines limit the area of existence of one-peak LS. Vertical lines denote the onset of motion of selected states. All lines only serve as guidance in the parameter plane.

solutions arise for any  $v_0 > 0$ .

If, on the other hand, diffusion is too strong, motion can be completely suppressed.  $v_c$  might reach values too high to allow for traveling states since resting crystals decay at a finite  $v_0$ . As  $v_c$  only slightly varies for different solutions, results for  $v_c$  of periodic states as depicted in Fig. 4.18 are also valid for LS. The folds of most resting LS for instance are located around  $v_0 \approx 0.2$  for parameters used here. If  $v_c$  exceeds this value, no drifting LS will appear. The resting LS melt before motion can set in. Resting crystals cease to exist at  $v_0 \approx 0.35$  (cf. Fig. 4.1(a)).

## 4.7 Temperature and the onset of motion

Second, we consider the influence of the temperature-like parameter  $\epsilon$  on the onset of motion of crystals. We find that even though  $\epsilon$  has a strong influence on the stability of the liquid phase and  $\epsilon < 0$  is necessary for solidification and crystalline states,  $v_c$  does practically not depend on it. Figure 4.19 shows that  $v_c$  remains almost unchanged for varying temperatures. The crystal used for the two-parameter continuation corresponds to the periodic solution in Fig. 4.1 at  $\bar{\psi} = -0.5$ . As expected from phase diagrams in the  $(\bar{\psi}, \epsilon)$ -plane (see, e.g., [ML13]), the crystal melts around  $\epsilon \approx -1.2$ .



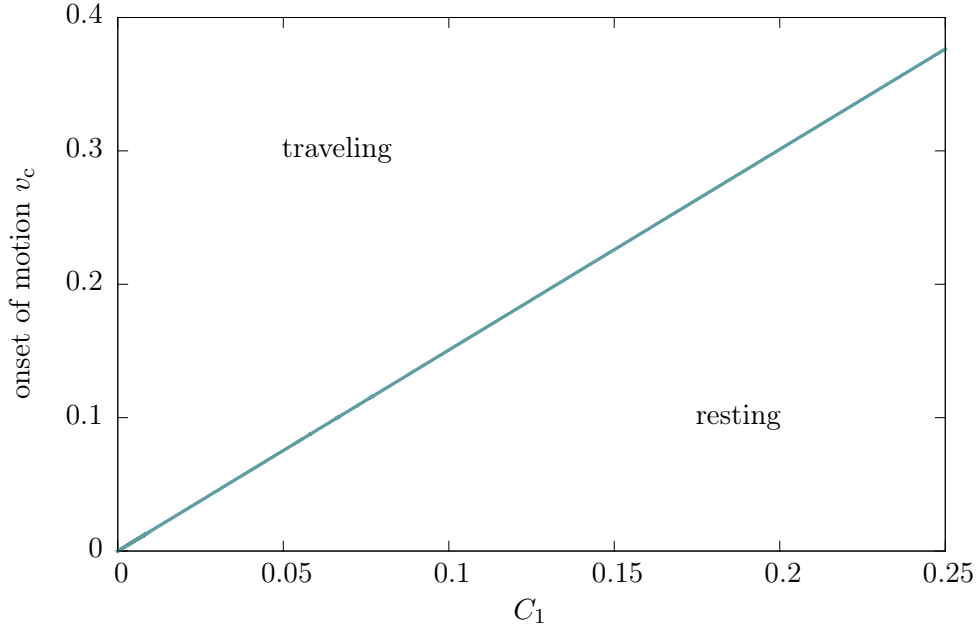


Figure 4.18: Two-parameter continuation of the onset of motion in the plane spanned by diffusion constant  $C_1$  and activity  $v_0$ . The position of the critical activity for traveling crystals  $v_c$  is tracked.  $\bar{\psi} = -0.5$ , remaining parameters as in Fig. 4.1.

## 4.8 Spontaneous polarization

So far, a linear equation has been used for the temporal evolution of the polarization  $P$ . Via  $C_2 = 0$  and  $C_1 > 0$  spontaneous polarization is suppressed and diffusion always equilibrates  $P$ . Only gradients in  $\psi$  cause growth in the polar order.

For  $C_2 > 0$  and  $C_1 < 0$ , the unpolarized state  $P = 0$  is unstable and polarization can emerge spontaneously. A net driving of the crystalline structures then arises for any non-vanishing coupling between the fields,  $v_0 > 0$ . There is no threshold activity  $v_c$  that has to be exceeded for migration. For spontaneous polarization, the drift velocity  $c$  grows proportional to  $v_0$ .

Following former approaches [ML13, MOL14, PVWL18] we avoid spontaneous polarization and concentrate on the case  $C_1 > 0$  and  $C_2 = 0$ . It exhibits a richer solution behavior where resting states occur besides traveling states resulting in an intricate bifurcation structure.

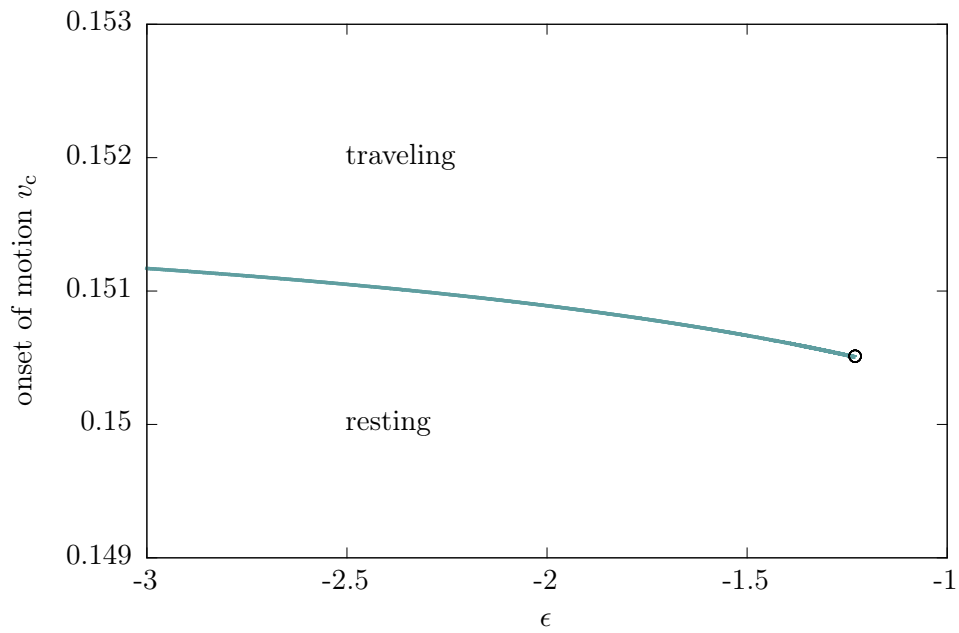


Figure 4.19: Two-parameter continuation of the onset of motion in the plane spanned by temperature  $\epsilon$  and activity  $v_0$ . The position of the critical activity for migration  $v_c$  is tracked for the crystal state. The temperature-like parameter  $\epsilon$  has only a small influence. As expected, the crystal at low  $\bar{\psi} = -0.5$  melts at  $\epsilon \approx -1.2$  marked by the circle.  $C_1 = 0.1$  and also remaining parameters as in Fig. 4.1.

# 5 Active Crystals and Crystallites in Two Spatial Dimensions

In chapter 4, we have gained an extensive overview of different solutions types arising in the one-dimensional active PFC model, their connections via various bifurcations and the influence of control parameters. As a next step, we expand the physical space to two dimensions (2d).

In nature, collective motion often effectively occurs in 2d. Tissue cells, bacteria and amoebae crawl on substrates while ungulates like gnu or sheep display herding and organize in two-dimensional swarms. In the context of artificial active matter, e.g., colloidal particles swimming on the surface of a liquid can form two-dimensional crystals [PSS<sup>+</sup>13].

We investigate how two-dimensional active crystals described by the aPFC model evolve from single localized states (LS) to spatially extended states (crystals) under the influence of activity. As in chapter 4, we focus on mean density  $\bar{\psi}$  and activity  $v_0$  as main control parameters. The activity parameter  $v_0$  will turn out to have a major influence not only on the transition from resting to traveling states but also on the structure of 2d crystals and pattern selection.

## 5.1 The aPFC model in 2d

Initially, we recall from Sec. 2.3 the kinetic equations for the conserved scalar density  $\psi$  and the polarization field  $\mathbf{P}$  in two spatial dimension :

$$\partial_t \psi = \nabla^2 \left\{ \left[ \epsilon + (1 + \nabla^2)^2 \right] \psi + (\bar{\psi} + \psi)^3 \right\} - v_0 \nabla \cdot \mathbf{P}, \quad (5.1)$$

$$\partial_t \mathbf{P} = C_1 \nabla^2 \mathbf{P} - D_r C_1 \mathbf{P} - v_0 \nabla \psi, \quad (5.2)$$

with activity parameter  $v_0$ , mean density  $\bar{\psi}$ , temperature-like parameter  $\epsilon$  and diffusion coefficients  $C_1$  and  $D_r$ . For details see Sec. 2.3.

### 5.1.1 Steady and stationary states

The equations for steady and stationary states in 2d (where stationary states are states that are steady in a comoving frame moving with velocity  $\mathbf{c}$ ) with  $\partial_t \psi = -(\mathbf{c} \cdot \nabla) \psi$  and  $\partial_t \mathbf{P} = -(\mathbf{c} \cdot \nabla) \mathbf{P}$  read

$$0 = \nabla^2 \left\{ \left[ \epsilon + (1 + \nabla^2)^2 \right] \psi + (\bar{\psi} + \psi)^3 \right\} - v_0 \nabla \cdot \mathbf{P} + \mathbf{c} \cdot \nabla \psi \quad (5.3)$$

$$\mathbf{0} = C_1 \nabla^2 \mathbf{P} - D_r C_1 \mathbf{P} - v_0 \nabla \psi + (\mathbf{c} \cdot \nabla) \mathbf{P}. \quad (5.4)$$

Once more, we stress that the velocity  $c = |\mathbf{c}|$  is equal to zero for resting states. For traveling states,  $\mathbf{c}$  has to be determined alongside the solution profiles.

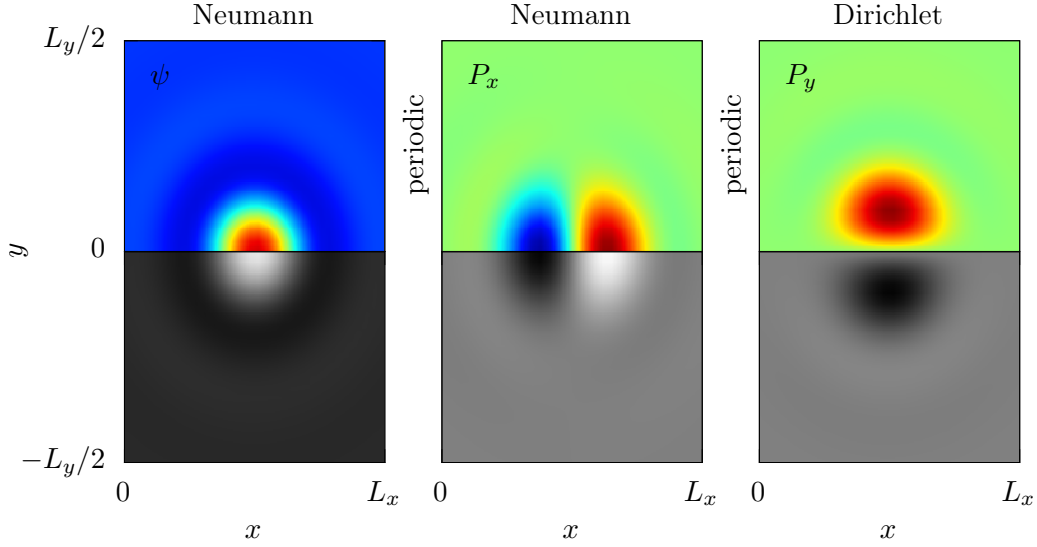


Figure 5.1: Structures that are reflection-symmetric w.r.t. the  $x$ -axis are computed on the colored area  $[0, L_x] \times [0, L_y/2]$  with periodic boundary conditions in  $x$ -direction and Neumann conditions for  $\psi$  and  $P_x$  in  $y$ -direction at  $y = 0$  and  $L_y/2$ . For  $P_y$  Dirichlet boundaries apply there with  $P_y = 0$ . Then only motion in  $x$ -direction is allowed and structures remain vertically pinned. For the visualization of solutions, the entire domain  $\Omega_{\text{exp}} = [0, L_x] \times [-L_y/2, L_y/2]$  is used (indicated by colored and gray regions).

### 5.1.2 Numerical continuation in 2d

Similar to our approaches to the aPFC model in 1d, we employ numerical parameter continuation to determine steady ( $c = 0$ ) and stationary ( $c > 0$ ) periodic and localized solutions of Eqs. (5.3) and (5.4). For the 2d problem, we use the MATLAB package PDE2PATH [UWR14]. Like AUTO07P for 1d problems, PDE2PATH allows us to follow branches of solutions in parameter space, detect bifurcations, switch branches and in turn follow the bifurcating branches. A phase condition that breaks translational invariance and a constraint that controls the volume are included as integral conditions. This implies that in each continuation run beside the main control parameter one has two auxiliary parameters that have to be adapted. Again, we use the mean density  $\bar{\psi}$  or the activity  $v_0$  as main control parameters while the velocity  $c$  and a Lagrange multiplier for the volume constraint are the auxiliary parameters that are adapted. For details on numerical continuation see Sec. 2.4.2.

Since 2d computations are much more expensive and time-consuming as compared to 1d problems we make use of the symmetries of the fields  $\psi$  and  $\mathbf{P} = (P_x, P_y)^T$  to reduce computational efforts. If not differently stated in the caption of respective figures, all computations were carried out only for half of the shown solution profiles. In Fig. 5.1, the colored area  $\Omega = [0, L_x] \times [0, L_y/2]$  marks the part of the domain on which actual computations are performed. The entire solution profile is then obtained by exploiting the

following symmetries:

$$\psi(x, y) = \psi(x, -y), \quad P_x(x, y) = P_x(x, -y), \quad P_y(x, y) = -P_y(x, -y),$$

where  $y = 0$  corresponds to the horizontal line separating the colored and gray areas. The expanded area used for visualization and classification of the solutions is  $\Omega_{\text{exp}} = [0, L_x] \times [-L_y/2, L_y/2]$  with volume or area  $V = L_x L_y$ . From the linear stability analysis of the uniform state in chapter 3, we know that at onset only the unstable mode  $k_c = 1 \Leftrightarrow L_c = 2\pi$  grows.

Next, we define the boundary conditions (BC) of  $\Omega = [0, L_x] \times [0, L_y/2]$ . In order to pin the solutions such that the applied symmetries are conserved, we use Neumann BC in  $y$ -direction for  $\psi$  and  $P_x$ . According to its symmetry,  $P_y$  is kept zero at  $y = 0$  and  $y = L_y$ , i.e. these are Dirichlet BC. Combined the BC in  $y$ -direction read

$$\partial_y \psi(x, y = 0, L_y/2) = 0, \quad \partial_y P_x(x, y = 0, L_y/2) = 0, \quad P_y(x, y = 0, L_y/2) = 0$$

at  $y = 0$  and  $y = L_y/2$ . In  $x$ -direction, periodic BC are applied for all three fields.

Due to the chosen BC, the  $y$ -component  $c_y$  of the drift velocity  $\mathbf{c}$  always remains zero. This implies that crystalline structures have to be orientated such that the desired drift, e.g., as observed in time simulations or experiments, is in  $x$ -direction, i.e.,  $c_x \neq 0$ .

Besides the rectangular geometry, we make use of a hexagonal domain when discussing the passive PFC model and the phenomenon of slanted snaking of branches of steady LS. There, the numerical continuation is done for a triangular domain, namely, a right angle triangle with a hypotenuse of the side length of the hexagon and Neumann boundaries for  $\psi$ . In the passive case,  $P_x$  and  $P_y$  remain zero. The triangle defined by the vertices at  $(x, y) = 2\pi(0, 0)$ ,  $2\pi(0, 3)$  and  $2\pi(1, 3/\sqrt{3})$  is one twelfth of the entire domain as pictured in Fig. 5.3. Note that the equilateral triangles found in the hexagon have a height of  $L_c = 2\pi$  and a side length of  $L_a = \frac{2}{\sqrt{3}}L_c = \frac{4\pi}{\sqrt{3}}$ .

All resulting bifurcation diagrams are given in terms of the  $L^2$ -norm of the obtained density profile that we use as main solution measure. In 2d, it is defined by

$$\|\psi\|_2 = \sqrt{\frac{1}{V} \int_V \psi(\mathbf{r})^2 d^2r} \quad (5.5)$$

with area  $V$  and  $\mathbf{r} = (x, y)^T \in V \subset \mathbb{R}^2$ .

In addition to numerical continuation, we perform numerical time simulations employing the same pseudo-spectral method with semi-implicit Euler steps as employed for the aPFC model in 1d. For details see 2.4.1.

## 5.2 Localized states

As known from the passive PFC model [TAR<sup>+</sup>13] and from our results in one spatial dimension, we can identify a transition region where patches of liquid state and crystalline state coexist. In the vicinity of the linear stability threshold of the liquid state (cf. Sec. 3.1), a broad variety of spatially localized states (LS or crystallites) exists.

By employing numerical continuation of Eqs. (5.3) and (5.4), we explore the bifurcation structure of active crystallites in 2d. How do (active) crystallites grow in the plane as a

function of mean density  $\bar{\psi}$ ? Which influence has the activity parameter  $v_0$ ? Do traveling states arise as in one spatial dimension? Do traveling LS exhibit the same slanted snaking as resting LS do?

### 5.2.1 Passive PFC model: slanted snaking

We start by constructing bifurcation diagrams as a function of the mean density  $\bar{\psi}$  for the passive PFC model. The passive PFC model is restored by  $v_0 = 0$  resulting in uncoupled Eqs. (5.3) and (5.4) and  $\mathbf{P} = \mathbf{0}$  for all times. For the studies of LS in 1d, we used the parameter set given in Eq. (4.5). These parameters have to be slightly amended and three different combinations of parameters are used throughout the studies of two-dimensional active crystals and LS.

Figures 5.2 and 5.3 depict the typical slanted snaking of the branches of LS on their path to a spatially extended crystal. For both bifurcation diagrams, the continuation in  $\bar{\psi}$  is started with the uniform state of  $\psi = 0$  again referred to as *liquid* state (gray branch). At a critical density close to  $\bar{\psi} = -0.6$ , the trivial state is destabilized and a branch of periodic solutions of hexagonal order bifurcates (black branch). In contrast to the one-dimensional periodic pattern shown in Fig. 4.3 (corresponding to stripes in 2d), the bifurcation is a transcritical bifurcation. We did not follow the other part of the emerging branch that corresponds to so-called cold hexagons or down-hexagons. In contrast, the 1d pattern emerges in a supercritical pitchfork-bifurcation.

As expected, a secondary bifurcation is detected on the branch of periodic states close to the primary bifurcation. On the rectangular domain as used for Fig. 5.2, the bifurcating branch (blue lines) corresponds to localized hexagonal crystallites. Similar to the 1d case (discussed in Sec. 4.3), the branch undergoes a series of folds while whole layers of density peaks are added. At each fold, the stability of the branch changes. Solid lines correspond to stable solutions and dotted lines indicate unstable solutions. Eventually, the branch of LS ends on the branch to the spatially extended crystal and the entire domain is filled by the crystalline state. Henceforth, the crystal is stable. Again, due to conservation of  $\psi$ , the loci of subsequent saddle-node bifurcations form lines slanted towards higher  $\bar{\psi}$ . Since the model is passive with  $v_0 = 0$  and, hence,  $\mathbf{P} = \mathbf{0}$ , no traveling states can exist and all solutions are at rest.

Figure 5.3 presents a similar bifurcation diagram obtained from continuation on a hexagonal domain. In contrast to the rectangle used in Fig. 5.2, a rotationally symmetric solution (red line, also cf. Fig. 5.3(I)) emerges at the secondary bifurcation. This type of LS has been termed *target* solution. Its branch is tracked until interactions with the Neumann boundaries of the triangular computation domain are not negligible anymore. Apparently, the hexagonal geometry favors the emergence of target-like solutions as it is closer to a rotational symmetry than the previously used rectangle.

The snaking branch of LS (blue line) bifurcates in a tertiary bifurcation from the branch of target solutions. This bifurcation is actually imperfect due to numerical grid effects. However, in Fig. 5.2, this cannot be seen by eye. The crystalline patch of hexagonal order enlarges, until, ultimately, the hexagonal domain is completely filled and the branch terminates on the branch of the periodic crystal (black line). As the hexagonal domain is of larger area than the rectangular one of Fig. 5.2, more density peaks fit into it and the snaking path of the LS consists of more undulations.

For Figs. 5.2 and 5.3, the temperature-like parameter  $\epsilon$  is increased from the value  $\epsilon =$

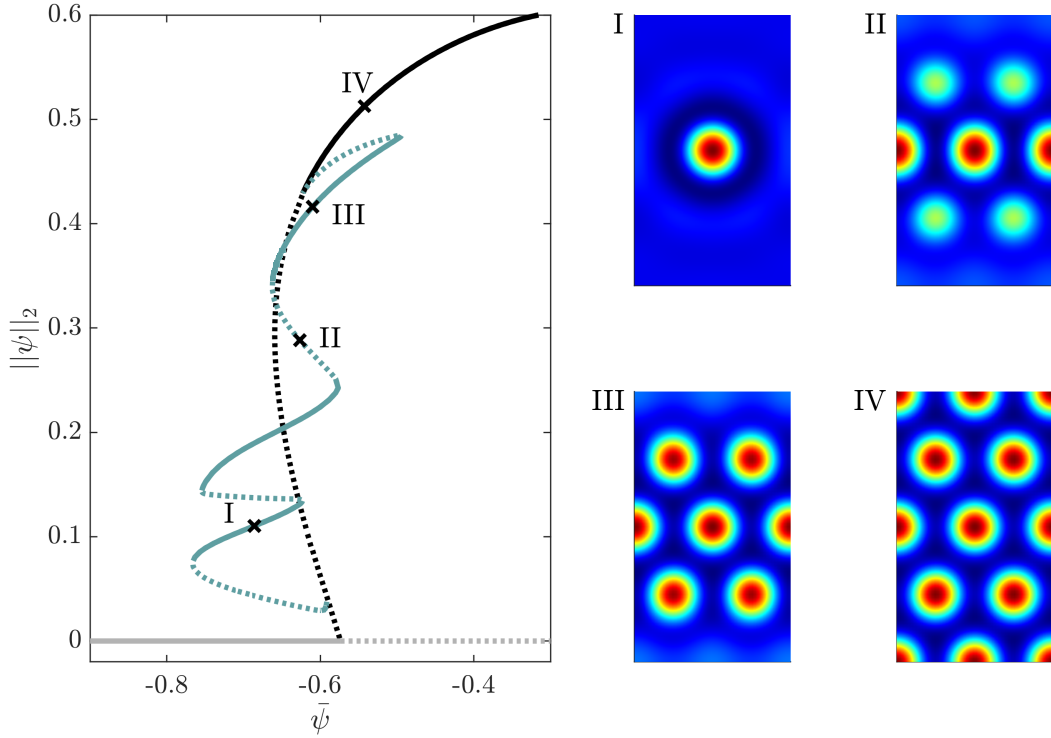


Figure 5.2: (left) Bifurcation diagram of homogeneous, periodic and localized steady state solutions of the passive PFC model in 2d as a function of the mean density  $\bar{\psi}$ . The solutions are characterized by their  $L^2$ -norm  $\|\psi\|_2$ . (Un)stable solutions are shown as (dotted) solid lines. The liquid phase (gray line with norm zero) is destabilized at  $\bar{\psi} \approx -0.55$  and an unstable branch of periodic patterns (black line, cf. IV) emerges. In a secondary bifurcation, a branch of LS (blue line) is created. After various folds causing alternating stabilities, the branch terminates on the branch of the periodic patterns. (right) Selected solution profiles  $\psi(\mathbf{r})$  at loci labeled (I-IV) in the left panel. Rectangular domain of size  $2L_a \times 4L_c$  with  $L_a = 4\pi/\sqrt{3}$  being the side length of a hexagon/triangle and  $L_c = 2\pi$  the critical wavelength and height of triangles. Parameters:  $\epsilon = -0.98$ ,  $v_0 = 0$ .

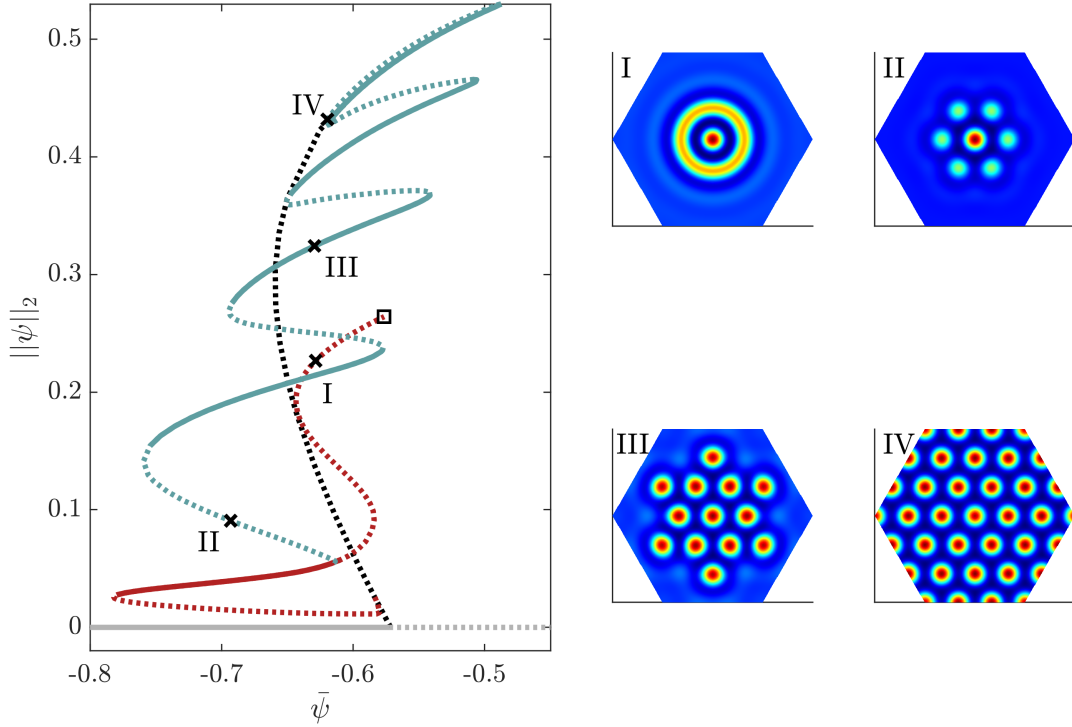


Figure 5.3: (left) Bifurcation diagram for the passive PFC model computed on a hexagonal domain. Shown is the norm  $\|\psi\|_2$  as a function of the mean density  $\bar{\psi}$ . Gray: liquid phase with norm zero. Black: periodic pattern (cf. IV). Dark red: target solution (cf. I). Blue: LS. In a primary bifurcation, the liquid is destabilized and the branch of periodic crystal emerges. Rotationally symmetric localized target solutions are created in a secondary bifurcation. The square marks where interactions of the target solution and Neumann boundaries are no longer negligible and the continuation is stopped. The snaking branch of LS bifurcates in a tertiary bifurcation from the target solutions. (right) Solution profiles  $\psi(\mathbf{r})$  at loci indicated by (I-IV). Hexagonal domain with side length  $3L_a$  and  $L_a = 4\pi/\sqrt{3}$  being the side length of an individual triangle. Parameters are as in Fig. 5.2.



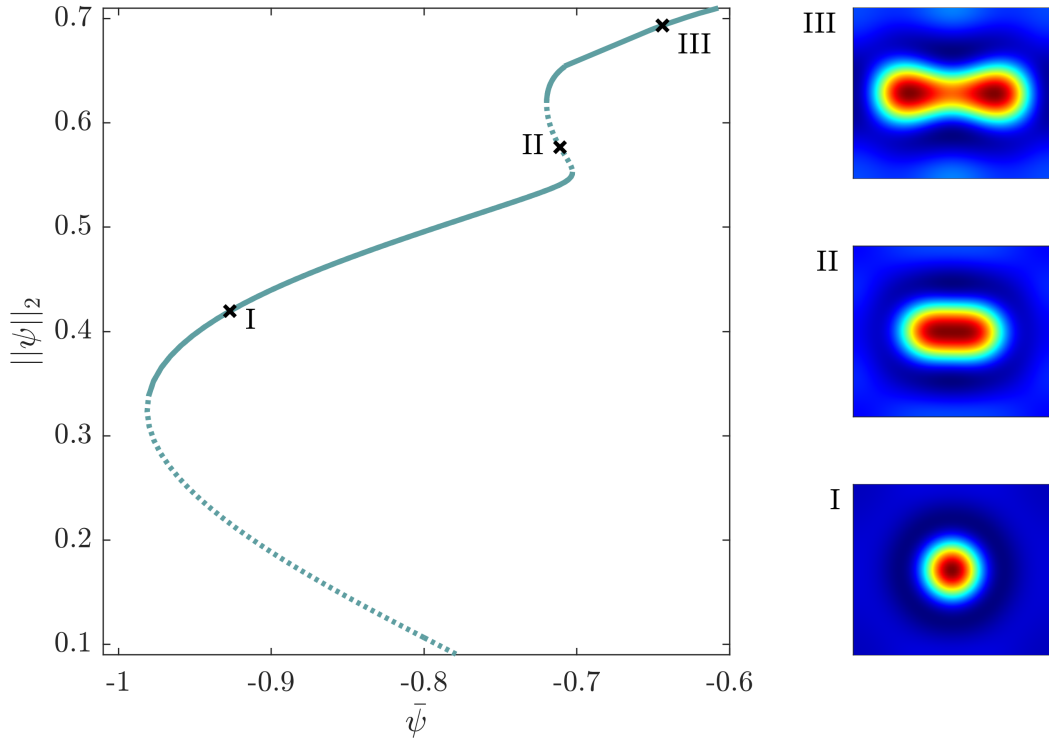


Figure 5.4: Suppressed snaking: At low values of  $\epsilon = -1.5$ , passive LS do not exhibit slanted snaking but rather grow towards elongated stripe-like structures. In contrast to  $\epsilon = -0.98$  (cf. Figs. 5.2 and 5.3) crystalline patches do not grow by adding layers of density peaks. Rectangular domain of size  $2L_a \times 2L_c$ . Note that the result of an elongating LS are also obtained on larger domains and is independent of possible interaction due to periodic boundaries. Remaining parameter:  $v_0 = 0$ .

$-1.5$  used in our analyses of the 1d model to  $\epsilon = -0.98$  as employed in former studies [ML13, MOL14, PVWL18]. At  $\epsilon = -1.5$ , the localized density peak does not grow into a patch of hexagonal order but rather elongates and forms stripe-like patterns. Apparently, hexagons are not stable in this region, but stripes are. Figure 5.4 visualizes this particular behavior as function of  $\bar{\psi}$ . In order to exclude effects of boundaries, the continuation was carried out on various domains with the same result of an elongating density peak. In contrast to all other solution profiles shown in this chapter,  $\psi(\mathbf{r})$  in Fig. 5.4 is not computed on half of the depicted domain and mirrored, but (I)-(III) depict the actual obtained solution profiles. Here, the density peak is placed in the middle of the computational domain in order to avoid a possible influence of the boundaries.

Next, we move on to the active PFC model and investigate the influence of activity  $v_0$ . By continuations in  $\bar{\psi}$  at  $v_0 = 0$ , we produce various LS whose response to activity is then studied. As explained in Sec. 5.1.2, we use a rectangular domain and symmetries of the  $\psi$  and  $\mathbf{P}$  to use the continuation on a reduced-size domain. In Sec. 5.2.4, we return to slanted snaking and study to what extent snaking is modified by activity. In particular, we study the bifurcation structure of traveling states as a function of  $\bar{\psi}$ .

### 5.2.2 Active PFC model: onset of motion

We now systematically explore how LS in 2d respond to increasing activity by employing the activity  $v_0$  as main control parameter. From results obtained for LS in one spatial dimension, as depicted, e.g., in Fig. 4.7, we expect transitions from resting to traveling LS (RLS and TLS, respectively) associated with a symmetry breaking between the two fields  $\psi$  and  $\mathbf{P}$ , as centers of density peaks are shifted w.r.t.  $+1$  defects in  $\mathbf{P}$  at a critical activity  $v_c$ .

For resting crystals,  $\mathbf{P}$  points downwards gradients of  $\psi$ , hence, leading to a defect at the center of the density peak, similar to the vector field a monopole would cause. These defects are termed  $+1$  defects (cf. Fig. 5.6(a)).

Figure 5.5 shows a typical bifurcation diagram as a function of  $v_0$ . A stable one-peak LS at rest (represented by a solid blue line) undergoes a drift-instability at  $v_c \approx 0.15$ . The detected  $v_c$  is practically the same as found for LS in 1d, since all parameters that control  $\mathbf{P}$  are set to the same values as in Sec. 4.3.1. The traveling one-peak LS (orange branch) is stable up to values of  $v_0 \approx 0.24$  where the branch folds back to smaller  $v_0$ . Unstable branches are given as dotted lines. The drift velocity  $c$  of the TLS increases as  $\sqrt{v_0 - v_c}$  as previously observed. Due to larger grid effects in 2d (we use an adaptive grid), the onset of motion is not perfectly sharp in  $c$  (cf. Fig. 5.5). Since the derived criterion for the onset of motion (Sec. 4.4) can be extended to two spatial dimension without loss of generality, tracking  $\|\psi\|_2^2 - \|\mathbf{P}\|_2^2$  reveals a zero crossing at  $v_c$  helping us to identify drift bifurcations.

Taking a closer look at the onset of motion reveals the symmetry breaking in 2d between  $\psi$  and the vector field  $\mathbf{P}$  at sufficiently large coupling. Centers of density peaks are shifted with respect to the  $+1$  defects in  $\mathbf{P}$  as depicted in Fig. 5.6. In 1d, the shift was w.r.t to zeros of  $P_x$  (cf. Figs. 4.1 and 4.2), now it is w.r.t. topological defects in the polarization field. For resting states, averaging  $\mathbf{P}$  over the area of a single density peak gives zero. Above  $v_c$ , a net orientation of  $\mathbf{P}$  emerges and traveling crystals or crystallites come into existence. In Fig. 5.6(b), the net polarization points to the left leading to a negative drift velocity  $c$ . The direction of the shift and the resulting sign of the velocity are random. Both directions correspond to the branch of traveling solutions.

If  $\bar{\psi}$  is chosen too low, i.e., too close to the solid-liquid transition, activity can also melt crystallites before motion sets in. This is what happens to the resting two-peak LS. Besides the one-peak LS from Fig. 5.5, also a LS consisting of two bound density peaks coexist with the homogeneous phase at the fixed mean density of  $\bar{\psi} = -0.9$ .

However, the branch of the resting two-peak LS as shown in Fig. 5.7 does not reach far enough in  $v_0$  to fulfill the criterion for the onset of motion and activity melts the structure before the drift starts. The position of the fold is at  $v_0 \approx 0.14 < v_c$ . Close to the fold, there is a subcritical pitchfork bifurcation. Here, the steady asymmetric solutions (dotted black branch, cf. Fig. 5.7(right) central panel) bifurcate off from the blue branch that corresponds to solutions with a left-right symmetry in  $\psi(\mathbf{r})$  (upper and lower panels). Note that the dotted black line represents a double branch of two different asymmetric solutions related by a reflection at the central vertical line:  $[\psi(x, y), P_x(x, y), P_y(x, y)] \leftrightarrow [\psi(-x, y), -P_x(-x, y), P_y(-x, y)]$ . At  $\bar{\psi} = -0.9$ , all two-peak solutions are unstable.

Yet, when increasing  $\bar{\psi}$  to  $-0.8$ , also the two-peak LS start to move. Due to the additional spatial degree of freedom and a structure at rest that is not rotationally symmetric, the overall picture changes rather drastically. Figure 5.8 summarizes the intricate bifurcation structure of the two-peak crystallite at  $\bar{\psi} = -0.8$ . The complicated structure is disassembled into Figs. 5.9 and 5.10 shedding light on the different emerging branches of TLS.

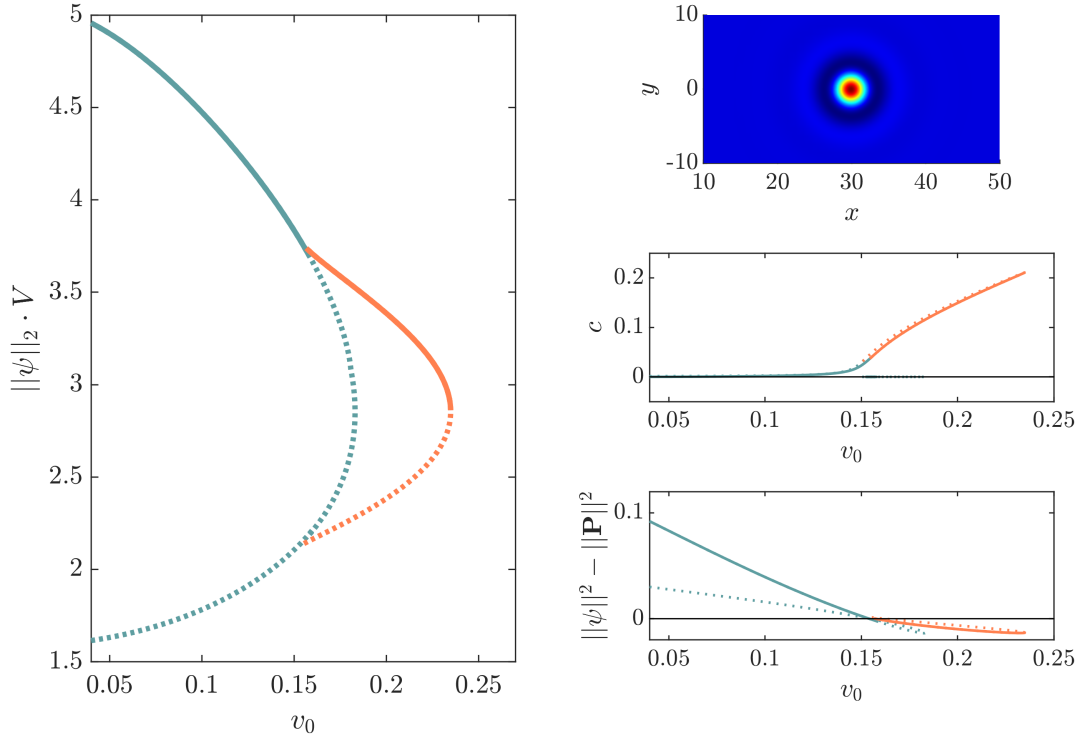


Figure 5.5: (left) Bifurcation diagram of resting and traveling one-peak LS at mean concentration  $\bar{\psi} = -0.9$ . The  $L^2$ -norm is given as a function of activity  $v_0$ . Resting solutions are indicated by blue lines, traveling states by orange lines. Branches of (un)stable states are plotted in (dotted) solid lines. At  $v_c \approx 0.15$ , the stable resting LS undergoes a drift pitchfork bifurcation and a branch of traveling states emerges. The region of existence of the TLS is limited by a fold at  $v_0 \approx 0.24$ . Panels on the right: (top) Selected solution profile  $\psi(\mathbf{r})$  at  $v_0 = 0.1$  showing only the central part of the domain. (center) Drift velocity  $c$  vs.  $v_0$ . Above  $v_c \approx 0.15$ , the velocity increases  $\propto \sqrt{v_0 - v_c}$ . Deviations from a sharp onset of motion are due to grid effects. (bottom) The difference  $\|\psi\|_2^2 - \|\mathbf{P}\|_2^2$  crosses zero at the onset of motion. Note that, in the left panel,  $\|\psi\|_2$  times the area  $V$  is plotted for clarity. Norms of LS tend to have very small values on large domains. Domain size:  $V = L_x \times L_y = 60 \times 30$ . Remaining parameters are  $\epsilon = -1.5$ ,  $C_1 = 0.1$ ,  $C_2 = 0$  and  $D_r = 0.5$ .

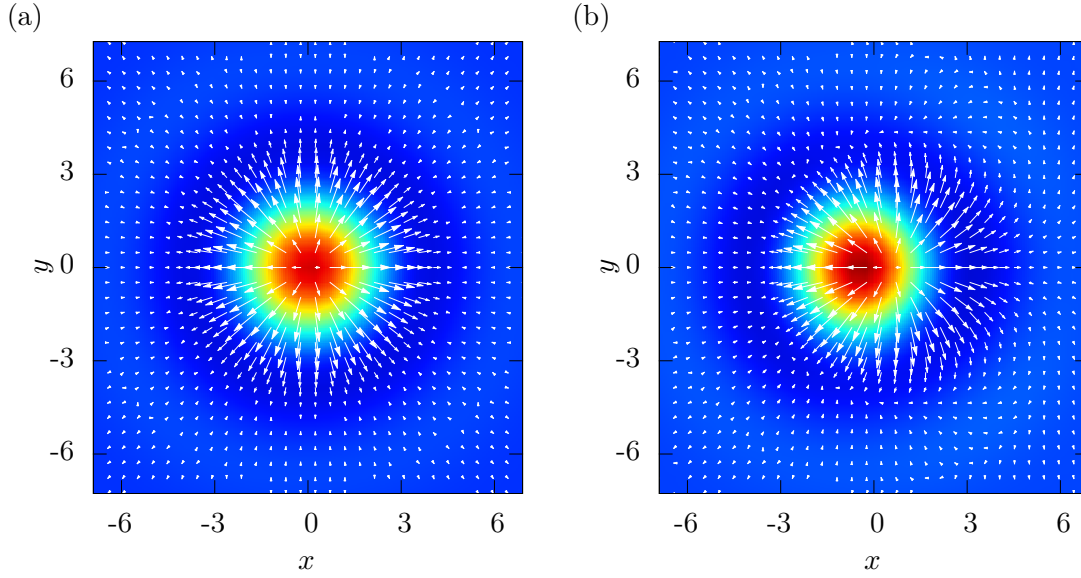


Figure 5.6: Detailed view of density field  $\psi(\mathbf{r})$  (color coded) and polarization  $\mathbf{P}(\mathbf{r})$  given as white arrows. (a) depicts a one-peak LS at rest ( $v_0 = 0.13$ ). The density maximum coincides with the +1 defect of the polarization field. Averaging  $\mathbf{P}$  over the peak shows zero net polarization. (b) depicts a traveling one-peak LS at higher activity ( $v_0 = 0.22 > v_c$ ). Peak maximum and location of the +1 defect of  $\mathbf{P}$  are shifted w.r.t. each other breaking the symmetry of (a). The shift induces a net polarization to the left. This leads to a net propulsion and the crystallite travels to the left with  $c \approx -0.19$ . Only a part of the domain used for numerical continuation is shown. Remaining parameters as in Fig. 5.5. For the vector field  $\mathbf{P}$  of a spatially extended crystal see Fig. 5.18.

Interestingly, its drift can occur parallel and also perpendicular to the orientation of the dumbbell shaped two-peak LS – the latter stretching to higher values of  $v_0$ . Figure 5.9 depicts branches of TLS moving parallel to the orientation of the elongated LS while Fig. 5.10 shows the branches of TLS moving orthogonal to the long axis of the LS.

The elongated two-peak LS is connected to the rotationally symmetric one-peak solution as marked in Fig. 5.10(III). This point also marks a fold. The branch of stable resting one-peak LS (solid gray line) folds and the LS emerges towards a two-peak LS. In fact, all (symmetric) resting LS in Fig. 5.8 correspond to one single branch, similar to the result for the snaking branches as a function of  $\bar{\psi}$ . The branches of one-peak LS (moving and resting) are given in light gray with solid (dotted) lines for (un)stable states.

Unfortunately, as at the lower mean density of  $\bar{\psi} = -0.9$  (Fig. 5.7), also here all two-peak LS are unstable. Admittedly, this makes understanding the bifurcation structure of the active two-peak LS a problem of rather academic nature.

At  $v_c \approx 0.15$ , various TLS emerge at drift bifurcations marked in Figs. 5.9 and 5.10 by black circles. TLS moving parallel to their long axis (Fig. 5.9) do not reach activities as high as TLS moving orthogonal to their long axis. Two branches of TLS originate in a drift-transcritical bifurcation on the branch of resting asymmetric states (black). Due to

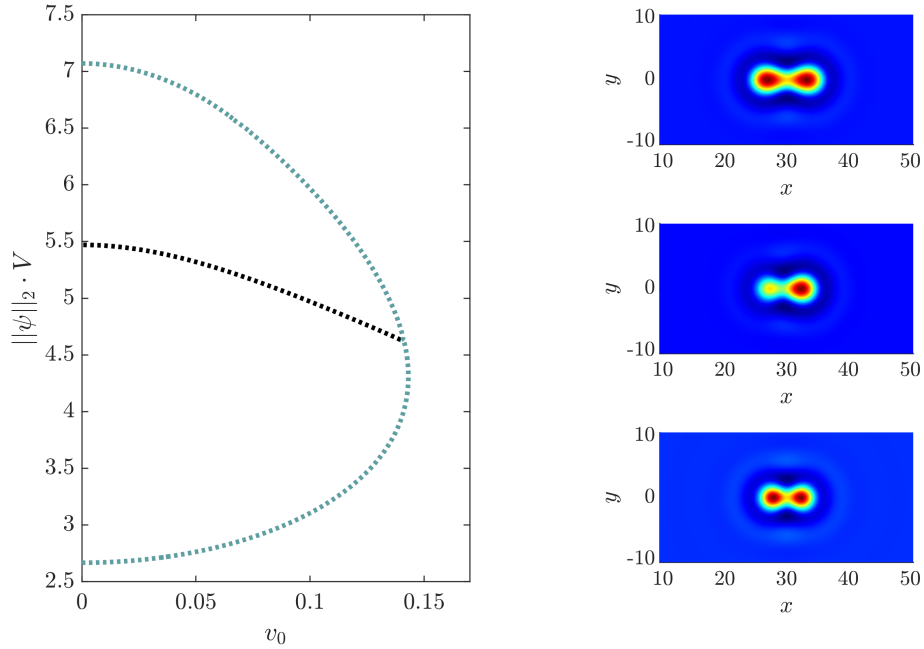


Figure 5.7: (left) Bifurcation diagram of resting two-peak LS at a low density of  $\bar{\psi} = -0.9$ :  $L^2$ -norm of  $\psi$  as a function of activity  $v_0$ . (right) Selected density profiles  $\psi(\mathbf{r})$ . From top to bottom, they correspond to the upper half of the blue branch, the black branch of asymmetric solutions and the lower half of the blue branch. The blue branch represents solutions with a left-right symmetry. All solutions are unstable (dotted lines). In contrast to the one-peak LS, only resting two-peak LS exist. The fold of the symmetric states is located at  $v_0 < v_c \approx 0.15$  and no traveling states come into existence. Parameters and domain size as in Fig. 5.5.

the lack of a left-right symmetry of the density profile, each direction of the drift results in a single branch. Hence, for asymmetric states, the drift bifurcation is not a pitchfork bifurcation but a transcritical bifurcation. TLS of the upper branch move to the left with the larger density peak at their tip (cf. Fig. 5.9(III)). The second branch that emerges (bending towards lower norms) corresponds to TLS with a slightly smaller density peak at the tip (II). Both branches of TLS terminate on the branch of resting symmetric LS (blue) in respective drift pitchfork bifurcations (marked by circles).

Note that on the scale of Fig. 5.9 the bifurcation occurring on the branch of asymmetric RLS does not exhibit the typical shape of a transcritical bifurcation as both branches of TLS seem to bifurcate towards larger  $v_0$ . We believe that one of them undergoes a fold very close to the transcritical bifurcation. A similar behavior was observed for transcritically bifurcating TLS in 1d. Figure 4.11 in chapter 4 depicts this case. Grid effects make it very hard to remain on branches of RLS and lead to rather blurred onsets of the drift velocity  $c$  vs.  $v_0$ . However, with the help of the derived onset criterion, we are able to determine the exact loci of drift bifurcations (lower panels of Fig. 5.9).

Note that the state on the unstable branch of asymmetric RLS (dotted black) grows towards a stripe-like structure with a small density bump at its head when leaving the range

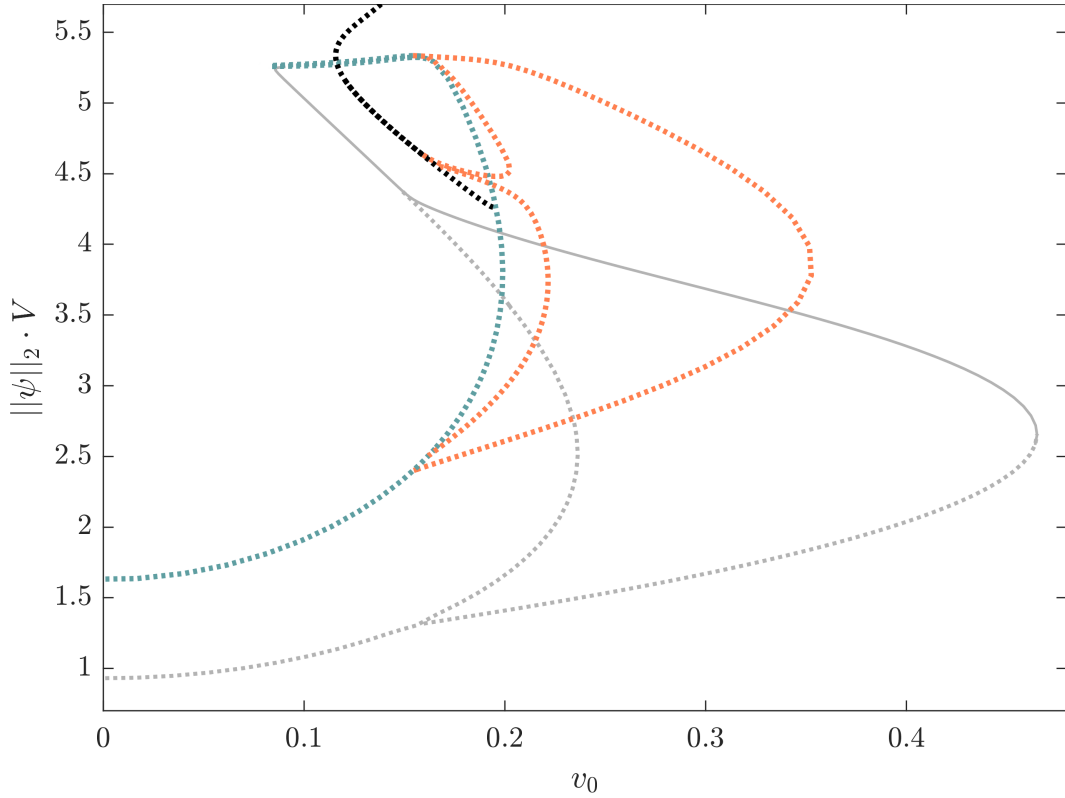


Figure 5.8: Summary of bifurcation diagram for a dumbbell shaped two-peak LS showing the  $L^2$ -norm of  $\psi$  as a function of  $v_0$ . Blue lines indicate branches of resting symmetric LS, black stands for resting asymmetric LS. At  $v_0 \approx 0.15$ , states traveling in different directions (orange branches) emerge in various drift bifurcations. See Figs. 5.9 and 5.10 for explanatory details and selected solution profiles. Thin gray branches correspond to resting and traveling one-peak LS. Domain size:  $V = 60 \times 30$ .  $\bar{\psi} = -0.8$ . Remaining parameters are as in Fig. 5.5.

of Figs. 5.8 and 5.9 at the top. The branch does not have any stable sections.

Figure 5.10 explores the branches of traveling two-peak LS that move orthogonal to their long axis. Here, the picture is simpler. As for the traveling one-peak LS, a branch of TLS stretches between two drift bifurcations highlighted by black circles. Panels on the right show selected density profiles.

Overall, the bifurcation structure of traveling two-peak LS is much more intricate than the one of the single-peak LS. Also, we have seen that increasing  $\bar{\psi}$  from -0.9 to -0.8 drastically changes the bifurcation structure. Figure 5.11 illustrates how drift bifurcations and TLS come into existence by showing a series of four bifurcation diagrams for increasing values of mean density  $\bar{\psi}$ . Between  $\bar{\psi} = -0.67$  and -0.65 a pair of drift bifurcation is created. Their origin coincides with the fold of the branch of resting states (blue lines) as two-parameter continuations shows (cf. Fig. 4.8). For increasing  $\bar{\psi}$ , the region of existence of TLS grows as the fold of their branch moves to higher values of  $v_0$ . The threshold activity for migration  $v_c$  stays practically constant. Consistent results were obtained by extensive fold continuations in 1d. Note that, in Fig. 5.11,  $\epsilon = -0.98$  in contrast to previous figures with  $\epsilon = -1.5$ .

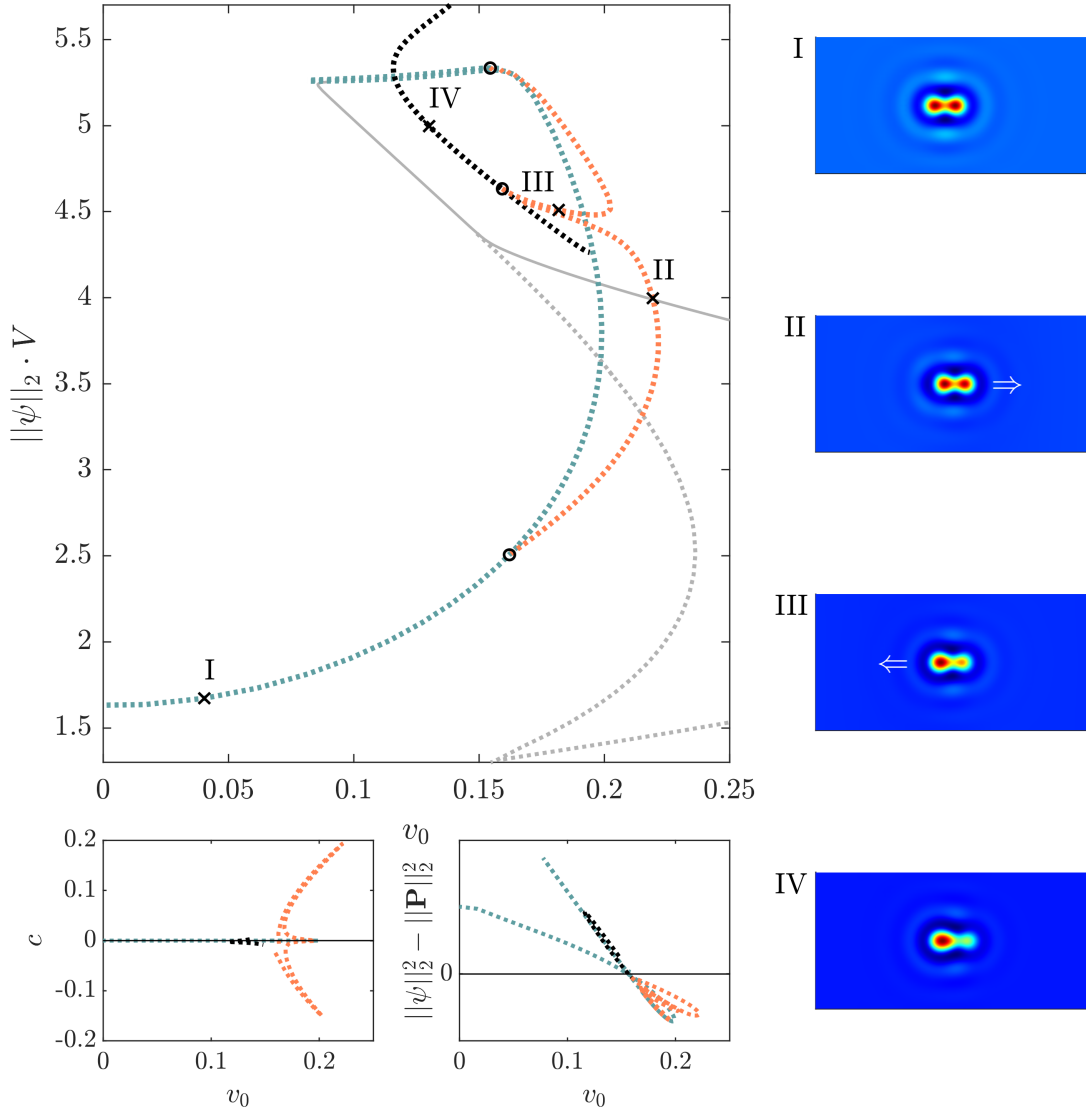


Figure 5.9: Onset of motion parallel to the long axis of two-peak dumbbell-shaped LS. Main panel: bifurcation diagram of two-peak LS giving the norm of  $\psi$  vs. activity  $v_0$ . On the right, selected solution profiles  $\psi(\mathbf{r})$  at loci labeled (I-IV) are shown. Blue branches correspond to resting symmetric LS with a left-right symmetry in  $\psi$  as shown in panel I. The black branch denotes resting asymmetric solutions, cf. panel IV. The resting two-peak LS are destabilized w.r.t. parallel motion in drift bifurcations at  $v_c \approx 0.16$ , marked by black circles. Orange branches indicate traveling LS (II and III). III travels with the larger density peak at its tip, for II it is the opposite. (Dotted) solid lines correspond to (un)stable solutions. Note that again all two-peak LS are unstable. The asymmetric solution is destabilized in a transcritical drift bifurcation marked by a circle on the black branch. Here, two branches of TLS (orange) with opposite drift velocities emerge. Due to the lack of symmetry in  $\psi$ , they do not correspond to the same solution as for symmetric LS. The lower panels show velocity  $c$  vs.  $v_0$  and the criterion  $\|\psi\|_2^2 - \|\mathbf{P}\|_2^2$ , that crosses zero at the respective onsets of motion. Parameters and domain size as in Fig. 5.8.

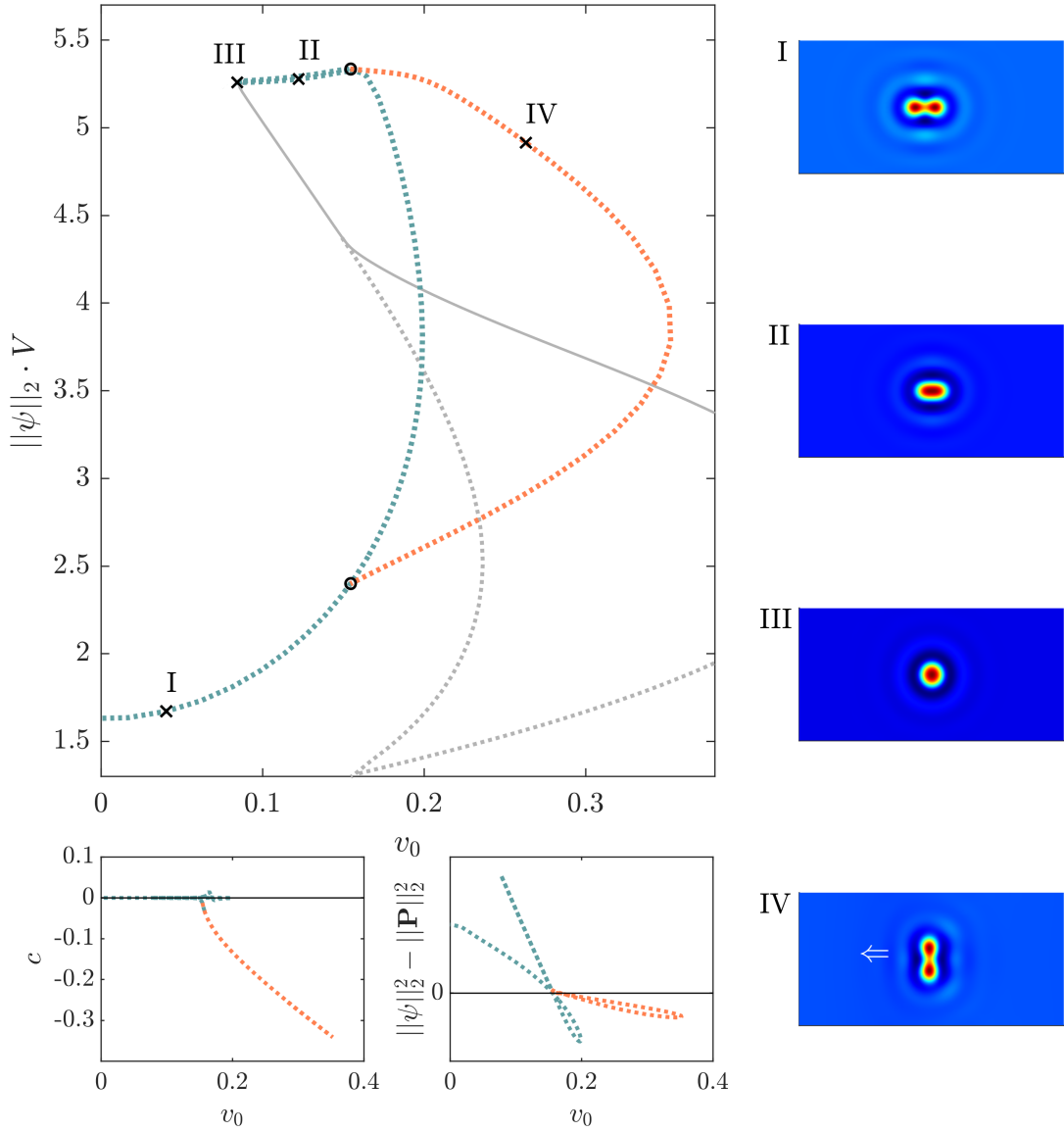


Figure 5.10: Onset of motion perpendicular to the long axis of the dumbbell-shaped two-peak LS. Main panel: bifurcation diagram giving the norm of  $\psi$  vs. activity  $v_0$ . On the right, selected solution profiles  $\psi(\mathbf{r})$  at loci labeled (I-IV) are shown. Line styles, symbols and parameters as in Fig. 5.9. The resting two-peak LS changes its shape towards the fold at point III evolving into a one-peak LS. The resting two-peak LS belongs to the same branch as the resting one-peak LS whose branches are given in light gray. Stable resting and traveling one-peak LS correspond to solid lines. At two drift-pitchfork bifurcations (marked by circles), the resting LS are further destabilized and start to travel. The motion is perpendicular to the orientation of the LS. The small panels show velocity  $c$  vs.  $v_0$  and  $\|\psi\|_2^2 - \|\mathbf{P}\|_2^2$  crossing zero at the two drift bifurcations.



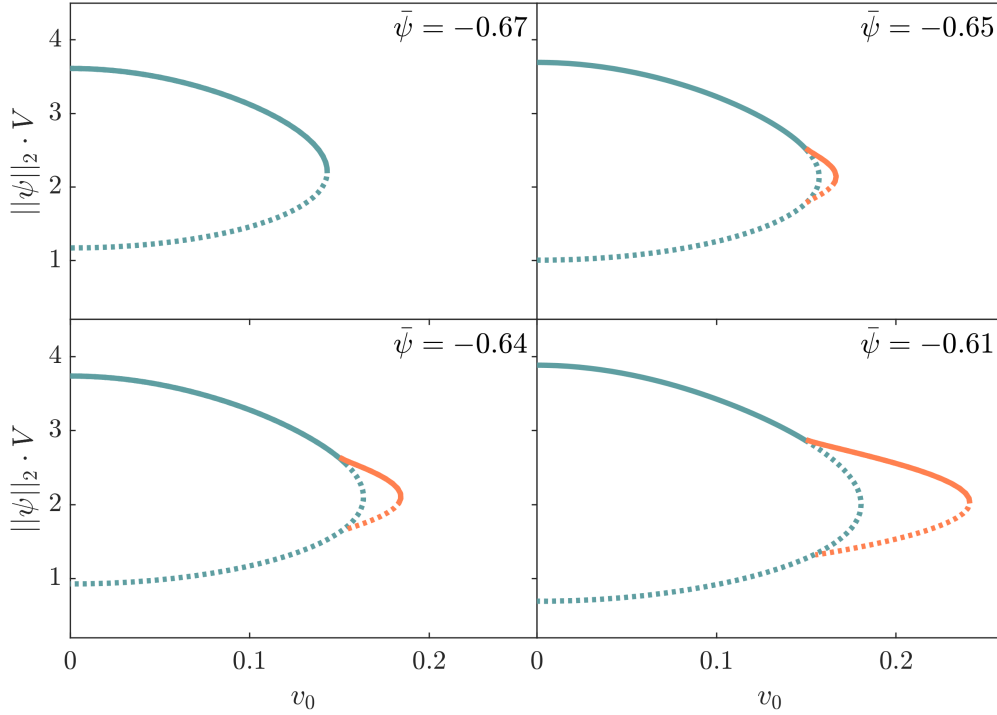


Figure 5.11: A sequence of bifurcation diagrams shows how traveling states come into existence with increasing mean density  $\bar{\psi}$ . Shown is the norm of resting one-peak LS (blue) and traveling LS (orange) vs. activity  $v_0$ . The mean density  $\bar{\psi}$  increases from top left to bottom right. Two drift pitchfork bifurcations emerge at the fold of the branch of RLS. At higher  $\bar{\psi}$ , the range of existence of TLS expands to larger  $v_0$  and the positions of drift-pitchfork bifurcations separate further. The onset of motion is always at  $v_c \approx 0.15$ . Solid (dotted) lines represent (un)stable solutions. Parameters:  $\epsilon = -0.98$ ,  $C_1 = 0.1$ ,  $C_2 = 0$  and  $D_r = 0.5$ .

With various TLS obtained by continuation in  $v_0$ , we next give a parameter map with a morphological phase diagram before returning to bifurcation diagrams as a function of the mean density  $\bar{\psi}$  and investigating the phenomenon of slanted homoclinic snaking for active crystallites at  $v_0 > 0$  in Sec. 5.2.4.

### 5.2.3 Morphological phase diagram

Before discussing the bifurcation structure as function of  $\bar{\psi}$  in detail and changing the temperature-like parameter  $\epsilon$  to allow for snaking, we conclude the discussion of active crystallites at  $\epsilon = -1.5$  by presenting a large scale morphological phase diagram in the parameter plane spanned by  $v_0$  and  $\bar{\psi}$ . The phase diagram is determined numerically by counting peaks of  $\psi(\mathbf{r}, t)$  after a sufficiently long transient. To favor the creation of LS, six density bumps are placed at random positions on the homogeneous phase marginally perturbed by white noise. For the polarization  $\mathbf{P}$ , we choose a randomly perturbed trivial

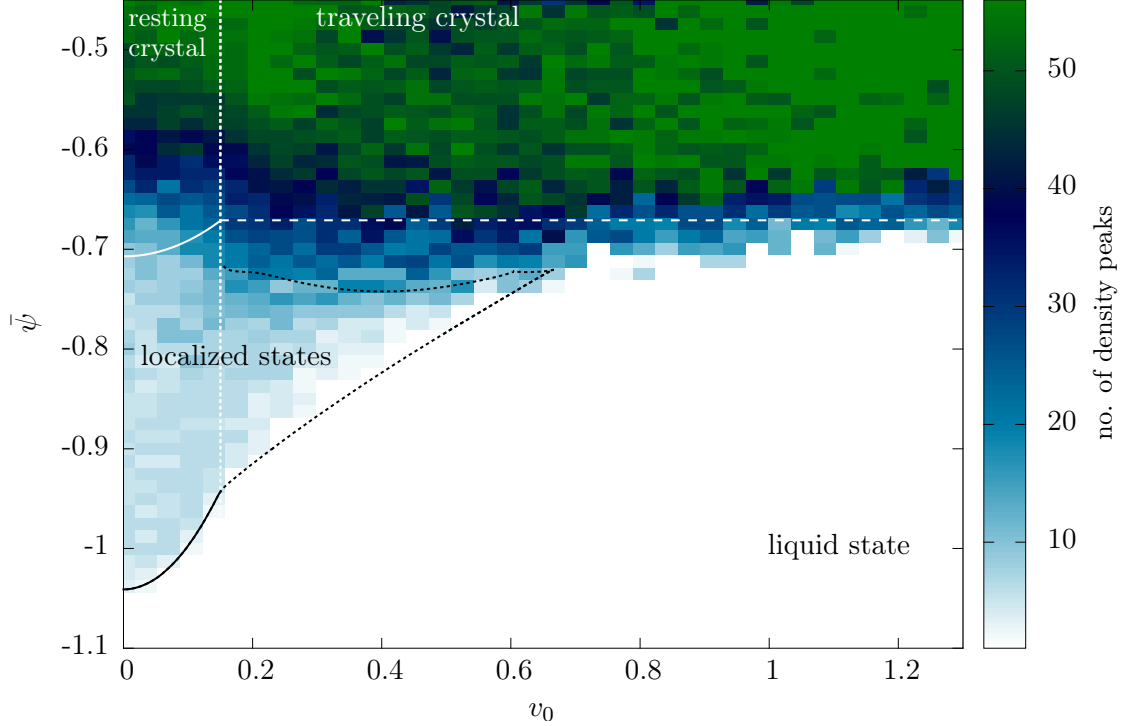


Figure 5.12: Morphological phase diagram for the active PFC model in 2d. Different states are characterized by the total number of density peaks formed in the domain. The rectangular domain is of size  $8L_c \times 7L_a$  with  $L_a = 4\pi/\sqrt{3}$  and  $L_c = 2\pi$ . A total number of 56 density peaks of hexagonal order fit into the domain. Horizontal white lines (solid and dashed) give limits of the linear stability of the liquid state. The vertical dotted line marks the onset of motion. Black lines give the position of the fold of resting one-peak LS (solid) and of traveling one-peak LS (dotted). The color coding results from time simulations. The liquid state refers to a uniform density phase with zero peaks (white). Resting and traveling LS exist in the regions marked in blue with cluster sizes ranging from a single peak (light blue) up to sizes that almost fill the entire domain (dark blue). Spatially extended, periodic hexagonal patterns are indicated in green (56 peaks). Above  $v_0 \approx 0.3$  in the regime of traveling crystals, the number of peaks decreases again as hexagonal patterns are transformed towards stripe patterns and each ridge is only counted as one peak. Here, some blue pixels appear in the green area. Remaining parameters are  $\epsilon = -1.5$ ,  $C_1 = 0.1$ ,  $C_2 = 0$  and  $D_r = 0.5$  as used throughout Sec. 5.2.2. Increments:  $\Delta v_0 = 0.035$ ,  $\Delta \bar{\psi} = 0.0125$ . See Fig. 5.13 for a zoom and profiles.

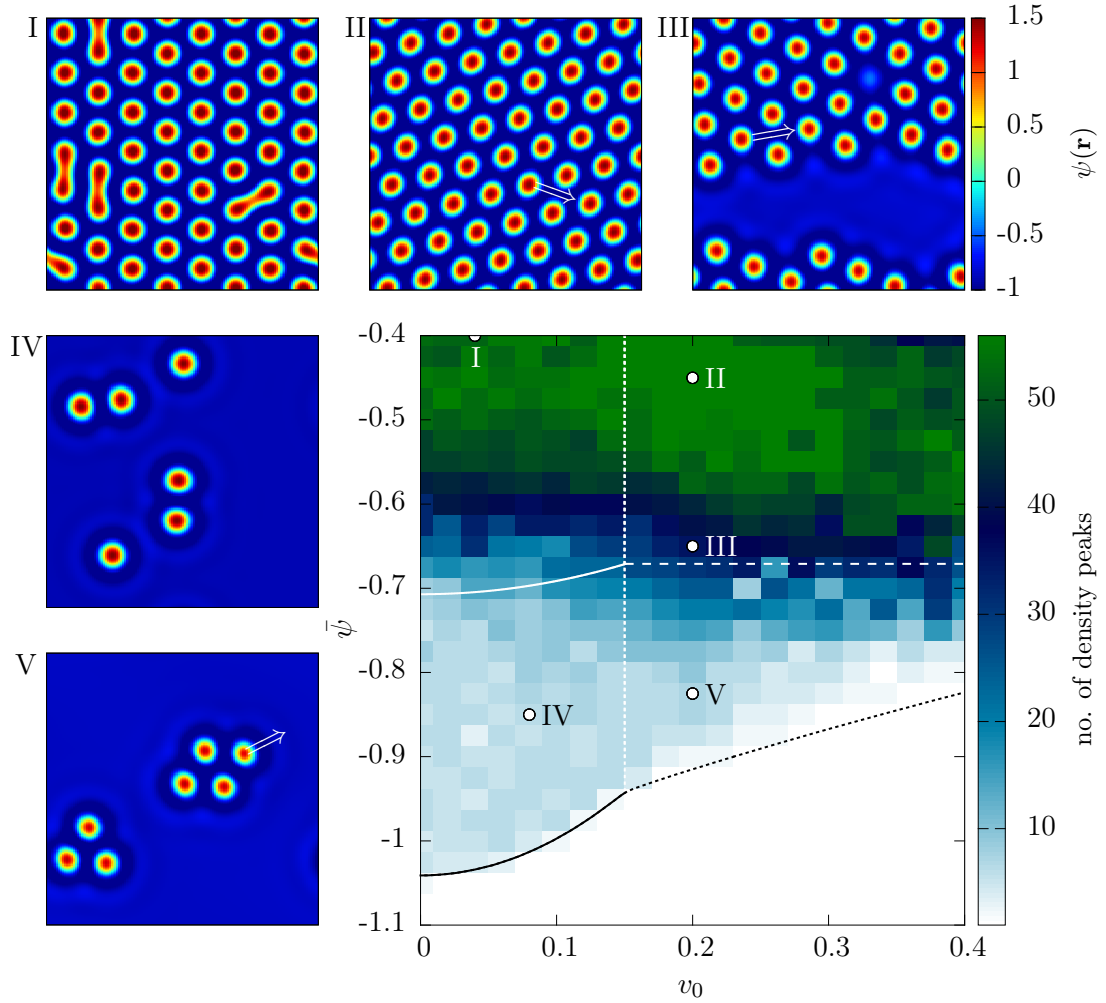


Figure 5.13: Details of the phase diagram for the active PFC model at low activities. Color coding, lines and parameters as in Fig. 5.12. Selected converged solutions profiles  $\psi(\mathbf{r})$  (I-V) correspond to loci labeled in the phase diagram. Arrows indicate direction of motion. (I) Resting hexagons close to the transition to stripes. (II) Traveling hexagons. (III) Traveling cluster of hexagonal order. (IV) Resting LS. (V) Traveling LS. Increments:  $\Delta v_0 = 0.02$ ,  $\Delta \bar{\psi} = 0.025$ .

state  $\mathbf{P}_0 = \mathbf{0}$  as initial conditions.

The domain with periodic boundaries has a size of  $8L_c \times 7L_a$  with  $L_a = 4\pi/\sqrt{3}$  being the side length of a hexagon/triangle and  $L_c = 2\pi$  the critical wavelength at the onset of crystallization.  $L_c$  is the height of triangles found in the hexagonal pattern. This domain size results in a maximal number of 56 density peaks in a periodic array (cf. Fig. 5.13(I)).

In Fig. 5.12, periodic states with around 56 density peaks are displayed in green, whereas LS exist within the blueish area. The white area without any density peaks corresponds to the liquid state  $\psi(\mathbf{r}) = 0$ . The white lines mark limits of the linear stability of the liquid phase. The vertical white lines follow the onset of motion at  $v_c$  (note  $v_c \approx 0.15$  independent of  $\bar{\psi}$ ). The limits of existence of LS are determined by a two-parameter continuation of their fold (for 1d fold continuation cf. Fig. 4.8). The black lines give the position of folds of resting one-peak LS (solid black) and of traveling one-peak LS (dotted black). The position of the saddle-node bifurcations of 2d TLS shifts again backwards towards smaller values of  $v_0$  at  $v_0 \approx 0.7$ . This is a major difference to one-peak TLS in 1d, that exist up to arbitrarily high  $v_0$ .

The time simulations indicate large areas of existence of various active LS (blueish area). The size of LS ranges from single density peaks (light blue) to patches of LS almost filling the entire domain (dark blue). For selected solution profiles  $\psi(\mathbf{r})$  see Fig. 5.13. The phase diagram also illustrates how hexagonal periodic states change their shapes towards stripe patterns resulting in a lower number of density peaks (Fig. 5.13(I)). For stripe patterns each ridge is only counted as a single density peak. Close to the limit of linear stability of the liquid state, large patches of localized crystalline order coexist with the uniform state (Fig. 5.13(III)). Resting LS ( $v_0 < 0.15$ , left of the vertical dotted line denoting the onset of motion) exist at low values of  $\bar{\psi} \approx -1.05$ . Increasing activity melts most of these LS ( $\bar{\psi} < -0.8$ ) and the  $v_0$ -range of existence becomes smaller for higher values of  $\bar{\psi}$ . Higher  $v_0$  also favors traveling crystals that fill the entire domain. Namely, above the linear stability threshold of the liquid state, around  $\bar{\psi} = -0.65$ , the blue range shrinks for increasing  $v_c < v_0 < 0.6$  and loses ground to green areas.

As in the 1d case, we observe that traveling periodic states exist at arbitrarily high activities and do not melt as most of the LS do for increasing self-propulsion.

### 5.2.4 Snaking of active crystallites

In this section, we explore in detail the bifurcation structure as a function of mean density  $\bar{\psi}$  of resting and traveling *active* crystallites. Having analyzed the slanted snaking of passive LS (Sec. 5.2.1) and the bifurcation structure of active LS in 1d (Sec. 4.3.1), we now want to answer the question how the snaking of LS in two spatial dimension is influenced by activity and how TLS respond to varying  $\bar{\psi}$ .

The value  $\epsilon = -1.5$  of the effective temperature turns out to be too low to support continuous snaking branches and it suppresses the snaking path of passive LS (cf. Fig. 5.4). Most likely they become disconnected pieces. That is why we increase the temperature to  $\epsilon = -0.98$  as done for passive crystallites in Sec. 5.2.1. In addition, this value is also employed in [ML13] where the aPFC model was introduced. There, diffusion is set to  $C_1 = 0.2$  leading to  $v_c \approx 0.3$  (cf. Sec. 4.6). The high diffusion causes many crystallites to melt before motion can set in. Therefore, we stick to  $C_1 = 0.1$  as used in the previous sections. Then, the threshold for migration is  $v_c \approx 0.15$ .

Figure 5.14 depicts the bifurcation diagram at  $v_0 = 0.151$  slightly above  $v_c$ . Activity is

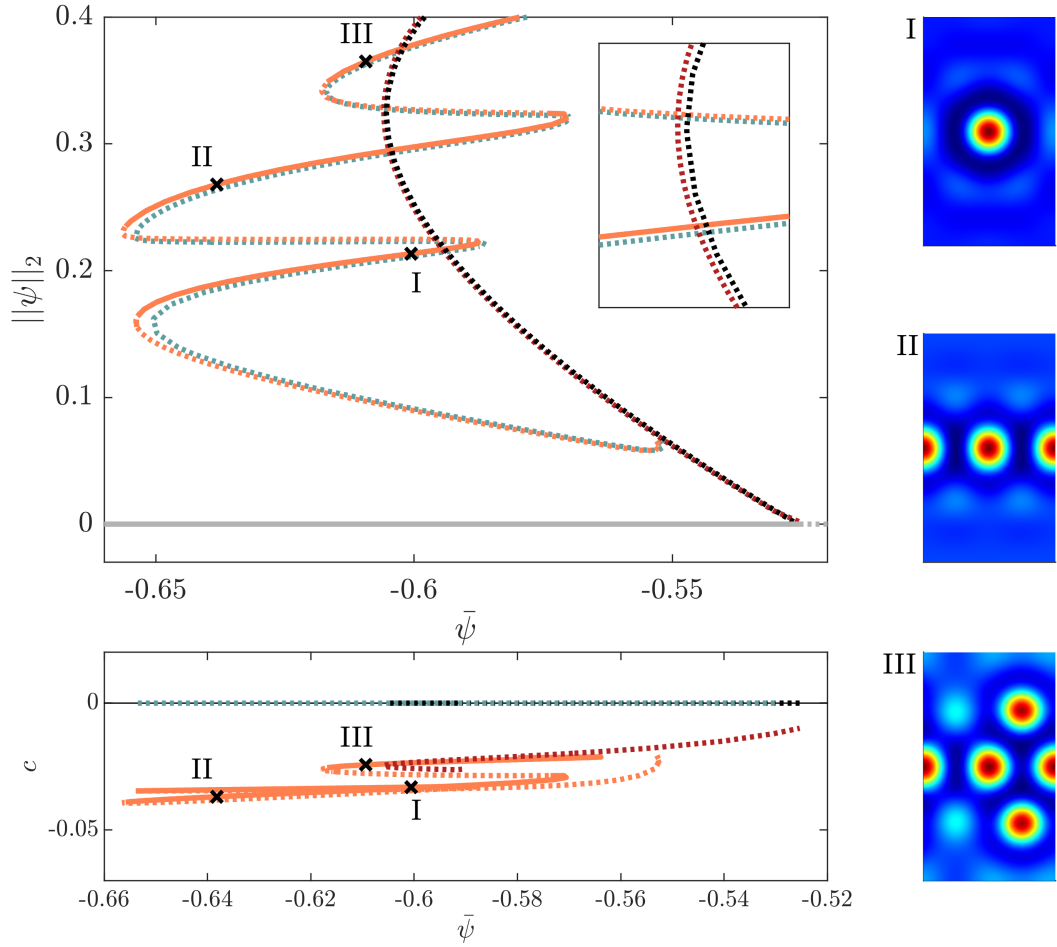


Figure 5.14: Bifurcation diagram showing slanted snaking of resting and traveling LS as a function of the mean density  $\bar{\psi}$ . Activity is fixed at the relatively low value  $v_0 = 0.151 > v_c$  allowing for the coexistence of resting and traveling states. (Un)stable solutions are given as (dotted) solid lines. Labels (I)-(IV) indicate the loci of profiles of stable traveling LS shown on the right. The liquid phase (gray line) with norm zero is destabilized at  $\bar{\psi} \approx -0.53$  and a branch of traveling periodic patterns (dark red) emerges. Close to the first primary bifurcation, also a branch of resting crystals (black) emerges in another primary bifurcation. In secondary bifurcations on those branches, resting and traveling LS (blue and orange), respectively, bifurcate. Since  $v_0 > v_c$ , all resting solutions are unstable. The inset illustrates the small separation of the branches in terms of their norm. The lower panel depicts the drift velocity  $c$  vs.  $\bar{\psi}$ . The mean density has no strong influence on  $c$ . Note that, as  $c < 0$ , all TLS move to the left. Rectangular domain of size  $2L_a \times 4L_c$ . Parameters:  $\epsilon = -0.98$ ,  $C_1 = 0.1$ ,  $C_2 = 0$ ,  $D_r = 0.5$ .

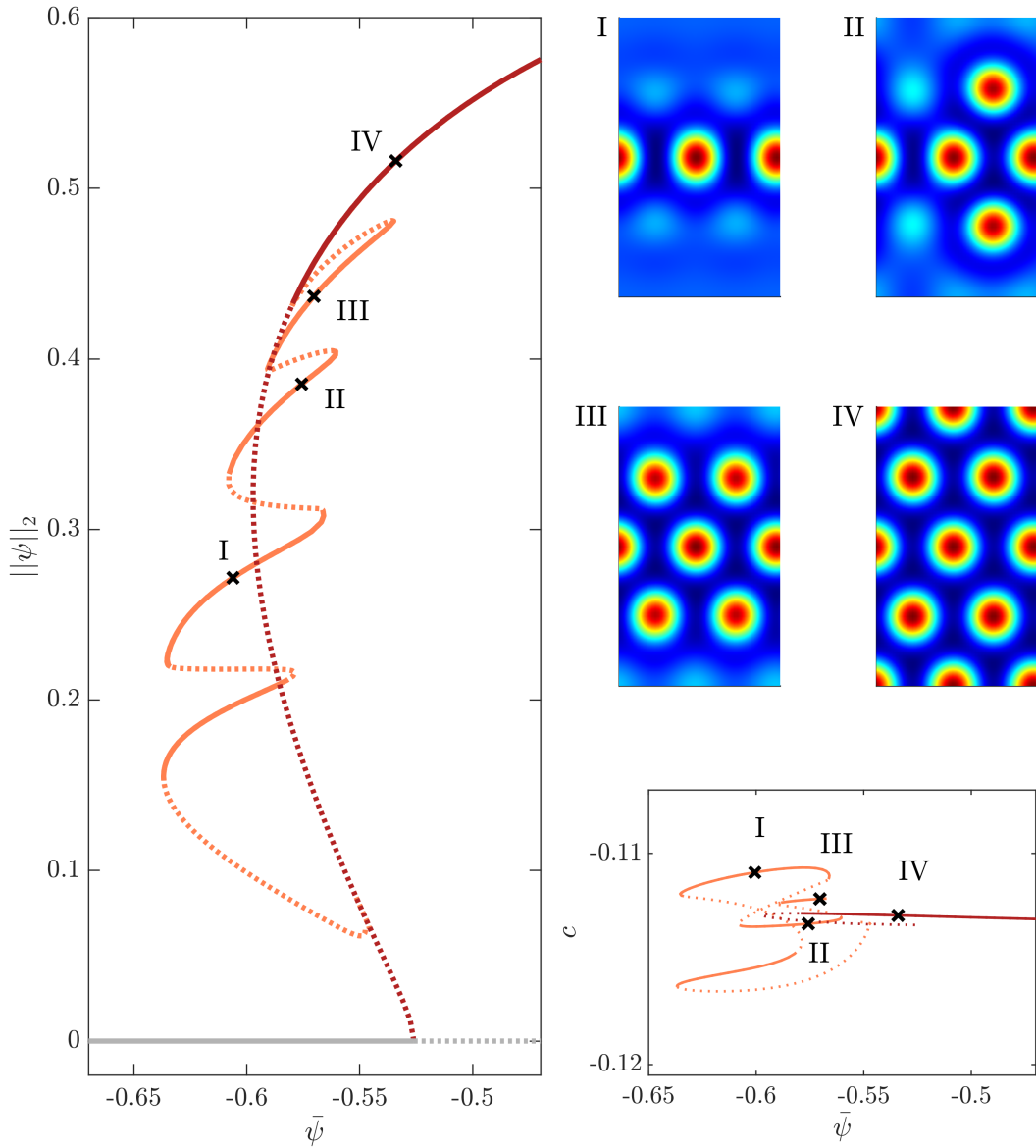


Figure 5.15: Bifurcation diagram of traveling crystal and LS as a function of the mean density  $\bar{\psi}$ . Activity is fixed at  $v_0 = 0.18$ . Due to high activity, no resting states exist. Traveling LS (orange) bifurcate from the traveling crystal (dark red) and exhibit slanted homoclinic snaking. The liquid state (gray) coexist with TLS. The patches of TLS (I)-(III) grow by adding density peaks and terminate on the periodic pattern (IV) once the entire domain is filled. Labels (I)-(IV) indicate the loci of the selected density profiles. The bottom right panel depicts the drift velocity  $c$  as a function of  $\bar{\psi}$ .  $\bar{\psi}$  only has a small influence on the velocity of the TLS. The drift velocity of the crystal (dark red) is nearly independent of  $\bar{\psi}$ . Domain size and remaining parameters as in Fig. 5.14.

large enough to allow for TLS. Still, it is not beyond the folds of RLS, i.e. small enough to keep branches of (unstable) RLS in existence. The overall picture is similar to the slanted homoclinic snaking found for passive LS. The branches of LS bifurcate from periodic solutions that emerge in primary bifurcations from the destabilized liquid state. Besides the resting crystal (Fig. 5.14, dotted black branch), there is a branch of traveling spatially extended patterns (red). Both crystals are of hexagonal order and their norms only slightly differ. The inset in Fig. 5.14 enlarges a part of the branches close to the fold, illustrating their small separation.

In a secondary bifurcation, the resting and traveling LS branch off from the resting and traveling periodic solutions, respectively. Since activity is beyond the threshold for migration, all RLS (blue branch) are unstable as indicated by dotted lines. The TLS exhibit the typical alternation of stable and unstable states. Just like the branches of periodic solutions and since  $v_0 \approx v_c$ , resting and traveling solutions are not largely separated in terms of the  $L^2$ -norm.

The lower panel of Fig. 5.14 visualizes the drift velocity  $c$  of the respective solutions as a function of  $\bar{\psi}$ . Evidently, RLS (blue) and the resting crystal (black) have  $c = 0$ . The velocity of the traveling crystal (red) rises slightly as the crystal grows. In contrast to the main panel, here it is easy to see how the TLS branch off from the traveling periodic solution. All in all, the drift velocity  $c$  does not strongly depend on  $\bar{\psi}$ .

The same holds at  $v_0 = 0.18$  as shown in Fig. 5.15. The bottom right panel reveals that  $c$  does nearly not depend on the mean density  $\bar{\psi}$ . Because  $v_0 = 0.18$  is beyond the positions of the folds of RLS, resting solutions have disappeared. As also observed at smaller  $v_0$ , the TLS (orange) emerge in a secondary bifurcation from the branch of the traveling crystal (red). For increasing  $\bar{\psi}$ , the TLS enlarge by adding density peaks and, ultimately, the whole domain is filled by crystalline structure. Here, the branch of LS terminates on the branch of the periodic solution (cf. Fig 5.15(IV)). In contrast to the passive snaking, the growth of the LS does not happen by adding layers of density peaks. The broken symmetry at  $v_0 > v_c$  seems to favor a growth by single density peaks as panels (I) and (II) show. The different growth is reflected by more undulations of the snaking branch as compared to the passive snaking in Fig. 5.2.

Overall, we can state that, first, the mean density  $\bar{\psi}$  does not have a strong influence on the drift velocity  $c$ . Second, the bifurcation structure of TLS as a function of  $\bar{\psi}$  is different for LS (2d) at  $\epsilon = -0.98$  as compared to LS (1d) at  $\epsilon = -1.5$  (cf. Fig. 4.3 and following). At  $\epsilon = -1.5$ , there is no continuously snaking branch of TLS starting and terminating on the branch of traveling crystals. Branches of one-dimensional TLS at  $\epsilon = -1.5$  are rather branching off from RLS, while at  $\epsilon = -0.98$ , there is no connection between the branches of RLS (of hexagonal order) and TLS (also hexagonal patches) when varying  $\bar{\psi}$ . Hence, changes in the mean density cannot directly induce drift instabilities (although a suitable  $\bar{\psi}$  is necessary for drift instabilities to occur when varying  $v_0$ ). And rather unexpected (when taking 1d results as a guide), the branch of TLS at  $\epsilon = -0.98$  exhibits slanted homoclinic snaking as observed for RLS in the passive system and in active ones at small  $v_0$ . We do not expect the spatial dimensions to play a role, here. Most likely, this is an effect solely due to the effective temperature  $\epsilon$ .

### 5.3 Periodic States

In two spatial dimensions, different periodic patterns can be distinguished. Besides stripes that can be regarded as the two-dimensional extension of the periodic states determined in 1d (Sec. 4.2), the aPFC model exhibits hexagonal patterns and also rhombic structures. In this chapter, we analyze periodic states that emerge in the two-dimensional aPFC model and, in particular, study their bifurcation structure.

#### 5.3.1 Crystal structure and activity $v_0$

The original passive PFC model exhibits crystalline hexagonal patterns in certain ranges of temperature  $\epsilon$  and mean density  $\bar{\psi}$ . Changing the mean density can lead to transitions to stripes [TAR<sup>+</sup>13]. These transitions can also be induced by the activity  $v_0$ . In the original paper [ML13] introducing the aPFC model, numerical time simulations show with increasing  $v_0$  a transition from a resting hexagonal pattern to traveling hexagons. A further increase leads to a transition to traveling rhombic patterns and, ultimately, to traveling stripes. Snapshots from time simulations at certain values of  $v_0$  and the same set of control parameters as in [ML13] are shown in Fig. 5.16. They reproduce previously made observations.

The domain is of size  $6L_c \times 5L_a$  with critical wavelength  $L_c = 2\pi$  and side length  $L_a = 4\pi/\sqrt{3}$  of emerging hexagons accounting for 30 density peaks in hexagonal order. At  $v_0 = 0$ , resting hexagons are orientated parallel to the  $y$ -axis and perfectly match the aspect ratio of  $L_x$  and  $L_y$ . As  $v_0$  is increased the wave vector and geometry of the formed pattern change. The whole crystalline pattern reacts by a rotation in the periodic domain (cf. Fig. 5.16(a),(b)). Due to the periodic boundaries, in this way it can adjust its position such that dominant wave vectors fit into the domain.

Rhombic (Fig. 5.16(c)) and stripe patterns (d) orient themselves parallel to the  $y$ -axis as  $L_x$  is a multiple of  $L_c = 2\pi$ . Following the drift-instability at  $v_c \approx 0.3$ , these patterns travel with a constant speed  $c$  while keeping their spatial periodicity. White arrows indicate the direction of motion. Stripes always travel perpendicular to their orientation. Also hexagons and rhombuses show distinct directions of motion. Therefore, the patterns have to be correctly orientated when employing numerical continuation with the particular boundary conditions discussed in Sec. 5.1.2. The boundary conditions only allow for motion in  $x$ -direction.

#### 5.3.2 Pattern selection and bifurcation structure

From time simulations in previous studies [ML13, MOL14], it is known that the activity parameter  $v_0$  does not only lead to a transition from resting to traveling patterns, but also strongly influences the crystal structure. Next, we use numerical continuation to investigate if the different patterns are connected via bifurcations and how patterns are selected.

Starting with the steady state solution of a resting hexagonal pattern at  $v_0 = 0$  in a suitable domain, we follow the branch of hexagonal crystals in  $v_0$ . Figure 5.17(I) illustrates the chosen domain. Its aspect ratio corresponds to the ratio between the height  $L_c$  and the side length  $L_a$  of the equilateral triangles within in the hexagon. The hexagons are orientated with one edge parallel to the direction of motion observed in time simulations close to the onset of motion (cf. Fig. 5.16). Due to the employed boundary conditions (see Sec. 5.1.2 for details) only motion along the  $x$ -axis is possible.

The resulting bifurcation diagram is depicted in the main panel of Fig. 5.17. The branch



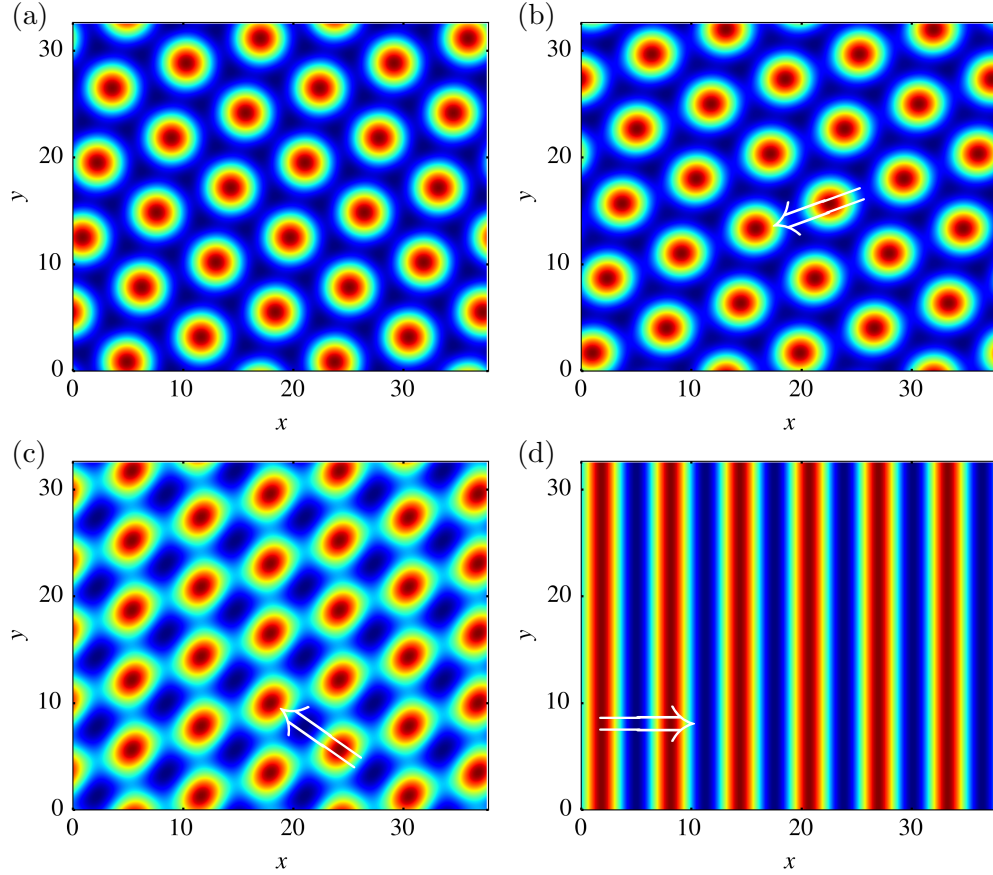


Figure 5.16: Snapshots of periodic density patterns  $\psi(\mathbf{r})$  for increasing activity  $v_0$  from numerical time simulations. From (a) to (d) values of  $v_0$  are (0.25, 0.3, 0.8, 1.5). Domain size:  $6L_c \times 5L_a$  with critical wavelength  $L_c = 2\pi$  and side length  $L_a$ . Simulations reproduce the previous observation [ML13] of a transition from (a) resting hexagonal crystals to (b) traveling hexagons. For higher activities the pattern consists of (c) traveling rhombic cells and, eventually, (d) traveling stripes. The respective direction of motion is indicated by white arrows. Remaining parameters are  $\bar{\psi} = -0.4$ ,  $\epsilon = -0.98$ ,  $C_1 = 0.2$ ,  $C_2 = 0$  as employed in Ref. [ML13].

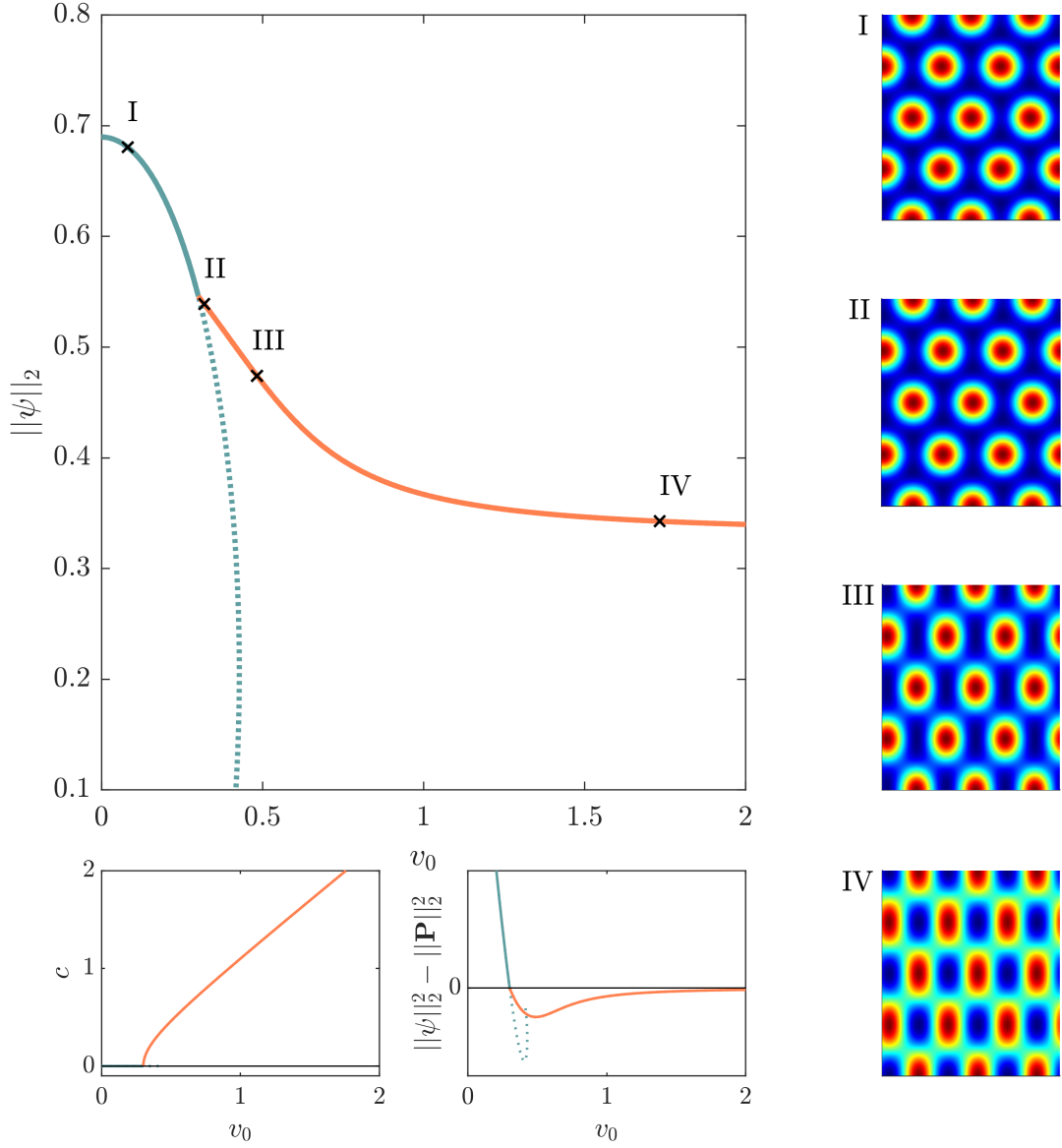


Figure 5.17: Hexagonal patterns in the 2d aPFC model. Main panel: bifurcation diagram showing the  $L^2$ -norm of  $\psi$  as a function of  $v_0$ . Resting hexagons (blue branch) are stable (solid line) until a drift-instability occurs at  $v_c \approx 0.3$ . A branch of stable moving hexagons (orange) bifurcates. Its drift velocity  $c$  is given in the lower left panel. The lower right panel shows that  $\|\psi\|_2^2 - \|\mathbf{P}\|_2^2$  crosses zero at the drift bifurcation. On the right: Selected solution profiles  $\psi(\mathbf{r})$  at loci labeled (I-IV). Profiles (II-IV) move to the right. Domain size:  $V = 3L_a \times 4L_c$ . Parameters as in Fig. 5.16.

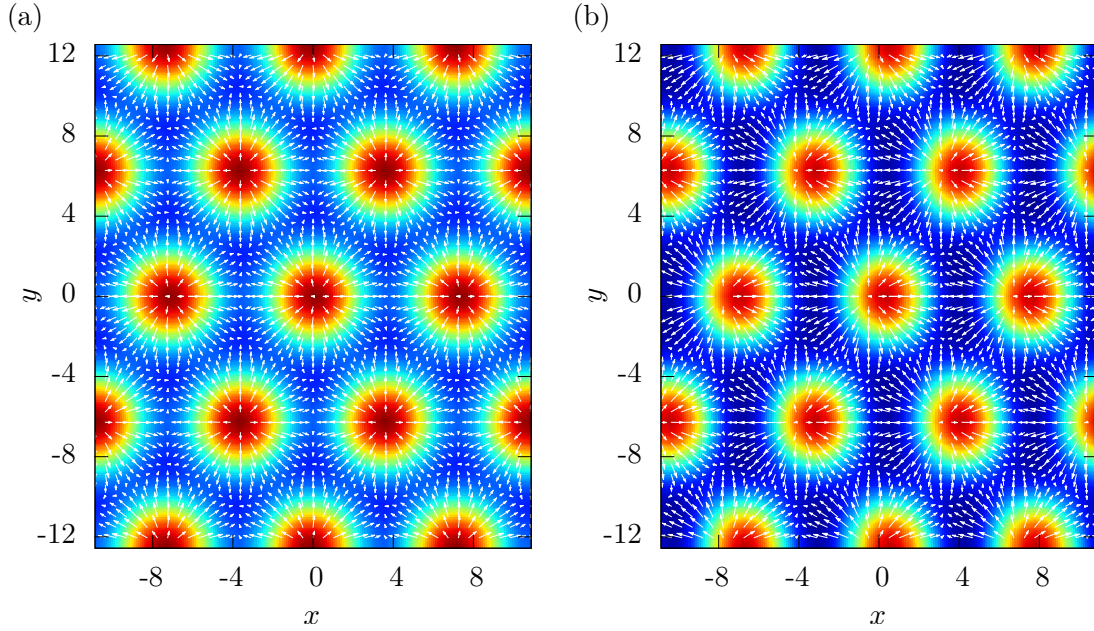


Figure 5.18: Detailed view of density field  $\psi(\mathbf{r})$  (color coded) and polarization  $\mathbf{P}(\mathbf{r})$  as white arrows. (a) depicts a hexagonal crystal at rest ( $v_0 = 0.25$ ). The density peaks coincide with the +1 defects of the polarization field. Averaging  $\mathbf{P}$  over single peaks shows zero net polarization. (b) depicts a traveling crystal at higher activity ( $v_0 = 0.4 > v_c$ ). Peak maximums and locations of the +1 defects of  $\mathbf{P}$  are shifted w.r.t. each other breaking the symmetry of (a). The shift induces a net polarization to the right. This leads to a net propulsion and the crystal travels to the right with  $c \approx 0.3$ . Parameters and domain size as in Fig. 5.17.

of resting hexagons is given in blue, whereas the traveling hexagonal pattern corresponds to the orange branch. At a critical activity of  $v_c \approx 0.3$ , the resting pattern is destabilized in a drift-pitchfork bifurcation. The left bottom panel shows the characteristic growth of the drift velocity  $c$ . Close to the drift instability it is  $c \propto \sqrt{v_0 - v_c}$ . The resting state is unstable for  $v_0 > v_c$  and eventually decays to the uniform liquid phase. The second small panel depicts how the criterion  $\|\psi\|_2^2 - \|\mathbf{P}\|_2^2$  crosses zero at the onset of motion. Note that the onset of motion at  $v_c \approx 0.3$  corrects earlier studies [ML13] and confirms the critical activity found in [PVWL18].

Four selected solution profiles  $\psi(\mathbf{r})$  (I)-(IV) correspond to loci marked in the main panel. The density profiles illustrate how the hexagonal order of the crystal is preserved for increasing  $v_0$ . However, the individual density peaks change their shape from circular bumps towards oval and even rectangular peaks, cf. Fig. 5.17 (III) and (IV). The branch of traveling hexagons is stable up to very high values of activity, in other words, we did not detect a destabilizing bifurcation on the branch.

Figure 5.18 gives details on the symmetry breaking associated with the onset of motion of the hexagonal pattern. The density field  $\psi(\mathbf{r})$  is given as a color map and the polarization field  $\mathbf{P}(\mathbf{r})$  is indicated by white arrows. (a) depicts the two fields for a resting crystal. As

discussed for LS in Sec. 5.2.2 for resting states, centers of density peaks coincide with  $+1$  defects of  $\mathbf{P}$ . One of the corresponding symmetries is broken beyond the onset of motion. The topological defects of  $\mathbf{P}$  are shifted w.r.t to the peaks of  $\psi$ . Hence, when averaging the polarization over a density peak, a net polarization and drift emerge. Figure 5.18(b) shows a moving hexagonal crystal with a positive net polarization. In the red area of the maximum of  $\psi$ , more arrows point to the right than to the left and, thus, the crystal moves to the right as an entity.

For the next bifurcation diagram Fig. 5.19, the orientation of the hexagon is rotated by  $90^\circ$ , i.e., the drift is forced to occur perpendicular to the an edge of the hexagon. The domain size is adapted to match the hexagons by switching the lengths of  $L_x$  and  $L_y$  from Fig. 5.17. As in Fig. 5.17, the resting hexagonal pattern (blue branch) is destabilized in a drift-pitchfork bifurcation. The exact value reads  $v_{c,\perp} = 0.3015$  as compared to  $v_{c,\parallel} = 0.3008$  in Fig. 5.17. The slightly larger threshold is in agreement with results from time simulations where the drift parallel to an edge (cf. Fig. 5.17) is found for motion at the onset. Black circles highlight drift bifurcations in the main panel of Fig. 5.19. Besides stable resting hexagons, an unstable resting stripe pattern exists in this setup (red branch). The resting stripes undergo a drift bifurcation at  $v_c \approx 0.3$ , too.

In contrast to traveling hexagons moving parallel to an edge (Fig. 5.17), here, traveling hexagons do not exist at arbitrarily high  $v_0$ . To be specific, the branch terminates on the branch of travelling stripes (horizontal orange line) in a supercritical pitchfork bifurcation and does not continue towards arbitrarily high  $v_0$  as in Fig. 5.17. Even before reaching it, the branch loses stability at about  $v_0 = 0.6$ . Along this branch, the crystal continuously changes from traveling deformed hexagons (Fig. 5.19(II)) to traveling modulated stripes (III). The horizontal branch of moving stripes confirms results for periodic states in one spatial dimension that also keep a constant norm just shifting the relative positions between  $\psi(x)$  and  $P(x)$  for changing  $v_0$  (cf. Fig. 4.1). Eventually, the traveling stripes gain stability at about  $v_0 = 1.5$  after undergoing various bifurcations (not shown). At  $v_0 = 1.5$ , random initial conditions evolve into drifting stripes in numerical time stepping. Note that vertical stripes do not fit into the domain of Fig. 5.17 as  $L_x$  is not a multiple of  $L_c = 2\pi$ .

Even though, time simulations show a different direction at the onset of motion of the traveling hexagons, the detected branch of modulated stripes (Fig. 5.19(III)) corresponds to a solution type that arises within large scale parameter scans presented in Sec. 5.3.3. In addition, continuation confirms that resting stripes are unstable for all values of  $v_0$  as time simulations suggested. Since time simulations also point to rhombic patterns, we additionally exploit a square domain. Fig. 5.20 illustrates how the branch of moving squares (orange) becomes stable at about  $v_0 \approx 0.7$  – again in perfect agreement with traveling squares observed in time simulations (cf. Fig. 5.16 (c)). Traveling squares branch off from the unstable resting states and after a fold extend to higher values of  $v_0$ . Again, the utilized domain favors the investigated pattern and allows for stable traveling squares at seemingly arbitrarily high activity.

Finally, Fig. 5.21 combines the results from continuation runs on different domains. Around practically identical values about  $v_c = 0.3$ , all resting crystals undergo drift instabilities. As for the resting states at small  $v_0$ , only hexagons (blue branch) are stable (solid line). Traveling squares and traveling stripes gain stability at higher values of  $v_0$  that are in perfect agreement with numerical time simulations. Numerical continuation suggests that different traveling crystals coexist and the considered domain and its aspect ratio seems to select the moving pattern.

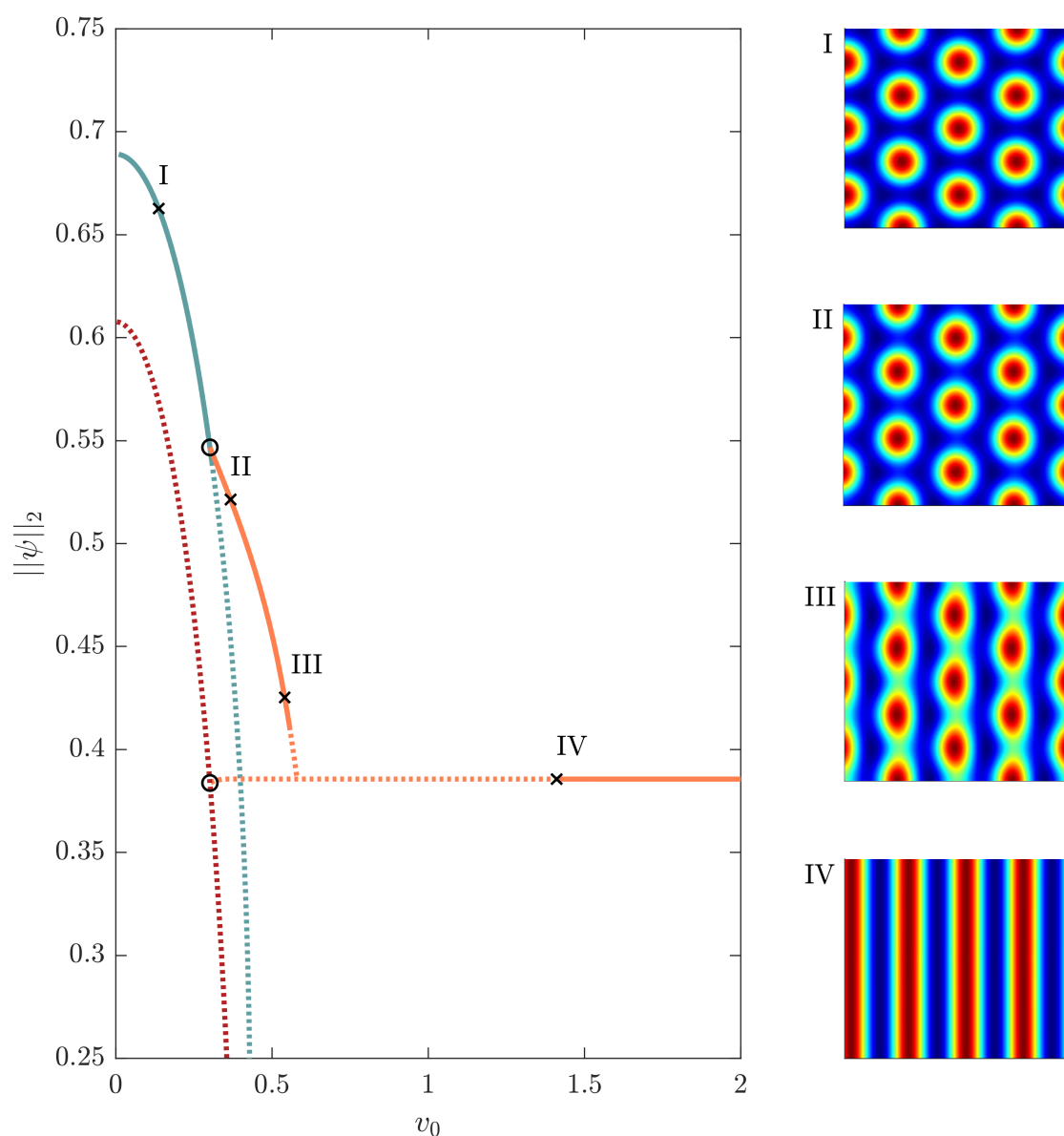


Figure 5.19: Onset of motion perpendicular to edge and continuous deformation of hexagonal patterns. Main panel: bifurcation diagram showing the norm of  $\psi$  as a function of  $v_0$ . The blue (red) branch corresponds to resting hexagons (stripes), cf. panel I (IV). At about  $v_0 \approx 0.3$  the resting hexagonal pattern starts to migrate perpendicular to an edge. Black circles indicate drift-pitchfork bifurcations and orange branches denote patterns in motion. The moving hexagonal pattern (II) is deformed towards modulated stripes as  $v_0$  is increased, cf. panel (III). The horizontal branch corresponds to moving stripes as shown in (IV). Velocities point in  $x$ -direction. On the right: Selected solution profiles  $\psi(\mathbf{r})$  at loci labeled (I)-(IV). Profiles (II)-(IV) move to the right. Domain size:  $4L_c \times 3L_a$ . Parameters as in Fig. 5.16.

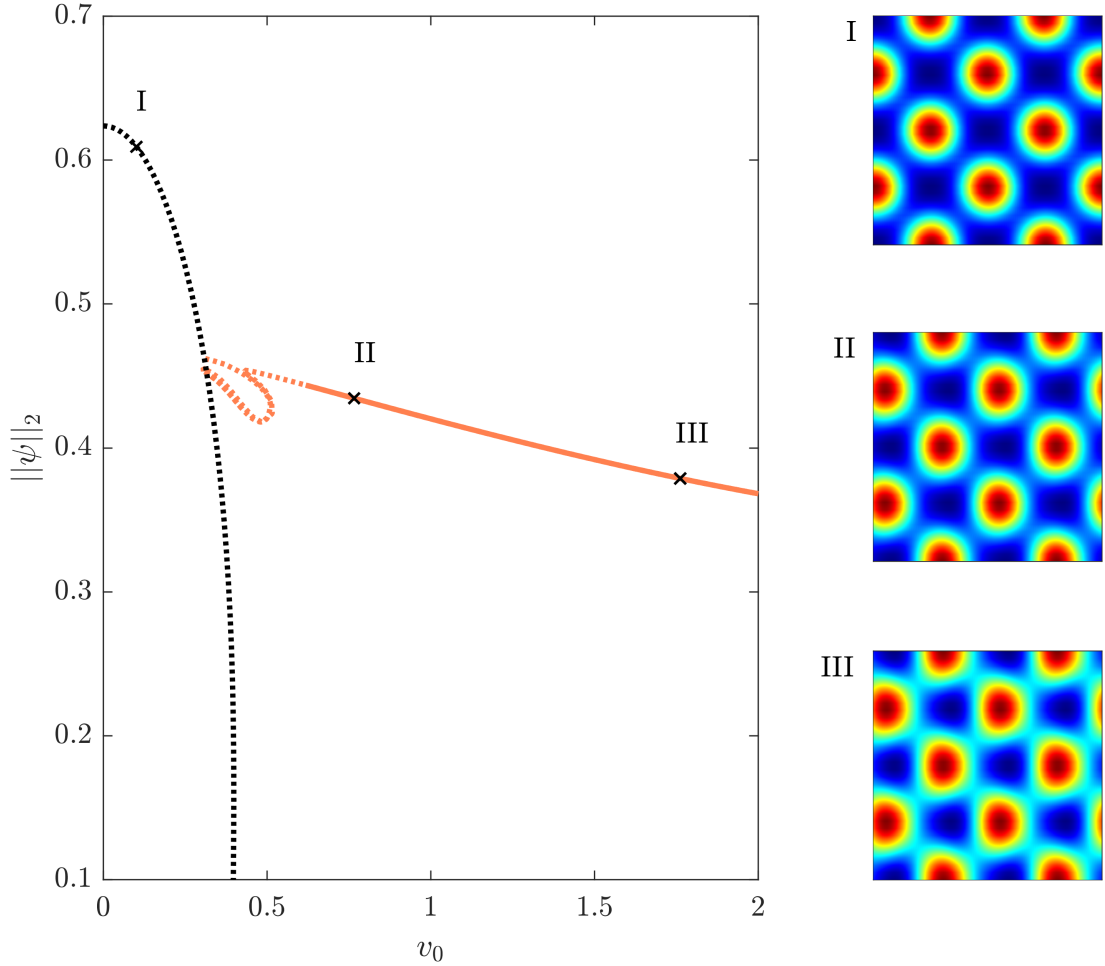


Figure 5.20: Square patterns in the 2d aPFC model. Main panel: bifurcation diagram showing the norm of  $\psi$  as a function of  $v_0$ . Black (orange) branches correspond to resting (traveling) squares with solid (dotted) lines indicating (un)stable solutions. For the employed parameter set (same as in Fig. 5.16), resting squares are unstable. After the branch of moving squares undergoes a series of folds, traveling squares gain stability at  $v_0 \approx 0.7$ . They seem to exist at arbitrarily high activities. For increasing  $v_0$ , the crystal keeps its rhombic order. However, the circular shape of individual density peaks changes. On the right: Selected solution profiles  $\psi(\mathbf{r})$  at loci labeled (I)-(IV). Domain size:  $2\sqrt{2}L_c \times 2\sqrt{2}L_c$ , where  $L_c = 2\pi$  is the side length of a square and  $\sqrt{2}L_c$  its diagonal.

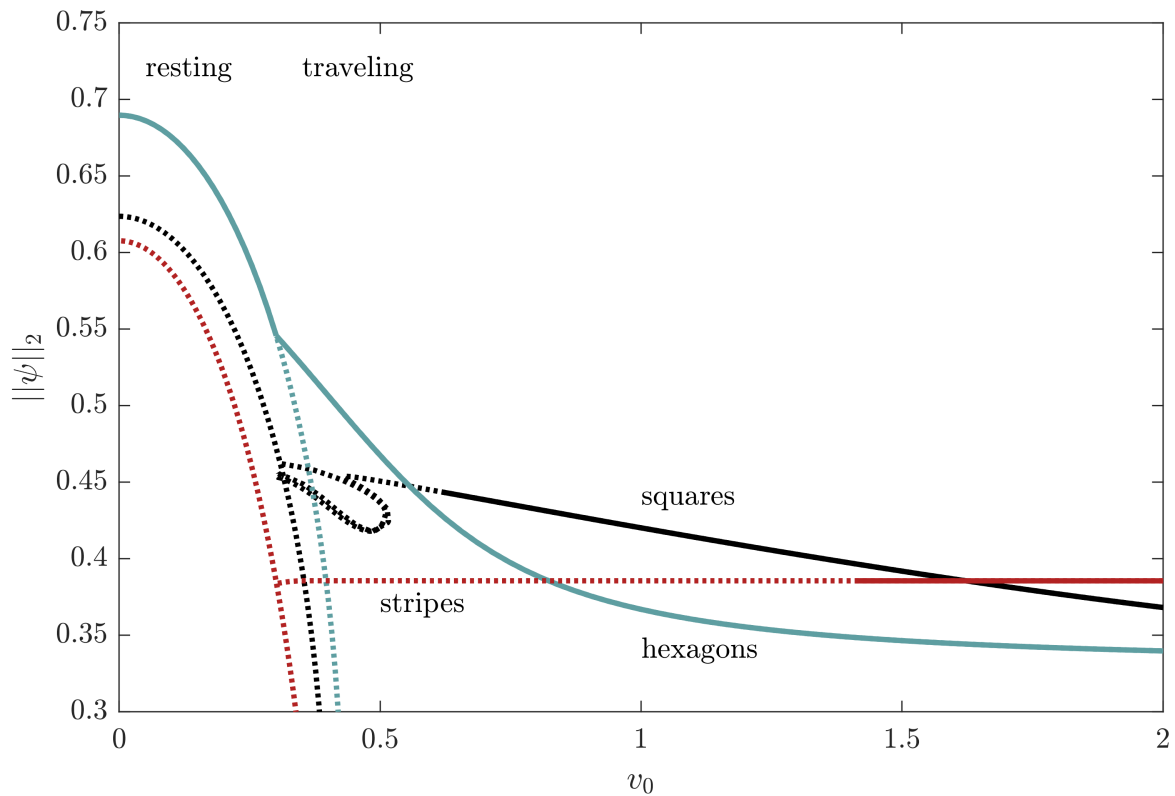


Figure 5.21: Combined bifurcation diagrams of resting and traveling periodic states showing the  $L^2$ -norms of  $\psi$  as a function of  $v_0$ . Blue branches correspond to hexagons, black branches to squares and red branches to stripes. Solid (dotted) lines indicate (un)stable solutions. Domain sizes and aspect ratios vary for the different branches. At practically identical values of  $v_c \approx 0.3$  all resting crystals undergo drift instabilities. Different traveling states coexist at large activities. The aspect ratio of the employed domain selects the shape of the crystal and determines its stability. Parameters as in Fig. 5.16.

### 5.3.3 Morphological phase diagram

In order to complete the picture of crystalline states and the influences of  $v_0$  and  $\bar{\psi}$ , we again perform numerous time simulations and construct a morphological phase diagram in the  $(v_0, \bar{\psi})$ -plane for the parameter set employed in this section. The time simulations are carried out in the same way as previously described in Sec. 5.2.3 and again LS and various periodic states are distinguished in terms of the number of peaks of  $\psi(\mathbf{r})$ . The resulting phase diagram is shown in the main panel of Fig. 5.22.

The used parameter set from Ref. [ML13] includes a high diffusion of  $C_1 = 0.2$  – twice the value we used in the 1d analysis and in Sec. 5.2.2. The high diffusion leads to, first, a higher  $v_c \approx 0.3$  (cf. vertical dotted line) and, second, suppresses the existence of LS for increasing activity (no blue areas for  $v_0 > 0.5$ ). The green crystalline area exhibits density fields with more than 56 peaks for high activities. Here, solution profiles show traveling rhombic patterns (Fig. 5.22(II)) with smaller wavelength as the hexagonal states. Thus, more peaks fit into the considered domain. Approaching higher mean densities towards  $\bar{\psi} = -0.4$  the rhombic patterns transform into stripe patterns. However, the stripes are still sufficiently modulated to account for a high number of peaks as Fig. 5.22(III) depicts. Accordingly, the number of counted density peaks does not decrease.

Figure 5.22 gives a detailed overview of arising active crystals and crystallites for the parameter set from [ML13]. It also evidences a neat interplay of numerical continuation and time simulations as results from fold continuation (black lines) nicely border the area of existence of LS.



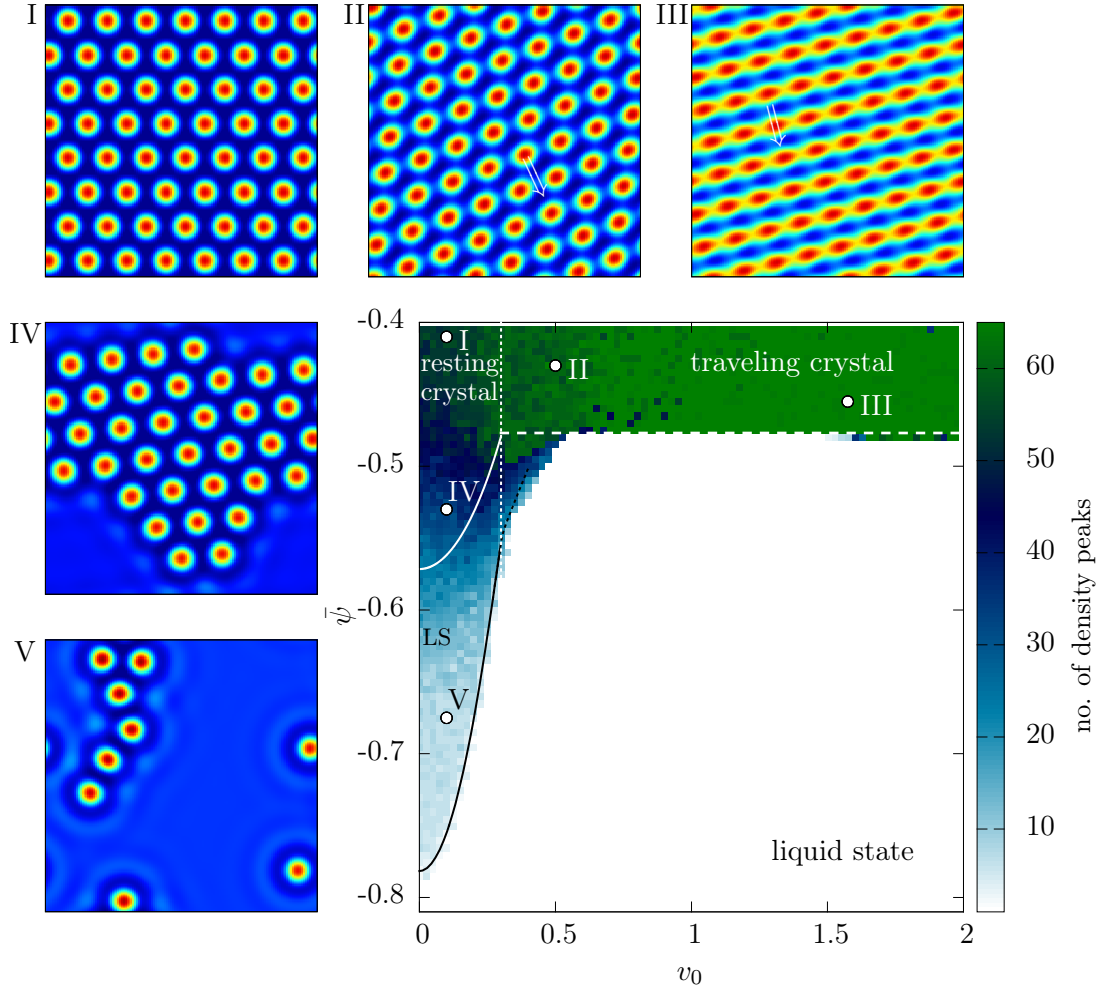


Figure 5.22: Morphological phase diagram for the aPFC model accompanied by selected density profiles at loci labeled (I)-(V). Large panel: Different states are characterized by the total number of density peaks formed in the domain. The rectangular domain is of size  $7L_a \times 8L_c$ . White lines give limits of the linear stability of the liquid state. Black lines from fold continuation border the existence of resting one-peak LS (solid) and traveling one-peak LS (dotted, terminated where it folds back). The vertical white line marks the onset of motion. Color coding and density peaks from time simulations. The liquid state refers to a uniform density phase with zero peaks (white area). LS exist in the regions marked in blue. Periodic hexagonal patterns (green) fill the domain with  $7 \cdot 8 = 56$  density peaks (I). Around  $v_0 > 1$  the number of peaks slightly increases as resting hexagonal patterns (I) are transforming towards traveling rhombic patterns (II) with a smaller wavelength allowing for more density peaks. Arrows indicate the direction of motion. At even higher  $v_0$ , traveling stripe patterns (III) arise. They are modulated such that individual peaks can still be found on each ridge and the number of density peaks does not drop. (IV) and (V) give examples of resting LS coexisting with the liquid phase. Remaining parameters are  $\epsilon = -0.98$ ,  $C_1 = 0.2$ ,  $C_2 = 0$  and  $D_r = 0.5$  as in [ML13].



## 6 Interaction of Active Crystallites

A helpful and common interpretation of a spatially extended pattern is to regard it as a superposition of spatially localized units, commonly referred to as *particles*. Particles do interact when they reach a certain distance and encounter each other. Having obtained an extensive description of individual localized states in terms of their bifurcation structure and existence regions in parameter space, we next explore the interaction between two and more localized states.

### 6.1 Collision experiments

A simple way to determine how particles interact is to study collision kinematics. As a first step, we will examine two colliding one-peak LS in one spatial dimension. Due to the periodic boundaries of the considered domain, collisions will repeatedly occur. By studying the outcome of collisions, we can distinguish different types of interaction between traveling crystallites that approach one another. As before, main control parameters to be varied between the individual simulations are the activity  $v_0$  setting mainly the velocity of the colliding crystallites and the mean density  $\bar{\psi}$ .<sup>1</sup>

#### 6.1.1 Two colliding crystallites

We place two identical traveling one-peak LS with opposite drift velocities on a one dimensional domain of length  $L$  and integrate this setup (cf. Fig. 6.1) forward in time. During each of these numerical scattering experiments, all parameters, especially  $v_0$  that determines the velocity of the collision partners, remain constant. The domain has periodic boundaries and, hence, collisions occur repeatedly. If the colliding LS are regularly spaced,  $L/2$  equals the free path  $\lambda$  between two collisions.

A generic type of interaction between two bodies is an elastic collision. In a perfectly elastic collision, the kinetic energy is conserved and there is no net conversion into other forms of energy. Two bodies encounter each other and are reflected.

Figure 6.2 illustrates an elastic collision process between two LS by a number of snapshots from time simulations. The density peaks approach each other with steady velocities ( $t < 40$ ), seem to merge for a moment into a single resting peak when clashing ( $t = 55$ ) and are eventually reflected by the collision partner ( $t > 60$ ). Their velocity has switched sign, but keeps its magnitude. The inclination of the trajectories of the two LS in the space-time plot (Fig. 6.3(a)) reveals that the LS are not slowed down by the collision. Also their density profile regains its original shape prior to the collision ( $t > 90$ ). As long as the colliding crystallites have enough space to recover from the previous collision before the next one

---

<sup>1</sup>Please note, that Johannes Kirchner did similar studies on the scattering behavior of active LS in the aPFC model for his Master's thesis in 2017 [Kir17]. Minor parts here may seem to overlap with results he obtained. In fact, the time steps used there in the simulation of collisions proved to be too large and the present results provide a correction.

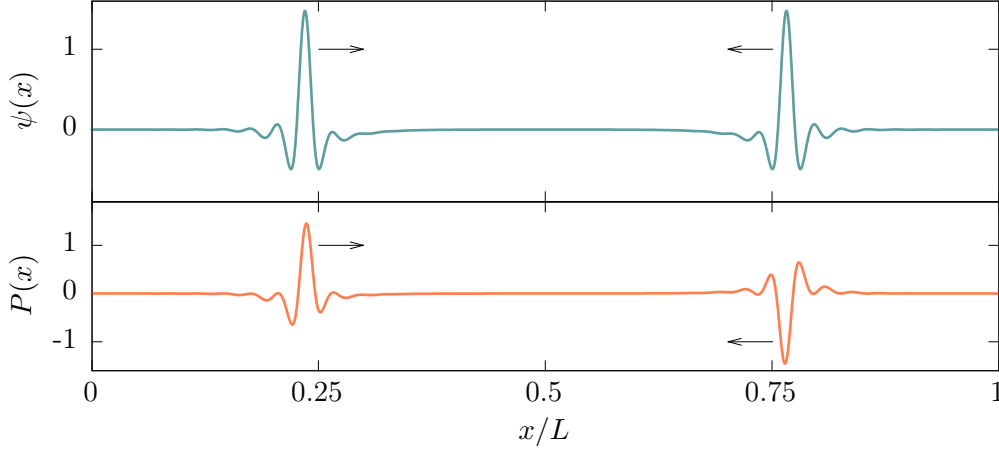


Figure 6.1: Setup of scattering experiments. Two traveling one-peak LS with opposite drift velocities are placed on a domain of size  $L$ , here  $L = 200$ . The two initial LS correspond to the same solution family of the stable traveling one-peak LS (cf. Sec. 4.3.1). The two collision partners only differ in the sign of their polarization  $P$  and, hence, the sign of their drift velocity  $c$ . Arrows indicate the direction of motion. The domain has periodic boundary conditions leading to a regular repetition of fully elastic collisions with a free path of  $\lambda = L/2$  between two collisions.

(periodic BC), the number of collision partners is conserved. The recovery time corresponds to a critical free path that needs to be exceeded (see Sec. 6.1.3 for details).

The main control parameters  $v_0$  and  $\bar{\psi}$  strongly influence the outcome of a collision. Figure 6.3 shows space-time plots of four different examples. In Fig. 6.3(a), the spatial density profile of two elastically colliding LS as depicted in Fig. 6.2 is plotted versus time  $t$ . Note that  $t$  increases downwards. Figure 6.3(b) demonstrates an inelastic collision where the reflected crystallites fade away. As compared to the elastic collision, the mean density is slightly lower, going from (a)  $\bar{\psi} = -0.7$  to (b)  $\bar{\psi} = -0.75$ . At the lower mean density (b), the perturbation by the collisions is large enough to leave the basin of attraction of the stable traveling one-peak LS and the traveling crystallites decay towards the uniform liquid state  $\psi = 0$  that is also linearly stable in this parameter region.

The collision outcomes drastically change when the velocity of the LS is lowered by decreasing the activity  $v_0$  from 0.5 in Figs. 6.3(a) and (b) to values close to the onset of motion at  $v_c \approx 0.16$ . The low velocities of the collision partners lead to merging and oscillating crystallites. In (c) ( $v_0 = 0.2$ ), the colliding LS do not scatter, but rather come to rest for an extended period of time ( $250 < t < 500$ ) and eventually start drifting as a single LS. In a transient phase ( $500 < t < 800$ ) before merging into a single density peak, we observe one of the oscillatory state described in Sec. 4.5.2. In particular, it shows two density peaks where group velocity and drift velocity differ and  $c = v_{\text{group}} < v_{\text{phase}}$ . The parameters are consistent with the area of existence of oscillating states in Fig. 4.17. The velocity of the ultimately evolving single LS is the same as of the initial collision partners.

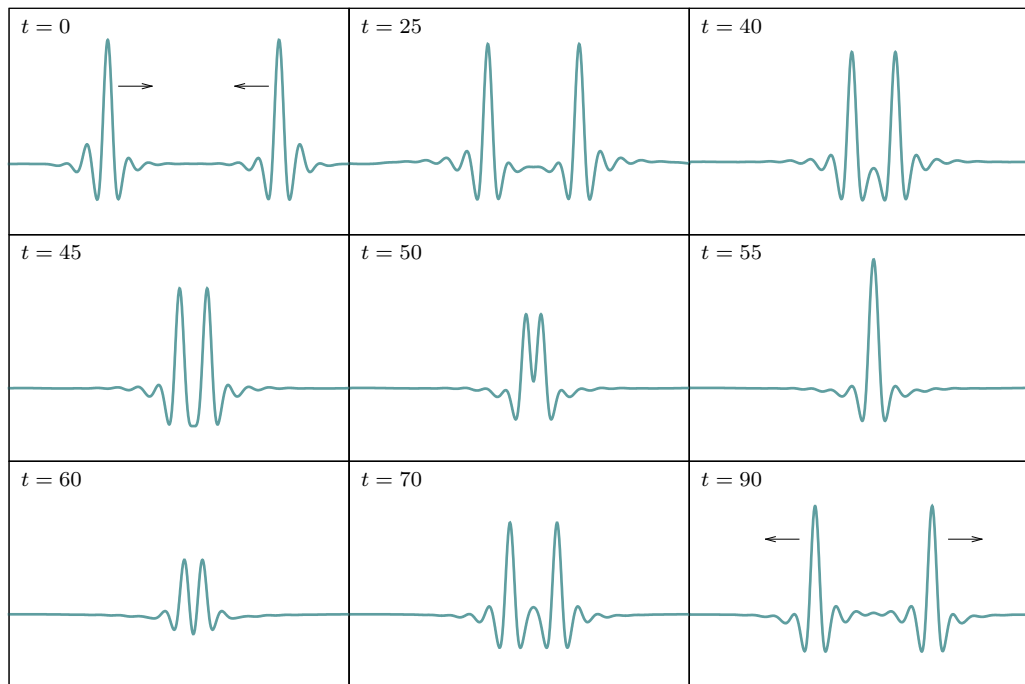


Figure 6.2: Snapshots taken at different times  $t$  of the density profile  $\psi(x)$  of two colliding one-peak LS with opposite velocities. Arrows indicate the direction of motion. The peaks approach each other with a steady velocity. The impact at  $t = 55$  is followed by a reflection of the LS. The LS completely recover from the collision and regain their original height of  $\psi$ . A space-time plot of this collision is given in Fig. 6.3(a). Parameters:  $v_0 = 0.5$ ,  $\bar{\psi} = -0.7$  and  $\epsilon = 1.5$ ,  $C_1 = 0.1$ ,  $C_2 = 0$ ,  $D_r = 0.5$ .

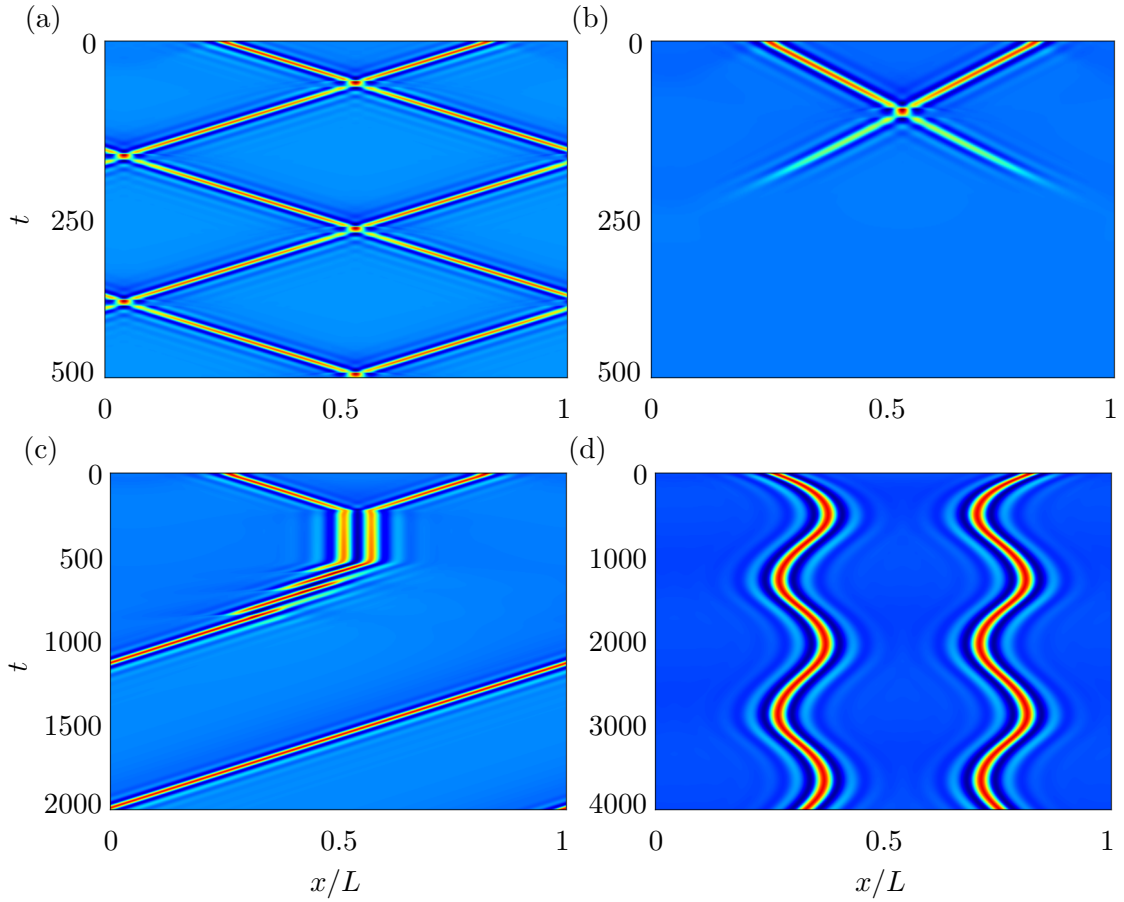


Figure 6.3: Space-time plots of the density field  $\psi(x)$  (color coded) of two colliding one-peak LS. Time increases from top to bottom. (a)  $v_0 = 0.5$ ,  $\bar{\psi} = -0.7$ . Elastic collisions occur repeatedly due to periodic boundaries. The drifting crystallites are reflected after the impact. They keep a steady velocity and have enough space to recover between collisions. Directly after a collision, their amplitude in  $\psi$  is significantly decreased. (b)  $v_0 = 0.5$ ,  $\bar{\psi} = -0.75$ . At lower mean densities, the perturbation by the collision is large enough to detach the stable one-peak LS from their basin of attraction resulting in a decay towards the uniform liquid state  $\psi = 0$ . (c)  $v_0 = 0.2$ ,  $\bar{\psi} = -0.75$ . At lower activities and lower corresponding drift velocities, the LS do not scatter. They come to a halt ( $250 < t < 500$ ) before starting to drift with an oscillation ( $500 < t < 800$ ). Eventually, one of the two density peaks fades away and a single density peaks evolves traveling as fast as prior to the collision ( $t > 800$ ). (d)  $v_0 = 0.163$ ,  $\bar{\psi} = -0.71$ . At even lower activity, the LS drift back and forth, seemingly attracting and repelling each other. Collisions do not occur. Domain size:  $L = 100$ . Remaining parameters as in Fig. 6.2.

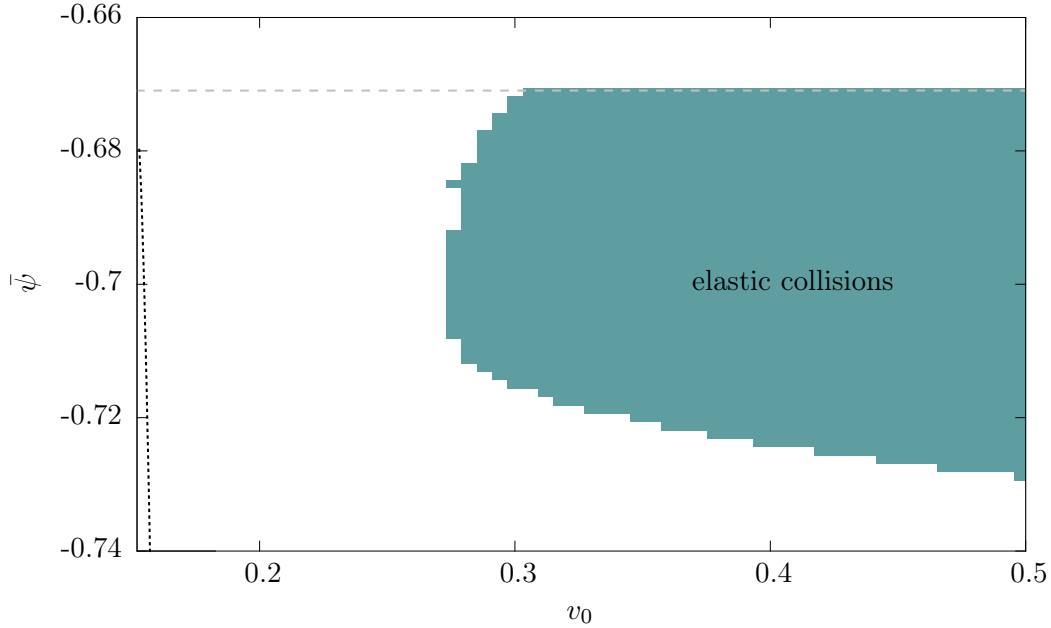


Figure 6.4: Parameter map of elastic collisions (colored area) as a function of activity  $v_0$  and mean density  $\bar{\psi}$  for a free path of  $\lambda = L/2 = 100$  with domain size  $L$ . Within the green area, elastic collisions take place. The white area marks parameter values at which collisions are inelastic and the number of colliding LS is not conserved. The horizontal dashed line at the top marks the limit of the linear stability of the background uniform state the drifting LS are embedded in. The nearly vertical dotted line denotes the onset of motion of one-peak LS and the lower bound of existence of TLS. Increments between simulations:  $\Delta v_0 = 0.006$ ,  $\Delta \bar{\psi} = 0.00125$ . Remaining parameters as in Fig. 6.2.

In fact, it is the same solution.

As a last example of the rich outcome of collisions, Fig.6.3(d) presents two crystallites that oscillate back and forth. The activity is further lowered to  $v_0 = 0.163$  and the LS have no net drift velocity. They seem to attract and repel each other. In fact, no collision takes place but the LS avoid close contact.

### 6.1.2 Elastic collisions

Next, we explore larger parameter spaces of  $v_0$  and  $\bar{\psi}$  and determine where elastic collisions take place. Again we place two traveling one-peak LS equally spaced on a domain of size  $L$  resulting in a free path of  $L/2$  between collisions. For each set of  $(v_0, \bar{\psi})$ , time simulations are performed and finally a parameter map of the region where elastic collisions occur is created.

Figure 6.4 presents the result of such large scale time simulations for a one-dimensional domain of size  $L = 200$ . The greenish colored region marks where the collision partners are reflected when colliding and recover their original shape with opposite velocities. The horizontal dashed line marks the limit of the linear stability of the uniform state. At higher mean densities  $\bar{\psi}$  spatially modulated perturbations grow everywhere. The uniform

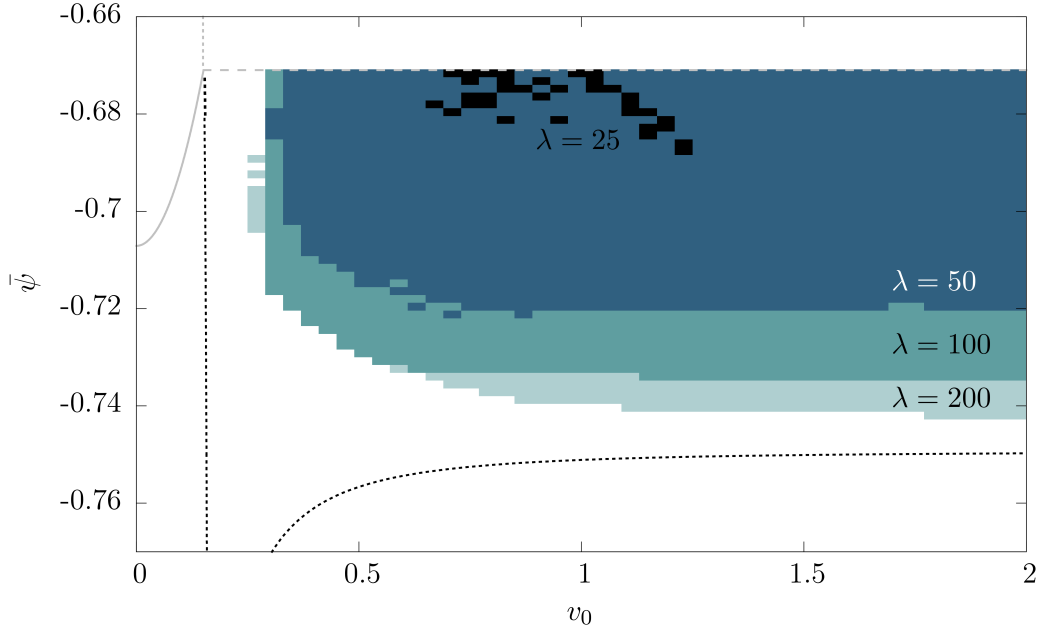


Figure 6.5: Parameter map of elastic collisions (colored areas) as a function of activity  $v_0$  and mean density  $\bar{\psi}$  with different free paths  $\lambda$  between collisions. In the colored areas, the number of colliding LS is conserved. The light gray lines mark the limits of the linear stability of the uniform phase that is surrounding the drifting LS. The dotted black lines limit the area of existence of traveling one-peak LS. They are obtained by two-parameter continuation. Colliding crystallites need a free path of about  $\lambda = 50$  to recover from the impacts. For smaller free paths, i.e., domain sizes, collisions are inelastic (white area) and the crystallites fade away. For  $\lambda = 25$  (black region) almost no elastic collisions occur anymore.

background state is unstable and patterns form. We do not perform time simulations for larger values of  $\bar{\psi}$ .

The nearly vertical dotted line in Fig. 6.4 marks the onset of motion of one-peak LS and, thus, the lower bound of existence of the collision partners. It was obtained by a two-parameter continuation of the drift-pitchfork bifurcation. Regarding the parameter map, we notice a rather sharp transition at  $v_0 \approx 0.28$  where fully elastic collisions set in. For values of  $v_0$  lower than this, the colliding crystallites spend too much time in the collision process and perturbations from it are too large to let them recover. Higher  $v_0$ , i.e., faster crystallites and less time during the actual impact are necessary for elastic collision and a conservation of the collision partners.

Second, mean densities need to exceed values of  $\bar{\psi} \approx -0.73$  for this type of scattering. The two-parameter continuations in Sec. 4.3.2 revealed that traveling LS exist up to higher values of activity  $v_0$  for increasing  $\bar{\psi}$ . We can observe this tendency here, too.

### 6.1.3 Free path and recovery

In order to complete our studies of elastic scattering, we examine the influence of the mean free path  $\lambda$ . By gradually dividing the domain size in half, we can determine a minimal mean



free path that the colliding crystallites need to recover from the perturbation of a collision. Starting from  $L = 400$  and two regularly spaced LS being equivalent to  $\lambda = 200$  we reduce the domain to  $L = 200$ ,  $L = 100$  and  $L = 50$ . Figure 6.5 reveals that for  $L = 50$  (small black area at the head of the figure) most of the region of elastically colliding LS has vanished. The gray-blue area marks the region in which the two colliding LS are preserved on  $L = 100$ , i.e.  $\lambda = 50$ . For a free path of  $\lambda = 100$  (greenish area) we restore the results from Fig. 6.4. For even larger domains ( $\lambda = 200$ , gray) the region grows only slightly towards lower  $\bar{\psi}$ . The relatively sharp boundary at  $v_0 \approx 0.3$  does only weakly depend on the size of the free path. Overall, a free path of about  $\lambda \geq 50$  seems necessary for elastic collisions and a conservation of the number of colliding bodies.

## 6.2 Gas of colliding crystallites

Based on our results for the elastic scattering of active crystallites we can construct a larger volume with a preserved number of colliding “particles“, that could be termed a “gas“ of crystallites. Figure 6.6 demonstrates that a minimal free path is crucial for the conservation of the LS. For a number of 12 equally spaced one-peak LS (Fig. 6.6(a),(b)) with alternating velocities, the domain  $L = 600$  provides sufficient space to recover from the impacts. A free path of  $\lambda = 50$  gives all peaks enough space to regain their original height and survive the consecutive collisions. Figure 6.6(b) enlarges a time range and shows the regular pattern of collisions and free paths in  $\psi(x)$  vs. time.

In Fig. 6.6(c),(d) the initial positions of the crystallites are randomly shifted from their regular spacing. The random spacing corresponds to the same average spacing above the critical  $\lambda$  but results in smaller distances between certain collisions. Accordingly, some of the LS cannot fully recover between consecutive collisions and decay into the uniform background. From 12 initialized LS only 4 survive the scattering. All of them travel in the same direction. Figure 6.6(d) zooms into the first half of the time range. LS that experience multiple clashes in short times have soon faded away.

This implies that the state of a stable gas is not possible as a mechanism for the creation of individual peaks out of the uniform background is missing.

## 6.3 Scattering behavior in 2d

As a closing section of this chapter, we give a brief outlook on the behavior in two spatial dimensions. The scattering behavior in 2d is not systematically examined, the presented simulations shall rather serve as a starting point for future studies.

Nonetheless, the snapshots shown in Fig. 6.7 provide interesting insights into the scattering behavior of LS that travel on a surface. The experiment is initialized with six randomly placed one-peak LS that drift with a steady velocity  $c \approx 0.15$  according to an activity of  $v_0 = 0.2$ . The number of colliding crystallites is conserved, but in contrast to the scattering in 1d, clusters of multiple LS are soon formed that move as entities. Especially, an equilateral triangle seems to correspond to a stable configuration. Bound states of two density peaks can also be observed. Due to the additional spatial degree of freedom, the clusters can rotate and drift. Rotational modes seem to become active at parameter values close to the drift-instability.

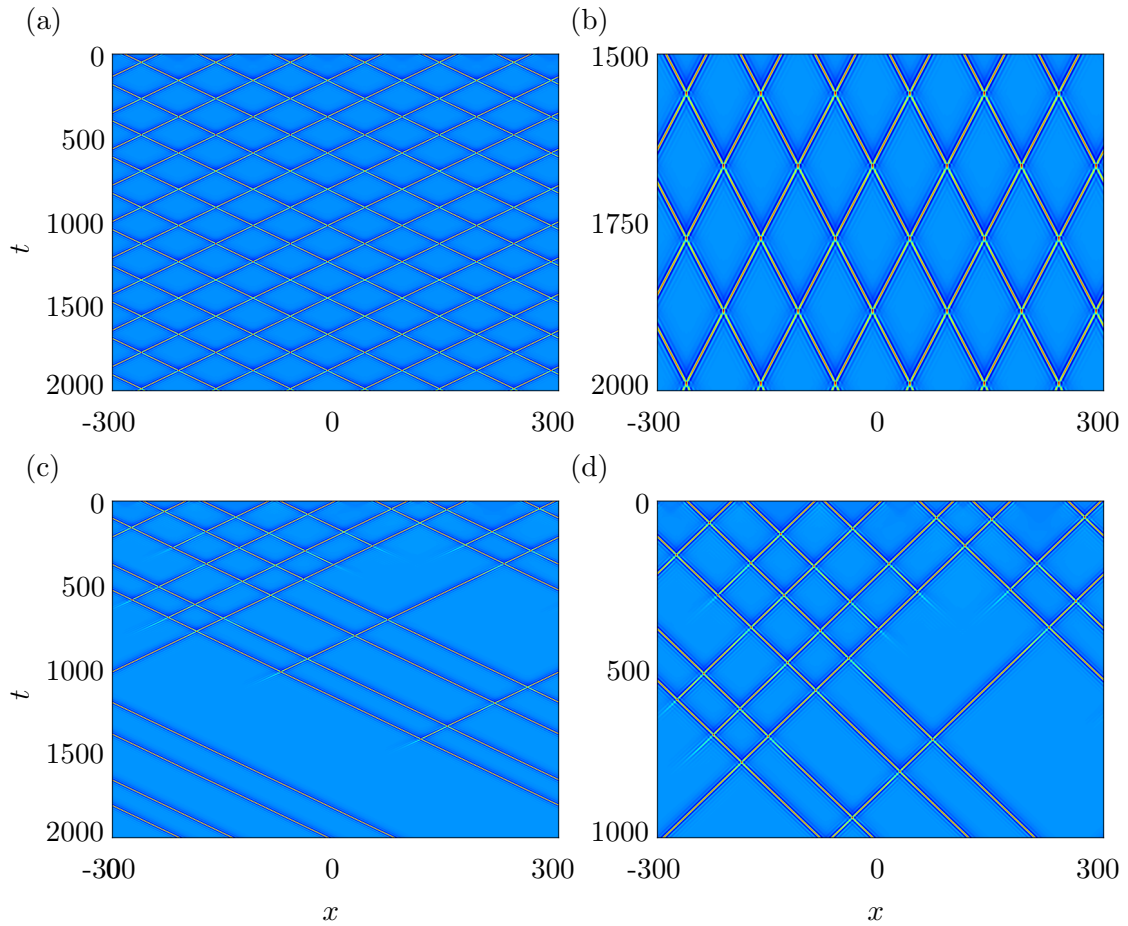


Figure 6.6: (a) Space-time plot of a stable "gas" of traveling one-peak LS on a large domain with  $L = 600$ . Twelve one-peak LS are equally spaced on the domain resulting in a free path of  $\lambda = 50$ . (b) shows a zoom into the final 500 time units of (a). (c) The 12 particles are initially randomly shifted from the regular spacing. Due to smaller distances and shorter times between collisions, the majority of LS decays after a number of collisions. (d) depicts the first 1000 time units of (c). Eventually, four LS with the same direction of motion emerge as a stable state.  $v_0 = 0.5$ ,  $\bar{\psi} = -0.7$  and remaining parameters as in Fig. 6.2.

Up to  $t = 100$  (Fig. 6.7) most LS travel as single one-peak structures. However, between  $60 < t < 100$  we can observe the formation of a traveling bound state in the shape of a triangle. At  $t = 80$ , a third density peak approaches two peaks that have been drifting as a bound state since  $t = 40$ . The third peak is linked to the structure at the middle of the two peaks. The formed triangle is stable for a long period of time (cf.  $t = 720$ ) until, eventually, the remaining LS are "collected" and added to the bound state.

After a long transient and multiple collisions, a single cluster has emerged (cf. Fig. 6.7,  $t = 4000$ ). Within the cluster, the density peaks are placed in a hexagonal pattern. A white arrow in Fig. 6.7 ( $t = 4000$ ) indicates its direction of motion. The arrow is perpendicular to one side of the equilateral triangle at the tip of the cluster. Before this direction emerges, rotational modes are visible and the direction of the collective drift changes a few times.

Active particles often exhibit dynamical clustering, where particles form extended clusters that move as one entity. In experiments as in [BBK<sup>+</sup>13], where carbon-coated colloidal Janus particles dispersed in a mixture of water and lutidine and propulsion speed is varied by changing the laser illumination, the formation of clusters is a dynamical process and they do also break up. In our 2d time simulations of ensembles of LS in the active PFC model, we could, however, not observe that clusters split up again when once formed. Nonetheless, our observations may serve as a starting point for future investigations of, e.g., distribution of cluster sizes as a function of the drift velocity  $c$  or the onset of rotational modes.

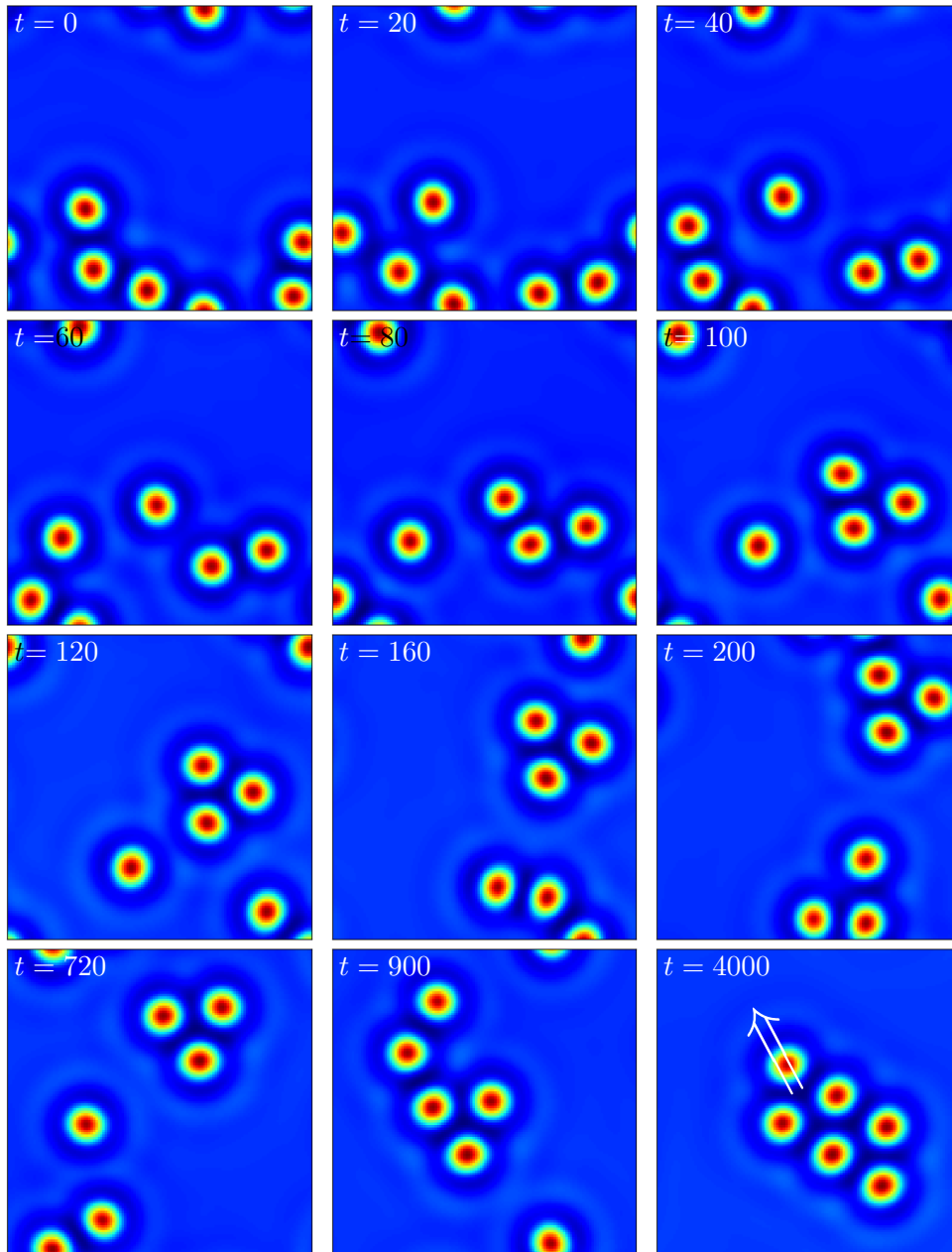


Figure 6.7: Time series of snapshots of the density profile  $\psi(\mathbf{x}, t)$  with six traveling LS. Respective times  $t$  are given in the panels. Boundary conditions are periodic. Up to  $t = 80$ , collisions are mostly elastic and collision partners are reflected. A traveling two-peak LS can be spotted at  $t = 40$ . At  $80 < t < 100$ , a third density peak joins the cluster forming a traveling triangle. The triangle configuration is drifting for a long period of time, until, eventually, all LS form a single cluster ( $t = 4000$ ). Its direction of motion is indicated by a white arrow. Note that for all  $t$ , all LS are in motion. Domain:  $L_x = 8L_a$ ,  $L_y = 7L_c$ ,  $v_0 = 0.2$ ,  $\bar{\psi} = -0.8$  and remaining parameters as in Fig. 6.2

# 7 Towards Other Models for Active Patterns

After extensive studies of the active PFC model, we raise the question how other pattern forming models react to a coupled polarization field and activity. Instead of following a formal derivation of these models, we rather state two examples by coupling the vector field  $\mathbf{P}$  to the passive models in the same way as derived for the active PFC model.

In particular, we investigate different solution types, the onset of motion and demonstrate the universality of the derived criterion for the drift instability. The models we investigate are an active version of the Swift-Hohenberg equation (SH) and an active Cahn-Hilliard model (CH). The two models are chosen to study a non-conserved model (SH) and an additional prominent model with a conserved dynamics (CH).

The Swift-Hohenberg equation often serves as a paradigm for pattern-forming systems [CH93] while the Cahn-Hilliard equation is a basic model for phase separation and decomposition dynamics [CH58, Cah65].

## 7.1 Active Swift-Hohenberg equation

### 7.1.1 The model

Using the same free energy functional as in Eq. (2.33) and identical coupling terms between the two fields we can amend the active PFC model towards an active Swift-Hohenberg-type model. By dropping the outer Laplacian in the dynamic equation for the density  $\psi$  (replacing it by a minus sign), the mass conservation is removed. The model then reads

$$\partial_t \psi = -\frac{\delta \mathcal{F}}{\delta \psi} - v_0 \nabla \cdot \mathbf{P}, \quad (7.1)$$

$$\partial_t \mathbf{P} = \nabla^2 \frac{\delta \mathcal{F}}{\delta \mathbf{P}} - D_r \frac{\delta \mathcal{F}}{\delta \mathbf{P}} - v_0 \nabla \psi \quad (7.2)$$

with

$$\mathcal{F} = \mathcal{F}_{\text{pfc}} + \mathcal{F}_{\mathbf{P}} \quad (7.3)$$

as before. Executing the variations and restricting space to one dimension yields

$$\partial_t \psi = -\left\{ \left[ \epsilon + (1 + \partial_{xx})^2 \right] \psi + (\psi + \bar{\psi})^3 \right\} - v_0 \partial_x P, \quad (7.4)$$

$$\partial_t P = C_1 \partial_{xx} P - D_r C_1 P - v_0 \partial_x \psi \quad (7.5)$$

with the main control parameters activity  $v_0$ . Note that the density is not fixed anymore and that  $\bar{\psi}$  is not a control parameter. It remains in the model for the sake of convenience.  $\epsilon$  sets the temperature. Patterns emerge at  $\epsilon < 0$ .  $C_1$  and  $D_r$  control the diffusion of the polarization.

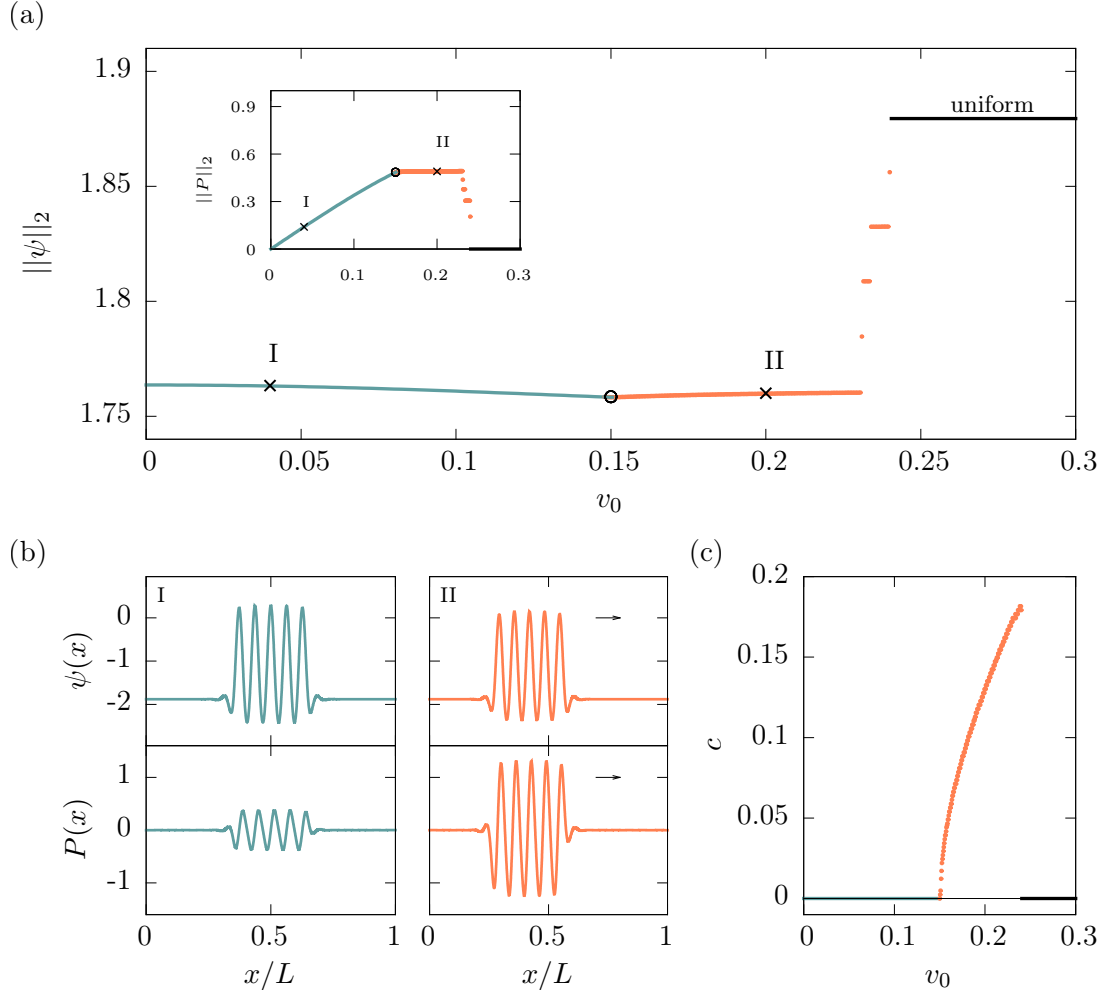


Figure 7.1: (a) Bifurcation diagram of a five-peak LS in the active SH model from time simulations:  $\|\psi\|_2$  as a function of activity  $v_0$ . The resting density peaks (corresponding to the blue branch) shrink minimally as  $v_0$  is increased. In contrast, the polarization  $P$  grows from zero to a comparable height as peaks of  $\psi$  (inset). The circle marks the drift-pitchfork bifurcation. Branches of traveling LS are denoted in orange. At around  $v_0 = 0.23$ , the traveling LS successively loses peaks until a uniform state (black) is reached. (b) shows profiles at loci labeled in (a) of a resting LS (blue) and a traveling LS (orange). I:  $v_0 = 0.04$  and II:  $v_0 = 0.2$ . (c) The drift velocity  $c$  grows monotonically with  $v_0$ . Parameters:  $\bar{\psi} = 0.9$ ,  $\epsilon = -1.5$ ,  $C_1 = 0.1$ ,  $C_2 = 0$ ,  $D_r = 0.5$ ,  $L = 100$ .

### 7.1.2 Resting and traveling patterns

Similar to former analyses, we track steady states  $(\psi_0, P_0)$  of Eqs. (7.4) and (7.5) while varying the activity parameter  $v_0$ . Figure 7.1 depicts the corresponding bifurcation diagram and selected solution profiles from time simulations of the underlying evolution equations. The time simulations are carried out via a pseudo-spectral method for spatial derivatives (implying periodic boundary conditions) and a semi-implicit Euler time-stepping method.

Using the example of a localized five-peak solution (cf. Fig. 7.1 (b)), time simulations reveal an onset of motion at a threshold of  $v_c \approx 0.15$  and a monotonically growing drift velocity  $c$  for  $v_0 > v_c$ . As seen for active crystallites within the active PFC model, the spatial profile of  $\psi$  does not significantly change its shape when varying  $v_0$ . Here, its norm  $\|\psi\|_2$  (Fig. 7.1 (a)) stays almost constant. The polarization  $P$ , on the other hand, grows from zero to peaks of the same order of magnitude as  $\psi$ . Since it is modulated around  $P = 0$ , its norm remains smaller as  $\|\psi\|_2$  (cf. inset). At the onset of motion, density peaks are not equally negatively and positively polarized anymore and a shift in the relative positions of  $\psi$  and  $P$  leads to a net polarization and the onset of a drift. At the critical activity of  $v_c \approx 0.15$ , the LS starts to travel with a steady drift velocity  $c$ . The velocity grows approximately as  $c \propto \sqrt{v_0 - v_c}$ . The same observation was made for drift-pitchfork bifurcations in the active PFC model (cf. Sec. 2.3). The resulting direction of the drift in the simulations is random. It depends on the direction of the relative shift between  $\psi$  and  $P$  and the sign of the resulting polarization of the pattern.

At around  $v_0 = 0.23$ , the traveling five-peak LS loses stability and the state drops onto a branch of traveling four-peak LS. At slightly higher  $v_0$ , the state evolves to a traveling three-peak LS. For increasing  $v_0$ , the LS loses its peaks successively, until, eventually, it melts at  $v_0 \approx 0.24$ . After four small plateaus that correspond to traveling four-peak LS, three-peak LS, two-peak LS and one-peak LS, respectively, the spatial modulation of the state has completely decayed. The system reaches a homogeneous state of  $\psi_0 \approx -1.8795$ . Since there are no gradients in  $\psi$  anymore, the polarization decays to  $P_0 = 0$ . The homogeneous state of  $\psi_0 \approx -1.8795$  can analytically be calculated by evaluating  $-(\epsilon + 1)\psi_0 - (\psi_0 + \bar{\psi})^3 = 0$ .

As in the active PFC model, the less peaks a LS consists of, the wider is the range of existence in terms of  $v_0$ . However, the difference in  $v_0$  is almost vanishing, here. All this occurs in a very small  $v_0$ -range. Note that the widest of the four small levels in Fig. 7.1 (a) corresponds to traveling two-peak LS.

### 7.1.3 Onset of motion

Using analogous considerations as in Sec. 4.4 about the system's translation symmetry and a corresponding Goldstone mode we are able to derive a criterion for the onset of motion for this active model with a non-conserved density field.

Linearizing the right-hand side of the evolution equations (7.4) and (7.5) about a steady state  $(\psi_0, P_0)^T$  one obtains the operator

$$\mathcal{L}(\psi_0, P_0) = \begin{pmatrix} - \left[ \left( \epsilon + (1 + \partial_{xx})^2 \right) + 3 (\bar{\psi} + \psi_0(x))^2 \right] & -v_0 \partial_x \\ -v_0 \partial_x & C_1 (\partial_{xx} - D_r) \end{pmatrix} \quad (7.6)$$

$$= \begin{pmatrix} L_{SH} & -v_0 \partial_x \\ -v_0 \partial_x & L_{22} \end{pmatrix} \quad (7.7)$$

for the evolution of the perturbations.

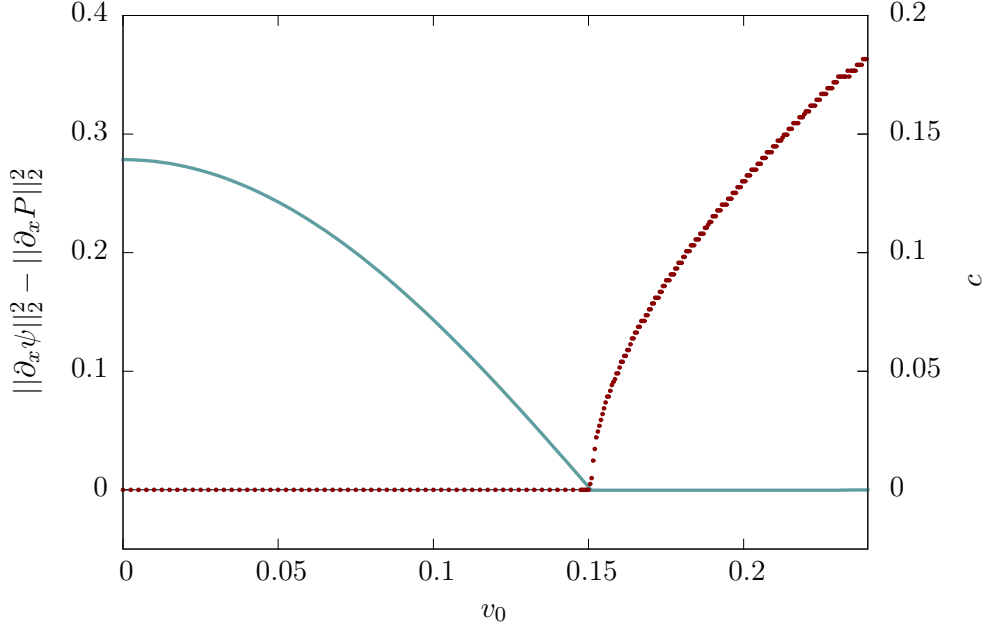


Figure 7.2: Onset of motion for an active Swift-Hohenberg equation in 1d: Norms  $\|\partial_x \psi\|_2^2 - \|\partial_x P_0\|_2^2$  (blue) and drift velocity  $c$  (dark-red, dotted) of a five-peak LS as a function of activity  $v_0$ . The resting LS is destabilized at  $v_c \approx 0.15$  and starts to travel with  $c$ . The solvability condition Eq. (4.55)  $\|\partial_x \psi\|_2^2 - \|\partial_x P_0\|_2^2$  crosses zero at the drift bifurcation. It remains zero for the traveling LS ( $v_0 > 0.15$ ).  $c$  grows monotonically for increasing  $v_0$ . The bifurcation diagram is constructed with results from time simulations and only depicts stable branches. Parameters as in Fig. 7.1.

The corresponding neutrally stable Goldstone mode of translation is denoted as  $\mathcal{G}$ . In order to evaluate  $\langle \mathcal{G}^\dagger | \mathcal{G} \rangle$  that crosses zero at the onset of the drift (find details in Sec. 4.4), we need to determine the adjoint linearized operator  $\mathcal{L}^\dagger$  and its neutrally stable eigenfunction  $\mathcal{G}^\dagger$ , i.e.,  $\mathcal{L}^\dagger \mathcal{G}^\dagger = \mathbf{0}$ . The adjoint operator reads:

$$\mathcal{L}^\dagger = \begin{pmatrix} L_{\text{SH}} & v_0 \partial_x \\ v_0 \partial_x & L_{22} \end{pmatrix}. \quad (7.8)$$

The equations for the neutrally stable adjoint eigenmode  $\mathcal{G}^\dagger = (\psi_{\mathcal{G}}^\dagger, P_{\mathcal{G}}^\dagger)^T$  are then

$$L_{\text{SH}} \psi_{\mathcal{G}}^\dagger + v_0 \partial_x P_{\mathcal{G}}^\dagger = 0 \quad (7.9)$$

$$v_0 \partial_x \psi_{\mathcal{G}}^\dagger + L_{22} P_{\mathcal{G}}^\dagger = 0. \quad (7.10)$$

Differentiating w.r.t.  $x$  the steady state equations for  $(\psi_0, P_0)^T$  restores the equation of the Goldstone mode of translation:

$$L_{\text{SH}} \partial_x \psi_0 - v_0 \partial_{xx} P_0 = 0 \quad (7.11)$$

$$-v_0 \partial_{xx} \psi_0 + L_{22} \partial_x P_0 = 0. \quad (7.12)$$



Comparing Eqs. (7.9) and (7.10) with (7.11) and (7.12) results in

$$\psi_{\mathcal{G}}^{\dagger} = \partial_x \psi_0 \quad (7.13)$$

$$P_{\mathcal{G}}^{\dagger} = -\partial_x P_0. \quad (7.14)$$

We can now evaluate the solvability condition setting the criterion for the onset of motion:

$$\langle \mathcal{G}^{\dagger} | \mathcal{G} \rangle = \langle \psi_{\mathcal{G}}^{\dagger} | \psi_{\mathcal{G}} \rangle + \langle P_{\mathcal{G}}^{\dagger} | P_{\mathcal{G}} \rangle \quad (7.15)$$

$$= \langle \partial_x \psi_0 | \partial_x \psi_0 \rangle - \langle \partial_x P_0 | \partial_x P_0 \rangle = 0 \quad (7.16)$$

$$\Leftrightarrow 0 = \|\partial_x \psi_0\|_2^2 - \|\partial_x P_0\|_2^2. \quad (7.17)$$

Tracking the difference of the norms of the spatial derivatives  $\|\partial_x \psi_0\|_2^2 - \|\partial_x P_0\|_2^2$  reveals a perfect match of its zero crossing and the onset of motion. Figure 7.2 shows how the difference decreases until reaching zero where the drift ( $v_c \approx 0.15$ , velocity shown in dotted dark-red) sets in. As observed for the active PFC model in one spatial dimension, the difference of the norms stays zero for traveling states. The bifurcation diagram is constructed by the direct time simulation of Eqs. (7.11) and (7.12) and, hence, does not show the unstable branch of resting solutions. The derived criterion also holds for periodic structures (not shown).

Recall that for the aPFC model with conserved dynamics, the condition reads  $0 = \|\psi_0\|_2^2 - \|P_0\|_2^2$  (Eq. (4.55)) in contrast. The difference of the norms of the fields itself is zero at the onset of motion.

## 7.2 Active Cahn-Hilliard model

As a second prominent model, we investigate an active version of the Cahn-Hilliard (CH) model [Cah65]. The CH equation describes the process of phase separation in a binary mixture as a fairly simple phenomenological macroscopic mean-field continuum model. Two components spontaneously decompose and form coexisting domains that purely consist of one type of the components.

The well-studied model has many applications in fields ranging from complex fluids, soft matter physics and many industrial applications like Langmuir-Blodgett transfer [LKG<sup>+</sup>12, KT14, WTG<sup>+</sup>15]. It is regarded to capture the dominant paradigms of phase separation dynamics.

### 7.2.1 The model

The Cahn-Hilliard (CH) equation has the form of a conservation law where the dynamics of a scalar concentration-like order parameter  $\phi$  is expressed as the divergence of a flux. The equation can be written as gradient dynamics with an underlying free energy functional  $\mathcal{F}_{\text{CH}}$  that is minimized by the decomposition of a binary fluid [CH58, Lan92].

$$\mathcal{F}_{\text{CH}}[\phi] = \int d^n r \left[ \frac{1}{2} (\nabla \phi)^2 - \frac{1}{2} \phi^2 + \frac{1}{4} \phi^4 \right] \quad (7.18)$$

The two minima of  $\mathcal{F}_{\text{CH}}$  at  $\phi = \pm 1$  represent the two phases.

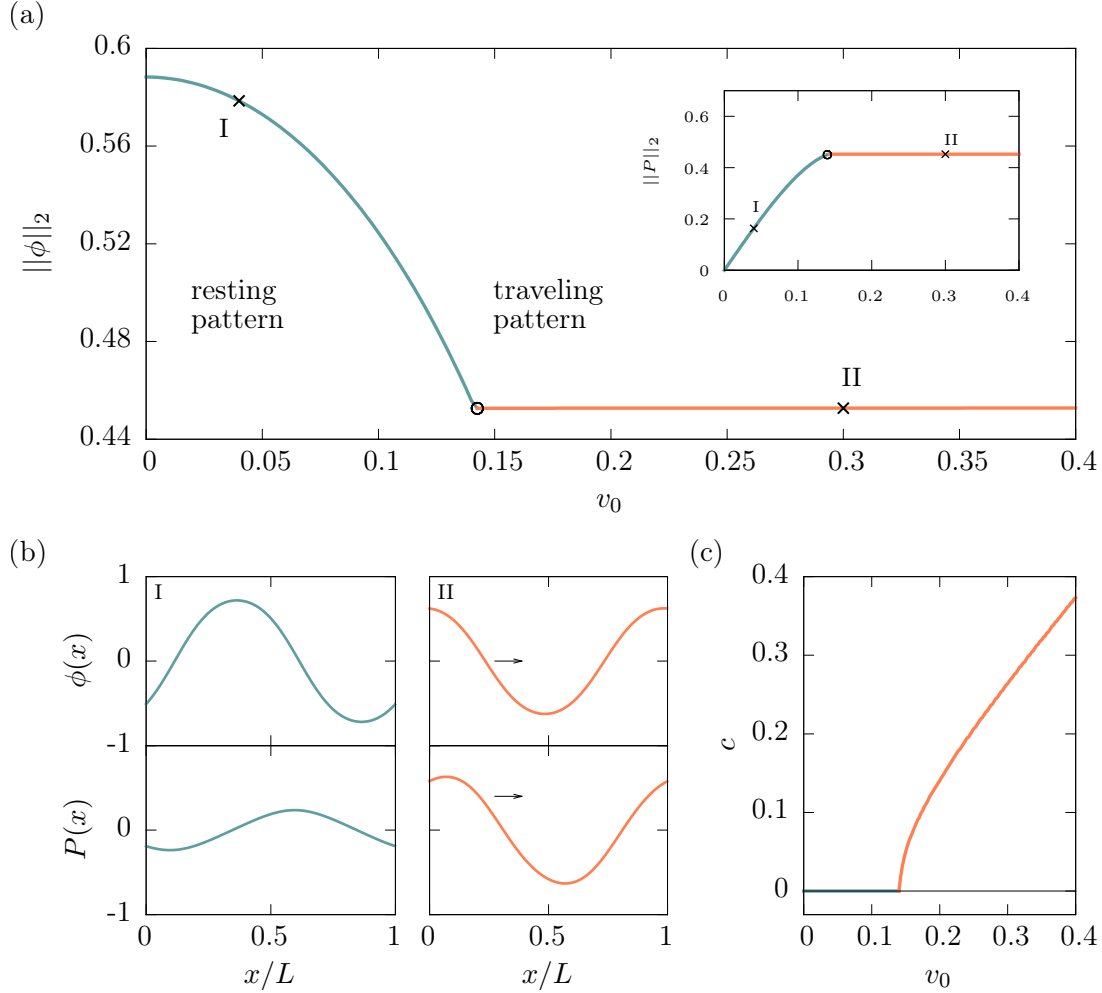


Figure 7.3: (a) Bifurcation diagram of a periodic pattern in the active CH model from time simulations:  $\|\phi\|_2$  as a function of activity  $v_0$ . The resting pattern (I) corresponds to the blue branch. Its profile slightly decreases as  $v_0$  is increased. In contrast, the polarization  $P$  grows from zero to peaks of the same amplitude as  $\psi$  (inset). The circle marks the drift-pitchfork bifurcation. Traveling patterns (II) and corresponding branches are denoted in orange. (b) shows the profiles at loci labeled in (a) of a resting pattern (blue) and a traveling pattern (orange). I:  $v_0 = 0.04$  and II:  $v_0 = 0.3$ . (c) The drift velocity  $c$  grows monotonically with  $v_0$ . Parameters:  $C_1 = 0.1$ ,  $C_2 = 0$ ,  $D_r = 0.5$ ,  $L = 2\pi/k_{\max}$  with  $k_{\max} = 1/\sqrt{2}$  being the dominant mode obtained from LSA of the trivial solution.

The model is now amended by the same coupling to a polarization  $\mathbf{P}$  as previously derived for the active PFC model. Also the evolution equation for  $\mathbf{P}$  remains unchanged. An active CH equation with  $\mathcal{F} = \mathcal{F}_{\text{CH}} + \mathcal{F}_{\mathbf{P}}$  then reads

$$\partial_t \phi = \nabla^2 \frac{\delta \mathcal{F}}{\delta \phi} - v_0 \nabla \cdot \mathbf{P}, \quad (7.19)$$

$$\partial_t \mathbf{P} = \nabla^2 \frac{\delta \mathcal{F}}{\delta \mathbf{P}} - D_r \frac{\delta \mathcal{F}}{\delta \mathbf{P}} - v_0 \nabla \phi. \quad (7.20)$$

Restricting the physical space to one dimension and carrying out the variations yields

$$\partial_t \phi = \partial_{xx} (\phi^3 - \phi - \partial_{xx} \phi) - v_0 \partial_x P, \quad (7.21)$$

$$\partial_t P = C_1 \partial_{xx} P - D_r C_1 P - v_0 \partial_x \phi. \quad (7.22)$$

We note that the coupling preserves the conservation of  $\phi$  and its dynamics can still be expressed as the divergence of a flux. For simplicity, we have scaled out further control parameters (such as mobility etc.) in the CH equation and use the simple version above.

### 7.2.2 Resting and traveling patterns

Following former approaches we want to study steady and stationary states  $(\phi_0, P_0)^T$ , where stationary states are steady states in some comoving frame with velocity  $c$ . Again, we are particularly interested in the onset of motion and traveling states with  $c \neq 0$ . For that purpose we integrate Eqs. (7.21) and (7.22) forward in time (same methods as in 7.1.2 with random initial conditions and periodic boundaries) and construct a bifurcation diagram from the simulation data for different values of activity  $v_0$ .

Figure 7.3 (b)(I) depicts a typical profile of the concentration  $\phi$ . The fluid has decomposed into two phases with  $\phi \approx +1$  and  $\phi \approx -1$ , respectively. The values of the two extrema have decreased due to the coupling to  $P$ . The domain size is chosen as  $L = 2\pi/k_{\text{max}}$ , where  $k_{\text{max}} = 1/\sqrt{2}$  is the wavenumber of the dominant mode in the dispersion relation from the linear stability analysis of the trivial solution.

For  $v_0 > 0$ , a polarization  $P$  forms. Once again, we notice the symmetry between the two fields for resting states: peaks and dips in  $\phi$  coincide with zero crossings of  $P$  making each density bump equally positively and negatively polarized. The symmetry  $(\psi, P, x) \rightarrow (\psi, -P, -x)$  holds w.r.t. the center of the density peak (and dip). Hence, integrating  $P$  over the width of a density peak (dip), i.e. the net polarization, is zero.

The amplitude of  $P$  grows monotonically with  $v_0$  whereas the norm of  $\phi$  decreases as the activity is increased. At a critical  $v_c \approx 0.14$ , the symmetry between  $P$  and  $\phi$  breaks. A net polarization emerges, the drift sets in and we follow a branch of moving states (orange branch/profile in Fig. 7.3). As observed before, the traveling pattern has a constant norm as the profiles keep their shape and only shift their relative position. The drift velocity  $c$  (Fig. 7.3(c)) grows monotonically with activity  $v_0$ . The drift pitchfork bifurcation is marked by a black circle.

### 7.2.3 Onset of motion

The introduced active CH model is translationally invariant. For steady states  $(\phi_0, P_0)^T$  we can deduce a neutrally stable Goldstone mode that shifts the solutions,  $\mathcal{G} = (\partial_x \phi_0, \partial_x P_0)^T$ .

In order to derive a criterion for the drift instability, we again need to find  $\mathcal{G}^\dagger$ , the kernel of the adjoint linearized operator  $\mathcal{L}^\dagger$ . Linearizing Eqs. (7.21) and (7.22) around a steady states leads to

$$\mathcal{L}(\phi_0, P_0) = \begin{pmatrix} \partial_{xx} (-\partial_{xx} - 1 + 3\phi_0(x)^2) & -v_0\partial_x \\ -v_0\partial_x & C_1 (\partial_{xx} - D_r) \end{pmatrix}. \quad (7.23)$$

Following all steps from subsections 4.4.3 and 4.4.4 one finds

$$\mathcal{L}^\dagger(\phi_0, P_0) = \begin{pmatrix} (-\partial_{xx} - 1 + 3\phi_0(x)^2) \partial_{xx} & v_0\partial_x \\ v_0\partial_x & C_1 (\partial_{xx} - D_r) \end{pmatrix}. \quad (7.24)$$

This is the same structure as for the active PFC model and the adjoint eigenfunctions are also spatial integrals over the steady states (times -1 for one component) and the solvability condition (4.39) reads

$$\begin{aligned} \langle \mathcal{G}^\dagger | \mathcal{G} \rangle &= \langle \psi_{\mathcal{G}}^\dagger | \psi_{\mathcal{G}} \rangle + \langle P_{\mathcal{G}}^\dagger | P_{\mathcal{G}} \rangle \\ &= -\langle \psi_0 | \psi_0 \rangle + \langle P_0 | P_0 \rangle = 0 \end{aligned} \quad (7.25)$$

$$\Leftrightarrow 0 = \|\psi_0\|_2^2 - \|P_0\|_2^2, \quad (7.26)$$

as found for the conserved dynamics of the active PFC model (cf. Eq. (4.55)). Equation (7.26) holds at the onset of motion. Following  $\|\psi_0\|_2^2 - \|P_0\|_2^2$  for the steady states computed by the time simulations reveals indeed a perfect match in its zero crossing and the onset of the drift. Figure 7.4 depicts the results.

After the onset of the drift,  $\phi(x)$  and  $P(x)$  of the traveling pattern remain unchanged, only shifting their relative position. That is why the difference of the norms stays constantly zero for  $v_0 > v_c \approx 0.14$ .

### 7.3 Universality of the criterion for the onset of motion

The two examples suggest that the derived criteria for the onset of motion hold for any continuum model in which the two fields are symmetrically coupled via  $-v_0\nabla$ . And indeed we only employed two constraints: Firstly, the active model must fulfill a translation symmetry. Secondly, when linearized, the diagonal elements of  $\mathcal{L}$  need to be either self-adjoint or for models with conserved dynamics read  $\partial_{xx}$  times a self-adjoint operator for the first element, i.e.  $L_{11} = \partial_{xx} L_{\text{self-adjoint}}$ . Note that a non-linear equation for  $\mathbf{P}$  results in an operator that is not self-adjoint, i.e.,  $L_{22}^\dagger \neq L_{22}$  and not fulfilling the conditions.

In the first case for non-conserved models as the active SH model,  $\|\partial_x \psi\|_2^2 - \|\partial \mathbf{P}\|_2^2 = 0$  holds at the onset of motion. For models with conserved dynamics (active PFC, active CH),  $\|\psi\|_2^2 - \|\mathbf{P}\|_2^2$  crosses zero where the drift sets in. And even though, the equations were derived for one-dimensional models for simplicity, the criteria also hold in two spatial dimensions. Without loss of generality, the derivation can be extended to 2d.

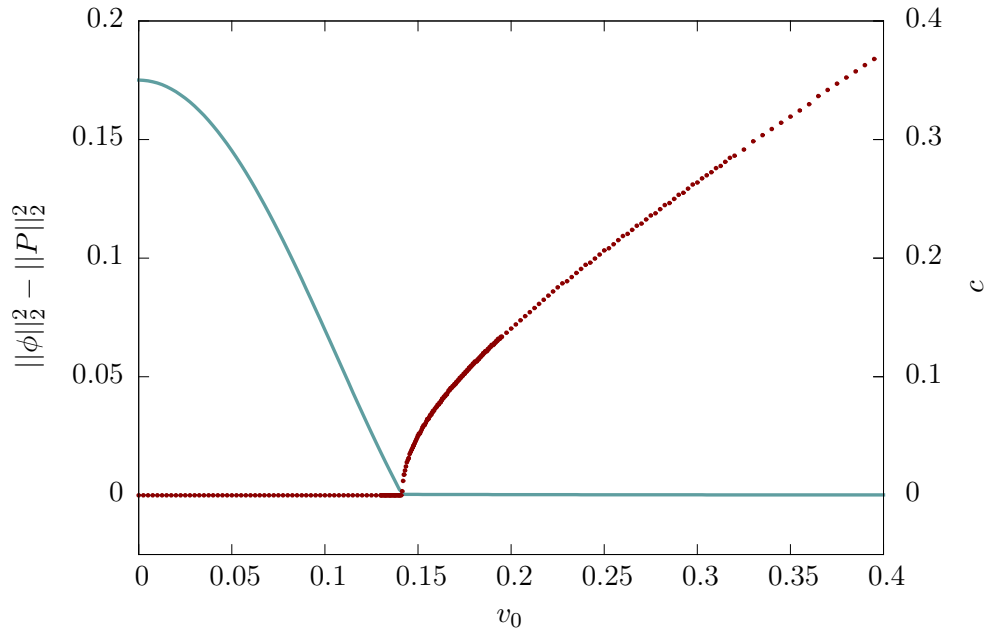


Figure 7.4: Onset of motion for an active Cahn-Hilliard equation in 1d: Norms  $\|\psi_0\|_2^2 - \|P_0\|_2^2$  (blue) and drift velocity  $c$  (dark-red, dotted) of a periodic pattern as a function of activity  $v_0$ . The resting pattern is destabilized at  $v_c \approx 0.14$  and starts to travel with  $c$ . The solvability condition Eq. (4.55)  $\|\psi_0\|_2^2 - \|P_0\|_2^2 = 0$  is fulfilled at the drift bifurcation. It remains zero for the traveling pattern ( $v_0 > 0.14$ ).  $c$  grows monotonically for increasing  $v_0$ . The bifurcation diagram is constructed with results from time simulations and only depicts stable branches. Around the onset of motion, increments of  $v_0$  are decreased and more dots are plotted. Parameters as in Fig. 7.3.



## 8 Summary and Outlook

We have in depth studied the bifurcation structure of the active phase-field-crystal model in one and two spatial dimensions. After discussing the linear stability of the liquid (homogeneous) state with respect to monotonous and oscillatory modes in chapter 3, we have briefly discussed the existence and stability of stable domain-filling resting and traveling crystalline (periodic) structures in 1d. In the one-dimensional case (chapter 4), our main focus has been on crystallites (crystals of finite extension) that correspond to stable and unstable localized states of different symmetries. We have analyzed how the classical slanted snakes-and-ladders structure (slanted homoclinic snaking) known from the phase-field-crystal model [TAR<sup>+</sup>13] is amended by activity. In particular, we have shown that increasing activity, one finds a critical value for the onset of motion of the various localized states and of the domain-filling crystal. Using the mean concentration  $\bar{\psi}$  as the control parameter we have found that traveling states emerge either through drift-pitchfork bifurcations of the resting parity (left-right) symmetric localized states or through drift-transcritical bifurcations of resting asymmetric localized states that form the rungs of the snakes-and-ladders bifurcation structure. In 1d, at the employed parameter values, these traveling localized states always occur within the  $\bar{\psi}$ -range limited by the snaking branches of resting localized states.

Note that this onset behavior differs from the case of the non-variational Swift-Hohenberg equations as studied in [HK11]. There, at any value of the driving parameter in front of the non-variational term, all asymmetric states drift and all symmetric states are at rest. Here, however, the coupling of the two fields allows for resting asymmetric states even at a finite activity parameter and moving states emerge through drift bifurcations that are not present (in any form) in the variational limit.

The second investigated main control parameter has been the activity. Here, the general tendency is that an increase in activity suppresses the resting localized and periodic states. Resting LS ultimately annihilate in saddle-node bifurcations at critical activities that are of a similar magnitude for all studied states. Resting periodic states, in contrast, vanish in a supercritical pitchfork bifurcation on the homogeneous state. In other words, activity eventually melts all resting crystalline structures as the driving force overcomes the attractive forces that stabilize the equilibrium crystals and crystallites that exist in the reference system without activity. This corresponds to the melting of equilibrium clusters by activity observed in the Brownian dynamics simulations of Ref. [RBH13] for self-propelled particles with short-range attraction.

However, at values of the activity below this melting point, branches of resting states show drift bifurcations for suitable diffusion and mean densities. There, branches of traveling states emerge that may exist in a small range of activity or even extend towards infinite activity (in 1d) as we have shown by numerical two-parameter continuation of the relevant bifurcations. In other words, depending on parameters, although activity may melt traveling crystallites, there are extended parameter regions where this is not the case. In fact, we have found that although a high activity melts most traveling localized states, i.e., traveling crystalline patches, this is not the case for traveling periodic states, i.e., traveling domain-

filling crystals. They can be driven with arbitrarily high activity and then show high corresponding drift velocities. We believe that this is most likely the case because the periodicity of the domain-filling crystals is fixed, while the traveling localized states naturally adapt their peak spacing. This additional degree of freedom could make them less stable. Note that the found crystallites are not related to the motility-induced clusters discussed, e.g., in [GTL<sup>+</sup>15, SSW<sup>+</sup>15, CT15]. The latter effect has not yet been found in an active PFC model as they are mainly considered to study how equilibrium crystallization is amended by activity. It should be further investigated whether it may also describe motility-induced clustering, especially when allowing for spontaneous polarization ( $C_1 < 0$ ,  $C_2 > 0$ ).

Furthermore, we have investigated the region of existence of traveling localized states and have shown that they are generic solutions for extended regions of the plane spanned by mean concentration and activity. Whereas extended traveling localized states of three and more peaks quickly vanish into the homogeneous background, narrow localized states (one and two density peaks) can be driven at quite high activities where they reach high velocities. This does not seem to be the case in the non-variational systems studied in [HK11, BD12]. Therefore, a future comparative study of the present system, the systems studied in [HK11, BD12] and the ones reviewed and discussed in [KT07] would be beneficial.

A main focus has been the onset of motion that occurs at a critical activity which only slightly depends on the particular size of localized state in terms of density peaks. We have considered drift instabilities for the system of two coupled equations where one represents a mass-conserving dynamics of a density-like quantity and the second one is a linear equation for the polarization. Also, the non-variational coupling of the two equations is linear. Under these conditions, we have derived a general criterion for the onset of motion. Namely, the zero crossing of the difference of the squared norms of the two steady fields ( $\|\psi_0\|_2^2 - \|P_0\|_2^2$ ) marks the onset of motion for all localized and extended crystalline states. The criterion holds for both types of drift instabilities that occur in the aPFC model: drift-pitchfork bifurcations and drift-transcritical bifurcations and may be used to determine the critical strength of activity that is needed for collective traveling states. As shown later, the criterion also applies to other models of active patterns that fulfill the described constraints. What needs further clarification is the question of whether such a simple criterion can be derived for more complicated active models that do more faithfully model specific properties of the experimental systems and of the particular active particles at hand.

Besides results from numerical continuation, we have employed numerous time simulations to construct morphological phase diagrams in the plane spanned by mean concentration and activity. These condense many results and demonstrate the powerful interplay of continuation methods and time simulations as results from fold continuations nicely border the existence regions obtained by time simulations. In certain regions of the parameter plane, we have observed a novel type of solution of active crystallites, namely oscillatory states. Their origin in a Hopf bifurcation has been discussed. Oscillatory states also undergo a drift instability resulting in a intricate state with differing phase velocity and group velocity. Physically speaking, this corresponds to a state where parts of the crystals vanish into the liquid background while at the other end of the crystal new crystalline structure is created.

The chapter dealing with crystals and crystallites in 1d has been closed by discussing the influence of the remaining model parameters. The effective temperature has turned out to only play a minor role in the transition from resting to traveling states. The diffusion of polarization, in contrast, directly influences the critical activity for motion. Fold continuation has revealed the expected linear relation between the threshold activity for motion and a



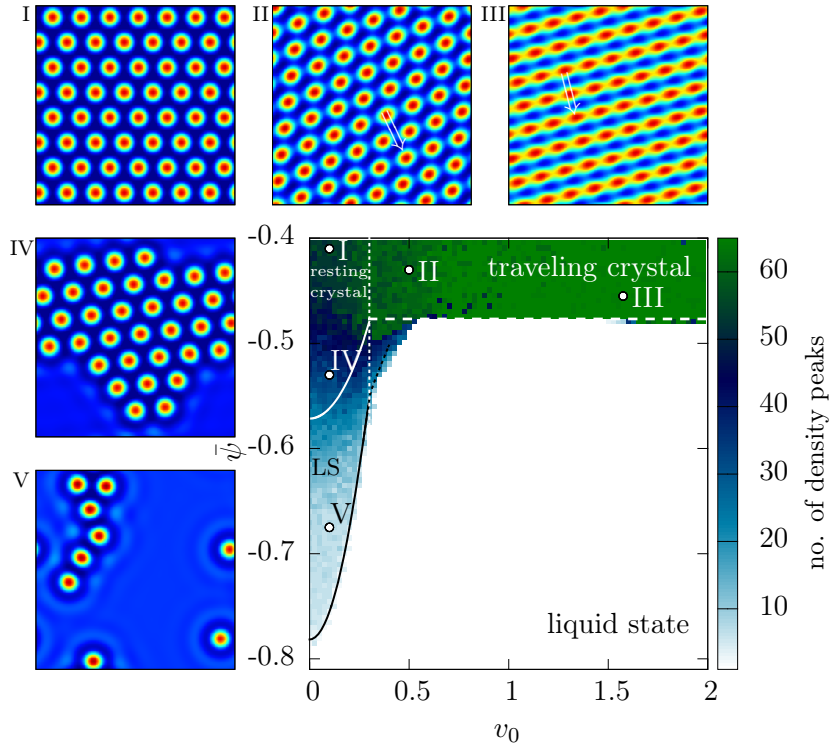


Figure 8.1: The morphological phase diagram condenses large parts of our results and demonstrates the powerful interplay of continuation methods and time simulations. The color coding distinguishing different solution types is obtained by time simulations, whereas lines mostly originate from continuation. The lines nicely border regions of existence of resting and traveling LS. For details see Fig. 5.22.

diffusion coefficient. High diffusion can even completely suppress the drift instability of resting LS. Spontaneous polarization without any threshold for motion has been briefly discussed as well.

Due to additional degrees of freedom, the bifurcation structure of active crystallites in 2d (chapter 5) has proven to be much more complicated. Besides translation modes, also rotational modes can be destabilized and the particular direction of the drift w.r.t. the symmetry axes of the LS has to be taken into account. A rotational symmetric one-peak LS has shown many similarities to the 1d case, while a less symmetric dumbbell shaped two-peak LS has turned out to be unstable for any non-vanishing value of activity. For the employed value of the effective temperature, in 2d, the active crystallites exhibit slanted homoclinic snaking. Resting LS as well as traveling LS have shown the same behavior of an undulating branch. The LS, whether resting or traveling, are enlarged until they fill the entire domain and terminate on the periodic resting and traveling solution, respectively. Their branches do neither interfere nor are they torn apart like at lower values of the effective temperature.

In 2d, the activity parameter also strongly influences the crystal structure of space filling, fully periodic solutions. We have found a multistability region for traveling hexagons, traveling rhombuses and traveling stripes. Here, finite size effects as the aspect ratio of the employed domain control the pattern selection. As done for the 1d case, information

from time simulations and continuation are compressed in morphological phase diagrams. Figure 8.1 contains many results and is shown as a summary, here. It also demonstrates the impressive capability of fold continuation to predict limits of existence of various solutions found in time simulations.

After studying individual solution types of the active PFC model, we have conducted numerical collision experiments of traveling LS to determine generic interactions between active crystallites. We have identified different collision outcomes and determined a parameter map of fully elastic collisions that preserve the number of colliding density peaks. A minimal free path between collisions has been experimentally deduced. Due to its considerable size, a stable gas of colliding density peaks has not been found for random initial conditions without equal spacing.

Having extensively discussed the active PFC model, we have stated two more models for active patterns. By using the same implementation of activity, namely the coupled polarization field, we have introduced an active version of the non-conserved Swift-Hohenberg equation and of the Cahn-Hilliard equation. Within both models, we have identified resting and traveling solutions. Criteria for the onset of motion that are derived similarly as for the aPFC model have turned out to be valid for these models as well, emphasizing its universality.

Finally, we highlight a number of questions that merit further investigation. Our main aim has been to establish an overview of the rather involved overall bifurcation structure that is related to the onset of motion in continuum models of active crystals. As experimental studies often focus on the collective behavior of many interacting clusters [TCBP<sup>+</sup>12, GTL<sup>+</sup>15, GTD<sup>+</sup>18], it should be investigated further whether it is possible to derive statistical models from single cluster bifurcation studies as the present one. Such a methodology has recently been presented for ensembles of sliding drops [WTE<sup>+</sup>17]. We hope that the provided study will serve as a reference for other such analyses of more detailed models for active crystals. Here, we have focused on a rather simple coupling of concentration and polarization and have also excluded spontaneous polarization. The obtained results regarding the onset of motion should also be compared to related results regarding the bifurcation structure of other more realistic models of active matter. This will allow one to develop a clearer general understanding of observed multistabilities of states, hysteresis effects and thresholds where qualitative changes occur.

## List of Publications

- [OGT18] L. Ophaus, S. V. Gurevich and U. Thiele. Resting and traveling localized states in an active phase-field-crystal model. *Phys. Rev. E*, 98:022608, August 2018.  
Original research article analyzing LS in the aPFC model. Numerical data, analytical calculations, text and figures were produced by LO, with critical review by SVG and UT.

Currently in preparation (authors marked with an asterisk contributed equally to the publication):

- [OKTX] L. Ophaus\*, J. Kirchner\* and U. Thiele. Scattering of Active Crystallites. (*in preparation*).
- [OTXX] L. Ophaus and U. Thiele. Bifurcation analysis of resting and traveling crystals and crystallites in a two-dimensional active PFC model (*in preparation*).



# Bibliography

- [AASC96] N. N. Akhmediev, V. V. Afanasjev, and J. M. Soto-Crespo. Singularities and special soliton solutions of the cubic-quintic complex ginzburg-landau equation. *Phys. Rev. E*, 53:1190–1201, 1996.
- [AC85] M. V. Abrahams and P. W. Colgan. Risk of predation, hydrodynamic efficiency and their influence on school structure. *Environ. Biol. Fishes*, 13(3):195–202, 1985.
- [ALB<sup>+</sup>10] D. Avitabile, D. J. B. Lloyd, J. Burke, E. Knobloch, and B. Sandstede. To snake or not to snake in the planar Swift-Hohenberg equation. *SIAM J. Appl. Dyn. Syst.*, 9:704–733, 2010.
- [ARRS19] A. J. Archer, D. J. Ratliff, A. M. Rucklidge, and P. Subramanian. Deriving phase field crystal theory from dynamical density functional theory: Consequences of the approximations. *Phys. Rev. E*, 100:022140, Aug 2019.
- [ARTK12] A. J. Archer, M. J. Robbins, U. Thiele, and E. Knobloch. Solidification fronts in supercooled liquids: How rapid fronts can lead to disordered glassy solids. *Phys. Rev. E*, 86:031603, 2012.
- [AT03] I. S. Aranson and L. S. Tsimring. Model of coarsening and vortex formation in vibrated granular rods. *Phys. Rev. E*, 67:021305, 2003.
- [BB99] P. Ball and N. R. Borley. *The self-made tapestry: pattern formation in nature*, volume 198. Oxford University Press Oxford, 1999.
- [BBK<sup>+</sup>13] I. Buttinoni, J. Bialké, F. Kümmel, H. Löwen, C. Bechinger, and T. Speck. Dynamical clustering and phase separation in suspensions of self-propelled colloidal particles. *Phys. Rev. Lett.*, 110:238301, 2013.
- [BCR08] U. Bortolozzo, M. G. Clerc, and S. Residori. Local theory of the slanted homoclinic snaking bifurcation diagram. *Phys. Rev. E*, 78:036214, 2008.
- [BD12] J. Burke and J. Dawes. Localized states in an extended swift-hohenberg equation. *SIAM J. Appl. Dyn. Syst.*, 11:261–284, 2012.
- [BDLL<sup>+</sup>16] C. Bechinger, R. Di Leonardo, H. Lowen, C. Reichhardt, G. Volpe, and G. Volpe. Active particles in complex and crowded environments. *Rev. Mod. Phys.*, 88:UNSP 045006, 2016.
- [Bes06] M. Bestehorn. *Hydrodynamik und Strukturbildung: Mit einer kurzen Einführung in die Kontinuumsmechanik*. Springer, 2006.

- [BFL01] P. Brunet, J. Flesselles, and L. Limat. Parity breaking in a one-dimensional pattern: A quantitative study with controlled wavelength. *Europhys. Lett.*, 56:221–227, 2001.
- [BK06] J. Burke and E. Knobloch. Localized states in the generalized swift-hohenberg equation. *Phys. Rev. E*, 73:056211, 2006.
- [BK07] J. Burke and E. Knobloch. Homoclinic snaking: Structure and stability. *Chaos*, 17:037102, 2007.
- [BKL<sup>+</sup>09] M. Beck, J. Knobloch, D. J. B. Lloyd, B. Sandstede, and T. Wagenknecht. Snakes, ladders, and isolas of localized patterns. *SIAM Journal on Mathematical Analysis*, 41(3):936–972, 2009.
- [But16] J. C. Butcher. *Numerical methods for ordinary differential equations*. John Wiley & Sons, 2016.
- [BZB01] I. V. Barashenkov, E. V. Zemlyanaya, and M. Bär. Traveling solitons in the parametrically driven nonlinear schrödinger equation. *Phys. Rev. E*, 64:016603, 2001.
- [Cah65] J. W. Cahn. Phase separation by spinodal decomposition in isotropic systems. *J. Chem. Phys.*, 42(1):93–99, 1965.
- [CGT16] A. Chervanyov, H. Gomez, and U. Thiele. Effect of the orientational relaxation on the collective motion of patterns formed by self-propelled particles. *Europhys. Lett.*, 115:68001, 2016.
- [CH58] J. W. Cahn and J. E. Hilliard. Free energy of a nonuniform system. i. interfacial free energy. *J. Chem. Phys.*, 28(2):258–267, 1958.
- [CH93] M. C. Cross and P. C. Hohenberg. Pattern formation outside of equilibrium. *Rev. Mod. Phys.*, 65:851–1112, 1993.
- [CK14] Y. Chen and T. Kolokolnikov. A minimal model of predator–swarm interactions. *J. Royal Soc. Interface*, 11(94):20131208, 2014.
- [CRT00] P. Couillet, C. Riera, and C. Tresser. Stable static localized structures in one dimension. *Phys. Rev. Lett.*, 84:3069–3072, 2000.
- [CT65] J. W. Cooley and J. W. Tukey. An algorithm for the machine calculation of complex fourier series. *Mathematics of computation*, 19(90):297–301, 1965.
- [CT15] M. Cates and J. Tailleur. Motility-induced phase separation. *Annu. Rev. Condens. Matter Phys.*, 6:219–244, 2015.
- [Daw08] J. H. P. Dawes. Localized pattern formation with a large-scale mode: Slanted snaking. *SIAM J. Appl. Dyn. Syst.*, 7:186–206, 2008.
- [Deu04] P. Deuffhard. *Newton methods for nonlinear problems: affine invariance and adaptive algorithms*. Springer Series in Computational Mathematics, Springer, Berlin Heidelberg, 2004.

- 
- [DKK91] E. J. Doedel, H. B. Keller, and J. P. Kernevez. Numerical analysis and control of bifurcation problems (I) Bifurcation in finite dimensions. *Int. J. Bifurcation Chaos*, 1:493–520, 1991.
- [DLHG17] J. Delfau, C. Lopez, and E. Hernandez-Garcia. Active cluster crystals. *New J. Phys.*, 19:095001, 2017.
- [DOC<sup>+</sup>12] E. J. Doedel, B. E. Oldeman, A. R. Champneys, F. Dercole, T. F. Fairgrieve, Y. Kuznetsov, R. C. Paffenroth, B. Sandstede, X. J. Wang, and C. H. Zhang. *AUTO-07p: Continuation and bifurcation software for ordinary differential equations*. Concordia University, 2012.
- [DWC<sup>+</sup>14] H. A. Dijkstra, F. W. Wubs, A. K. Cliffe, E. Doedel, I. F. Dragomirescu, B. Eckhardt, A. Y. Gelfgat, A. Hazel, V. Lucarini, A. G. Salinger, E. T. Phipps, J. Sanchez-Umbria, H. Schuttelaars, L. S. Tuckerman, and U. Thiele. Numerical bifurcation methods and their application to fluid dynamics: Analysis beyond simulation. *Commun. Comput. Phys.*, 15:1–45, 2014.
- [EE03] W. Ebeling and U. Erdmann. Dynamics and stochastics of swarms of self-propelled brownian particles. In *Fluctuations and Noise in Biological, Biophysical, and Biomedical Systems*, volume 5110, pages 161–172. International Society for Optics and Photonics, 2003.
- [EG04] K. R. Elder and M. Grant. Modeling elastic and plastic deformations in nonequilibrium processing using phase field crystals. *Phys. Rev. E*, 70:051605, 2004.
- [EGU<sup>+</sup>19] S. Engelnkemper, S. V. Gurevich, H. Uecker, D. Wetzels, and U. Thiele. *Computational Modeling of Bifurcations and Instabilities in Fluid Mechanics*, chapter Continuation for thin film hydrodynamics and related scalar problems, pages 459–501. Computational Methods in Applied Sciences, vol 50. Springer, Berlin, 2019.
- [EKHG02] K. R. Elder, M. Katakowski, M. Haataja, and M. Grant. Modeling elasticity in crystal growth. *Phys. Rev. Lett.*, 88:245701, 2002.
- [ELW<sup>+</sup>12] H. Emmerich, H. Löwen, R. Wittkowski, T. Gruhn, G. I. Tóth, G. Tegze, and L. Gránásy. Phase-field-crystal models for condensed matter dynamics on atomic length and diffusive time scales: an overview. *Adv. Phys.*, 61(6):665–743, 2012.
- [ERK<sup>+</sup>12] K. R. Elder, G. Rossi, P. Kanerva, F. Sanches, S. C. Ying, E. Granato, C. V. Achim, and T. Ala-Nissila. Patterning of heteroepitaxial overlayers from nano to micron scales. *Phys. Rev. Lett.*, 108:226102, 2012.
- [Eva10] L. C. Evans. *Partial Differential Equations*, volume 19. American Mathematical Socie, 2nd edition, 2010. Graduate studies in mathemat.
- [FDT91] S. Fauve, S. Douady, and O. Thual. Drift instabilities of cellular patterns. *Journal de Physique II*, 1(3):311–322, 1991.

- [Fis95] F. E. Fish. Kinematics of ducklings swimming in formation: consequences of position. *J. Exp. Zool.*, 273(1):1–11, 1995.
- [Fri05] R. Friedrich. Group theoretic methods in the theory of pattern formation. In G. Radons, W. Just, and P. Häussler, editors, *Collective Dynamics of Nonlinear and Disordered Systems*, pages 61–84. Springer Berlin Heidelberg, 2005.
- [GBM<sup>+</sup>04] S. V. Gurevich, H. U. Bödeker, A. S. Moskalenko, A. W. Liehr, and H.-G. Purwins. Drift bifurcation of dissipative solitons due to a change of shape: experiment and theory. *Physica D: Nonlinear Phenomena*, 199(1):115 – 128, 2004.
- [GGGC91] R. E. Goldstein, G. H. Gunaratne, L. Gil, and P. Coulet. Hydrodynamic and interfacial patterns with broken space-time symmetry. *Phys. Rev. A*, 43:6700–6721, 1991.
- [GSB<sup>+</sup>06] G. Garrity, J. T. Staley, D. R. Boone, P. De Vos, M. Goodfellow, F. A. Rainey, G. M. Garrity, and K.-H. Schleifer. *Bergey’s Manual® of systematic bacteriology: volume two: the proteobacteria*. Springer Science & Business Media, 2006.
- [GTD<sup>+</sup>18] F. Ginot, I. Theurkauff, F. Detcheverry, C. Ybert, and C. Cottin-Bizonne. Aggregation-fragmentation and individual dynamics of active clusters. *Nature communications*, 9(1):696, 2018.
- [GTL<sup>+</sup>15] F. Ginot, I. Theurkauff, D. Levis, C. Ybert, L. Bocquet, L. Berthier, and C. Cottin-Bizonne. Nonequilibrium equation of state in suspensions of active colloids. *Phys. Rev. X*, 5:011004, Jan 2015.
- [GYU11] R. Golestanian, J. M. Yeomans, and N. Uchida. Hydrodynamic synchronization at low reynolds number. *Soft Matter*, 7:3074–3082, 2011.
- [HJR<sup>+</sup>07] J. R. Howse, R. A. L. Jones, A. J. Ryan, T. Gough, R. Vafabakhsh, and R. Golestanian. Self-motile colloidal particles: From directed propulsion to random walk. *Phys. Rev. Lett.*, 99:048102, 2007.
- [HK64] P. Hohenberg and W. Kohn. Density functional theory (dft). *Phys. Rev*, 136:B864, 1964.
- [HK11] S. M. Houghton and E. Knobloch. Swift-hohenberg equation with broken cubic-quintic nonlinearity. *Phys. Rev. E*, 84:016204, 2011.
- [JBT05] K. John, M. Bär, and U. Thiele. Self-propelled running droplets on solid substrates driven by chemical reactions. *Eur. Phys. J. E*, 18:183–199, 2005.
- [JYS10] H.-R. Jiang, N. Yoshinaga, and M. Sano. Active motion of a janus particle by self-thermophoresis in a defocused laser beam. *Phys. Rev. Lett.*, 105:268302, 2010.
- [KAC09] G. Kozyreff, P. Assemat, and S. J. Chapman. Influence of boundaries on localized patterns. *Phys. Rev. Lett.*, 103(16):164501, 2009.



- 
- [Kap95] R. Kapral. *Chemical Waves and Patterns, Understanding Chemical Reactivity*, volume 10. Kluwer Academic Publishers, Dordrecht, 1995.
- [Kel79] H. B. Keller. *Constructive methods for bifurcation and nonlinear eigenvalue problems*. Computing Methods in Applied Sciences and Engineering, 1977. I. Springer, 1979.
- [Kir17] J. Kirchner. *Scattering of localized states in the active phase field crystal (aPFC) model*. Master's thesis, WWU Münster, 2017.
- [KM94] K. Krischer and A. Mikhailov. Bifurcation to traveling spots in reaction-diffusion systems. *Phys. Rev. Lett.*, 73:3165–3168, 1994.
- [Kno89] E. Knobloch. Pattern selection in binary-fluid convection at positive separation ratios. *Phys. Rev. A*, 40:1549–1559, 1989.
- [Kno16] E. Knobloch. Localized structures and front propagation in systems with a conservation law. *IMA J. Appl. Math.*, 81(3):457–487, 2016.
- [KOGV07] B. Krauskopf, H. M. Osinga, and J. Galan-Vioque, editors. *Numerical Continuation Methods for Dynamical Systems*. Springer, Dordrecht, 2007.
- [KP12] S. G. Krantz and H. R. Parks. *The implicit function theorem: history, theory, and applications*. Springer Science & Business Media, 2012.
- [KT07] G. Kozyreff and M. Tlidi. Nonvariational real Swift-Hohenberg equation for biological, chemical, and optical systems. *Chaos*, 17:037103, 2007.
- [KT14] M. H. Köpf and U. Thiele. Emergence of the bifurcation structure of a langmuir–blodgett transfer model. *Nonlinearity*, 27(11):2711, 2014.
- [Kuz10] Y. A. Kuznetsov. *Elements of Applied Bifurcation Theory*. Springer, New York, 3rd edition, 2010.
- [Lam98] L. Lam. *Nonlinear physics for beginners: fractals, chaos, solitons, pattern formation, cellular automata and complex systems*. World Scientific, 1998.
- [Lan92] J. S. Langer. *An introduction to the kinetics of first-order phase transitions*. Cambridge University Press, 1992.
- [LHA<sup>+</sup>99] O. Lioubashevski, Y. Hamiel, A. Agnon, Z. Reches, and J. Fineberg. Oscillons and propagating solitary waves in a vertically vibrated colloidal suspension. *Phys. Rev. Lett.*, 83:3190–3193, 1999.
- [LJBK11] D. Lo Jacono, A. Bergeon, and E. Knobloch. Magnetohydrodynamic convectons. *J. Fluid Mech.*, 687:595–605, 2011.
- [LKG<sup>+</sup>12] L. Li, M. H. Köpf, S. V. Gurevich, R. Friedrich, and L. Chi. Structure formation by dynamic self-assembly. *Small*, 8(4):488–503, 2012.
- [LNH06] M. Leonetti, J. Nuebler, and F. Homble. Parity-breaking bifurcation and global oscillation in patterns of ion channels. *Phys. Rev. Lett.*, 96:218101, 2006.

- [LSAC08] D. J. B. Lloyd, B. Sandstede, D. Avitabile, and A. R. Champneys. Localized hexagon patterns of the planar Swift-Hohenberg equation. *SIAM J. Appl. Dyn. Syst.*, 7:1049–1100, 2008.
- [MBK10] Y. P. Ma, J. Burke, and E. Knobloch. Defect-mediated snaking: A new growth mechanism for localized structures. *Physica D*, 239:1867–1883, 2010.
- [Mei82] H. Meinhardt. *Models of Biological Pattern Formation*. Academic Press, London, 1982.
- [Men13] A. M. Menzel. Unidirectional laning and migrating cluster crystals in confined self-propelled particle systems. *J. Phys.-Condes. Matter*, 25:505103, 2013.
- [Men15] A. M. Menzel. Tuned, driven, and active soft matter. *Physics reports*, 554:1–45, 2015.
- [MGvH<sup>+</sup>04] E. Meron, E. Gilad, J. von Hardenberg, M. Shachak, and Y. Zarmi. Vegetation patterns along a rainfall gradient. *Chaos, Solitons & Fractals*, 19(2):367 – 376, 2004. Fractals in Geophysics.
- [MJR<sup>+</sup>13] M. C. Marchetti, J. F. Joanny, S. Ramaswamy, T. B. Liverpool, J. Prost, M. Rao, and R. A. Simha. Hydrodynamics of soft active matter. *Rev. Mod. Phys.*, 85:1143–1189, 2013.
- [ML13] A. M. Menzel and H. Löwen. Traveling and resting crystals in active systems. *Phys. Rev. Lett.*, 110:055702, 2013.
- [MMYZ10] E. M. Mauriello, T. Mignot, Z. Yang, and D. R. Zusman. Gliding motility revisited: how do the myxobacteria move without flagella? *Microbiol. Mol. Biol. Rev.*, 74(2):229–249, 2010.
- [MOL14] A. M. Menzel, T. Ohta, and H. Löwen. Active crystals and their stability. *Phys. Rev. E*, 89:022301, 2014.
- [MSAU<sup>+</sup>13] B. M. Mognetti, A. Saric, S. Angioletti-Uberti, A. Cacciuto, C. Valeriani, and D. Frenkel. Living clusters and crystals from low-density suspensions of active colloids. *Phys. Rev. Lett.*, 111:245702, 2013.
- [Mur93] J. D. Murray. *Mathematical Biology*. Springer, Berlin, 1993.
- [MVC18] S. Mallory, C. Valeriani, and A. Cacciuto. An active approach to colloidal self-assembly. *Annu. Rev. Phys. Chem.*, 69:59–79, 2018.
- [NKEG14] N. H. P. Nguyen, D. Klotsa, M. Engel, and S. C. Glotzer. Emergent collective phenomena in a mixture of hard shapes through active rotation. *Phys. Rev. Lett.*, 112:075701, 2014.
- [NMR06] V. Narayan, N. Menon, and S. Ramaswamy. Nonequilibrium steady states in a vibrated-rod monolayer: tetratic, nematic, and smectic correlations. *J. Stat. Mech.-Theory Exp.*, 2006(01):P01005, 2006.

- 
- [OGBSP98] M. Or-Guil, M. Bode, C. P. Schenk, and H.-G. Purwins. Spot bifurcations in three-component reaction-diffusion systems: The onset of propagation. *Phys. Rev. E*, 57:6432–6437, 1998.
- [OGT18] L. Ophaus, S. V. Gurevich, and U. Thiele. Resting and traveling localized states in an active phase-field-crystal model. *Phys. Rev. E*, 98:022608, Aug 2018.
- [Osi96] V. Osipov. Criteria of spontaneous interconversions of traveling and static arbitrary dimensional dissipative structures. *Physica D: Nonlinear Phenomena*, 93(3):143 – 156, 1996.
- [PAC<sup>+</sup>17] B. Pradenas, I. Araya, M. G. Clerc, C. Falcon, P. Gandhi, and E. Knobloch. Slanted snaking of localized Faraday waves. *Phys. Rev. Fluids*, 2:064401, 2017.
- [Pis01] L. M. Pismen. Nonlocal boundary dynamics of traveling spots in a reaction-diffusion system. *Phys. Rev. Lett.*, 86:548–551, Jan 2001.
- [Pis06] L. M. Pismen. *Patterns and interfaces in dissipative dynamics*. Springer Science & Business Media, 2006.
- [PJK83] B. L. Partridge, J. Johansson, and J. Kalish. The structure of schools of giant bluefin tuna in cape cod bay. *Environ. Biol. Fishes*, 9(3-4):253–262, 1983.
- [PL14] A. Petroff and A. Libchaber. Hydrodynamics and collective behavior of the tethered bacterium *thiovulum majus*. *Proceedings of the National Academy of Sciences*, 111(5):E537–E545, 2014.
- [PS05] J. Peiró and S. Sherwin. Finite difference, finite element and finite volume methods for partial differential equations. In *Handbook of materials modeling*, pages 2415–2446. Springer, 2005.
- [PSS<sup>+</sup>13] J. Palacci, S. Sacanna, A. P. Steinberg, D. J. Pine, and P. M. Chaikin. Living crystals of light-activated colloidal surfers. *Science*, 339(6122):936–940, 2013.
- [PVWL18] S. Praetorius, A. Voigt, R. Wittkowski, and H. Lowen. Active crystals on a sphere. *Phys. Rev. E*, 97:052615, 2018.
- [PWL15] A. P. Petroff, X.-L. Wu, and A. Libchaber. Fast-moving bacteria self-organize into active two-dimensional crystals of rotating cells. *Phys. Rev. Lett.*, 114:158102, Apr 2015.
- [RATK12] M. J. Robbins, A. J. Archer, U. Thiele, and E. Knobloch. Modelling fluids and crystals using a two-component modified phase field crystal model. *Phys. Rev. E*, 85:061408, 2012.
- [RB05] R. Richter and I. V. Barashenkov. Two-dimensional solitons on the surface of magnetic fluids. *Phys. Rev. Lett.*, 94:184503, 2005.
- [RBH13] G. S. Redner, A. Baskaran, and M. F. Hagan. Reentrant phase behavior in active colloids with attraction. *Phys. Rev. E*, 88:012305, 2013.

- [REESG08] P. Romanczuk, U. Erdmann, H. Engel, and L. Schimansky-Geier. Beyond the keller-segel model. *Eur. Phys. J.-Spec. Top.*, 157:61–77, 2008.
- [RKBH18] H. Reinken, S. H. L. Klapp, M. Bär, and S. Heidenreich. Derivation of a hydrodynamic theory for mesoscale dynamics in microswimmer suspensions. *Phys. Rev. E*, 97:022613, Feb 2018.
- [RNS<sup>+</sup>99] W.-J. Rappel, A. Nicol, A. Sarkissian, H. Levine, and W. F. Loomis. Self-organized vortex state in two-dimensional dictyostelium dynamics. *Phys. Rev. Lett.*, 83:1247–1250, 1999.
- [RY79] T. V. Ramakrishnan and M. Yussouff. First-principles order-parameter theory of freezing. *Physical Review B*, 19(5):2775, 1979.
- [SAKR18] P. Subramanian, A. J. Archer, E. Knobloch, and A. M. Rucklidge. Spatially localized quasicrystalline structures. *New Journal of Physics*, 20(12):122002, 2018.
- [SBML14] T. Speck, J. Bialké, A. M. Menzel, and H. Löwen. Effective cahn-hilliard equation for the phase separation of active brownian particles. *Phys. Rev. Lett.*, 112:218304, 2014.
- [SFAL00] B. Schäpers, M. Feldmann, T. Ackemann, and W. Lange. Interaction of localized structures in an optical pattern-forming system. *Phys. Rev. Lett.*, 85:748–751, 2000.
- [SOGBP97] C. P. Schenk, M. Or-Guil, M. Bode, and H.-G. Purwins. Interacting pulses in three-component reaction-diffusion systems on two-dimensional domains. *Phys. Rev. Lett.*, 78:3781–3784, May 1997.
- [SSG<sup>+</sup>06] B. Szabó, G. J. Szöllösi, B. Gönci, Z. Jurányi, D. Selmeczi, and T. Vicsek. Phase transition in the collective migration of tissue cells: Experiment and model. *Phys. Rev. E*, 74:061908, 2006.
- [SSW<sup>+</sup>15] A. P. Solon, J. Stenhammar, R. Wittkowski, M. Kardar, Y. Kafri, M. E. Cates, and J. Tailleur. Pressure and phase equilibria in interacting active brownian spheres. *Phys. Rev. Lett.*, 114:198301, 2015.
- [Sum10] D. J. Sumpter. *Collective animal behavior*. Princeton University Press, Princeton, 2010.
- [TAR<sup>+</sup>13] U. Thiele, A. J. Archer, M. J. Robbins, H. Gomez, and E. Knobloch. Localized states in the conserved swift-hohenberg equation with cubic nonlinearity. *Phys. Rev. E*, 87:042915, 2013.
- [TCBP<sup>+</sup>12] I. Theurkauff, C. Cottin-Bizonne, J. Palacci, C. Ybert, and L. Bocquet. Dynamic clustering in active colloidal suspensions with chemical signaling. *Phys. Rev. Lett.*, 108:268303, Jun 2012.
- [TFHE<sup>+</sup>19] U. Thiele, T. Frohoff-Hülsmann, S. Engelnkemper, E. Knobloch, and A. J. Archer. First order phase transitions and the thermodynamic limit. *arXiv preprint arXiv:1908.11304*, 2019.

- [TGT<sup>+</sup>09] G. Tegze, L. Granasy, G. I. Toth, F. Podmaniczky, A. Jaatinen, T. AlaNissila, and T. Pusztai. Diffusion-controlled anisotropic growth of stable and metastable crystal polymorphs in the phase-field crystal model. *Phys. Rev. Lett.*, 103:035702, 2009.
- [Thi10] U. Thiele. Thin film evolution equations from (evaporating) dewetting liquid layers to epitaxial growth. *J. Phys. Condens. Materie*, 22(8):084019, 2010.
- [Thi15] U. Thiele. Münsterian torturials: Lindrop - linear stability of steady solutions of a thin film equation for a horizontal homogeneous substrate. In Thiele et al. [TKG14]. <http://www.uni-muenster.de/CeNoS/Lehre/Tutorials>.
- [TK02] R. Thar and M. Kühl. Conspicuous veils formed by vibrioid bacteria on sulfidic marine sediment. *Appl. Environ. Microbiol.*, 68:6310, 2002.
- [TK05] R. Thar and M. Kühl. Complex pattern formation of marine gradient bacteria explained by a simple computer model. *FEMS Microbiol. Lett.*, 246:75, 2005.
- [TKG14] U. Thiele, O. Kamps, and S. V. Gurevich, editors. *Münsterian Torturials on Nonlinear Science: Continuation*. CeNoS, Münster, 2014. <http://www.uni-muenster.de/CeNoS/Lehre/Tutorials>.
- [Tri18] S. Trinschek. *Thin-Film Modelling of Complex Fluids and Bacterial Colonies*. PhD thesis, Institute of Theoretical Physics, Westfälische Wilhelms-Universität Münster, 2018.
- [TT95] J. Toner and Y. Tu. Long-range order in a 2-dimensional dynamical xy model - how birds fly together. *Phys. Rev. Lett.*, 75:4326–4329, 1995.
- [TT98] J. Toner and Y. Tu. Flocks, herds, and schools: A quantitative theory of flocking. *Phys. Rev. E*, 58:4828–4858, 1998.
- [TTR05] J. Toner, Y. H. Tu, and S. Ramaswamy. Hydrodynamics and phases of flocks. *Ann. Phys.*, 318:170–244, 2005.
- [UG11] N. Uchida and R. Golestanian. Generic conditions for hydrodynamic synchronization. *Phys. Rev. Lett.*, 106:058104, 2011.
- [UMS96] P. B. Umbanhowar, F. Melo, and H. L. Swinney. Localized excitations in a vertically vibrated granular layer. *Nature*, 382:793–796, 1996.
- [UWR14] H. Uecker, D. Wetzel, and J. D. M. Rademacher. pde2path - a matlab package for continuation and bifurcation in 2d elliptic systems. *Numerical Mathematics: Theory, Methods and Applications*, 7(1):58–106, 2014.
- [VCBJ<sup>+</sup>95] T. Vicsek, A. Czirók, E. Ben-Jacob, I. Cohen, and O. Shochet. Novel type of phase transition in a system of self-driven particles. *Physical review letters*, 75(6):1226, 1995.
- [vNW93] J. von Neumann and E. Wigner. Über das verhalten von eigenwerten bei adiabatischen prozessen. In *The Collected Works of Eugene Paul Wigner*, pages 294–297. Springer, 1993.

- [vRBMF95] R. van Roij, P. Bolhuis, B. Mulder, and D. Frenkel. Transverse interlayer order in lyotropic smectic liquid crystals. *Physical Review E*, 52(2):R1277, 1995.
- [WCHM12] W. Wang, L. A. Castro, M. Hoyos, and T. E. Mallouk. Autonomous motion of metallic microrods propelled by ultrasound. *ACS Nano*, 6(7):6122–6132, 2012. PMID: 22631222.
- [WHD<sup>+</sup>13] C. A. Weber, T. Hanke, J. Deseigne, S. Leonard, O. Dauchot, E. Frey, and H. Chate. Long-range ordering of vibrated polar disks. *Phys. Rev. Lett.*, 110:208001, 2013.
- [Wil16] M. Wilczek. *Pattern Formation in Driven Thin Layers of Simple and Complex Liquids*. PhD thesis, Institute of Theoretical Physics, Westfälische Wilhelms-Universität Münster, 2016.
- [WL08] H. H. Wensink and H. Löwen. Aggregation of self-propelled colloidal rods near confining walls. *Phys. Rev. E*, 78:031409, Sep 2008.
- [WN07] H. Wada and R. R. Netz. Model for self-propulsive helical filaments: Kink-pair propagation. *Phys. Rev. Lett.*, 99:108102, 2007.
- [WTE<sup>+</sup>17] M. Wilczek, W. B. H. Tewes, S. Engelnkemper, S. V. Gurevich, and U. Thiele. Sliding drops - ensemble statistics from single drop bifurcations. *Phys. Rev. Lett.*, 119:204501, 2017.
- [WTG<sup>+</sup>15] M. Wilczek, W. B. Tewes, S. V. Gurevich, M. H. Köpf, L. Chi, and U. Thiele. Modelling pattern formation in dip-coating experiments. *Mathematical Modelling of Natural Phenomena*, 10(4):44–60, 2015.
- [You15] P. Young. *Everything you wanted to know about data analysis and fitting but were afraid to ask*. Springer, 2015.

# Danksagung

An dieser Stelle möchte ich meinen Dank aussprechen

- ... Prof. Dr. Uwe Thiele für die kompetente, engagierte und unkomplizierte Betreuung und die Unterstützung bei zahlreichen Bewerbungen für Stipendien und Auslandsvorhaben.
- ... der Studienstiftung des deutschen Volkes für die langjährige finanzielle und ideelle Förderung.
- ... PD Dr. Svetlana Gurevich für ihre Ideen zur Drift-Instabilität.
- ... Prof. Dr. Stefan Linz für die bereitwillige Übernahme der Zweitbegutachtung dieser Arbeit.
- ... Professor Edgar Knobloch for a beautiful time in Berkeley.
- ... meinen Korrekturlesern Tobias Frohoff-Hülsmann, Simon Hartmann, Max Holl, Moritz Ophaus, Fenna Stegemerten und Franziska Veit für zahlreiche Verbesserungsvorschläge.
- ... abermals Tobias Frohoff-Hülsmann für seine unermüdliche Hilfe rund um PDE2PATH.
- ... insbesondere meinen Mitstreitern Sarah Trinschek und Felix Tabbert, aber auch vielen weiteren AG-Mitgliedern, für die schöne gemeinsame Zeit im Büro, auf der Zaferna-Hütte und abseits der Uni.
- ... meiner Familie für viele Dinge, die zu wichtig sind, um als letzter Stichpunkt auf Seite 127 aufzutauchen.





# Lebenslauf

Name: Lukas Ophaus  
Geburtsdatum: 06.04.1989  
Geburtsort: Coesfeld  
Staatsangehörigkeit: deutsch  
Familienstand: ledig

## Ausbildung

seit 10/2014 **Promotionsstudium** am Institut für Theoretische Physik der Westfälischen Wilhelms-Universität Münster unter der Betreuung von Prof. Dr. Uwe Thiele und Prof. Dr. Stefan J. Linz

2013 – 2014 **Masterstudium im Fach Physik**  
an der WWU Münster, Abschluss: M.Sc., Note: 1,0

2011 – 2012 **Erasmusstudium**  
an der University of Strathclyde, Glasgow, GB

2009 – 2013 **Bachelorstudium im Fach Physik**  
an der WWU Münster, Abschluss: B.Sc., Note: 1,1

06/2008 **Allgemeine Hochschulreife**  
am St.-Pius-Gymnasium, Coesfeld, Note: 1,0

## Stipendien

04/2016 – 03/2019 Promotionsstipendium der Studienstiftung des deutschen Volkes

04/2019 – 05/2019 Forschungsstipendium des WWU-Programms International Promovieren für einen Aufenthalt an der University of California, Berkeley, USA

09/2011 – 06/2012 Auslandsstipendium (Studienstiftung des deutschen Volkes und Erasmus-Stipendium) für ein Auslandsjahr im Rahmen des Bachelorstudiums Physik an der University of Strathclyde, Glasgow, GB

11/2009 – 09/2014 Stipendium der Studienstiftung des deutschen Volkes

**Berufstätigkeit**

seit 10/2019	Wissenschaftlicher Mitarbeiter am Center for Nonlinear Science (CeNoS), Drittmittelprojekt: Koordinationsfonds SPP 2171
04/2019 – 08/2019	Wissenschaftliche Hilfskraft (Werkvertrag) am CeNoS der WWU Münster
04/2016 – 03/2019	Wissenschaftliche Hilfskraft am Institut für Theoretische Physik der WWU Münster
10/2014 – 03/2016	Wissenschaftlicher Mitarbeiter am Institut für Theoretische Physik der WWU Münster
04/2013 – 09/2014	Studentische Hilfskraft am Institut für Theoretische Physik der WWU Münster
10/2010 – 09/2011	Studentische Hilfskraft am Institut für Didaktik der Physik der WWU Münster
08/2008 – 09/2009	Zivildienst und anschließende Beschäftigung an der BHD-Seniorenwohnanlage St. Johannes, Coesfeld-Lette